Finding Excited-State Decays of Germanium-76

Kareem Kazkaz

A dissertation submitted in partial fulfillment
of the requirements for the degree of

Doctor of Philosophy

University of Washington

2006

Program Authorized to Offer Degree: Physics

University of Washington
Graduate School

This is to certify that I have examined this copy of a doctoral dissertation by

Kareem Kazkaz

and have found that it is complete and satisfactory in all respects,
and that any and all revisions required by the final
examining committee have been made.

Chair of the Supervisory Committee:

_____
John F. Wilkerson

Reading Committee:

_____
Steven R. Elliott

_____
Gordon Watts

_____
John F. Wilkerson

Date: _____

In presenting this dissertation in partial fulfillment of the requirements for the doctoral degree at the University of Washington, I agree that the Library shall make its copies freely available for inspection. I further agree that extensive copying of this dissertation is allowable only for scholarly purposes, consistent with "fair use" as prescribed in the U.S. Copyright Law. Requests for copying or reproduction of this dissertation may be referred to ProQuest Information and Learning, 300 North Zeeb Road, Ann Arbor, MI 48106-1346, 1-800-521-0600, to whom the author has granted "the right to reproduce and sell (a) copies of the manuscript in microform and/or (b) printed copies of the manuscript made from microform."

Signature_____

Date_____

University of Washington

Abstract

Finding Excited-State Decays of Germanium-76

Kareem Kazkaz

Chair of the Supervisory Committee:
Professor John F. Wilkerson
Department of Physics

Of all the fermions in the Standard Model of Particle Physics, the neutrinos alone are still lacking measurements of the fundamental properties of absolute mass and the Majorana/Dirac nature of the particles. The Majorana experiment is a proposed ^{76}Ge-based search for neutrinoless double-beta ($0\nu\beta\beta$) decay, a decay which, if observed, may answer the questions of the neturino's mass and nature. Majorana's sensitivity will also allow for searches of two-neutrino double-beta decays to an excited state (ES2$\nu\beta\beta$) of the final nucleus. This latter class of experiments can be used to elucidate the theoretical nuclear matrix elements that govern a broad array of nuclear interactions.

A GEANT4- and ROOT-based simulation framework called MaGe was used to determine Majorana's ES2$\nu\beta\beta$ observation efficiency. The reliability of MaGe was tested by comparing a calculated efficiency against an experimentally measured efficiency using two surrogate signals, each with a decay signature similar to ES2$\nu\beta\beta$ decays. The surrogate signals come from the decay of ^{77}Ge, created via neutron activation of a natural germanium, multi-crystal radiation detector. The ratio of the experimental and simulation efficiencies were 1.17 ± 0.17 (stat.) ± 0.27 (sys.) and 0.96 ± 0.19 (stat.) ± 0.27 (sys.).

MaGe was then used to calculate the sensitivity of a Majorana detector module to the ES2$\nu\beta\beta$ decays. Depending on the segmentation scheme of the Majorana crystals, the Majorana module will observe 25 signal counts and 0.009 background counts (strict analysis cuts) or 330 signal counts and roughly 40 background counts (relaxed analysis cut) over 11 months of live time. These counts rates assume a half life of 10^{23} years for a two-neutrino double-beta decay to an excited state of the final nucleus. A measurement of the ES2$\nu\beta\beta$ half life can be used to test theoretical models of nuclear double-beta decays, leading to more accurate predictions of neutrino mass if a $0\nu\beta\beta$ decay signal is observed.

TABLE OF CONTENTS

LIST OF FIGURES

LIST OF TABLES

GLOSSARY

ACTIVATED ISOTOPES: Radioactive isotopes created by absorption of a neutron on a nucleus

ACTIVE NEUTRINO: A neutrino that acts according to the left-handed electroweak theory of the Standard Model of particle physics

CLOVER: A high-purity germanium detector made by Canberra/Urysis consisting of four germanium crystals each with two-fold segmentation

COINCIDENCE: Two or more particles emitted via the same or related processes on a time scale much shorter than the timing discrimination of a detector

COSMOGENIC ISOTOPES: Radioactive isotopes that are created by cosmic rays. The radioisotopes made be created by absorption of a proton or neutron or by breaking up a nucleus

DIRAC PARTICLE: A particle distinct from its charge-conjugate partner

ENRICHED GERMANIUM: Germanium that has been processed to increase its isotopic abundance of ^{76}Ge to 86%.

EXTERNAL ACTIVITY: Radioactive decays originating outside the active region of a radiation detector

INTERNAL ACTIVITY: Radioactive decays originating within the bulk of a material

MAGE: The GEANT4- and ROOT-based simulation package cooperatively developed by the Majorana and GERDA collaborations

MAJORANA PARTICLE: A particle that is self-conjugate under charge transformation

MEGA: The Multi-Element Germanium Array, a high-purity germanium detector developed by Pacific Northwest National Laboratory, Los Alamos National Laboratory, and the University of Washington

MULTI-SITE EVENT: A collection of simultaneous single-site events spatially distributed in a volume greater than the resolution capabilities of the detector hardware and software

N-HIT: The number of detector elements with energy deposition for any given event

SEGA: The Segmented Enriched Germanium Assembly, an enriched and segmented germanium detector developed by Triangle Universities Nuclear Laboratory and North Carolina State University

SEESAW MECHANISM: The theoretical prediction that if the light neutrinos emitted in beta decay are Majorana particles, every light neutrino will have a heavy neutrino partner

SINGLE-SITE EVENT: A total energy deposition within a detector localized to a volume smaller than the resolution capabilities of the detector hardware and software

STERILE NEUTRINO: A neutrino that does not interact in a manner specified by the Standard Model of particle physics

SUM PEAK: A feature in an energy spectrum that is created only by two or more particles depositing their full energy in a detector element at the same time

ACKNOWLEDGEMENTS

Obtaining a Ph.D. in physics has been a goal of mine for the past 14 years. It has been a long journey, and striving for this goal has introduced me to many wonderful people.

I thank my advisor, John Wilkerson, for demanding careful, conscientious analysis. Thanks also to Steve Elliott at Los Alamos National Laboratory for his hospitality and direction while I collected my experimental data. Thank you to Gordon Watts for guiding my first steps in graduate-level experimental physics.

Thank you, Craig Aalseth and Todd Hossbach at Pacific Northwest National Laboratory, for your patience during my start toward Low-Background Enlightenment. Thanks to Reyco Henning at Lawrence Berkeley National Laboratory for shepherding the development of MaGe, without which I would not have been able to report anything meaningful. Thanks to the UW peanut gallery for help in matters statistical and simulation as well as the ice cream accompaniment. Thank you to the entire Majorana collaboration for helping to fill in the billion and a half gaps in my understanding of just what it is we are doing.

There are people who have helped me beyond the bounds of science. Vic Gehman has been a great officemate and friend over the past years. Minesh Bacrania and Laura Stonehill have been wonderful people to commiserate with as we both approached our dissertation defense dates. My thanks also to Tom and Heather Butler for your friendship and compassion.

Thanks to my parents Ghaffar and Peggy and my sisters Rana and Lara for stalwartly and proudly remaining interested in my research, even though I couldn't always articulate how what I was doing at any particular time was important.

Finally, although there have been a number of people that have given me substantial amounts of support and encouragement, the only person who has had to deal with me day-in and day-out, through every equation, every graph, every collaboration meeting, every victory and defeat, is my wife, Helene. I hope the people mentioned above will forgive me for saying that of everyone of whom I've made demands, it is her support that was the most valuable.

The sun shine above
Noise and shade spread from dense trees
The first acorn falls

DEDICATION

To my family. You know who you are.

Chapter 1

THE HISTORY AND FUTURE OF THE NEUTRINO

In the late 19^{th} century, J. J. Thompson used an evacuated glass bulb with two charged electrodes inside it to create what was then known as a cathode ray. His experiment showed that this cathode ray carried a negative charge, and postulated that the cathode ray was in reality a stream of particles. By projecting the beam through appropriately tuned electric and magnetic fields, he was able to measure the ratio of the charge on these particles to their mass, and discovered their mass was very small [1]. Today, we know these particles by the name "electron", and Thompson's experiment was written into the history books as the first fundamental particle physics experiment.

Since that time, physicists have made enormous progress in expanding our knowledge of basic particles. Following Thompson's 1897 discovery of electrons, the nucleus was discovered in 1909 [2], the proton a decade later [3], and the neutron in 1932 [4]. Particle physics was on a roll.

Unfortunately, there was a stumbling block in the middle of all these discoveries. In 1914 James Chadwick published results from an experiment that measured the energy spectrum of the beta particles that are emitted as part of their namesake radiation [5]. The theory at the time held that these beta particles should all be emitted with discrete energies, and Chadwick's discovery to the contrary seemed to throw into doubt the law of Conservation of Energy. Since then, there have been blind alleys, dead ends, alternate explanations, a Desperate Remedy, a rejected theory that eventually proved correct, evidence, refutations, and finally acceptance of the explanation for Chadwick's results.

The particle that lies at the center of the confusion initiated by Chadwick is the neutrino. Neutrinos, of all fundamental particles so far observed, are the particles about which the least is known. We know they are electrically neutral, have exceedingly small mass, and are not an inherent part of the atom. Because neutrinos interact only via the weak nuclear force, to observe any specific neutrino would require a detector that is light-years long. Because of these inherent difficulties in detecting neutrinos, it was 42 years after that 1914 publication of the beta spectrum before researchers at Los Alamos National Laboratory, working on an experiment dubbed Project Poltergeist [6], confirmed their observation of the neutrino [7]. It took another five decades after Project Poltergeist for science to advance to the stage of precision neutrino experiments.

If neutrinos are so hard to observe, how did physicists come to guess at their existence in the

first place? What other questions about the neutrino have we answered? What questions remain? How will we fill in some of those gaps in our knowledge? What further questions await us?

1.1 Prediction and evidence of neutrinos

1.1.1 Early history

In 1896 Henri Becquerel found himself the chair of the physics department at the École Polytechnique. That year he made an amazing discovery, that uranium salts were able to expose a photographic plate even though the plate was wrapped with an opaque sheet of paper [8]. The year before Wilhelm Röentgen had discovered X-rays [9], but this new radiation coming from the uranium seemed to be different from X-rays—the latter were created using a beam of "cathode rays", but the uranium could expose the photo plate by itself, without any assistance from a secondary beam. Evidently, whatever radiation was present in uranium was inherent to the substance itself.

In the following years Becquerel was able to show that the particles emitted in this new kind of radiation had the same characteristics as electrons. Not yet able to conclusively show that these particles were indeed electrons, they were given the name beta particles. Little else was known about beta radiation, and the physics community was slightly confused by these particles. Betas had mass and charge, so some thought they should behave like alpha radiation, which also has mass and charge. Some surmised that since betas could penetrate through matter more easily than alphas, that they would ultimately behave more like X-rays, which are massless and neutral.

One thing that alphas and X-rays had in common, though, were their discrete energy levels. Surely, thought the physicists of the day, the beta spectrum will also be quantized. Unfortunately, beta radiation was not quite so simple. J. Chadwick's paper of 1914 showed a continuous beta spectrum, implying that some energy was disappearing. This sparked the question, if the beta particle doesn't have all the energy it should, where does the missing energy go? In response, Neils Bohr questioned the Law of Conservation of Energy. Others, such as Rutherford, proposed fixes [10] that turned out to be dead ends.

The debate continued for over a decade over whether or not the beta spectrum really was continuous, whether only one beta particle was emitted in each decay, and whether undetected betas were carrying away excess energy. The debate was put to rest in 1927 when Ellis and Wooster definitively responded to all these issues [11], in the process measuring the beta spectrum of Radium E (shown in Fig. 1.1).

There was an additional twist on the problem. Radium E and its decay product were known to have integer spin, yet the beta particle only has half-integer spin. Any excess energy carried away by gamma particles would also be integer spin, which means there was either a half integer deficit or surplus in the reaction. In either case, not only was conservation of energy seemingly violated,

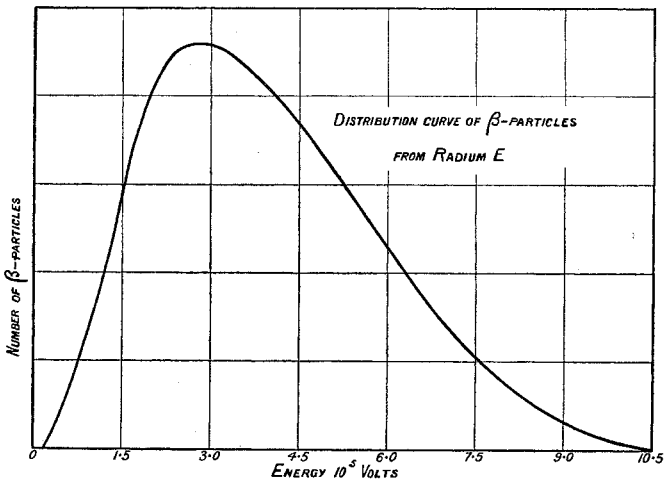

Figure 1.1: Beta spectrum of Radium E. The spectrum shows that only a small percentage of beta particles have close to the expected full kinetic energy (about 10.5×10^5 volts on this graph). A plurality of betas have a kinetic energy roughly one third the maximum amount. According to the theory of the day, *all* beta energies should have had the maximum kinetic energy. Nowadays, radium E is known as ^{210}Bi, and the missing energy is known to be carried away by an anti-neutrino. Figure taken from Ellis & Wooster [11].

but so was conservation of angular momentum.

After a few more years of argument and discussion, Wolfgang Pauli sent a letter to the Federal Institute of Technology in Zürich. Pauli's 1930 letter included the following[1]

> ...considering the 'false' statistics of N-14 and Li-6 nuclei, as well as the continuous β-spectrum, I have hit upon a desperate remedy to save the "exchange theorem" of statistics and the energy theorem. Namely...the possibility that there could exist in the nuclei electrically neutral particles...which have spin 1/2...The continuous β-spectrum would then become understandable by the assumption that in β decay [this particle] is emitted together with the electron, in such a way that the sum of the energies...is constant.

Interestingly enough, his doubts about the existence of this new particle were similar to those of many modern scientists. Pauli went on to write "I admit that my remedy may appear to have a

[1]This letter was published in Physics Today [12].

small *a priori* probability because [these particles], if they exist, would probably have long ago been seen."

With a new focus, the physics community set about testing for the existence of this new particle, eventually named a *neutrino* by Enrico Fermi. In a way, the continuous beta spectrum already provided proof of the existence of the neutrino. Many people remained skeptical, however, claiming that if this ghostly particle were involved in beta reaction, they should be able to induce inverse beta reactions in a detector far from the neutrino source. This remote detection was finally performed in 1953 by F. Reines and C. L. Cowan [13], and confirmed in 1956 [7] by the same group.

1.1.2 Modern history

Since the Reines and Cowan experiment, scientists have filled in much of their knowledge of the neutrino. Various experiments have made direct observations of neutrinos, identifying how they interact with other particles. Neutrino science has progressed to the point where we are not simply searching for them and measuring their properties, but using them as probes to gather information about the interior of warming of the Earth [14], the nuclear burning that powers our sun [15], and the catastrophic energies released in a supernova [16]. What was once a hypothetical conjecture has now entered a period of precision measurements, and this desperate remedy is taken for granted.

1.2 Properties of neutrinos

What is known today about the neutrino and what questions remain? First the basics:

- There are three active flavors of neutrino: ν_e, ν_μ, ν_τ.
- There are at least three masses of neutrinos: ν_1, ν_2, ν_3. Interestingly, the three masses of neutrinos do not correspond one-to-one with the flavors of neutrino.
- Neutrinos are neutral, fundamental particles.
- Neutrinos have spin 1/2.
- The ν_e's mass is at most about 2.2 eV [17], and probably weighs much less than that. By comparison, the electron's mass is 511,000 eV.
- The difference between the masses squared of the ν_1 and ν_2 (i.e., $\left|m_1^2 - m_2^2\right|$) is about 80 meV^2 [18].
- The difference between the masses squared of the ν_2 and ν_3 (i.e., $\left|m_2^2 - m_3^2\right|$) is about 2400 meV^2 [19].

While the basic information is not difficult to enumerate, there are a few mighty big devils hiding in all the details. It's true that there are three active flavors of neutrinos, but those three

flavors do not have well-defined masses, leading to neutrino mixing. To explain the very light masses of the neutrinos, a "seesaw" theory has been developed that requires three exceedingly heavy neutrino partners. One experiment has predicted the existence of what is called a sterile neutrino that does not interact via the same left-handed weak nuclear force as active neutrinos. We don't even have solid experimental evidence as to whether or not neutrinos have distinct antimatter partners like electrons and positrons (Dirac particles), or if they are their own antiparticles, like photons (Majorana particles).

1.2.1 Neutrino mixing

For an expanded introduction to the nonintuitive behavior of neutrinos, we take a closer look at neutrino mixing. Deeper explorations of other neutrino mystifications and bedazzlements are explored in Chapters 2 and 3.

Neutrinos exhibit a beautiful complexity governed by quantum mechanics. Part of this complexity is that neutrinos interact with other particles via the weak nuclear force, but when they are not interacting with another particle they still undergo processes that might induce the neutrino to change its identify. A neutrino born as a ν_e might interact later on as a ν_μ.

This schizophrenia can be written mathematically. We study the case of two-neutrino mixing here, and later expand to the case of three neutrinos. Consider the two neutrino weak eigenstates ν_e and ν_μ. These neutrinos do not have well-defined masses, but are instead made up of a superposition of mass eigenstates ν_1 and ν_2. We can express the weak eigenstates as a function of mass eigenstates via a single mixing angle, θ_{12}:

$$\begin{pmatrix} \nu_e \\ \nu_\mu \end{pmatrix} = \begin{pmatrix} \cos\theta_{12} & \sin\theta_{12} \\ -\sin\theta_{12} & \cos\theta_{12} \end{pmatrix} \begin{pmatrix} \nu_1 \\ \nu_2 \end{pmatrix} \tag{1.1}$$

Assume, for the sake of simplicity, that two protons in the sun fuse into a single deuteron, turning one proton into a neutron, and emitting a positron and a ν_e. What happens to this neutrino after it emerges from the sun and travels the 93 million miles of empty space to the Earth? When the neutrino is in flight (traveling through vacuum, and therefore not interacting with matter), it evolves according to the Schrödinger equation. The neutrino is created as a pure ν_e at a time 0, then a time t later, we have

$$\begin{aligned} |\nu_e(t)\rangle &= e^{-iHt} |\nu_e(t=0)\rangle \\ &= e^{-iHt} (\cos\theta_{12} |\nu_1\rangle + \sin\theta_{12} |\nu_2\rangle) \\ &= \cos\theta_{12} e^{-iE_1 t} |\nu_1\rangle + \sin\theta_{12} e^{-iE_2 t} |\nu_2\rangle \end{aligned} \tag{1.2}$$

where H is the Hamiltonian operator and E_1 (E_2) is the energy of the $|\nu_1\rangle$ ($|\nu_2\rangle$) mass eigenstate. The neutrinos here are free particles, so operating on the states with the Hamiltonian only picks out the particle's kinetic energy. We rewrite E_1 and E_2 using the relativistic energy equation of a free particle, with the speed of light c set to 1:

$$\begin{aligned} E^2 &= p^2 + m^2 \\ \implies E &= \sqrt{p^2 + m^2} \\ &= p\sqrt{1 + \left(\frac{m}{p}\right)^2} \\ &= p\left(1 + \frac{1}{2}\left(\frac{m}{p}\right)^2 - \frac{1}{8}\left(\frac{m}{p}\right)^4 + \ldots\right) \end{aligned} \tag{1.3}$$

where p is the momentum and m the mass of the particle. Neutrinos have at most about 2 eV of mass. Solar neutrinos, however, have a momentum over one million times as large as their mass. We can therefore simplify Eq. (1.3):

$$\begin{aligned} E &\approx p\left(1 + \frac{1}{2}\left(\frac{m}{p}\right)^2\right) \\ &= p + \frac{1}{2}\frac{m^2}{p} \end{aligned} \tag{1.4}$$

Plugging Eq. (1.4) for the two mass eigenstates into Eq. (1.2) gives

$$\begin{aligned} |\nu_e(t)\rangle &= \cos\theta_{12}\,\exp\left(-i\left(p + \frac{1}{2}\frac{m_1^2}{p}\right)t\right)|\nu_1\rangle + \sin\theta_{12}\,\exp\left(-i\left(p + \frac{1}{2}\frac{m_1^2}{p}\right)t\right)|\nu_2\rangle \\ &= \exp\left(-i\left(\frac{1}{2}\frac{m_1^2}{p}\right)t\right)\left(\cos\theta_{12}\,|\nu_1\rangle + \sin\theta_{12}\,|\nu_2\rangle\,\exp\left(-\frac{i}{2p}\Delta m_{12}^2 t\right)\right) \end{aligned} \tag{1.5}$$

where $\Delta m_{12}^2 = \left|m_2^2 - m_1^2\right|$. Note that the two mass states have the same momentum p. If we further assume that $E \approx p$ and that the neutrinos essentially travel at the speed of light, then the time the neutrinos are in flight is the same as the distance they travel: $t = L$ (with c set to 1). Thus we have

$$|\nu_e(t)\rangle = \exp\left(-i\left(\frac{1}{2}\frac{m_1^2}{p}\right)t\right)\left(\cos\theta_{12}\,|\nu_1\rangle + \sin\theta_{12}\,|\nu_2\rangle\,\exp\left(-\frac{i}{2}\Delta m_{12}^2\frac{L}{E}\right)\right) \tag{1.6}$$

By multiplying Eq. 1.6 by $\langle\nu_\mu|$ from the left and taking the absolute value squared, we can write

down the probability that what started life as a ν_e will have changed into a ν_μ:

$$P_{\nu_e \to \nu_\mu} = \sin^2(2\theta_{12}) \sin^2\left(\frac{\Delta m^2_{12}}{4}\frac{L}{E}\right) \tag{1.7}$$

According to Eq. (1.7), how quickly a ν_e oscillates into a ν_μ and back is related to the mass splitting squared Δm^2_{12} and the ratio of energy to distance traveled. The amplitude of that oscillation is set by the angle θ_{12}.

This formalism can be expanded to the case of three neutrinos. In the three-neutrino mixing matrix, there are *a priori* four unknowns: θ_{12}, θ_{23}, θ_{13}, and δ. The θ mixing angles appear in Eq. 1.8 as c_{nm} and s_{nm}, which stand for $\cos\theta_{nm}$ and $\sin\theta_{nm}$. The δ angle allows for CP violation. We use the Particle Data Group's convention [20] for the three-neutrino mixing matrix equation:

$$\begin{pmatrix} \nu_e \\ \nu_\mu \\ \nu_\tau \end{pmatrix} = \begin{pmatrix} c_{12}c_{13} & s_{12}c_{13} & s_{13}e^{-i\delta} \\ -s_{12}c_{23} - c_{12}s_{23}s_{13}e^{i\delta} & c_{12}c_{23} - s_{12}s_{23}s_{13}e^{i\delta} & s_{23}c_{13} \\ s_{12}s_{23} - c_{12}c_{23}s_{13}e^{i\delta} & -c_{12}s_{23} - s_{12}c_{23}s_{13}e^{i\delta} & c_{23}c_{13} \end{pmatrix} \begin{pmatrix} \nu_1 \\ \nu_2 \\ \nu_3 \end{pmatrix} \tag{1.8}$$

Values for the mixing angles are available from the same experiments that gave us measurements of the mass splittings. They give the best fit values as

$$\begin{aligned} \theta_{12} &= 33.9^\circ \text{ [18]} \\ \theta_{23} &= 45.0^\circ \text{ [19]} \\ \theta_{13} &< 10^\circ \text{ [21]} \end{aligned} \tag{1.9}$$

Note that the value for θ_{13} is an upper limit, and not a measurement.

1.2.2 Seesaw mechanism and sterile neutrinos

While an exhaustive review of neutrino theory is beyond the scope of this work, we introduce two more concepts in this Section that demonstrate additional aspects of current neutrino research.

The seesaw mechanism

One interesting aspect of the neutrinos is their very light mass compared to the masses of the other fundamental particles. One theory predicts that if neutrinos are Majorana particles, then in addition to the very light neutrinos ν_e, ν_μ and ν_τ, there are three very heavy partners N_e, N_μ, and N_τ. The masses between the light particles and heavy particles are related by the equation

$$M_\nu = M_D M_N^{-1} M_D^T \tag{1.10}$$

Each term in Eq. (1.10) is a 3×3 mass matrix. M_ν and M_N are the matrices of the light and heavy neutrinos, respectively. M_D is a mass matrix with values roughly determined by the mass of the other quarks and charged leptons, and can therefore range from about 1 MeV to 200 GeV. As can be seen, M_ν and M_N are inversely proportional. Plugging in the value of 10 meV for the mass of the light neutrino and using the mass of the electron (~1 MeV) as the Dirac mass results in a heavy neutrino mass of about 10^5 GeV. This mass scale would require a particle accelerator 100 times as powerful as Fermilab's Tevatron. If a value of 250 GeV is used in the Dirac mass term, the heavy neutrino mass becomes 10^{12} GeV. Building particle accelerator to probe that mass scale is ludicrously beyond today's technology, so one of the current avenues of theoretical neutrino research is how to test for the existence of the seesaw mechanism.

While the theory behind neutrinoless double-beta ($0\nu\beta\beta$) decay will be discussed in the next chapter, we will address how it might relate to the seesaw mechanism here. In $0\nu\beta\beta$ decay, the most prevalent theory suggests that a light neutrino is emitted from one neutron within a nucleus and is absorbed by another neutron in the same nucleus. The resulting decay nucleus may be in the ground state or in an excited state. It might be possible, however, for a heavy neutrino to be exchanged by the neutrons instead of a light neutrino. Measuring how often the decay proceeds to the ground state of the decay nucleus versus an excited state might elucidate the nature of the particle traveling between the neutrons [22].

Finally, one tantalizing aspect of the seesaw mechanism is that it could explain the apparent matter/anti-matter imbalance in the universe. Heavy Majorana neutrinos can decay via lepton-number-violating processes, leading to an overabundance of leptons over anti-leptons. This overabundance can create a prevalence of baryons over anti-baryons [23]. Neutrinos may actually explain how the matter around us came to exist.

Sterile neutrinos

At the beginning of this section we described the known properties of the neutrinos. Those properties include measurements of the neutrino mass splittings, and were found to be 80 meV^2 for $\left|m_1^2 - m_2^2\right|$ and 2400 meV^2 for $\left|m_2^2 - m_3^2\right|$. In 2001 an experiment called the Liquid Scintillator Neutrino Detector (LSND) found evidence for a third mass splitting somewhere between approximately 0.2 and 10 eV^2 [24]. This result might be explained by the existence of what are called *sterile neutrinos*.

Sterile neutrinos are neutrinos that do not interact via the left-handed weak nuclear force specified by the current Standard Model of particle physics. The Model stipulates that all neutrinos interact in a fundamentally left-handed manner, and all anti-neutrinos in a right-handed manner. It could be that the sterile neutrino is simply a right-handed neutrino. They could make their presence felt by participating in neutrino oscillations—a process similar to the one by which a ν_e may be

observed later to be a ν_μ, but not necessarily through direct Standard Model interactions.

LSND's results are currently being tested by an experiment at Fermilab called MiniBOONE [25]. If MiniBOONE confirms LSND's results, it would call for another drastic revision in how the Standard Model of particle physics treats neutrinos.

1.3 The Majorana Experiment

The current work is performed under the auspices of a proposed double-beta decay experiment called Majorana. Two-neutrino double-beta ($2\nu\beta\beta$ decay, although it is very rare, is allowed in the Standard Model, and has been observed in 11 isotopes. Neutrinoless double-beta decay ($0\nu\beta\beta$) decay, however, is not allowed by the Standard Model, and that is the focus of Majorana. All $0\nu\beta\beta$ decay experiments have two primary goals: determine whether the neutrino is its own anti-particle, and if so, determine the absolute mass of the neutrino.

The isotope that Majorana will use to study double-beta decays is ^{76}Ge. Germanium crystals can be used to make radiation detectors, so the idea behind the experiment is to make radiation detectors enriched with ^{76}Ge. The idea is that the nuclei in the detector will decay and provide the $0\nu\beta\beta$ signal. Majorana is conceived of as a modular detector, with each module using about 60 kg of enriched germanium crystals (86% ^{76}Ge). The crystals are in a close-packed configuration, and are segmented to make each individual detector act as an array of smaller detectors. The current plans involve one, two, or three modules, depending on the availability of funding.

Double-beta decays are the rarest events ever experimentally observed. The half-life of ^{76}Ge via $2\nu\beta\beta$ decay is around 10^{21} years, or 100 billion times the age of the universe itself. This means that if a lump of ^{76}Ge were created in the Big Bang and it started decaying away, the lump would still be 99.999999% ^{76}Ge. By contrast, the half-life of $0\nu\beta\beta$ of ^{76}Ge is at least 10,000 times as long as that of two-neutrino double-beta decay. At that rate, a 1 kilogram lump of ^{76}Ge would have a single nucleus decay via $0\nu\beta\beta$ about once every two years.

The low rate of $0\nu\beta\beta$ decays puts any such search for them in the low-background category. To be able to differentiate the signal from background requires the background levels be exceedingly low. For this reason, the Majorana detector would have to be built underground so that the Earth can shield the instruments from cosmic rays, and heroic efforts must be undertaken to reduce or identify all background radiation present in the environment near the detector. The close-packing and segmentation mentioned above are used to identify background radiation.

The Majorana collaboration has several detectors that are being used to analyze different aspects of the proposed Majorana experimental design. One detector at Los Alamos National Laboratory is used to study the effects of segmentation and pulse shape analysis in natural (i.e., unenriched), segmented germanium detectors in a close-packed array [26]. A detector at Triangle Universities Nuclear Laboratory, called the Segmented Enriched Germanium Assembly (SEGA), is used to study

background-reduction methods of a highly-segmented single enriched detector [27]. A third detector under construction at Pacific Northwest National Laboratory and the Waste Isolation Pilot Plant, called the Multi-Element Gamma Assay (MEGA) will be used to study, among other topics, coincidences and construction issues using a close-packed array of natural, unsegmented detectors [28].

Chapter 2

DOUBLE-BETA DECAY

As introduced in the previous chapter, the Majorana experiment studies double-beta decays to determine whether the neutrino is its own antiparticle. Just what is double-beta decay anyway? Why were scientists not able to directly observe the decay until 1987? What might double-beta decays be able to teach us about neutrinos, and how?

2.1 Beta Decay

In order to explain double-beta decay, it first makes sense to understand regular beta decay. An example of beta decay is when a neutron turns into a proton and ejects an electron and electron anti-neutrino:

$$n \rightarrow p + e^- + \overline{\nu}_e \tag{2.1}$$

Fig. 2.1 shows a cartoon of this process. This is actually only one form of beta decay. We can move particles from one side of the equation to the other if we turn the particle into its anti-particle. For instance, moving the antineutrino to the other side of the equation and reversing the arrow gives

$$p + e^- \rightarrow n + \nu_e$$

This electron capture reaction describes the nuclear reaction that occurs when a sun collapses into a neutron star. The equation

$$\overline{\nu}_e + p \rightarrow e^+ + n$$

describes the fundamental reaction in the 1953 Cowan and Reines experiment that first observed neutrinos far from their source [13].

For some isotopes, it's possible for a proton within a nucleus to decay, turning into a neutron and emitting a positron and electron neutrino. This is referred to as β^+ decay:

$$p \rightarrow n + e^+ + \overline{\nu}_e$$

For this chapter, the phrase "beta decay" will always refer to a decay that emits an electron, and β^+

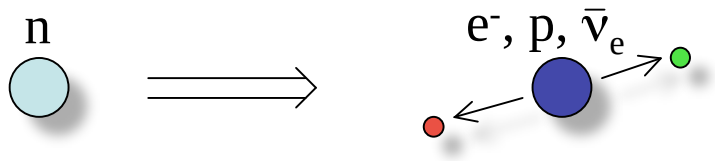

Figure 2.1: Cartoon of neutron decay. The neutron, composed of two down quarks and an up quark, turns into a proton composed of two up quarks and a down quark. An electron and electron anti-neutrino are ejected. The half life of a bare neutron is a little over 10 minutes.

decay will, when necessary, be explicitly denoted.

2.1.1 Calculating the half life of the bare neutron

Because it will aid in the discussion of the half life of an isotope that undergoes double-beta decay, we take some time to discuss the simpler case of single-beta decay. The simplest single-beta decay known is the decay of a bare neutron.

The half life of a particle can be calculated using Fermi's Golden Rule[1]:

$$d\Gamma = \frac{\left\langle |M|^2 \right\rangle}{2\hbar\, m_1} \left(\frac{d^3\overrightarrow{p_2}}{(2\pi)^3\, 2\, E_2} \right) \left(\frac{d^3\overrightarrow{p_3}}{(2\pi)^3\, 2\, E_3} \right) ... \left(\frac{d^3\overrightarrow{p_N}}{(2\pi)^3\, 2\, E_N} \right) (2\pi)^4 \delta^4(p_1 - p_2 - p_3 - ... - p_n) \qquad (2.2)$$

where particle 1 decays into particles 2 through N. M is called the *nuclear matrix element (NME)*, and m_x, $\overrightarrow{p_x}$, p_x, and E_x are the mass, 3-momentum, 4-momentum, and energy of particle x. Finally, $\delta^4(...)$ is a four-dimensional Dirac delta function, and as in the previous chapter the speed of light c is set to 1. Setting aside the nuclear matrix element term, the rest of the equation is the phase space. $d\Gamma$ is the differential decay rate, and before it is integrated it describes the energy spectrum of the outgoing particles. When integrated, Γ gives the inverse half life of the particle.

The neutron, as described above, decays into three particles, and its differential decay rate is given by

$$d\Gamma = \frac{\left\langle |M|^2 \right\rangle}{2\hbar\, m_n} \left(\frac{d^3\overrightarrow{p_\nu}}{(2\pi)^3\, 2\, E_\nu} \right) \left(\frac{d^3\overrightarrow{p_p}}{(2\pi)^3\, 2\, E_p} \right) \left(\frac{d^3\overrightarrow{p_e}}{(2\pi)^3\, 2\, E_e} \right) (2\pi)^4 \delta^4(p_n - p_\nu - p_p - p_e) \qquad (2.3)$$

where the neutrino, proton, and electron are explicitly labeled (see the Feynman diagram, Fig. 2.2).

[1] A concise derivation of Fermi's Golden Rule is found in Krane [29].

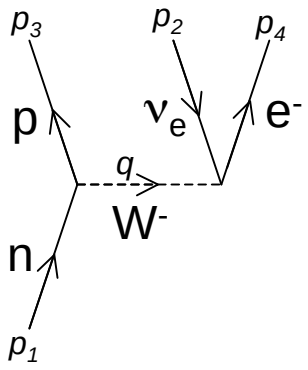

Figure 2.2: Feynman diagram of neutron decay. The p_n and q are 4-momenta. With a few approximations, the half life of the neutron is calculated to be within 6% of the experimental value (see Chapter 10 of Griffiths [30]).

We use the Feynman rules to calculate M. Referring to Fig. 2.2, the leptonic vertex contributes a factor of

$$\frac{-ig_W}{2\sqrt{2}}\,\gamma^\mu\left(1-\gamma^5\right) \tag{2.4}$$

where g_W is the weak coupling constant, and γ^μ and γ^5 refer to the Dirac matrices[2]. The $\left(1-\gamma^5\right)$ construction is the mathematical expression of the inherent left-handedness of the weak interaction. The hadronic vertex contributes a factor of

$$\frac{-ig_W}{2\sqrt{2}}\,\gamma^\mu\left(g_V-g_A\gamma^5\right)V_{ud} \tag{2.5}$$

In Eq. (2.5), g_V and g_A refer to the vector and axial vector coupling constants, and basically account for the fact that the neutron and proton are not fundamental particles, but are composite particles made of up and down quarks. Note again the basic left-handed interaction, where the g_V and g_A pull "double duty" describing the strength of the left-handedness. The V_{ud} term is present because of quark mixing, and is equal to $\cos\theta_c$, where θ_c is the Cabibbo angle ($\theta_c \approx 12.8°$).

Finally, the propagator contributes a term

[2]See any particle physics textbook for a discussion of the Dirac matrices.

$$\frac{-i\left(g_{\mu\nu}-\frac{q_\mu q_\nu}{M_W^2}\right)}{q^2-M_W^2} \xrightarrow[M_W^2 \gg q^2]{} \frac{ig_{\mu\nu}}{M_W^2} \tag{2.6}$$

where q is the momentum of the propagator and M_W is the mass of the W boson. The momentum of the outgoing particles is on the order of the mass difference between the neutron and proton, which is about 1 MeV. The W^- has a mass of about 80 GeV, making the approximation valid ($q^2 \approx 10^{-10} M_W^2$).

Putting together the terms from Eqs. (2.4), (2.5), and (2.6), we get the following expression for the nuclear matrix element of the bare neutron decay:

$$M = \frac{V_{ud}}{8}\left(\frac{g_W}{M_W}\right)^2 \left[\overline{u}(1)\gamma^\mu\left(g_V - g_A\gamma^5\right)u(3)\right]\left[\overline{u}(2)\gamma_\nu\left(1-\gamma^5\right)v(4)\right] \tag{2.7}$$

where $\overline{u}(1)$ represents the incoming neutron, and $\overline{u}(2)$, $u(3)$, and $u(4)$ represent the outgoing anti-neutrino, proton, and electron, respectively. After some algebra, we obtain

$$\begin{aligned}\left\langle |M|^2 \right\rangle = \frac{V_{ud}^2}{2}\left(\frac{g_W}{M_W}\right)^4 \Big\{ & (g_V + g_A)^2\,(p_1\cdot p_2)(p_3\cdot p_4) \\ & + (g_V - g_A)^2\,(p_1\cdot p_4)(p_2\cdot p_3) \\ & - (g_V^2 - g_A^2)\,m_p m_n\,(p_2\cdot p_4)\Big\}\end{aligned} \tag{2.8}$$

If we work in the rest frame of the neutron ($\overrightarrow{p_1} = 0$), Eq. (2.8), simplifies to

$$\begin{aligned}\left\langle |M|^2 \right\rangle = \frac{V_{ud}^2}{4}\left(\frac{g_W}{M_W}\right)^4 \Big\{ & (g_V + g_A)^2 E_2(a - 2m_n E_2) \\ & + (g_V - g_A)^2 E_4(a - 2m_n E_4) \\ & - (g_V^2 - g_A^2) m_p m_n c^2 (2m_n^2 - a - 2m_n E_3)\Big\}\end{aligned} \tag{2.9}$$

where $a = m_n^2 - m_p^2 + m_e^2$. At this point, Eq. (2.9) gets put back into Eq. (2.3), and the integration is performed. The integration gets to be somewhat involved, but is covered in detail by Griffiths [30].

As is hopefully becoming apparent, the calculation of the nuclear matrix elements can be a lengthy process, even when working with the simplest beta decay possible. What is actually heartening about the foregoing process is that it is, with a few simplifications, directly and analytically calculable. We will find that with double-beta decays, working with larger nuclei instead of a single nucleon greatly complicates the calculation.

2.1.2 Beta decay spectrum

Going back to Eq. (2.3), we can focus on the phase space part of the equation to obtain the basic energy spectrum of beta particles involved in beta decay. Performing the angular integrations, dropping all constant coefficients, and assuming the recoiling proton has negligible momentum, we rewrite the phase space as

$$dN \sim \vec{p}_e^{\,2}\, d\vec{p}_e\, \vec{p}_\nu^{\,2}\, d\vec{p}_\nu \tag{2.10}$$

where, as in Eq. (2.3), $\vec{p}_x$ is the 3-momentum of particle x. Because the proton is assumed to be at rest in the lab frame, p_ν can be expressed in terms of the electron parameters. Assuming the neutrino is moving relativistically, we can use the approximation $p_\nu \approx Q - T_e$, where T_e is the kinetic energy of the electron and Q is the total kinetic energy of the decay particles, in this case approximately $m_n - m_p - m_e$. We can also write down an expression for p_e in terms of T_e:

$$\begin{aligned} p_e &= \sqrt{E_e^2 - m_e^2 c^4} \\ &= \sqrt{(T_e + m_e)^2 - m_e^2} \\ &= \sqrt{T_e^2 + 2T_e m_e} \end{aligned} \tag{2.11}$$

Additionally, from Eq. (2.11) we have (again, dropping constant coefficients)

$$dp_e = \frac{T_e + m_e}{p_e} dT_e \tag{2.12}$$

Putting all of these expressions into Eq. (2.10), we get

$$\begin{aligned} dN &= p_e\,(T_e + m_e)\,(Q - T_e)^2\, dT_e \\ &= \sqrt{T_e^2 + 2T_e m_e}\,(T_e + m_e)\,(Q - T_e)^2\, dT_e \end{aligned} \tag{2.13}$$

A plot of Eq. (2.13) using the endpoint energy of the neutron decay (782 keV) is shown in Fig. 2.3.

The strongest correction to the shape of the beta spectrum comes in the form of the Fermi function, which alters the energy spectrum based on the Coulomb interactions between the outgoing beta particle and the decay nucleus. In e^- decay, the beta energy is shifted downward because the attractive force between the positive nucleus and the negative beta slows down the outgoing particle. Conversely, in e^+ decay, the Coulomb repulsion between positive charges of the decay particles adds energy to the outgoing beta, shifting the energy upwards. This effect can be seen clearly in the decay

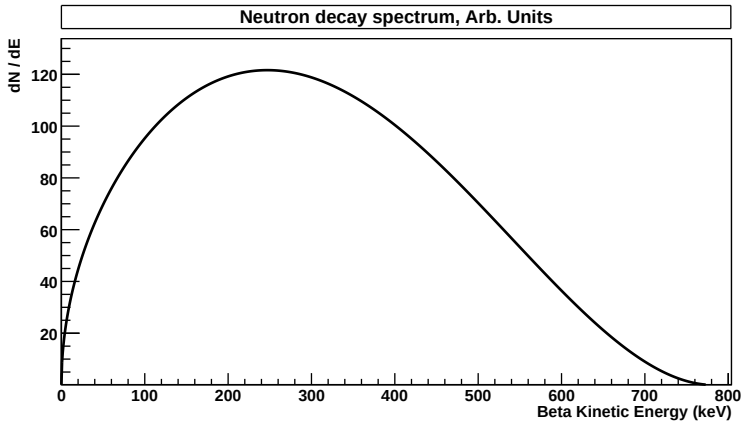

Figure 2.3: Simple neutron beta spectrum. Secondary effects such as relativistic Coulomb interactions with the decay proton and proton recoil are not accounted for in this curve. Compare to Fig. 1.1.

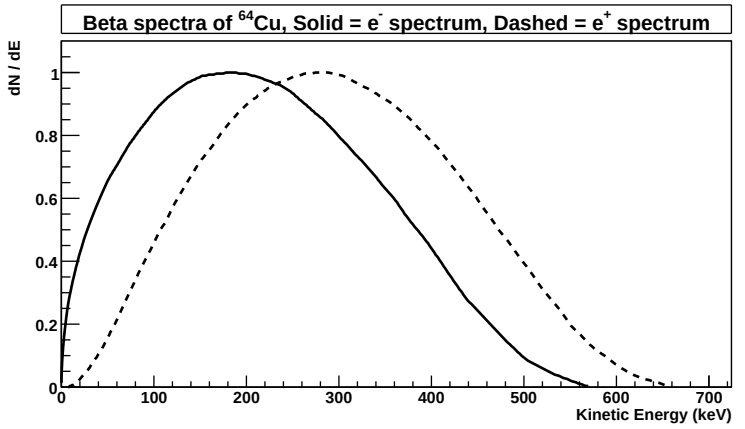

Figure 2.4: ^{64}Cu spectra. The Coulomb attraction and repulsion of the outgoing e^- or e^+ particles, respectively, alters the basic shape of the beta spectrum shown in Fig. 2.3. Both curves were normalized to have a maximum value at 1. Curves recalculated from graphs by J. R. Reitz [31].

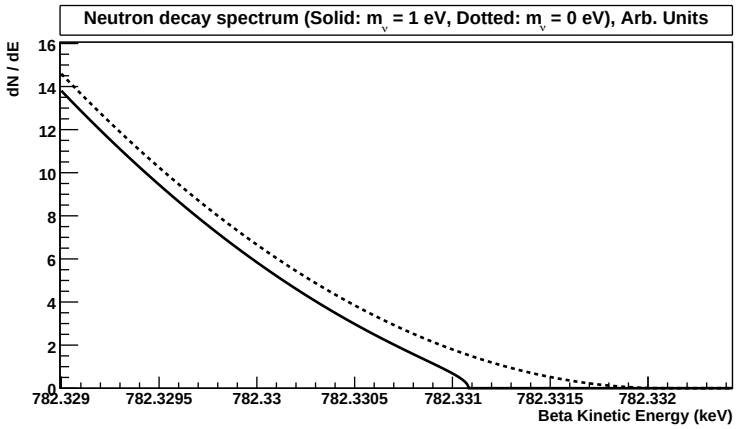

Figure 2.5: Neutron beta spectrum with massive neutrino. The two most striking features of the solid curve near the endpoint are the suppressed endpoint relative to the massless neutron case and the slope approaching $-\infty$. This graph is enhanced by a factor of 10^9 relative to that shown in Fig. 2.3. Like Fig. 2.3, though, the curves in this Figure do not take into account the Coulomb interactions nor the proton recoil.

of ^{64}Cu, which decays via both e^- and e^+ emission. Fig. 2.4 shows the e^- decays having a lower average energy than the e^+ decays.

A second correction to the beta decay spectrum, much smaller though much more closely related to the subject at hand, comes from the non-zero mass of the neutrino. Rewriting the beta spectrum equation without the simplification of zero neutrino mass gives the equation

$$dN = \sqrt{T_e^2 + 2T_e m_e}\,(T_e + m_e)\,(Q - T_e)\,\sqrt{(Q - T_e)^2 - m_\nu^2}\,dT_e \tag{2.14}$$

Plugging in the Q value for neutron decay and assuming $m_\nu = 1$ eV results in the solid curve shown in Fig. 2.5. Not only is the endpoint energy of the spectrum suppressed, but the slope of the curve at the endpoint is very highly negative, as opposed to the massless neutrino case where the slope approaches zero at the endpoint energy.

There are experiments that attempt to directly measure the mass of the neutrino by looking for a deviation in the beta decay spectrum at the end point energy (e.g., the differences shown in Fig. 2.5). Examples of these experiments are the completed Mainz [17] and Troitsk [32] experiments, with a next-generation effort being KATRIN [33]. Rather than examining the beta spectrum of neutrons, though, these experiments study the tritium spectrum. One reason for this choice is the increased number of counts near the endpoint energy of the tritium beta spectrum over that of neutron endpoint

region. Neutrons have an endpoint energy of 782 keV, and the proportion of beta particles above 781.999 keV is only about 1 in 10^{18}. By contrast, the endpoint energy of tritium is about 18.6 keV, and the proportion of beta particles above 18.599 keV is about 1 in 10^{13}. Thus for the same number of primary decays, there will be more counts observed near the endpoint of the tritium spectrum.

2.1.3 Beta decay of nuclei

The beta decay of a neutron is the simplest form of hadronic beta decay. The equations become more complicated when considering beta decay from heavier nuclei. Primakoff and Rosen examined the case of single-beta decay from nuclei [34], and developed an equation for calculating the half life for the decay:

$$T_{1/2}^{-1} \equiv \xi \int_0^Q F(\pm Z, T_e)\ \sqrt{T_e^2 + 2T_e m_e}(T_e + m_e)(Q - T_e)^2(m_e + b/(T_e + m_e))dT_e \tag{2.15}$$

where, as before, m_e is the mass of the electron, T_e is the kinetic energy of the outgoing beta, and Q is the summed maximum kinetic energy of all decay particles. Eq. (2.15) introduces the terms F (the "Fermi factor") and Z, the number of protons in the final nucleus[3]. Simplified, the factors b and ξ are given by

$$b = \pm\frac{2}{\xi}\Re\left\{\ |M_F|^2\left[F_S F_V^*\left(1 + \epsilon_S\epsilon_V^*\right)\right] + |M_{GT}|^2\left[F_T F_A^*\left(1 + \epsilon_T\epsilon_A^*\right)\right]\right\} \tag{2.16}$$

and

$$\begin{aligned}\xi = {} & |M_F|^2\left[|F_S|^2\left(1 + |\epsilon_S|^2\right) + |F_V|^2\left(1 + |\epsilon_V|^2\right)\right] + \\ & |M_{GT}|^2\left[|F_T|^2\left(1 + |\epsilon_T|^2\right) + |F_A|^2\left(1 + |\epsilon_A|^2\right)\right]\end{aligned} \tag{2.17}$$

In Eqs. (2.16) and (2.17), the F_x and $F_x\epsilon_x$ are parity conserving and non-conserving nucleon-lepton coupling constants. In this notation, x takes on the value of S for scalar, V for vector, T for tensor, and A for axial-vector couplings.

What we would like to focus on are the $|M_F|^2$ and $|M_{GT}|^2$ terms. The nuclear matrix element of Eq. (2.7) has been split into two parts: the Fermi (M_F) and Gamow-Teller (M_{GT}) matrix elements. In a Fermi transition, the outgoing beta and neutrino have their spins anti-aligned, so that there is no change in the total angular momentum of the nucleus. In a Gamow-Teller transition, the beta and neutrino have their spins aligned, resulting in a decay nucleus whose angular momentum differs

[3]The positive value of Z in the Fermi factor is used for β^- decay, and the negative for β^+ decay.

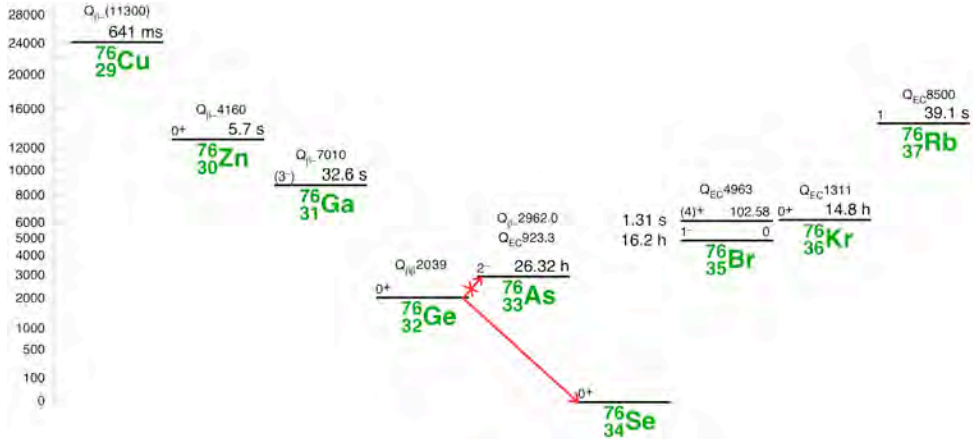

Figure 2.6: Energy levels of A = 76 nuclei. Single-beta decay of ^{76}Ge to ^{76}As is energetically forbidden, but double-beta decay to ^{76}Se is allowed. Figure adapted from [35].

from that of the parent nucleus by 1 unit.

Primakoff and Rosen go on to define these separated nuclear matrix elements as

$$|M_F|^2 = \left| \left\langle \Psi_f^* \left| \sum_{n=1}^{A} \tau_n^{\pm} \right| \Psi_i \right\rangle \right|^2 \tag{2.18}$$

and

$$|M_{GT}|^2 = \left| \left\langle \Psi_f^* \left| \sum_{n=1}^{A} \tau_n^{\pm} \vec{\sigma}_n \right| \Psi_i \right\rangle \right|^2 \tag{2.19}$$

where n refers to the nth nucleon, τ^+ is the neutron $\rightarrow$ proton and τ^- the proton $\rightarrow$ neutron operators, $\vec{\sigma}$ is the Pauli spin operator, and Ψ_i and Ψ_f refer to the initial and final nuclei wave functions, respectively.

Calculating the values of these nuclear matrix elements is a difficult process, and beyond the scope of this work. There is, however, additional discussion of their calculation in Chapter 3.

2.2 Two-Neutrino Double-Beta Decay

In some cases, it is possible for two neutrons within a nucleus to simultaneously beta decay. This can happen when, given a nucleus with Z protons, the Z ± 1 nucleus is at a higher energy level, but the Z ± 2 nucleus is at a lower energy level than the parent nucleus. Fig. 2.6 shows an example

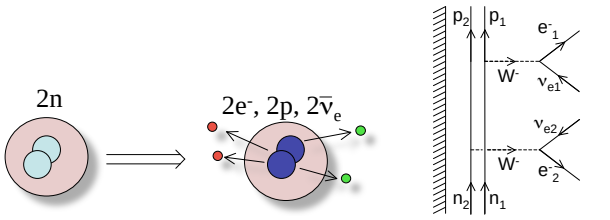

(a) Cartoon (b) Feynman diagram

Figure 2.7: Two neutrino double-beta decay. The $2\nu\beta\beta$ half life is on the order of 10^{18} – 10^{24} years, depending on the isotope. Compare this to the single-beta decay half life of the bare neutron, 10 minutes. The four weak vertices combined with the low-momentum propagators greatly lengthen the half life of this reaction.

of this energy relationship for ^{76}Ge. In this example, ^{76}Ge cannot spontaneously undergo single beta decay to ^{76}As because the latter nucleus is at a higher energy level–such a decay would violate conservation of energy.^{76}Ge can, however, double-beta decay to ^{76}Se.

In this double-beta decay example, the two decay protons remain embedded in the nucleus, and the two electrons and two electron anti-neutrinos are ejected (see Fig. 2.7(a)):

$$ {}^{A}_{Z}X \rightarrow {}^{A}_{Z+2}X + 2e^{-} + 2\overline{\nu}_{e} \tag{2.20} $$

There are additional processes that are all considered to be part of "double-beta decay", just as there are multiple forms of "beta decay". These other processes involve a proton within a nucleus becoming a neutron by either of two methods: emission of a positron or capture of an atomic electron. These double-beta decays are referred to as $2\nu\beta^{+}\beta^{+}$, $2\nu\beta^{+}$EC, or 2νECEC:

$$ \begin{aligned} {}^{A}_{Z}X &\rightarrow {}^{A}_{Z-2}X + 2e^{+} + 2\nu_{e} \\ {}^{A}_{Z}X + e^{-} &\rightarrow {}^{A}_{Z-2}X + e^{+} + 2\nu_{e} \\ {}^{A}_{Z}X + 2e^{-} &\rightarrow {}^{A}_{Z-2}X + 2\nu_{e} \end{aligned} $$

Thus far, most of the isotopes observed to undergo double-beta decay do so via $2\nu\beta\beta$ decay. ^{130}Ba is the only isotope experimentally observed to undergo 2νECEC decay [36].

2.2.1 The $2\nu\beta\beta$ Hamiltonian

By using the $2\nu\beta\beta$ decay Feynman diagram (see Fig. 2.7(b)), we can develop an equation to calculate the rate of the reaction. The procedure is covered in detail by Doi, Kotani, and Takasugi [37]. In

their language, the generalized Hamiltonian for two-neutrino double-beta decay is

$$
\begin{aligned}
H_W = \frac{GV_{ud}}{\sqrt{2}} \Big\{ & \bar{e}\gamma^\rho (1-\gamma_5)\, \nu_{eL} \overline{\Psi}\tau^+ \Big[g_V\gamma_\rho - g_A\gamma_\rho\gamma_5 + g_W i\sigma_{\rho\nu}Q^\nu + g_P Q_\rho \gamma_5 \Big] \Psi \\
& + \chi\, \bar{e}\gamma^\rho (1-\gamma_5)\, \widetilde{\nu}_{eL} \overline{\Psi}\tau^+ \Big[g'_V\gamma_\rho + g'_A\gamma_\rho\gamma_5 + g'_W i\sigma_{\rho\nu}Q^\nu - g'_P Q_\rho \gamma_5 \Big] \Psi \\
& + \eta\, \bar{e}\gamma^\rho (1+\gamma_5)\, \widetilde{\nu}'_{eR} \overline{\Psi}\tau^+ \Big[g_V\gamma_\rho - g_A\gamma_\rho\gamma_5 + g_W i\sigma_{\rho\nu}Q^\nu + g_P Q_\rho \gamma_5 \Big] \Psi \\
& + \lambda\, \bar{e}\gamma^\rho (1+\gamma_5)\, \nu'_{eR} \overline{\Psi}\tau^+ \Big[g'_V\gamma_\rho + g'_A\gamma_\rho\gamma_5 + g'_W i\sigma_{\rho\nu}Q^\nu - g'_P Q_\rho \gamma_5 \Big] \Psi \Big\} \\
& + \text{Hermitian conjugate}
\end{aligned}
\tag{2.21}
$$

Eq. 2.21 is the most general Hamiltonian equation possible for double-beta decay. It allows for both right- and left-handed weak interactions, which explains the presence of the $(1 \pm \gamma_5)$ terms. The hadronic current includes both weak magnetism ($i\sigma_{\rho\nu}Q^\nu$) and nuclear recoil (Q_ρ) terms, with strength parameters specified by g_W and g_P, respectively. As for the rest of the terms, the χ, η, and λ terms denote the relative strength of the right-handed current mixing in either the leptonic or hadronic vertices, and the Ψ terms denote the doublet state of the nucleons involved in the decay. In Eq. (2.21), theV_{ud} term is explicitly shown, whereas in [37] it is absorbed into the g_V, g_A, g_W, and g_P strength parameters. The rest of the constant coefficients are replaced by G.

Turning the Hamiltonian in Eq. (2.21) into a nuclear matrix element is covered in Appendix B of [37]. Part of the difficulty difficulty of this theoretical treatment lies in the fact that in addition to the parent and final nuclei, there is an intermediate virtual nucleus. For example, the calculation of the double-beta decay rate of ^{76}Ge must pass through the virtual ^{76}As nucleus before transitioning to the ^{76}Se nucleus. This intermediate nucleus has many energy levels through which the decay can proceed, and they must be taken into account individually when calculating the half life.

2.2.2 2νββ Nuclear Matrix Elements

In the case of $2\nu\beta\beta$ decay, when one nucleon decays the beta and neutrino can come out with their spins parallel or anti-parallel. In the former case, the Gamow-Teller transition, only the states of the intermediate nucleus with one unit of angular momentum difference from the parent nucleus can contribute to the decay. In the latter case, the Fermi transition, only the states of the intermediate nucleus with the same angular momentum as the parent nucleus contribute. The inverse half life of each Gamow-Teller and Fermi transition must be summed to obtain the final inverse half life. Thus Fig. 2.6 was actually a simplistic diagram, and Fig. 2.8 shows a more subtle version of the process.

In Fig. 2.8, the spin/parity states of the initial and final nuclei are both 0^+. Doi *et al.* describe the nuclear matrix elements for this initial ground state to final ground state transition. They involve summing over each intermediate state:

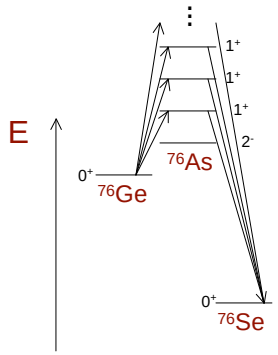

Figure 2.8: $\beta\beta$ transition of ^{76}Ge. Many energy levels of the intermediate nucleus contribute to the decay. Spin and parity of each energy level is shown next to the level itself. Note that the lowest level of ^{76}As does not contribute to the decay, as it is not in a compatible spin state.

$$M \sim \left| \sum_a \left[M^{(2\nu)}_{GTa} - \left(\frac{g_V}{g_A} \right)^2 M^{(2\nu)}_{Fa} \right] K_a \right|^2 \tag{2.22}$$

Eq. (2.22) is a second-order perturbation, and hidden in the K_a terms is the energy denominator:

$$K_a = 2m_e \frac{(E_a - M_i) + \left(E_a - M_f\right) + (T_1 - T_2)}{\left[(E_a - M_i) + \left(E_a - M_f\right) + (T_1 - T_2)\right]^2 - (\omega_1 - \omega_2)^2} \tag{2.23}$$

where E_a is the energy of the a^{th} intermediate nuclear state, M_i and M_f are the mass of the initial and final nuclei (i.e., the energy of the nuclear ground states), and T_n and ω_n are the kinetic energy of the n^{th} decay beta and neutrino, respectively. Because the values of the ϵ_n and ω_n run from 0 to $M_i - M_f - 2m_e$, it is not possible to simplify Eq. (2.23) in a general fashion.

The Gamow-Teller and Fermi elements in Eq. (2.22) are given by

$$M^{(2\nu)}_{Fa} \equiv \left\langle 0^+_f \left\| \sum_n \tau^+_n \right\| N_a(0^+) \right\rangle \left\langle N_a(0^+) \left\| \sum_m \tau^+_m \right\| 0^+_i \right\rangle \tag{2.24a}$$

$$M^{(2\nu)}_{GTa} \equiv -\left\langle 0^+_f \left\| \sum_n \tau^+_n \overrightarrow{\sigma_n} \right\| N_a(1^+) \right\rangle \left\langle N_a(1^+) \left\| \sum_m \tau^+_m \overrightarrow{\sigma_m} \right\| 0^+_i \right\rangle \tag{2.24b}$$

where the τ^+ and $\overrightarrow{\sigma}$ are isospin-raising and spin operators, respectively, and are summed over the

n participating neutrons. The N_a are the intermediate nuclear states. The Fermi matrix elements are explicitly summed over the 0^+ intermediate states, and the Gamow-Teller matrix elements are explicitly summed over the 1^+ intermediate states[4].

2.2.3 The $2\nu\beta\beta$ half life equation

To calculate the final half life of $2\nu\beta\beta$ decay, the matrix elements must be folded together with the phase space factors. Haxton and Stephenson [38] performed this calculation and obtain, after simplification, the partial differential cross-section

$$d\Gamma \sim |M^{2\nu}|^2 \, p_{e,1}^2 \, p_{e,2}^2 \, p_{\nu,1}^2 \, p_{\nu,2}^2 \, dp_{e,1} \, dp_{e,2} \, dp_{\nu,1} \, dcos\theta \tag{2.25}$$

where $p_{e,x}$ and $p_{\nu,x}$ are the momenta of the x^{th} electron and neutron, respectively, and θ is the angle between the two outgoing beta particles. $p_{\nu,2}$ is a function of $p_{e,1}$, $p_{e,2}$, and $p_{\nu,1}$ (the nuclear recoil is neglected here). Totaling up the powers of momentum over which the integration is performed, the inverse half life Γ goes as Q^{11}.

2.2.4 Experimental values of $2\nu\beta\beta$ decay

Earlier in this section the half life of the decay was listed as being between 10^{18} and 10^{24} years. Barabash compiled results from various experiments and combined them to obtain recommended averages of the decay half lives [39]. Those results are reproduced in Table 2.1.

2.3 Zero-Neutrino Double-Beta Decays

With a basis in understanding single-beta decay and two neutrino double-beta decay, we turn our attention at last to zero neutrino double-beta decay. In Section 1.3 we mentioned that a search for $0\nu\beta\beta$ decay might answer the questions

- Is the neutrino its own antiparticle?
- If so, what is the mass of the neutrino?

What exactly is $0\nu\beta\beta$ decay, and why might it answer these questions? To start with, Fig. 2.9 shows a cartoon and Feynman diagram of this process. Note in the Feynman diagram that what was

[4] At this point, someone may wonder why the summation does not also include the 1^- intermediate states. In a nuclear transition, when spin changes by 0 or 1 and the parity does not change, the transition is an "allowed" transition. A transition where the spin changes by 0, 1, or 2 and the parity does change is a "first-forbidden" transition, and happens much less frequently. Thus the decay occurs primarily via the intermediate 0^+ and 1^+ states, with the other channels suppressed.

Table 2.1: Experimental values of double-beta decay halflives for eleven isotopes. The uncertainties combine statistical and systematic effects. All decays are $2\nu\beta\beta$ except that of ^{130}Ba, which is 2νECEC. See Barabash [39] for details of which results were included in the half life estimations.

Isotope	Double-beta $T_{1/2}$ (yr)
^{48}Ca	$\left(4.2^{+2.1}_{-1.0}\right) \times 10^{19}$
^{76}Ge	$(1.5 \pm 0.1) \times 10^{21}$
^{82}Se	$(0.92 \pm 0.07) \times 10^{20}$
^{96}Zr	$(2.0 \pm 0.3) \times 10^{19}$
^{100}Mo	$(7.1 \pm 0.4) \times 10^{18}$
^{116}Cd	$(3.0 \pm 0.2) \times 10^{19}$
^{128}Te	$(2.5 \pm 0.3) \times 10^{24}$
^{130}Te	$(0.9 \pm 0.1) \times 10^{21}$
^{150}Nd	$(7.8 \pm 0.7) \times 10^{18}$
^{238}U	$(2.0 \pm 0.6) \times 10^{21}$
^{130}Ba	$(2.2 \pm 0.5) \times 10^{21}$

emitted as an anti-neutrino (ν_1 in Fig. 2.7(b)) must be absorbed as a neutrino. The only way this can happen is if $\nu = \overline{\nu}$.

How does $0\nu\beta\beta$ decay contain information about the neutrino mass? There is an extra twist, so to speak, on the requirements of the neutrino for the process shown in Fig. 2.9(b) to happen. The Standard Model of particle physics requires the anti-neutrino emitted from one neutron be right-handed, but it must be absorbed as a left-handed neutrino by the second neutron.

When a particle switches from being left-handed to right-handed, it undergoes what's called a "helicity flip". It it possible to change the helicity of a particle by boosting to a frame of reference

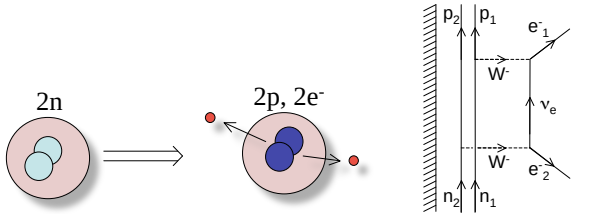

(a) Cartoon (b) Feynman diagram

Figure 2.9: Zero neutrino double-beta decay. The neutrino is emitted from one neutron within the nucleus and absorbed by another (compare to Fig. 2.7). The $0\nu\beta\beta$ half life lower limits are several orders of magnitude longer than the $2\nu\beta\beta$ half lives.

faster than the particle itself in the laboratory rest frame. Fig. 2.10 demonstrates this phenomenon. The relationship between neutrino mass and the half life of neutrinoless double-beta decay is therefore causally connected:

1. The more massive a ν is for a given total energy, the slower it is moving in the lab frame.
2. The slower a neutrino is moving in the laboratory, the "easier" it is for another particle, in this case a neutron, to be traveling faster than it.
3. The easier it is for a particle to be moving faster than the neutrino, the easier it is for the neutrino's helicity to flip, in the frame of reference of that faster particle.
4. The easier it is for the helicity to flip, the more often the $0\nu\beta\beta$ interaction can occur.
5. The more often the interaction occurs, the lower the half life.

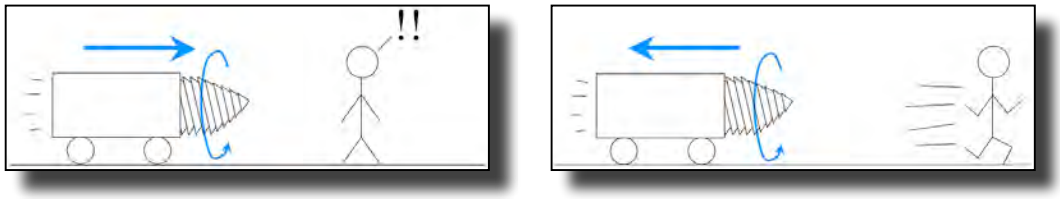

Figure 2.10: Dramatic re-enactment of a helicity flip. In the situation on the left, a drill is rolling toward a miner. The drill is spinning counter-clockwise as the miner sees it. This makes the drill a right-handed drill. After self-preservation kicks in, the drill is moving away from the miner from the miner's point of view, yet is still spinning counter-clockwise. The drill's helicity has flipped.

Of course, if a neutron is receding from a neutron (as implied in Fig. 2.10), the two will never interact. In $0\nu\beta\beta$ decay, therefore, after one neutron decays and emits an anti-neutrino, the second neutron actually has to slam into the anti-neutrino from behind.

This description is a bit misleading in that the decay itself does not occur in such distinct, macroscopic steps, as all events are occurring at the quantum level. Expressed in the language of quantum mechanics, we would simply say that because neutrinos have mass, they exist as a superposition of helicity eigenstates, and that the "absorbing" nucleus only interacts with the left-handed eigenstate of the mediating neutrino. The preceding description may be used, however, as a kind of illustrative cartoon to help reconcile the momenta necessary in the helicity flip.

2.3.1 *The* $0\nu\beta\beta$ *Rate Equation*

With the basic conception of neutrino eigenstates, mixing angles, phase space, and nuclear matrix elements, we are ready to pick apart the equation linking the neutrino mass to the rate of neutrinoless double-beta decay:

$$\frac{1}{T^{0\nu}_{1/2}} = G^{0\nu}(E_o, Z)\left|M^{0\nu}\right|^2 \left|\left\langle m_{\nu,\beta\beta}\right\rangle\right|^2 \tag{2.26}$$

where $M^{0\nu}$ is the nuclear matrix element term, and the last term is the effective Majorana mass of the electron neutrino. The $G^{0\nu}$ term is the calculable phase space factor which Rodin *et al.* evaluate at $0.30 \times 10^{-25}\text{yr}^{-1}$ for ^{76}Ge [40].

$0\nu\beta\beta$ *nuclear matrix elements*

Similar to Eq. (2.22), the nuclear matrix element in Eq. (2.26) is given by

$$M^{0\nu} = M^{0\nu}_{GT} - \left(\frac{g_V}{g_A}\right)^2 M^{0\nu}_F \tag{2.27}$$

where M_{GT} and M_F are the usual Gamow-Teller and Fermi nuclear matrix elements, and g_V and g_A the vector and axial-vector strength couplings. The expressions for M_{GT} and M_F are more complicated than those given in Eqs. (2.24) because, as shown in Fig. 2.9(b), the neutrino is now a propagator between the two nuclei. This means that the nuclear matrix elements are now not only related to the energies of the initial, intermediate, and final states, but they also include a neutrino potential and an extra integration over the allowed values of its momentum. There are many articles that go into the detail of the $0\nu\beta\beta$ decay half life calculation ([37] [38] [41] [42] [43], just to cite a few).

Another extra complication in the calculation of the $0\nu\beta\beta$ decay NMEs versus those of $2\nu\beta\beta$ decays is the fact that the neutrino propagator is virtual. Because of this, there are no longer any restrictions on spin or parity with regards to which intermediate states are included in the calculation. Referring to Fig. 2.8, the ground state of ^{76}As participates in the decay, along with other states excluded in $2\nu\beta\beta$ decay. Thus the nuclear matrix elements in $0\nu\beta\beta$ are actually greater than those in $2\nu\beta\beta$. What, then, causes the $0\nu\beta\beta$ half life to be so much greater than in the 2ν case? There are two parts to that answer. One, the ratio of phase space for 0ν decays to 2ν decays in the case of ^{76}Ge is about 10^{-7} [37]. Additionally, referring to Eq. (2.26), the very small Majorana mass of the neutrino, if it exists, may also serve to increase the $0\nu\beta\beta$ half life.

The calculation of the nuclear matrix elements of Eq. (2.27) is not possible to perform analytically. Over the past few decades, two methods of calculating the matrix elements, known as the Shell Model and the Quasiparticle Random Phase Approximation (QRPA) have been used most

often for performing these calculations. These methods and their results will be discussed in the next chapter. For now, however, we simply make the additional note that in the case of $0\nu\beta\beta$ decay (see [38])

$$d\Gamma \sim |M^{0\nu}|^2 \, T_1 \, T_2 \, p_{e,1} \, p_{e,2} \, dT_1 \, dcos\theta \tag{2.28}$$

where the terms are as before. Totaling up these powers of energy and momentum shows that in the case of $0\nu\beta\beta$ decay, the inverse half life Γ goes as Q^5.

Absolute neutrino mass

The neutrino mass term in Eq. (2.26) incorporates the neutrino mass mixing matrix:

$$\left|\left\langle m_{\nu,\beta\beta}\right\rangle\right| = \left|\sum_i \lambda_i^{CP} m_i \left|U_{ei}^L\right|^2\right| \tag{2.29}$$

In this equation, the λ_i^{CP} are the potential CP-violating terms, m_i are the neutrino eigenmasses, and the U_{ei}^L are the matrix values relating the neutrino mass eigenstates to the electron neutrino. The neutrino mixing matrix given in Eq. (1.8) is intended for use with Dirac neutrinos–if neutrinos and anti-neutrinos are distinct particles. In the case of Majorana neutrinos, there is an extra term that must be included to allow for CP-violation:

$$\begin{pmatrix} \nu_e \\ \nu_\mu \\ \nu_\tau \end{pmatrix} = \begin{pmatrix} c_{12}c_{13} & s_{12}c_{13} & s_{13}e^{-i\delta} \\ -s_{12}c_{23} - c_{12}s_{23}s_{13}e^{i\delta} & c_{12}c_{23} - s_{12}s_{23}s_{13}e^{i\delta} & s_{23}c_{13} \\ s_{12}s_{23} - c_{12}c_{23}s_{13}e^{i\delta} & -c_{12}s_{23} - s_{12}c_{23}s_{13}e^{i\delta} & c_{23}c_{13} \end{pmatrix} \begin{pmatrix} e^{i\alpha_1/2} & 0 & 0 \\ 0 & e^{i\alpha_2/2} & 0 \\ 0 & 0 & 1 \end{pmatrix} \begin{pmatrix} \nu_1 \\ \nu_2 \\ \nu_3 \end{pmatrix} \tag{2.30}$$

Using Eq. (2.30), we can write down the mass of the electron neutrino in terms of the masses of ν_1, ν_2, and ν_3:

$$\left|\left\langle m_{\nu,\beta\beta}\right\rangle\right| = \left|m_1 c_{12}^2 c_{13}^2 + m_2 s_{12}^2 c_{13}^2 e^{i(\alpha_2-\alpha_1)} + m_3 s_{13}^2 e^{-i(2\delta+\alpha_1)}\right| \tag{2.31}$$

Using the values of the mixing angles from Eq. (1.9), we can rewrite the mass of the electron neutrino as

$$\left|\left\langle m_{\nu,\beta\beta}\right\rangle\right| = \left|0.70 \, m_1 + 0.30 \, m_2 \, e^{i(\alpha_2-\alpha_1)}\right|$$

Neutrino mass hierarchy

Note that in Section 1.2.1 the difference between the squares of the masses is listed, but that the difference is actually the *absolute value* of that difference. Solar neutrino measurements provide evidence that m_1 is less than m_2, but there is no experimental evidence whether m_2 is greater or less than m_3. This leads to two possible neutrino mass hierarchies, normal ($m_2 < m_3$) and inverted ($m_2 > m_3$), shown in Fig. 2.11.

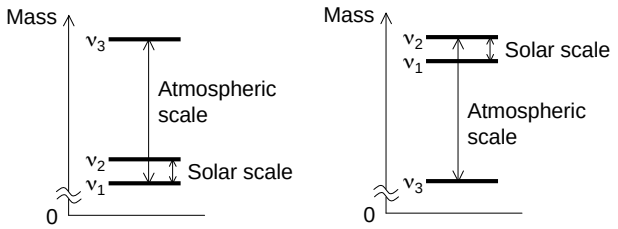

(a) Normal hierarchy (b) Inverted hierarchy

Figure 2.11: Neutrino mass hierarchies. m_1 is less than m_2 by convention, but m_2 may be less than m_3, which leads to the normal hierarchy, or m_2 may be greater than m_3, leading to the inverted hierarchy.

Using the measurements of the mass splittings from Section 1.2.1, we can develop an equation relating the mass of the lightest mass eigenstate (m_1 in the normal hierarchy, m_3 in the inverted hierarchy) to the mass of $\langle m_{\nu,\beta\beta}\rangle$. Even within each hierarchy, though, there is a spread of values for $\langle m_{\nu,\beta\beta}\rangle$ because of the relative phases of the CP angles α_1 and α_2. If $\alpha_1 = \alpha_2$, the mass of $\langle m_{\nu,\beta\beta}\rangle$ is maximal. If $\alpha_1 = \alpha_2 + \pi$, the mass of m_e is suppressed[5]. Fig. 2.12 shows the mass space graph with a spread in values assuming the full range of CP-violating angles.

Fig. 2.12 is only applicable if a signal is observed. If the next generation of $0\nu\beta\beta$ searches puts an upper limit on the mass of the ν_e at, for example, 10 meV, that does not necessarily rule out the inverted hierarchy, as the absence of a signal could be because neutrinos are Dirac particles. Another caveat concerning Fig. 2.12 is that is does not include uncertainties on either the mass splittings or the mixing angles. If these errors are included in the graph, the degenerate region grows (see, for example, page 2107 of [44]).

Analysis of cosmological data can put a model-dependent upper limit on the sum of the neutrino masses $m_1 + m_2 + m_3$. Over the past few years as more data has become available, the upper limit on the neutrino mass sum has steadily decreased from 2500 meV in 2002 [45] to 170 meV today [46].

[5]In the normal hierarchy, it's possible for the mass of m_e to be suppressed all the way down to zero, if $\alpha_1 = \alpha_2 + \pi$ and $m_1 \sim 4.25$meV.

By comparison, the KATRIN experiment [33], a direct search for neutrino mass using the beta decay of tritium, is anticipated to have a lower limit sensitivity to the mass of the lightest mass eigenstate of about 200 meV in the case of the normal hierarchy, and 194 meV in the case of the inverted hierarchy.

2.3.2 *Differentiating* 2ν *and* 0ν *double-beta decay*

After all this discussion of the various forms of double-beta decay, we have yet to describe the signal that $0\nu\beta\beta$ decay searches look for. Essentially, all such experiments measure the energy of the outgoing beta particles. In the case of $2\nu\beta\beta$ decay, the betas share the available kinetic energy with the neutrinos, resulting in a continuum of beta energies. With $0\nu\beta\beta$ decay, however, there are no outgoing neutrinos, so adding the energy from the beta particles results in a single total energy. This "single total energy" is seen as a sharp spike at the Q value of a double-beta decay spectrum. Fig. 2.13 shows the comparison of the spectra. (Incidentally, this is essentially the same peak that early particle physicists were expecting to see in the first few decades of the 20^{th} century and, having seen the continuum of beta energy, eventually led to the discovery of the neutrino. It seems neutrino physics has come full circle.)

In any given $\beta\beta$ experiment, the presence of a statistically significant peak at the endpoint energy indicates that the neutrino is a Majorana particle. The size of the peak determines the half life of the decay, and is proportional to the effective Majorana mass of the neutrino involved in $0\nu\beta\beta$ decay.

Using germanium to search for $0\nu\beta\beta$ *decay*

To give the current theory discussion an experimental context, we will discuss briefly how to observe $0\nu\beta\beta$ decay of ^{76}Ge. There is a large body of work built up around using large germanium crystal diodes as radiation detectors. The idea, therefore, is to construct such detectors out of germanium enriched in ^{76}Ge. We can construct a large array of such crystals, and wait for the detector itself to decay and provide the signal. Because the decays are internal to the detector, and beta particles in the MeV range do not travel far in germanium (on the order of a couple millimeters, which should be compared to the size of a germanium crystal with a typical dimension of about 8 cm), the efficiency for observing a $0\nu\beta\beta$ decay is close to 100%.

2.3.3 *Half life limits*

Table 2.1 shows the values of $2\nu\beta\beta$ decay for eleven isotopes. How do the experimental results of $0\nu\beta\beta$ searches compare in half lives? In a recent review of double-beta decay [47], Elliott and Engle compile results from various experiments, and their data is reproduced in Table 2.2. Note

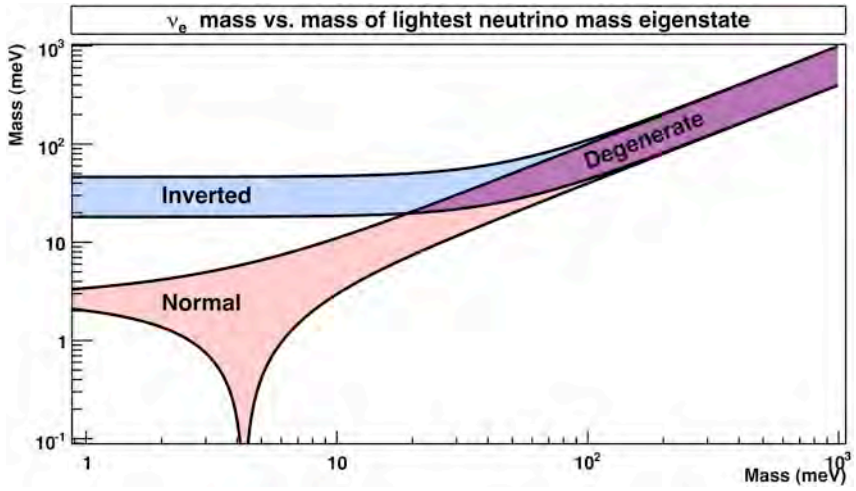

Figure 2.12: Phase space of neutrino mass hierarchy. In the normal hierarchy m_1 is the lightest mass eigenstate, and in the inverted hierarchy m_3 is the lightest. This figure is applicable only if a $0\nu\beta\beta$ signal is observed.

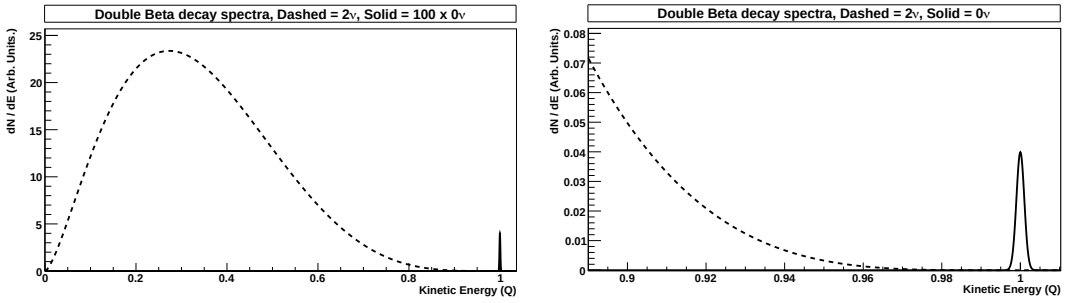

(a) $\beta\beta$ spectra

(b) $\beta\beta$ endpoint

Figure 2.13: Comparison of 2ν and 0ν double-beta spectra. For these Figures, the $0\nu\beta\beta$ half life was assumed to be 10^5 times the $2\nu\beta\beta$ half life. The energy resolution is assumed to be $\sigma = 0.1\%$ at the endpoint energy (a resolution typical of germanium-based radiation detectors). In the figure on the left the $0\nu\beta\beta$ spectrum is exaggerated by a factor of 100 to allow it to be seen on the same scale as the $2\nu\beta\beta$ decay spectrum.

that the lower limits on the half lives are on the order of 10 to 10,000 times as long as the half life measurements of the corresponding $2\nu\beta\beta$ decays.

Table 2.2: Experimental values of $0\nu\beta\beta$ decay halflives for nine isotopes. See [47] for experimental details.

Isotope	Double-beta $T_{1/2}$ (yr)
^{48}Ca	$> 1.4 \times 10^{22}$
^{76}Ge	$> 1.9 \times 10^{25}$
^{82}Se	$> 2.7 \times 10^{22}$
^{100}Mo	$> 5.5 \times 10^{22}$
^{116}Cd	$> 1.7 \times 10^{23}$
^{128}Te	$> 7.7 \times 10^{24}$
^{130}Te	$> 5.5 \times 10^{23}$
^{136}Xe	$> 4.4 \times 10^{23}$
^{150}Nd	$> 1.2 \times 10^{21}$

2.3.4 Observation of $0\nu\beta\beta$ decay?

In 2001, a subset [48] of the Heidelberg-Moscow experiment [49] published a claim of having observed neutrinoless double-beta decay in ^{76}Ge. Their claim sparked a number of critical articles ([50] [51] [52]). These criticisms elicited several responses ([53] [54]). The specific controversy revolved around the claimed statistical significance of the peak at the $0\nu\beta\beta$ end point of 2039 keV (see Fig. 2.14).

In 2004 an updated paper was published claiming a 4.2σ peak at 2039 keV [55]. The resulting $0\nu\beta\beta$ decay half life of ^{76}Ge was measured to be $1.19^{+2.99}_{-0.5} \times 10^{25}$ years (3σ error bars), with a corresponding neutrino mass of $0.44^{+0.14}_{-0.20}$ eV (3σ error bars) using the matrix element calculation from Staudt *et al.* [56]. Fig. 2.15 shows the graph with the claimed 4.2σ peak with the Gaussian fit removed, and Fig. 2.16 shows the original graph with the curves left in place. Fig. 2.15 was included in this work so that the reader may look at the data with a less-biased eye than is possible with Fig. 2.16.

The practical ramification of the reported observation of $0\nu\beta\beta$ decay is that the claim must be tested to an appreciably higher statistical significance than available from the Heidelberg-Moscow experiment. The Majorana experiment is proposing to build a modular, scalable detector that can first test the claim, and, if warranted, incorporate additional modules to increase the sensitivity to the $0\nu\beta\beta$ signal to $\sim 10^{27}$ years.

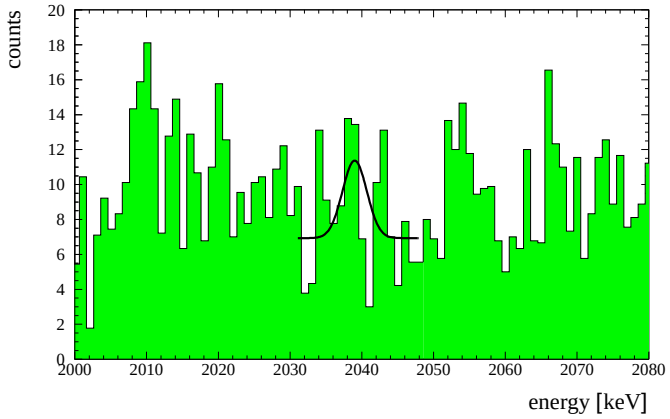

Figure 2.14: First report of $0\nu\beta\beta$ observation. The authors of this paper [48] report a peak significance of either 2.2σ or 3.1σ, depending on the statistical analysis used. Analysis of the peak performed by others reduces the peak significance to at most 1.5σ [52]. The data here represents 55.0 kg · yr of data.

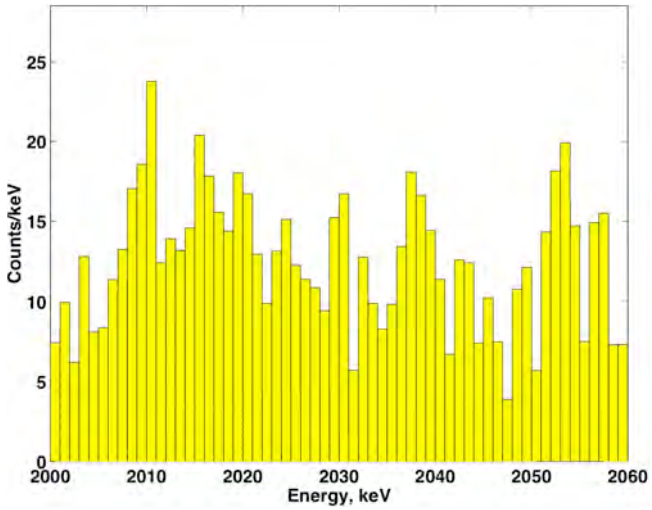

Figure 2.15: Second report of $0\nu\beta\beta$ observation (edited graph). The authors report the peak at 2039 keV has a significance of 4.2σ [55]. This data represents 71.7 kg · yr of data. This graph has had the fit background and peaks removed. The original can be seen in Fig. 2.16. The present graph is adapted from Klapdor-Kleingrothaus *et al.* [55].

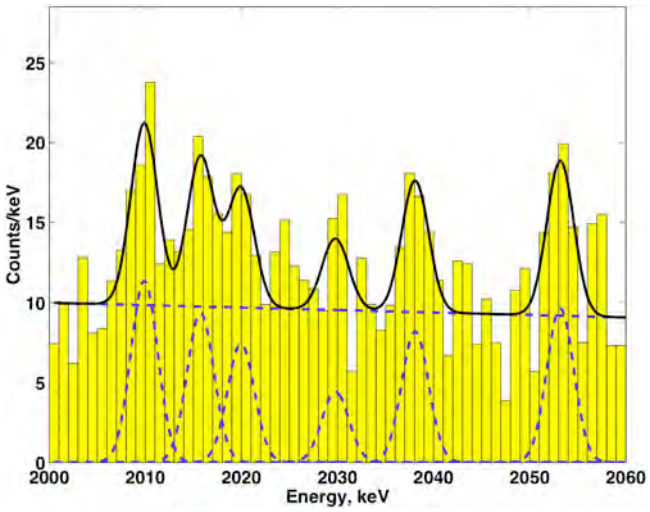

Figure 2.16: Second report of $0\nu\beta\beta$ observation (original graph). See Fig. 2.15 and text for details. Figure taken from Klapdor-Kleingrothaus *et al.* [55].

Chapter 3

TESTING THE NUCLEAR MATRIX ELEMENT CALCULATIONS

In Chapter 2 we discussed the theory behind β, $2\nu\beta\beta$, and $0\nu\beta\beta$ decay. In the latter two decays, the most challenging aspect of calculating the half life is the evaluation of the nuclear matrix element governing the decay. The two most commonly used methods of performing these evaluations, in the cases of $\beta\beta$ decays, are the Shell Model, and the Quasi-particle Random Phase Approximation, or QRPA.

Both the Shell Model and QRPA calculations take advantage of the fact that the nuclear ionization energy falls along a shell pattern as a function of the number of nucleons in a nucleus. Figure 3.1 shows this pattern. While this pattern does have overall motivation by the Shell Model itself, the relative energy level spacings have been measured experimentally, and are thus in a sense directly applicable to QRPA calculations. Within this shell pattern are "magic numbers" for nucleons that result in the outermost nucleon being more tightly bound than if one more nucleon is added. As Fig. 3.1 shows, the first few of these numbers turn out to be 2, 8, 20, 28, and 50.

This nuclear shell structure can help provide guidance for truncating the number of states a nucleon is allowed to occupy, thereby making both Shell Model and QRPA calculations much more tractable than if the nucleus were permitted to occupy any energy state above the ground state.

3.1 The Shell Model

In the Shell Model[1], each nucleon has an individual wave function classified by its isospin, angular momentum (both spin and orbital), and energy. Separating out the radial and angular components, the nucleon wavefunction takes on the form

$$\psi_{nljm}(r,\theta,\phi) = \frac{1}{r} R_{nlj}(r) Y_{nlm}(\theta,\phi) \tag{3.1}$$

where the function $R(r)$ must be solved in the Schrödinger equation, and $Y(\theta,\phi)$ is a function of spin and angular momentum coordinates as well as spherical hamonics. r is the radial coordinate of the nucleon, and n, l, j, and m denote its quantum numbers. This nucleon then moves in a central potential with a residual nucleon-nucleon interaction:

[1]The following treatments of both the Shell Model and the QRPA come primarily from deShalit and Feshbach [57], with other contributions stated where appropriate.

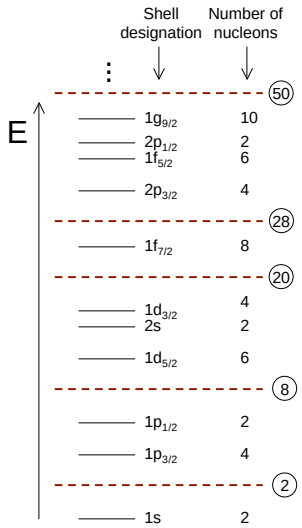

Figure 3.1: Energy levels in the nuclear shell model. The dashed lines show the divisions between the shells, and the numbers in circles are the total number of nucleons needed to fill the associated shell (i.e., the magic numbers). Both protons and neutrons follow the shell pattern. The energy scale is representative. This shell structure is shown in any text on nuclear theory. See, for example, de Shalit and Feshbach [57].

$$H = \sum_{i=1}^{A} [T_i + U_i] + \sum_{i<j=1}^{A} v_{ij} \tag{3.2}$$

where H is the Hamiltonian, A is the number of nucleons, T_i is the kinetic energy of the i^{th} nucleon, U_i is the central potential, and v_{ij} is the nucleon-nucleon potential. Both U_i and v_{ij} are scalar functions of the variables that denote the state of the nucleon. Finally, v_{ij} is "residual" in that it is small compared to U_i, and can therefore be treated as a perturbation on the central potential. Three-body interactions are not considered.

The U_i depends on the nucleon's radial coordinate $\mathbf{r}_i$, momentum $\mathbf{p}_i$, angular momentum σ_i, and isospin τ_{i3}. Specifically, because the treatment must be independent of orientation, the central potential can only depend on scalar parameters based on the four variables listed, and the resulting scalars must conserve parity. Thus the only terms that may show up in the potential are $\mathbf{r}_i^2$, $\mathbf{p}_i^2$, and $\sigma_i \cdot (\mathbf{r}_i \times \mathbf{p}_i)$. This last term is referred to as the "spin-orbit" potential, and is separated from the rest of the central potential U_i. Because of the Coulomb repulsion between protons, the isospin is incorporated into the central potential in the form of $(1/2)(1 + \tau_{i3})V_c(\mathbf{r}_i)$, with $\tau_{i3} = 1$ for protons

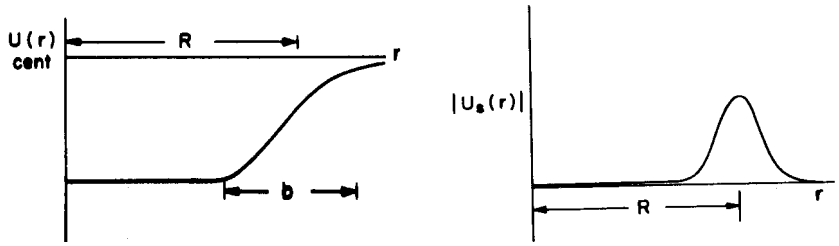

(a) Central potential (b) Spin-orbit potential

Figure 3.2: Shell Model nuclear potentials. Within the bulk of the nucleus (radius $r < R - b$, where R is the nuclear radius and b is the range of nucleon-nucleon interaction) a nucleon feels a constant interaction on all sides, making the central potential flat. The central potential then must increase at the nuclear radius to keep the nucleon bound. In the spin-orbit potential, the nucleon again feels a potential at the nuclear surface, but this potential does not bind the nucleon. Figures taken from [57].

and -1 for neutrons.

The equation of the central potential must have the following characteristics. Assume the maximum nucleon-nucleon interaction range is a distance b. If a nucleon is moving through the bulk of the nucleus (i.e., at a radius less than $R - b$, where R is the radius of the nucleus itself), it feels an equal interaction on all sides. U_i must therefore be flat from $r = 0$ to $r = R - b$. Outside $r = R - b$, the potential must rise to keep the nucleons bound within the nucleus. If the nucleon is greater than a distance b from the outermost nucleon (i.e., $r > R + b$), it must again feel no force, and the potential must again be flat. The spin-orbit potential must also be flat within the bulk of the nucleus, but may "turn on" in the vicinity of the nuclear radius. These qualitative arguments give rise to a central and spin-orbit potentials shown in Figs. 3.2.

In the case of ^{76}Ge, there are 32 protons and 44 neutrons. Thus the magic number = 28 shell is filled for both nucleon types. In the ground state of the nucleus, the protons fully occupy the $2p_{3/2}$ state, while the $1f_{5/2}$, $2p_{1/2}$, and $1g_{9/2}$ states are empty. Within a full Shell Model calculation these four protons can occupy any state that is not already occupied, resulting in 31 possible states. Each one of those states must be explicitly identified in the calculation. In the case of the neutrons, there are 16 particles, which results in 60 possible states. Thus there are 1860 total possible states for ^{76}Ge. ^{76}As has 33 protons and 43 neutrons, giving 3330 possible combinations, and for ^{76}Se (34 protons, 42 neutrons), there are 5160 possible combinations. A full Shell Model calculation of the $\beta\beta$ decay of ^{76}Ge would therefore have to incorporate almost 32 billion states.

One of the earliest Shell Model calculations of the half life of double-beta decay of ^{76}Ge was a truncated calculation performed by Haxton, Stephenson, and Strottman in 1981 [62]. The truncation was performed by allowing only four nucleons to be promoted to the $1g_{9/2}$ subshell, and the proton

and neutron states were considered independently. They obtained the result

$$T^{0\nu}_{1/2} = 4.42 \times 10^{12} \left(\frac{m_e}{\langle m_{\nu,\beta\beta} \rangle} \right)^2 \text{ years} \tag{3.3}$$

Plugging the lower limit of the half life from Table 2.2 into this expression gives an upper limit on $\langle m_{\nu,\beta\beta} \rangle$ of 0.25 eV.

Fifteen years later, Caurier *et al.* performed a large-scale Shell Model calculation of ^{76}Ge $0\nu\beta\beta$ decay [42]. This calculation was also truncated by allowing only four nucleons to be promoted to the $1g_{9/2}$ subshell. While in the Haxton *et al.* calculation the proton and neutron configurations were considered separately, though, in the Caurier *et al.* calculation the proton and neutron states were considered jointly, leading to a much greater total number of configurations. In addition, the nuclear potentials used were updated in the intervening time with phenomenological fits to more recent experimental results. The result from 1996 is

$$T^{0\nu}_{1/2} = 3.13 \times 10^{13} \left(\frac{m_e}{\langle m_{\nu,\beta\beta} \rangle} \right)^2 \text{ years} \tag{3.4}$$

Based on this calculation, the upper limit on the effective Majorana mass of the electron neutrino is 0.66 eV.

Computing power has of course increased greatly over the past decade, and there is currently a proposal in preparation to perform a full double-beta decay Shell Model calculation of ^{76}Ge (i.e., with no truncation of the state space) as a test case in studying supernovae [63] via the SciDAC program [64].

3.2 The Quasi-particle Random Phase Approximation (QRPA)

The description of QRPA begins with an explanation of the Random Phase Approximation. The quasi-particle modification will follow.

Assume there is a nucleus in a ground state, with an operator $\Omega^\dagger$ that promotes the nucleus to an excited state:

$$|E\rangle = \Omega^\dagger |E_o\rangle \tag{3.5}$$

We make a second assumption that the energy spacings of the nucleus are all roughly equal to $\hbar\omega$, so that the energy levels take on the values E_o (for the ground state), $E_o + \hbar\omega$, $E_o + 2\,\hbar\omega$, and so on. To obtain an excited state of the nucleus, the commutator of the Hamiltonian operator $\hat{H}$ with $\Omega^\dagger$ must satisfy the equation

$$[\hat{H}, \Omega^\dagger] = \hbar\omega\Omega^\dagger \tag{3.6}$$

so that, as expected,

$$\begin{aligned}\hat{H}|E\rangle &= \hat{H}\Omega^\dagger|E_o\rangle \\ &= (\hbar\omega\Omega^\dagger + \Omega^\dagger\hat{H})|E_o\rangle \\ &= (\hbar\omega + E_o)\Omega^\dagger|E_o\rangle \\ &= (\hbar\omega + E_o)|E\rangle \end{aligned} \tag{3.7}$$

The creation operator $\Omega^\dagger$ can be applied to the ground state n times to obtain the n^{th}-excited state of the nucleus. Thus Eq. (3.6) can be expanded to

$$[\hat{H}, (\Omega^\dagger)^n] = n\hbar\omega(\Omega^\dagger)^n \tag{3.8}$$

We may try to find a solution to Eq. (3.8) of the form

$$\Omega^\dagger = \sum_{m,i} X_{mi}a_m^\dagger a_i + Y^* a_m a_i^\dagger \tag{3.9}$$

where $a^\dagger$ and a are now the creation and annihilation operators for an individual nucleon in either an occupied state (denoted by index i) or unoccupied state (denoted by index m). They also obey the anti-commutation relations

$$\{a_k, a_{k'}\} = \{a_k^\dagger, a_{k'}^\dagger\} = 0 \qquad \{a_k, a_{k'}^\dagger\} = \delta_{kk'} \tag{3.10}$$

We may compare Eqs. (3.9) and (3.8), and recognize that successive applications of $\Omega^\dagger$ will result in terms with multiple pairs of nucleon creation and annihilation operators, such as (in the case $n = 2$ in Eq. (3.8)) $a_p^\dagger a_q^\dagger a_r a_s$. This expression, involving simultaneous promotion of two nucleons, can be simplified via an approximation

$$a_p^\dagger a_q^\dagger a_r a_s \rightarrow a_q^\dagger a_r\langle a_p^\dagger a_s\rangle - a_q^\dagger a_s\langle a_p^\dagger a_r\rangle - a_p^\dagger a_r\langle a_q^\dagger a_s\rangle + a_p^\dagger a_s\langle a_q^\dagger a_r\rangle \tag{3.11}$$

This approximation, where an average effect is taken for any pair of creation and annihilation operators, is itself the Random Phase Approximation.

We now address the relevance of the term "quasi-particle". Consider a nucleon in a state $|k\rangle$. It will have the same linear and angular momentum effects on the nucleus as a hole in a time-reversed state $|-k\rangle$. A new operator basis may be constructed in the following way

$$\begin{aligned} \alpha_k &= U_k a_k - V_k a_{-k}^\dagger & \alpha_{-k} &= U_k a_{-k} + V_k a_k^\dagger \\ \alpha_k^\dagger &= U_k a_k^\dagger - V_k a_{-k} & \alpha_{-k}^\dagger &= U_k a_{-k}^\dagger + V_k a_k \end{aligned} \tag{3.12}$$

These new creation and annihilation operators obey the same anti-commutation relations shown in

Eqs. 3.10, which places a restriction on U_k and V_k such that

$$U_k^2 + V_k^2 = 1 \tag{3.13}$$

Applying this new creation operator to the vacuum, $\alpha_k^\dagger|0\rangle$ results in a nucleon that exists as a superposition of a particle-hole pair, where the hole is in a time-reversed state, with the overall effect on the nucleus remaining about the same as that of a single nucleon in a state $|k\rangle$. This superposition is what gives rise to the term *quasi-particle*. QRPA makes use both of these superposition of creation and annihilation operators as well as the averaging shown in Eq. (3.11).

The quasi-particle random phase approximation was developed by Halbleib and Sorensen in 1967 [65], and it was first applied to ^{76}Ge $0\nu\beta\beta$ decay in 1989 [47]. Since the creation of QRPA, there have been a Bacchinalic proliferation of variations and extensions to the theory, an overview of which can be found in any number of double-beta decay review articles ([44] [47] [66] [67] [68]).

At its heart, the random phase approximation is used to describe collective motion of nucleons within a nucleus. Depending on which version of QRPA is being used, there are varying phenomenological parameters that must be adjusted to fit experimental data. There has been some debate over which classes of experimental results (e.g., single-beta decay [69] versus double-beta decay [70]) should be used to set these parameters. The number of variables and parameters within any given flavor of QRPA is also great enough that seemingly similar calculations by various groups have still led to different results. Fig. 3.3 shows the results of various QRPA-based calculations over a span of 14 years. Unfortunately, there does not seem to be much of a convergence as the theory has progressed.

Rodin *et al.* published a paper in February of 2006 detailing 13 variable parameters for which different choices may lead to different results [70]. Given this variability, a spread in NME calculations is to be expected. The authors of this paper argue that the historical differences in QRPA results is based more on parameter choice rather than on physical characteristics in the theory itself, and suggest future papers explicitly list their assumptions when making calculations.

The results for $0\nu\beta\beta$ decay of ^{76}Ge from [70] are

$$T_{1/2}^{0\nu} = 2.19 \times 10^{13} \left(\frac{m_e}{\langle m_{\nu,\beta\beta} \rangle} \right)^2 \text{ years} \tag{3.14}$$

for $g_A = 1.25$, corresponding to an upper limit on the electron neutrino mass of 0.55 eV based on the $0\nu\beta\beta$ half life of 1.9×10^{25} years. A second result assuming a phenomenologically-quenched Gamow-Teller matrix element, introduced by lowering g_A to 1.00, is

$$T_{1/2}^{0\nu} = 2.38 \times 10^{13} \left(\frac{m_e}{\langle m_{\nu,\beta\beta} \rangle} \right)^2 \text{ years} \tag{3.15}$$

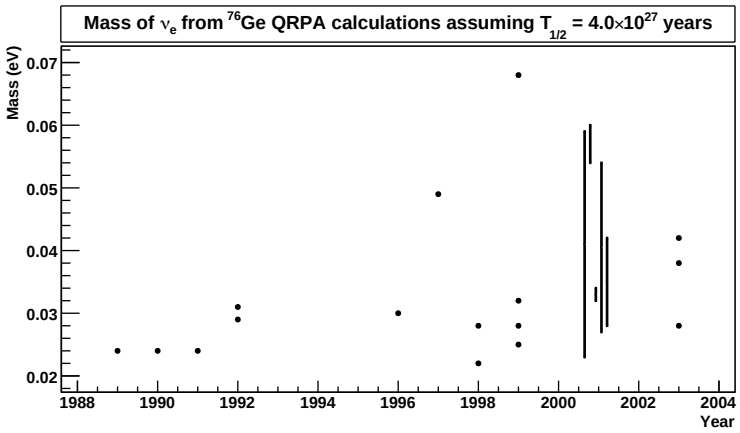

Figure 3.3: Values of $\langle m_{\nu,\beta\beta} \rangle$ from QRPA calculations. The cluster of values with a range, as opposed to single values, were all performed during 2001. Data taken from Elliott & Engle [47], which contains details on references.

This corresponds to an upper limit on the electron neutrino mass of 0.57 eV.

3.3 Comparing the Shell Model and the QRPA

These two theoretical methods, the Shell Model and QRPA, if they are to be considered viable, should agree with the experimentally measured half lives of $2\nu\beta\beta$ decays. Unfortunately, as both of these methods are approximations, the danger exists that they can be fine-tuned to reproduce such half lives. (Although, to be fair, the potential for such fine-tuning is greater in QRPA than in the Shell Model.) To have an increased measure of confidence in these methods, it behooves us to provide additional data to act as a test.

In this case, "additional data" is not only measurements of the $2\nu\beta\beta$ half life for a multitude of isotopes, although that is certainly necessary. We would also like to obtain multiple measurements for a single isotope. At the risk of pedantry, two possible measurements per isotope would be the half life of $2\nu\beta\beta$ and $0\nu\beta\beta$, the former of which we already have for a number of isotopes and the latter of which might not be possible to obtain at all.

What additional signal can we use as a test of the nuclear matrix element calculations? The answer to this comes in the form of yet another form of $\beta\beta$ decay: zero-neutrino and two-neutrino double-beta decays to excited states of the final nucleus, referred to either as ES$0\nu\beta\beta$ or ES$2\nu\beta\beta$ decays. Adding complexity to the decay structure, Fig. 3.4 shows a modification of Fig. 2.6.

Excited-state $\beta\beta$ decays have been observed in two isotopes: ^{100}Mo and ^{150}Nd. As discussed in

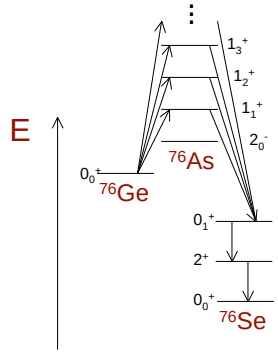

Figure 3.4: $\beta\beta$ decay of ^{76}Ge to excited states of ^{76}Se. The decay is shown to occur between the ground state of ^{76}Ge and the first excited 0^+ state of ^{76}Se.

Section 2.3.1, the phase space portion of the $2\nu\beta\beta$ inverse half life calculation goes as Q^{11}. In the $\beta\beta$ decay of ^{100}Mo, Q = 3034 keV to the ground state, and Q = 1904 keV to the excited state. The ratio of these values raised to the 11^{th} power would imply that the half life of the decay to the excited state would be 168 times larger than the half life of the decay directly to the ground state. The half life of the ES2$\nu\beta\beta$ decay is $6.1^{+1.8}_{-1.1} \cdot 10^{20}$ years [58]. Compare this to the half life of the decay to the ground state of $(7.1 \pm 0.4) \cdot 10^{18}$ years (see Table 2.1). Taking a ratio of these half lives gives a value of 86. This implies that the squared value of the nuclear matrix element for the $0_0^+ \rightarrow 0_1^+$ transition is 168 / 86 = 1.96 times as large as the squared nuclear matrix element for the $0_0^+ \rightarrow 0_0^+$ transition[2].

Suhonen and Civitarese have calculated the nuclear matrix elements for the 2ν ground- and excited-state transitions for ^{110}Mo using a single-particle estimate in a QRPA calculation [59]. They get a squared-NME ratio of $(0.016/0.011)^2 = 2.11$. This ratio is only 7% away from the expected ratio, and thus seems to be a reasonably accurate calculation compared to the historical spread in QRPA calculations (more on this in Section 3.2). Unfortunately, their ground-state transition nuclear matrix element is a factor of 10 lower than the experimentally measured value, casting doubt on the validity of simply taking a ratio. Šimkovic, Domin, and Semenov performed a separate calculation of the ^{100}Mo nuclear matrix elements, also using a QRPA calculation but assuming single-state dominance[3] [60]. Their ratio ends up being $(0.222/0.352)^2 = 0.89$. This ratio is still within a factor

[2]The notation "J_n^π" refers to the state of the nucleus, where J is the spin state, π refers to the parity, and n is the n^{th} excited J^π state. For example, 0_1^+ refers to the first excited state with positive parity and an angular momentum of zero.

[3]Single-state dominance is the hypothesis that the lowest-lying state of the intermediate nucleus contributes the majority of the nuclear matrix element, and thus including higher-energy states in the calculation will change the final result relatively little.

of two of the expected value.

In the ^{150}Nd case, the $0^+_0 \rightarrow 0^+_1$ $2\nu\beta\beta$ transition has a half life of $\left(1.4^{+0.4}_{-0.2}(\text{stat}) \pm 0.3(\text{sys})\right) \cdot 10^{20}$ years [61], which is $\sim$ 18 times the half life of the ground state transition. The phase space ratio value is $(3367/2626)^{11} = 15.4$. The ratio of squared nuclear matrix elements should therefore be 1.17. Suhonen and Civitarese, in the same work as the prior ratio calculation ([59]), calculate the ratio for ^{150}Nd to be $(0.179/0.141)^2 = 1.61$. Once again, however, their predictions for the ground-state NME differs from the experimentally-measured values, this time by a factor 6.4 times higher.

3.4 Using excited state decays to test nuclear matrix elements

As we have seen, there is a fair amount of uncertainty in the calculations of the nuclear matrix elements. In the Shell Model, the issue is how large a space to include in the calculation–in other words, what is the proper compromise between accuracy and ability to carry out the calculations? As far as QRPA calculations go, there are many choices of methods, approximations, and phenomenologically-fit parameters incorporated into every calculation. Which combination is best? And is that the combination that produces the most robust results for expansion on $\beta\beta$ predictions?

How do we test the NME calculations? One way would be to compare the results to the half life measurements of $2\nu\beta\beta$ decay, but that has limited use because, philosophically speaking, we can fit any number of curves through a single data point. To really solidify the theory would require one data point to lock down parameters and validate assumptions, but then once those decisions are made, the theory must be used to predict or explain, at the very least, a second data point. At the beginning of this chapter, we made the argument that a good measurement would be the half life of $2\nu\beta\beta$ decays to excited states of the final nucleus.

3.4.1 The excited-state (ES) signal

Now that we know we are looking for ES$2\nu\beta\beta$ decays, how do we identify them? Referring to Fig. 3.4, we see that ^{76}Ge emits two betas and two neutrinos simultaneously and decays to the first excited 0^+ state of ^{76}Se. The half lives of the 0^+_1 and 2^+_1 states are 5 picoseconds and 2 picoseconds, respectively. Given these extremely short lifetimes, the final signature as seen by a detector would be two beta particles simultaneous with two gammas. In the case of ^{76}Ge, the beta particles would have an endpoint energy of 917 keV, and the cascade gammas would have energy of 563 keV and 559 keV.

This multi-particle coincidence is both a blessing and a curse. It is curse because the efficiency for observing such a decay, with multiple gammas, is much lower than observing just two beta particles. It is a blessing because the background for this coincidence should be exceedingly low. The signal/background ratio of course depends on the geometry of the detector. Predictions of

efficiency in the Majorana detector will be made in Chapter 8.

3.4.2 Verifying Monte Carlo performance

To predict the efficiency of any given detector to observe this ES2$\nu\beta\beta$ decay requires a Monte Carlo simulation. This raises the question of how to test the simulation for accuracy. We cannot compare the MC results to theoretical calculations because it is the accuracy of the theoretical calculations themselves that are the goal of the experimental effort.

To test the simulation, we might be able to find an event that mimics the ES2$\nu\beta\beta$ decay to test the simulation. Within a germanium detector, a beta particle with 1 MeV of energy will only travel between 1 and 2 millimeters before losing all its kinetic energy, while gamma rays of similar energy tend to Compton scatter a few times before the photoelectric effect removes their remaining energy. (For direct comparison, the attenuation length of a 1 MeV γ in germanium is roughly 2.5 cm.) Because of this, a ^{76}Ge ES2$\nu\beta\beta$ decay within a germanium detector array actually appears as a triple, not quadruple, coincidence: the two betas appear as a single energy deposition, and the gammas each provide an extra tag. This β-γ-γ triple coincidence is what the surrogate signal needs to mimic.

3.4.3 Finding a surrogate signal

In looking for a nuclear event that mimics betas and gammas, we have a number of limitations on the candidate interactions beyond the β-γ-γ requirement. First, the signal should be homogeneously distributed throughout the detectors, requiring the decays be internal to the germanium crystals themselves. This requirement precludes the use of external sources to mimic an ES2$\nu\beta\beta$ signal.

Second, we do not want the decay to involve emission of β^+ particles. *A priori* they would be a wonderful source for the surrogate signal, since the annihilation gammas are relatively close in energy to the ES2$\nu\beta\beta$ decay cascade gammas. Unfortunately, any process that produces positrons, including high energy gammas and cosmic rays, would be a background as the positrons would annihilate with an electron, resulting in an annihilation gamma unrelated to the signal of interest.

Third, the particles emitted in the surrogate decay must be emitted "simultaneously". This word is in quotes because events that occur within roughly 0.2 μs of each other will be seen as a simultaneous by a germanium detector. The actual limitation, then, is to reject decay schemes with half lives on the order of 0.2 μ s.

Finally, the results must be statistically meaningful. If a surrogate signal is found but cannot be seen above background levels, it is still of no use.

Summarizing the restrictions:

1. Triple coincidence: β-γ-γ

Table 3.1: Properties of natural germanium. Natural abundances and cross-sections come from [87]. The thermal neutron capture cross section for natural germanium is (2.30 ± 0.07) barns.

Isotope	Natural Abundance	Thermal neutron capture cross-section (b)	Percentage of neutron captures relative to natural germanium
^{70}Ge	20.84(87)%	3.45(16)	(31.31 ± 2.14)%
^{72}Ge	27.54(34)%	0.95(11)	(11.39 ± 1.37)%
^{73}Ge	7.73(5)%	14.4(4)	(48.47 ± 1.96)%
^{74}Ge	36.28(73)%	0.53(5)	(8.372 ± 0.842)%
^{76}Ge	7.61(38)%	0.14(2)	(0.464 ± 0.071)%

2. Homogeneously distributed throughout the germanium crystals
3. No β^+ emission
4. Simultaneous decay particles
5. Plentiful

Two methods of creating radioactivity with a germanium detector are via cosmogenic and neutron activation. What choices of surrogate signal do natural germanium detectors provide?

Cosmogenic activation of germanium detectors

We used the COSMO [75] program to find spallation products within natural germanium that follow the restrictions in the list above. Natural germanium is made up of five isotopes (see Table 3.1). The detector we will be using to search for the surrogate signal is a CLOVER detector (described in detail in Chapter 4) at Los Alamos National Laboratory. The relevant detector characteristics for the current purposes is that the detector is made of 4 crystals, each about 750 grams of natural germanium, and it is located roughly 7200 feet above sea level.

The COSMO code assumes a cosmic ray flux at sea level, and the flux therefore had to be adjusted to the altitude at Los Alamos, or roughly nine times the cosmic ray flux at sea level [76]. Having modified COSMO accordingly, we calculated the production rate of various radioisotopes in the CLOVER detector, with the results shown in Table 3.2.

^{74}As decays via both β^+/EC and β^- decay with branching ratios of 66% and 34%, respectively. We want to avoid β^+ decays, but the β^- branch does not contain a triple coincidence. We therefore cannot use ^{74}As. ^{68}Ge decays via EC to ^{68}Ga, which decays via β^+/EC, making this decay chain also unusable. ^{58}Co is yet another β^+ emitter.

^{60}Co provides a wonderful triple coincidence, with the beta endpoint being 318 keV, and two

Table 3.2: COSMO predictions for activity in the CLOVER detector. The original COSMO flux was enhanced to match the flux at the altitude of Los Alamos. These radioisotopes have the highest creation rates within natural germanium.

Isotope	Creation rate in the CLOVER detector (day^{-1})
^{74}As	163
^{68}Ge	87
^{58}Co	35
^{60}Co	12

simultaneous gamma rays at 1173 keV and 1332 keV. Unfortunately, the steady-state ^{60}Co rate is only 12 events per day in the CLOVER. A typical photopeak efficiency of a 1 MeV gamma ray is roughly 5%, making the efficiency for observing this event less than one in 1000, assuming both gamma rays have to exit the crystal in which the decay occurred. Assuming we would want an uncertainty in the peak area of 10%, we would require at least 100 captured events. This means the CLOVER detector would have to accumulate data for over 6 years. This data rate is already very low, but compounding the low rate is the fact that the CLOVER was delivered to Los Alamos circa 2002, which means the ^{60}Co signal is at roughly 1/3 of maximum, as prior to 2002 it was not at Los Alamos altitude. The ^{60}Co rate would simply be too low to use.

Based on the foregoing analysis, cosmogenic activation of the CLOVER detector is not a viable method for obtaining a surrogate ES2$\nu\beta\beta$ signal.

Neutron activation of germanium detectors

Referring to Table 3.1, neutron activation of natural germanium creates the radioisotopes ^{71}Ge, ^{75}Ge, and ^{77}Ge. Might we be able to use one of these isotopes to obtain our surrogate signal? ^{71}Ge decays via EC, so there is no triple coincidence. ^{75}Ge decays via β^- emission, but the branching ratio of a useable triple coincidence is only one in one thousand. In addition, the triple coincidence of ^{75}Ge includes a 66 keV gamma, and a gamma ray of that low an energy loses energy primarily through photoelectric effect, making it very unlikely that the photon would escape the decay crystal.

It turns out that ^{77}Ge has all the features we are looking for. It has two useable branches, both with a β endpoint energy of 2070 keV. In one decay scheme with a branching ratio of 6.6%, the gamma energies are 367.4 keV and 264.4 keV. In the other scheme, with a branching ratio of 10.3%, the gamma energies are 416.3 keV and 215.5 keV. A partial decay scheme of ^{77}Ge is shown in Fig. 3.5 (the full decay scheme is shown in Appendix A). The event rate will depend on the strength of the neutron source we use, so we can control the rate of ^{77}Ge events. Finally, the half life of ^{77}Ge is about 11 hours, making it feasible to activate the germanium, then remove the neutron

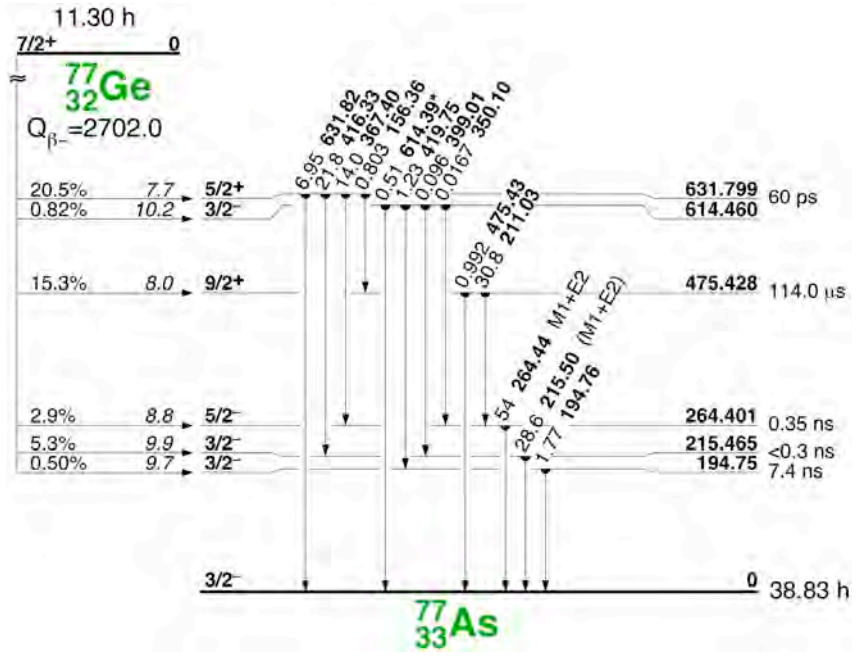

Figure 3.5: Partial ^{77}Ge decay scheme. The two candidate surrogate decays involve a decay to the 632 keV energy level. The β (Q = 2070 keV) would be followed by two cascade gammas at 416/215 keV or 367/264 keV. Figure adapted from [35], which contains the full decay structure.

source to look for the ^{77}Ge signal.

3.5 Further motivation for measurements of excited-state decays

In addition to providing another datapoint to test theoretical calculations, decays to excited states may indicate the nature of the underlying mediating particle in the decay. Neutrinoless double-beta decay is generally assumed to occur via exchange of a light neutrino. The decay might, however, proceed via exchange of a heavy neutrino, the seesaw partner to the light neutrino (see Section 1.2.2). It might also proceed via an as-yet undiscovered supersymmetric mechanism.

If the Klapdor-Kleingrothaus *et al.* measurement is confirmed and the rate of $0\nu\beta\beta$ decay is faster than earlier supposed, it may be possible to use the next generation double-beta decay experiments to measure the ratio of the half lives of neutrinoless decays to an excited state versus the ground state. As alluded to in Section 1.2.2, this ratio of half lives may indicate the nature of the mediating particle. Šimkovic and Faessler have calculated the ratio of the half lives for four iso-

topes, depending on what particle governs the decay [22]. In the case of ^{76}Ge, the 0ν half life to an excited state will be ~ 95, ~ 50, or ~ 120 times the half life of the decay to the ground state if the mediating particle is a light neutrino, heavy neutrino, or supersymmetric mechanism, respectively.

3.6 Excited-state surrogate summary

To recap, we want to test the theoretical predictions of both the Shell Model and QRPA with more than one $\beta\beta$-type event for ^{76}Ge. There already exists a measurement of the $2\nu\beta\beta$ decay to the ground state. Unfortunately, the theory may be tuned to the experimentally measured numbers (inadvertently or otherwise), so the theory must be tested before being applied to the $0\nu\beta\beta$ decays. We want to measure the rate of two-neutrino double-beta decays of ^{76}Ge to the first excited 0^+ state of ^{76}Se to provide such a test.

To measure the half life of ES2$\nu\beta\beta$ decays requires a Monte Carlo calculation of the detector efficiency for this event. To develop confidence in the Monte Carlo program, we test the simulation using a surrogate to the ES2$\nu\beta\beta$ signal. That surrogate signal is the decay of ^{77}Ge in the CLOVER detector at Los Alamos National Laboratory, obtained via neutron activation.

The next three chapters of this work focus on measuring the ^{77}Ge triple coincidence efficiencies. Chapter 7 covers the simulation and comparison to experimental results. Chapter 8 discusses predictions and ramifications for the proposed Majorana search for $0\nu\beta\beta$ decay.

Chapter 4

THE CLOVER DETECTOR

With the goal of using decays of ^{77}Ge to mimic excited state double-beta decays, we turn our attention to an experimental study using a CLOVER germanium detector at Los Alamos National Laboratory. This chapter provides a description of the CLOVER detector, including calibrations, environmental backgrounds and performance characterization.

4.1 Description of the CLOVER Detector

The CLOVER detector is a high-purity, solid-state natural germanium diode radiation detector made by Canberra [77]. It is an array of four cylindrical crystals, with the crystal axes parallel to the long dimension of the aluminum cryostat housing (see Fig. 4.1). Each crystal is two-fold segmented parallel to the axis of the crystals. Table 4.1 shows the masses of the four crystals.

Table 4.1: Masses of the CLOVER crystals. The masses were provided by the manufacturer.

Crystal	Mass (g)
1	753
2	754
3	755
4	755

Each of the four crystals is a coaxial well[1] n-type detector approximately 80 mm high and 50 mm wide with a central bore 10 mm in diameter and 65 mm deep. The outer dead layer thickness is 0.5 μm and the inner dead layer thickness is 0.5 mm. The passivated surface on germanium crystal radiation detectors (the flat surface between the inner and outer cylindrical surfaces) may have a dead layer anywhere between 1 and 100 nm. The exact thickness of the dead layer on the passivated surfaces of the CLOVER crystals is unknown.

The axes of adjacent crystals are separated by 44.6 mm. The sides of the crystals are machined flat as shown by Fig. 4.2. The crystals have a 0.6 mm separation by a proprietary method and

[1] A "well" detector is cylindrical with a hollow core and one closed end (i.e., the core is not drilled through the entire cylinder).

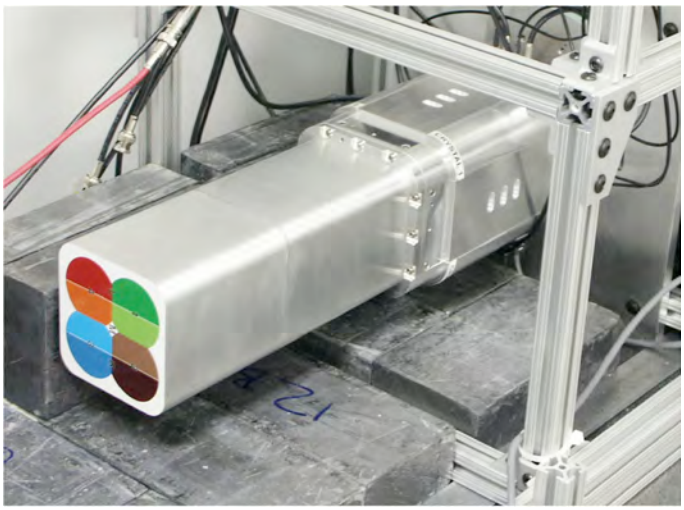

Figure 4.1: Canberra/Eurisys CLOVER detector. The crystals are packed in a square array within the aluminum cryostat, with the crystal axes running parallel to the long side walls of the cryostat. The segmentation planes are parallel to one set of cryostat walls. In this photo, the segmentation planes are horizontal. There is a colored sticker on the front of the cryostat showing the crystal placements.

material, though neutron activation gives clues as to the substance of this crystal spacer (more on this subject in Section 5.4.2). The inner contacts of the crystals is 5 μm of gold, although their shape or extent inside the central bore is also unknown.

The aluminum cryostat has walls 1 mm thick near the crystals, and farther away from the end of the detector the walls thicken to 3 mm. The coldplate within the cryostat is made of aluminum 1 cm thick, but is of a proprietary design. The physical method of mounting the crystals within the cryostat is also proprietary.

The CLOVER detector has seven outputs, one from each of the four crystals, and three ”position” channels that provide the segmentation output. The crystal channels are referred to as E1 through E4, and the position channels Pl, Pm, and Pr (left, middle, and right). The E channels have cold FET[2] front ends to provide high-resolution output of the energy deposition. The P channels have warm FETs, and while they also provide energy information, their resolution is not as good as

[2]Field Effect Transistors collect charge from the crystals. The description ”cold” means they are contained within the cryostat, placing them close to the crystals themselves. They closer the FETs are to a crystal, the shorter the cables between the crystal and the FET, which leads to reduced capacitive noise. Capacitance adds noise to the electronics, which is why it needs to be minimized.

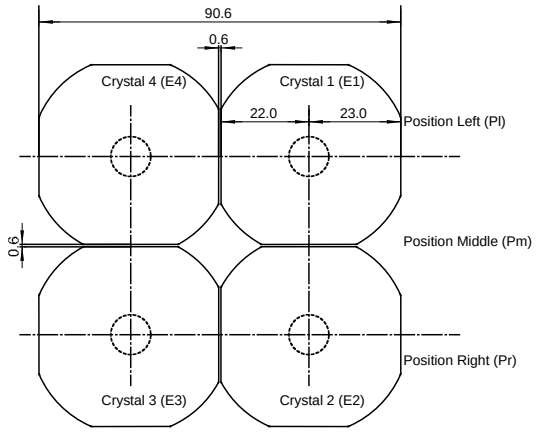

Figure 4.2: CLOVER crystal schematic. Each crystal has a radius of 25 mm, but the sides of the crystals are machined flat.

that of the E channels. As such, the P channels are not used to measure energy; rather, they provide simple ”hit or miss” information.

Using the E and P channel outputs provides information as to which segment had an energy deposition. Fig. 4.2 shows how the crystals and P channels are related. Here is an example of how these outputs are used: of the energy channels, if only E1 registers an energy deposition, along with both Pl and Pm, then both halves of crystal 1 had energy deposited in them. It is possible to observe an ambiguous situation, for instance if both E1 and E2 record energy deposition, as well as all the P channels. There is no way of knowing, based only on this information, whether both E1 and E2 contributed to the Pm readout, or if just one of the crystals did so.

Ideally, further analysis would be possible to reconstruct these degenerate events. Continuing with the example just outlined, if the energy deposited in E1 equals the energy deposited in Pl and Pm, then it is logical to assume only the outside segment of E2 had any energy deposition. Relatively poor energy resolution combined with a nonzero energy threshold, however, makes such analysis not wholly reliable. The position channels are, as mentioned above, used only as binary indicators of energy deposition. In practice, ambiguous events were either eliminated from the data sets or the segmentation information was not utilized in the analysis.

4.2 Calibrating and Optimizing the CLOVER detector

The first task prior to using the CLOVER detector was calibrating the energy response, so that we could properly identify lines in the resulting energy histograms. We also optimized the software DAQ for gamma ray spectroscopy.

4.2.1 DAQ Hardware and Software

The front-end electronics used with the CLOVER detector were preinstalled. For the digital data acquisition system, we used a CAMAC-based 4-channel Digital Gamma Finder (DGF4C) made by X-Ray Instrumentation Associates [78]. The DGF4C samples at 40 MHz and the front end ADC has a 14-bit conversion. Oversampling increases the effective resolution of the channel levels to 16-bit, or one part in 65,536. The DAQ computer is a Dell Pentium IV computer. It communicates with the CAMAC crate via a PCI card interface to a Wiener CC32 CAMAC controller [79].

The software used is provided by the manufacturer, and uses the Igor Pro environment by WaveMetrics [80]. The software comes with default values for various DAQ settings. These DAQ settings include threshold, gain, an energy filter, and a trigger filter. Other run-specific settings include how often the DGF4C is polled to determine if the buffers are full ("Polling Time"), as well as the maximum time until a "buffer spill"[3] is forced ("Time Out").

4.2.2 Detector calibration

We started the calibration of the detector with the default factory settings, shown in Table 4.2.

Table 4.2: Factory settings for the XIA DAQ software. The energy and trigger time settings are DAQ-specific settings, and affect resolution and the stability of the signal at low threshold, respectively.

Threshold	40 (arb. units)
Gain	1.0 V/V
Energy rise time	6.4 μs
Energy flat top time	1.2 μs
Trigger rise time	0.1 μs
Trigger flat top time	0.1 μs

[3] A "spill" occurs when one of the channels on the DGF4C buffer fills up. On a poll of the DGF4C modules, if one buffer is full then all four buffers are read out. A spill is therefore a measure of the number of events, and not empirically linked to either data rate or live time.

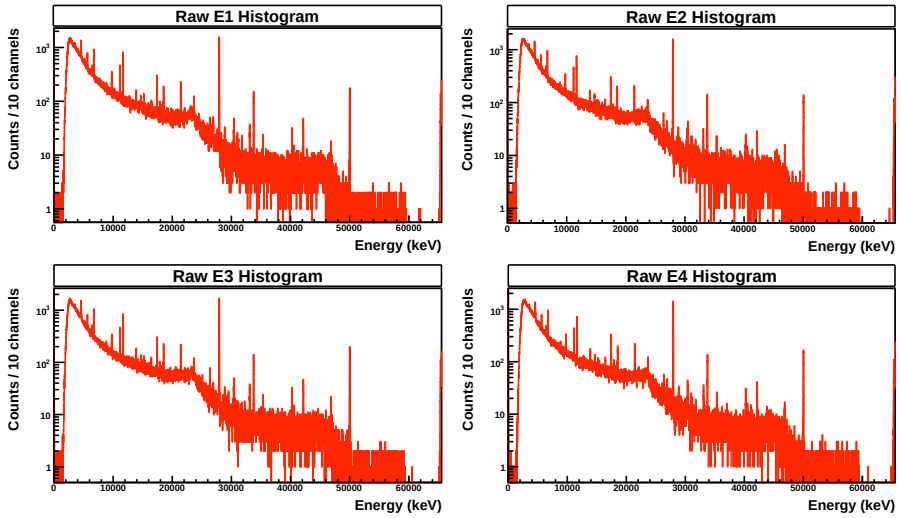

Figure 4.3: Raw histogram of the CLOVER E channels. The gains were set to place the presumed 2614.5 keV peak near raw bin 50000. Confirmation of this identification is performed by identifying peaks at other energies and verifying that the ratios of presumed energy to raw bin number are all roughly equal. The energy response of germanium detectors is strongly linear, which makes these simple ratio comparisons possible.

Using these initial settings, we put a thoriated welding rod near the CLOVER detector and acquired an energy histogram for approximately an hour. Gaussian curves were fit to the presumed 2614.5 keV peak from the decay of ^{208}Tl for each of the four E channels. We adjusted the gains to put the 2614.5 keV energy peak at approximately raw bin number 50000 for each of the four energy channels. This gain was adjusted to allow for E-channel energy measurements up to roughly 3 MeV.

Once the gains were set, we obtained background data without a lead shield or muon veto for 12.7 hours, and acquired an energy histogram for each of the energy channels (see Fig. 4.3). Because of concern of crosstalk between the CLOVER detectors, we populated these calibration histograms only with events where a single CLOVER crystal registered an energy deposition. This single-crystal cut was extended to overflow events that result from energy depositions outside the DAQ's range (i.e., if one crystal had an energy deposition and another had an overflow entry, we did not use the event in the calibration). We fit a quadratic background and Gaussian curve on top of several strong peaks using the ROOT [81] TH1D::Fit method, which displays the uncertainties of the fit parameters. Using the Gaussian centroids we fit several polynomials of order 1 through 4 to translate raw bin number to energy in keV.

Table 4.4 shows the χ^2-based goodness-of-fits for the various polynomial fits to the calibration

Table 4.3: CLOVER calibrations for the E channels.

Energy (keV)	Source	E1 Centroid (ch)	E2 Centroid (ch)	E3 Centroid (ch)	E4 Centroid (ch)
351.932(2)	^{214}Pb	6729.72(45)	6737.15(50)	6730.60(43)	6726.55(48)
583.191(2)	^{208}Tl	11153.1(6)	11162.4(6)	11153.7(7)	11152.2(7)
609.312(7)	^{214}Bi	11654.2(4)	11663.4(4)	11655.4(4)	11651.3(4)
911.204(4)	^{228}Ac	17430.4(7)	17442.9(8)	17431.1(7)	17427.3(8)
968.971(17)	^{228}Ac	18536.9(11)	18549.8(11)	18537.4(12)	18532.4(12)
1120.287(10)	^{214}Bi	21429.3(9)	21447.8(11)	21431.9(10)	21425.3(10)
1460.830(6)	^{40}K	27946.1(2)	27968.2(2)	27946.8(2)	27944.2(3)
1764.494(14)	^{214}Bi	33756.7(9)	33781.4(9)	33755.8(9)	33755.1(10)
2614.533(13)	^{208}Tl	50016.9(8)	50059.3(9)	50020.0(7)	50019.6(9)

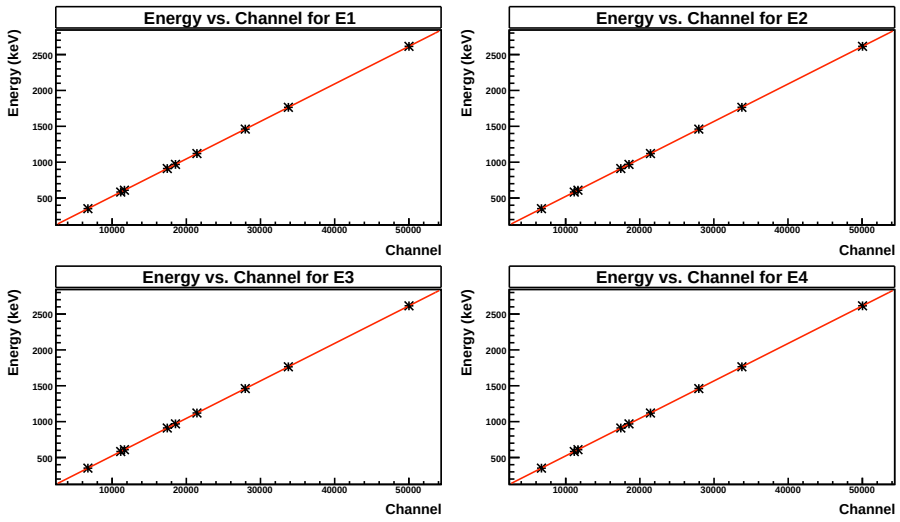

Figure 4.4: Energy calibration of the CLOVER detector. The error bars are smaller than the datapoint markers. The χ^2 / number of degrees of freedom (NDF) depends on the order of the fit. See text for details.

Table 4.4: Quality of calibration fits. The NDF is 7, 6, 5, and 4 for the 1^{st}-, 2^{nd}-, 3^{rd}-, and 4^{th}-order polynomial fits, respectively. The best fit for each crystal is in bold type, e.g., a quadratic calibration is the best fit for crystal 1, a 4^{th}-order fit is best for crystals 2 and 4, and a linear fit is best for crystal 3.

Polynomial order	E1		E2		E3		E4	
	χ^2	P-value	χ^2	P-value	χ^2	P-value	χ^2	P-value
1	13.9	0.053	18.2	0.011	**9.0**	**0.253**	10.4	0.167
2	**9.7**	**0.138**	12.3	0.056	8.9	0.179	8.1	0.231
3	8.9	0.113	6.8	0.234	7.9	0.162	8.0	0.156
4	8.3	0.081	**2.2**	**0.699**	7.1	0.131	**4.5**	**0.343**

data. We see that there is no single polynomial that provides the best fit for the calibrations of all four crystals. In light of this flexibility, we make the decision to utilize a quadratic fit for the final calibrations. This allows for responses that deviate from linear while minimizing any potential divergence outside the fit range. Eqs. (4.1) show the resulting energy calibrations, with the fits for each crystal graphed in Fig. 4.4. The equations convert channel number to energy in keV, and the uncertainties come from the ROOT fiting routine:

$$\begin{aligned}
E1 \text{ / keV} &= 23(3)\cdot 10^{-2} + 5.2262(2)\cdot 10^{-2}\ \text{ch} + 12(4)\cdot 10^{-11}\ \text{ch}^2 \\
E2 \text{ / keV} &= 8(4)\cdot 10^{-2} + 5.2235(3)\cdot 10^{-2}\ \text{ch} - 16(6)\cdot 10^{-11}\ \text{ch}^2 \\
E3 \text{ / keV} &= 13(3)\cdot 10^{-2} + 5.2268(3)\cdot 10^{-2}\ \text{ch} - 1(6)\cdot 10^{-11}\ \text{ch}^2 \\
E4 \text{ / keV} &= 34(4)\cdot 10^{-2} + 5.2268(3)\cdot 10^{-2}\ \text{ch} - 10(6)\cdot 10^{-11}\ \text{ch}^2
\end{aligned} \tag{4.1}$$

The fit equations are confirmed in Section 4.5.3, where comparisons are made between measured and published gamma ray energies. Recalibrations were performed throughout the life of the experiment, including after any lengthy hiatus and any time the liquid nitrogen coldsource was removed from the CLOVER. Since the raw bin numbers were recorded as part of the datasets, recalibration can be performed on any individual dataset using the peaks present (i.e., separate calibration runs are unnecessary), provided the Gaussian peaks used in the calibration have enough counts to provide statistically significant results. The goodness-of-fits for the subsequent recalibrations were comparable to those in Table 4.4.

4.2.3 Rebinning the raw data

Care must be taken when translating raw channel numbers to energy. The raw data, being digitized, is inherently binned. An energy histogram with an arbitrary number of bins per keV will most likely not have bin edges that line up with the bin edges of the raw data. Simply filling the en-

ergy histogram would therefore result in non-Poisson-distributed statistics, making goodness-of-fit calculations unreliable at best.

Compounding the issue is the fact that with a quadratic calibration, calibrating the raw channel numbers results in energy values that are not evenly spaced. For example, with a quadratic energy calibration there may be (for example) 1000 raw bins between the energies 1000 and 1200 keV, but only 997 raw bins between the energies 1200 and 1400 keV. This means we cannot use constant offsets from calibrated energy values to obtain the low and high bin edges for the data.

We therefore created lookup tables by calculating the energy for every possible channel value from 0 to 65535. There were separate lookup tables for each CLOVER crystal, as well as for every re-calibration throughout the life of the experiment. These lookup tables contained all the possible discrete energies after calibration, and the values in this table are represented by the vertical dotted lines in Fig. 4.5. The low and high bin edges were calculated by taking an average of two consecutive calibrated energies.

For example, the raw channels 10344, 10345, and 10346 would translate to energies 540.8410, 540.8932, and 540.9455 keV using Eqs. (4.1) for crystal 1. The low and high bin edges of this middle energy (the one corresponding to channel 10345) are 540.8671 and 540.9194, respectively.

Please refer to Fig. 4.5 when necessary during the following description. 'A' and 'B' are two calibrated energies, and 'b_{lo}' and 'b_{hi}' are the calibrated low and high bin edges. Then, when filling a histogram, if the edges of the calibrated energies fell wholly within the edges of the histogram bin (as is the case with energy 'A'), the count for the corresponding histogram bin (in this example, bin '1') was incremented by 1. If the bin edges overlapped, as in the case of energy 'B', a probability was calculated according to the amount of bin overlap. Referring to energy 'B', the proportion is set by

$$\text{Probability} = \frac{b_{hi} - 3_{lo}}{b_{hi} - b_{lo}} \tag{4.2}$$

The count was then randomly put into one of the two overlapping bins (in this case bin '2' or bin '3') according to a binomial distribution with the probability being set by Eq. 4.2. This count was fully entered into the returned histogram bin, so all bins in the final histogram have integer counts.

4.2.4 Detector optimization

With the CLOVER detector calibrated, we turned our attention to optimizing the output from the detector. The calibration was performed before the optimization for quicker identification of relevant features, but there is nothing that *a priori* requires calibration before optimization or vice versa.

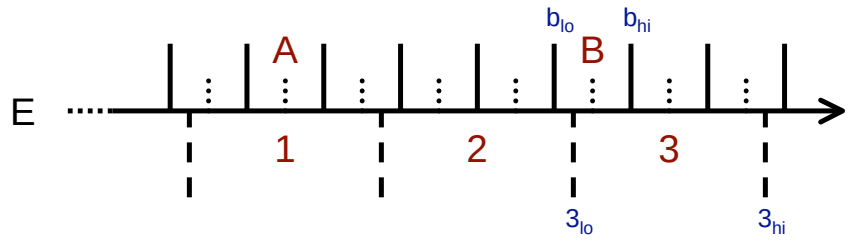

Figure 4.5: Rebinning the CLOVER data. The calibrated energies are represented by the vertical dotted lines. The calibrated energy "bin edges" are an average of consecutive calibrated energies, and are represented by the solid vertical bars. The energy histogram bin edges are represented by the dashed lines. Because of the quadratic calibration, the calibrated energy "bin widths" (i.e., b_{hi} - b_{lo} for any given energy B) are not constant throughout the spectrum. See text for further details.

Trigger filter optimization

Both the trigger and energy filters utilize a trapezoidal filter. Fig. 4.6 shows the detector input (as processed by the analog-to-digital converter, or ADC) and two filter outputs. The two user-defined values for each filter are the "rise time", shown by the parameter L, and the "flat top time", shown by the parameter G. The energy filter is a slow filter used to determine the height of an pulse, while the much faster trigger filter determines if an event has occurred. (A typical "2L + G" time for the energy filter is between 1 and 10 μs, while the "2L + G" time for the trigger filter is approximately 0.5 μs.)

If the threshold of the DAQ is set very low, random noise can lead to a false trigger. In these cases the energy reconstruction fails and the event is put into either an underflow or overflow bin. The trigger filter can be used to reduce the rate of these false triggers (though not without limit–setting the threshold lower and lower will still result in an increasing number of false triggers). The quality of the trigger filter settings is measured by the minimization of the total event rate for any given threshold setting. The optimization process, therefore, is to lower the threshold to a reasonable[4] value and adjust the trigger rise and flat top times until the total event rate is minimized.

We built a lead shield around the cryostat with 4" of lead around the top, bottom, left, right, and front faces of the CLOVER crystals and a 2" lead shield around the dewar. Although the 2" lead shield had unavoidable thin gaps between bricks, we strove to disallow any gaps that had a direct

[4]"Reasonable" in this case is subjective. The threshold is in arbitrary units, and scales only roughly linearly with the low-energy cutoff.

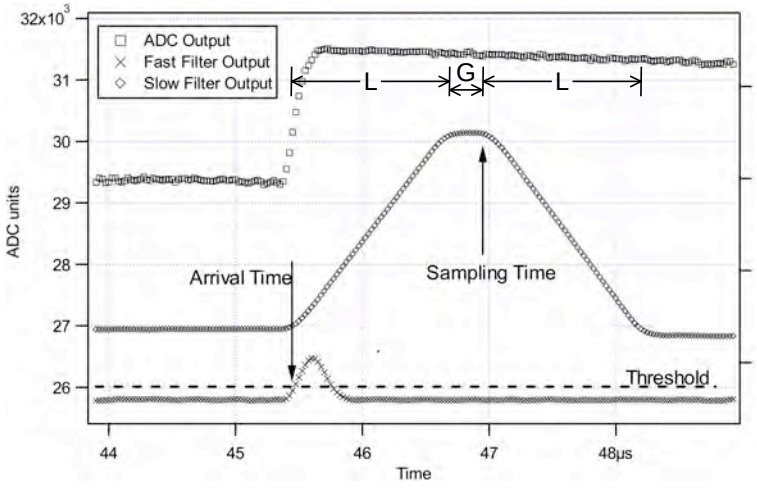

Figure 4.6: Trapezoidal filter processing. The curves show the ADC-processed detector output, as well as the fast (trigger) filter output and slow (energy) filter output. The user-defined parameters for each filter are L and G, referred to as the "rise time", and "flat top time", respectively. The labeled L and G are for the energy filter. The sampling time is the time the height of the energy filter output is recorded, and is equal to the energy filter's L + G. Figure adapted from the XIA User's Manual [82].

line-of-sight to the active detector.

We set the Polling Time to 0.5 s and the Time Out to 5 s. The trigger filter optimization process is to vary the flat top time until the event rate is minimized. Once the optimal flat top time is set, vary the rise time to minimize the event rate even further. The first step was to determine a "reasonable" threshold value. We ran with a trigger rise time of 0.1 μs and a flat top time of 0.0 μs. The event rate at a threshold of 10 was 11987 cps, at 15 it was 163 cps, and at 20 it was 7.99. The test value of 15 was chosen because it provided an event rate in the logarithmic middle of the rates encountered. Table 4.5 shows the progression of finding the minimum event rate.

Energy filter optimization

After optimizing the trigger filter, we optimized the energy filter. To do this we gathered data from a ^{60}Co source inside the shield. With a source that close to the detector we had to set the Polling Time to 0.01 s and the Time Out to 0.02 s. We then took a series of three-minute datasets, changing either the energy filter rise time or flat top time for each run. For each setting we measured the width of the 1332 keV energy peak and generated a table of FWHM as a percentage of the gamma energy.

Table 4.5: CLOVER E channel threshold optimization. With the threshold set to 15, the optimal settings are a 0.175 μs rise time, and a 0.05 μs flat top time. Since the DGF4C runs at 40 MHz, these time settings can only be set to integer multiples of 25 ns.

Rise time (μs)	Flat top time (μs)	Event rate (cps)
0.100	0.000	163
0.125	0.000	104
0.150	0.000	11.1
0.175	0.000	10.3
0.200	0.000	11.5
0.175	0.025	11.7
0.175	**0.050**	**9.05**
0.175	0.075	9.06
0.175	0.100	9.37

The optimal energy filter settings are those that correspond to the lowest average FWHM of the four energy channels.

Table 4.6 shows how the resolution changes with the energy filter rise and flat top times. We see that there is a minimum in the average FWHM for an energy rise time of 4.4 μs and an energy flat top time of 1.2 μs.

Low-Energy performance of the optimized CLOVER

With the CLOVER detector optimized for resolution and a stable trigger filter, we took background data inside the 4" Pb shield for 41.9 hours (33.7 hours of live time). Fig. 4.7 shows the calibrated low energy region of the resulting spectrum with data from all four crystals combined. A full analysis of the background spectrum is available in Section 4.5.3.

Measurement of livetime

The live time of the DAQ system can be measured from the data files themselves. When the DGF4C buffer is opened for recording events, the "buffer start time" is recorded in the buffer data header. The buffers acquire data until they are full or until a spill is forced. The live time for a spill can therefore be measured by subtracting the buffer start time from the time stamp of the last event in the buffer. To measure the total live time of a data run, this time difference is totaled for every spill in the data set. The live time as a percentage of the run time can be measured by dividing the total live time by the time difference between the last event in a file and the first buffer start time.

There is a small correction to the live time involving pileup rejection. When a trigger is initiated,

Table 4.6: CLOVER E channel resolution optimization. The optimal settings are a 4.4 μs rise time and a 1.2 μs flat top time. As with the trigger filter settings, the energy filter rise and flat top times are allowed to take on only discreet values. Starting with the factory settings, first the energy rise time is optimized. Once the best rise time is found, the flat top time is varied. The lowest possible flat top time allowed by the DAQ is 1.2 μs. The FWHM values are a percentage of the centroid energy, 1332 keV.

Rise time (μs)	Flat top time(μs)	$\langle$FWHM$\rangle$	E1 FWHM	E2 FWHM	E3 FWHM	E4 FWHM
6.4	1.2	0.2082	0.1959	0.2078	0.1969	0.2323
6.0	1.2	0.2123	0.1922	0.2113	0.2057	0.2401
5.6	1.2	0.2116	0.1912	0.2165	0.2059	0.2327
5.2	1.2	0.2083	0.1866	0.2155	0.2056	0.2258
4.8	1.2	0.2069	0.1890	0.1957	0.2098	0.2332
4.4	**1.2**	**0.2035**	0.1894	0.2015	0.2064	0.2167
4.0	1.2	0.2066	0.1910	0.1975	0.2057	0.2323
3.6	1.2	0.2055	0.1903	0.2079	0.2020	0.2219
3.2	1.2	0.2139	0.1990	0.2169	0.2158	0.2238
4.4	1.6	0.2064	0.1979	0.2030	0.1976	0.2270
4.4	2.0	0.2120	0.1916	0.2148	0.2130	0.2287

the height of the pulse is recorded a set "sampling time" later (see Fig. 4.6). This time is set by the energy filter parameters, and is equal to the energy filter's L + G + the time of one decimated clock tick[5]. If there is more than one trigger initiated within this time window, all participating events are rejected due to pileup. All but the last event within a spill have this associated dead time. This pileup rejection time therefore introduces an extra dead time equal to the total number of events less the total number of spills multiplied by the sampling time:

$$\text{Dead time correction} = (\#\text{ of events} - \#\text{ of spills}) \times \text{sampling time} \tag{4.3}$$

This dead time correction is small. Consider a data rate of 1 kHz. For the optimized energy filter settings, the sampling time (L + G + one decimated clock tick) is 6.000 μs. Within one second there would be 1000 events and 45 spills. The additional dead time would therefore be 5.7 ms over a run time of 1 s, for a correction of 0.57% of the run time.

[5]The DGF4C trigger and energy filters operate with a "filter decimation". This decimation is a measure of the number of clock ticks over which values are averaged before entering the filter logic. For a decimation of n the number of averaged clock ticks is 2^n. Thus with a clock period of 25 ns and a decimation of 4, one decimated clock tick for the CLOVER data is 25 ns $\times 2^4$ = 400 ns.

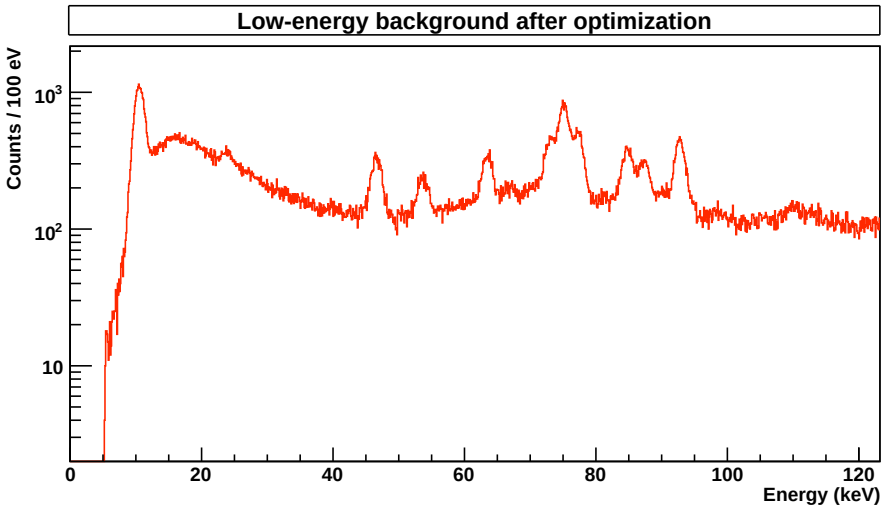

Figure 4.7: Low-energy histogram after optimization. Given the way the spectrum shows a dropoff at roughly 15 keV, the low-energy cutoff for coincidence analyses is set at 20 keV–if an energy is below this value, it is discarded. The peaks will be identified in Section 4.5.3. Data shown represents all events where a single crystal registered an energy deposition.

4.3 Shielding the CLOVER detector

To reduce the background rate in the dataset, we shielded the CLOVER detector using a passive lead shield and an active muon veto. In this section, we cover both of the shields used.

4.3.1 Passive Shielding

The most basic shielding material for small-scale experiments is lead bricks. While a simulation would have given us basic information as to the efficacy of the lead shielding, we would have had to verify the simulation using experimental measurements. The simulation might not have taken into account all the local forms and levels of background. Given the ease with which a lead shield can be built, we made the decision to simply measure shielding efficacy rather than model it. The question we had to answer was how much would the lead bricks reduce the background?

CsI shielding studies

To answer this question, we collected data using a CsI detector in four different configurations: no shielding, a 2” lead shield, a 4” lead shield, and a 6” lead shield. A CsI detector was used because its

small size allowed a full shield up to 6” thick, while the CLOVER detector and dewar taken together are large enough to exhaust the limited supply of lead bricks at less than a full 4” lead shield. We normalized the CsI spectra by the runtime and plotted the results on the same graph. Fig. 4.8 shows the results.

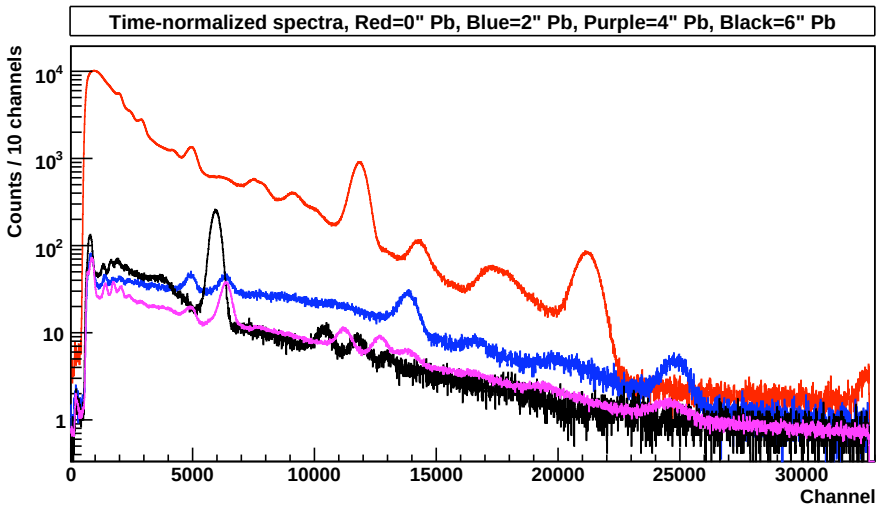

Figure 4.8: Comparing background rates with varying lead shielding thickness. The horizontal scale is not calibrated, and so is in raw channels. The large peak near bin 21000 in the top curve is presumed to be the 2614.5 keV gamma peak from ^{208}Tl decays. The large peak in the same curve near 12000 is assumed to be the 1460 keV peak from ^{40}K. The voltage of the detector fluctuated between data runs, resulting in a shift in the peak centroids among the four curves. The source of this fluctuation was not known, though the peaks in the data can be identified between spectra (e.g., the strong peak in the purple curve near channel 6500 corresponds to the strong peak in the black curve near channel 6000). If the figure is not available in color, the “red” curve is at the top, the “blue” curve is the one that lies just below the “red” curve between channel numbers 7000 and 22000, the “black” curve is the one with the very large peak near channel 6000, and the “purple” curve is the only curve remaining.

It turned out that some of the bricks we used in building the 6” shield were contaminated, which lead to the large peak near channel 6000 in the black curve (if the figure is not available in color, see the figure text for an explanation). Later studies showed this contamination to be from ^{137}Cs. Despite this contamination, the continuum is shown to be reduced going from no shielding to a 2” lead shield to a 4” lead shield. Moving from a 4” lead shield to a 6” lead shield, however, did not appreciably reduce the continuum background in the upper energies (i.e., above channel 20000). We

will therefore use a 4" lead shield with the CLOVER.

Because of the brick contamination, all the bricks in the shield were assayed. The contaminated bricks, numbering roughly 10 out of about 200, were removed from the laboratory and properly disposed of as mixed waste.

CLOVER shielding studies

Having made the decision to use a 4" passive lead shield around the CLOVER detector, we repeated the shielding study with the CLOVER. We collected background data using no shielding, a 2" lead shield, and a 4" lead shield[6]. Fig. 4.9 shows the resulting time-normalized histograms. We measured the areas of various energy peaks as well as several heights in the continuum, normalized the values by time and the zero-shielding rate, and plotted the results in Fig. 4.10. From this graph we can see that the background reduction varied from a factor of about 0.4 in the continuum near 2000 keV to almost two orders of magnitude in the 1460 keV ^{40}K peak. We would not expect all the background rates to be attenuated by the same factor. There may have been some backgrounds present in the lead shielding (e.g., inelastic fast neutron collisions on ^{208}Pb leading to a 2614 keV gamma ray) that were reduced less effectively than sources wholly external to the lead shield.

4.3.2 Active Shielding

To further reduce the background, we employed a muon veto shield. This active shield was made of two scintillator blocks, measuring roughly 10 cm × 30 cm × 8 cm, with photomultipliers attached. Their signals were added together by a linear fan in/fan out, the output of which was connected to one of the DGF4C channels. Fig. 4.11 shows the CLOVER detector with the production shield: 4" of lead around the cryostat, 2" lead shield around the dewar, and the muon veto scintillators on top of the lead shield.

This muon veto was used in the same manner as the position channels on the CLOVER detector, i.e., as a simple, binary readout. Events that included energy deposition in the scintillators are identified in post-processing as originating outside the lead shield. Because the scintillators were outside the shielding, their rate was much higher than the background rate of the CLOVER. The DAQ trigger on the scintillator channel was therefore turned off. This limited the effective rate of the scintillators to that of the background rate of the CLOVER inside the lead shield, which was roughly 10 Hz.

To verify the performance of the muon veto, we histogrammed all CLOVER events where there was also an energy deposition in the scintillators. Some of these events were accidental coinci-

[6]There were not enough bricks to build a 4" lead shield around the entire CLOVER detector and dewar, so we built a 5-wall 4" lead shield around CLOVER, and a 2" shield around the dewar, being sure to eliminate as much as possible any direct "lines of sight" through the shield to the germanium crystals.

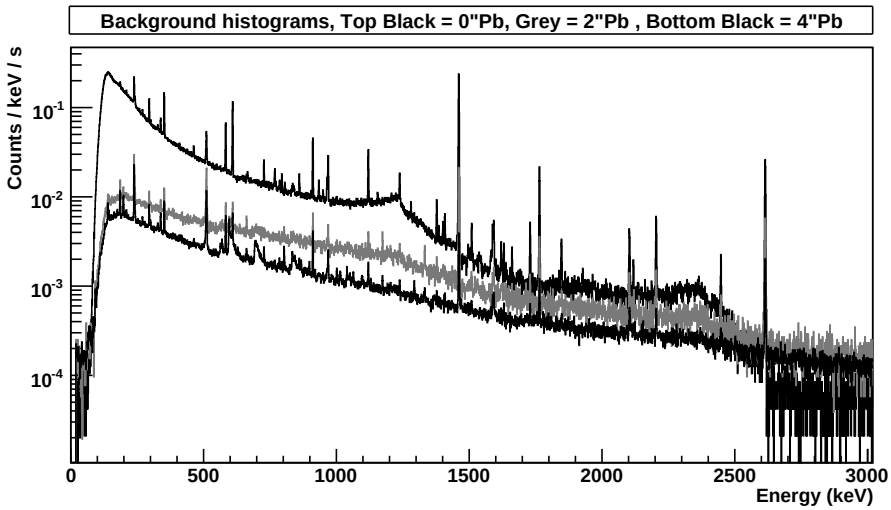

Figure 4.9: CLOVER shielding histogram comparison. A threshold of 50 was used to obtain these graphs, which is why the data acquisition low-energy cutoff is at roughly 150 keV.

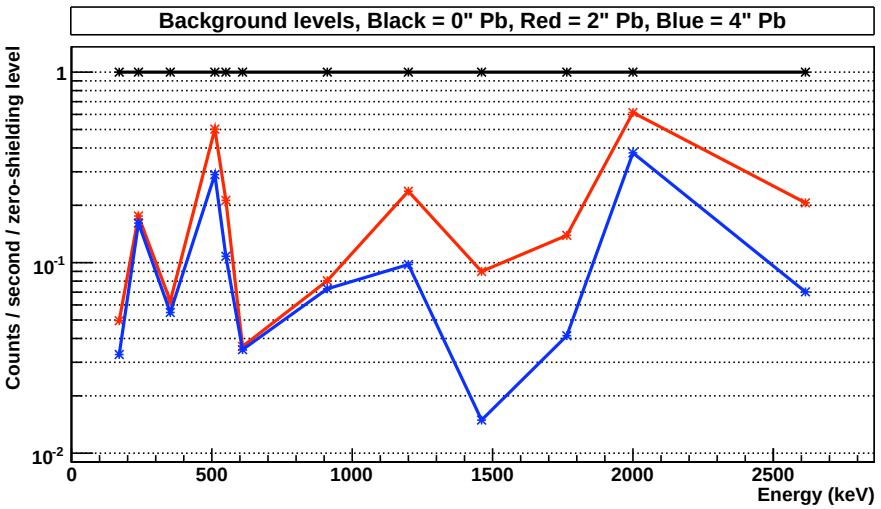

Figure 4.10: Comparing the efficacy of various thicknesses of lead shielding. The gamma peaks used in this comparison are 238.6, 351.9, 511.0, 609.3, 911.1, 1460.8, 1764.5, and 2614.5 keV. The continuum level was evaluated at 170, 550, 1200, and 2000 keV.

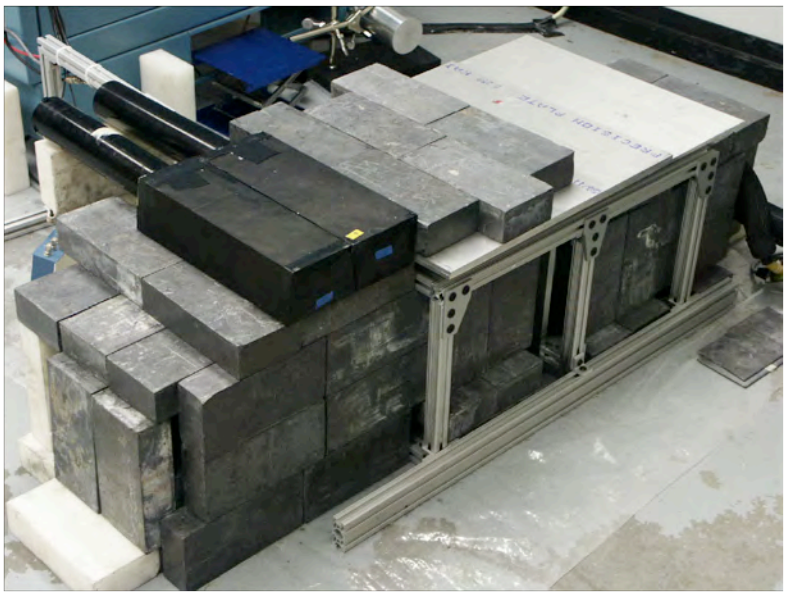

Figure 4.11: CLOVER detector with 4” lead shield and muon veto.

dences. To measure the accidental coincidence rate we measured the ratio of peak areas in both the muon-shield-coincident histogram and the raw histogram. Specifically, we analyzed three peaks at energies unrelated to muon activity. This accidental coincidence rate turned out to be (1.48 ± 0.61)%. Table 4.7 shows the ratio of the unrelated peak areas, as well as the peak area ratio of the more strongly correlated 511 keV annihilation peak area.

We determined the muon-related spectrum by multiplying the bin values of the full spectrum by 1.48% and subtracting those results from the bin values in the spectrum of events coincident with a muon tag. Fig. 4.12 shows the resulting histogram. Through this data-cleaning process, it is clear that the strongest muon-related peaks come from e^+e^- annihilation gamma rays and lead X-Rays. We estimated the energy deposited by a muon in a single CLOVER crystal to be greater than 20 MeV, and as such is outside the range of the DAQ.

In practice, we ended up not using the anti-muon veto in performing spectrum analyses or coincidence studies presented here. The accidental rate was only on the order of 1.5% for background data, and the only strongly-effected peaks are the lead X-Rays and annihilation gamma peaks, none of which is assumed to have a noticeable affect on the analyses. Finally, the lack of full anti-muon coverage around the largest mass source (the lead shield) precluded tagging many of the cosmic-ray-related events as such. Apart from the lead X-Ray and annihilation gamma peak areas, we

Table 4.7: Muon accidental rate. The ratios of peak areas from decays of ^{212}Pb (238 keV), ^{228}Ac (911 keV), and ^{40}K (1461 keV), which are unrelated to muon events, set the accidental muon coincidence rate at (1.48 ± 0.61)%. The 511 keV annihilation peak is related to the muon rate, as shown by its larger ratio.

Energy	Ratio of muon-coincident peak area to background peak area
238	(1.16 ± 0.16)%
911	(2.09 ± 0.54)%
1461	(1.19 ± 0.23)%
511	(5.24 ± 0.32)%

concluded that cosmic rays would only effect the background continuum level, but all events that contribute to the background will be accounted for via the background fits.

4.4 Gamma photopeak efficiency

A final characterization of the CLOVER detector before analyzing the full spectrum is a measurement of the photopeak efficiency of the individual CLOVER crystals. To obtain this measurement, an isotope must be used that has many strong gamma lines in a wide energy range. Fortunately, ^{228}Ac and ^{208}Tl, both contained in the ^{232}Th decay chain, satisfy these requirements. We placed a thorium wire inside the lead shield and gathered data for 2.07 hours.

To obtain the efficiency curve, we measured the areas of 29 gamma peaks associated with the decay of ^{228}Ac and normalized them by the area of the lowest-energy of these peaks, at 209.3 keV. We also measured the areas of 5 peaks associated with the decay of ^{208}Tl and normalized them by the area of the lowest-energy of these peaks, at 277.4 keV. A similar normalization was performed with the relative intensities of these same gamma lines for the two isotopes. Finally, a ratio of the normalized values (normalized peak area to normalized relative intensity for each of the two isotopes) is plotted in Fig. 4.13.

Gamma attenuation in matter is exponential, so if the detectors were a simple-shaped solid mass of germanium we would expect the efficiency curve to be exponentially falling with energy. The non-regular crystal geometry, however, leads to an efficiency curve that deviates from a simple exponential. Taking the gamma attenuation in matter as motivation, we fit a simple exponential decay plus constant background to the data. The equation ends up being

$$\text{Relative efficiency} = 0.153(7) + 0.93(11)\, e^{-(\text{energy}-148(87))\ /\ 766(27)} \tag{4.4}$$

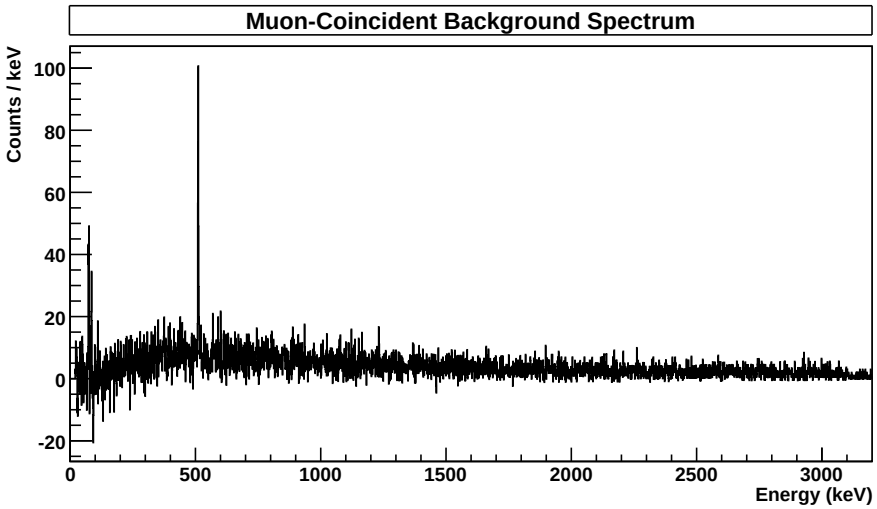

Figure 4.12: CLOVER data in coincidence with muon shield. The clearest evidence for the effects of muons are lead X-Rays near 75 and 85 keV, and the annihilation γ peak at 511 keV.

where the uncertainty in the last digit of every fit value is in parenthesis after the fit value itself. The goodness-of-fit is very low, but the fit is not intended to advocate any particular model, but is rather used to provide a smooth interpolation of photopeak efficiencies between the measured values. Given the lack of a good model in the photopeak efficiency curve, Eq. (4.4) will only be applied to external sources of gamma rays and only in the 209 - 2615 keV energy range.

To improve the goodness-of-fit in Fig. 4.13, we would need to run a Monte Carlo simulation and compare this simulation to experimental results. At this point, however, we want to rely on simulation results as little as possible, because it is the simulation itself we would like to verify.

4.5 Background spectrum of the CLOVER detector

With the shielding determined, the CLOVER detector calibrated and fully optimized, and gamma efficiency characterized, we turned our attention to the background spectrum. We analyzed background data in the 41.9-hour (33.7-hour live time) dataset.

A peak fitter was used to look for peaks in the spectrum. To make the peak fitting more accurate, though, the relationship between peak energy and peak width had to be determined. Once the list of peaks was created using the constrained peak fitter, it was ”hand-checked” against the spectrum, with multiple curves used if any additional features were within the fit window of the target peak.

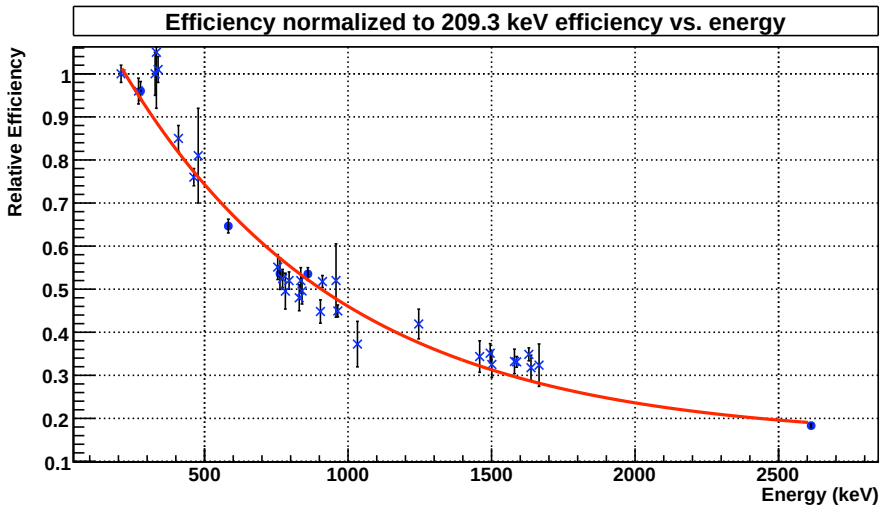

Figure 4.13: Gamma photopeak efficiency of the CLOVER crystals. The efficiency is normalized to a 209.3 keV gamma ray. The crosses are from ^{228}Ac decay gammas and the solid circles are from ^{208}Tl decay gammas. To match the efficiencies of the two isotopes, the efficiency of the 277 keV line from ^{208}Tl is set to the efficiency of the 270 keV line from ^{228}Ac. The exponential fit has a χ^2 / D.O.F. of 96.7928 / 29 = 3.34.

4.5.1 Determining the peak width of the CLOVER

In a germanium radiation detector a particle will hit the crystal and move charge carriers from the valence band to the conduction band. The number of charge carriers it excites is directly proportional to the energy deposited. It is reasonable to assume, then, that the uncertainty in the number of excited charge carriers is related to the square root of the total number of charge carriers. While the resolution of germanium detectors tends to be consistently better than this statistical approach would imply[7], we still make the assumption that part of the peak width is proportional to the square root of the peak energy.

In addition to this square root term, the electronics and cabling adds an average noise term to a pulse from the germanium crystal. These energy-indepedent and energy-dependent widths (the "a" and "b" terms, respectively, in the equation below) add in quadrature to obtain the final width of a peak:

$$\sigma = \text{peak width} = \sqrt{a^2 + b^2\,(\text{peak energy})} \tag{4.5}$$

[7]This effect is given the name "Fano factor". See Knoll [83] for further explanation and examples

A Gaussian plus quadratic background was fit to the peaks:

$$\text{Fit curve} = O + L \cdot \text{energy} + \frac{A}{\sqrt{2\pi}\,\sigma} \exp\left(-\frac{1}{2}\left(\frac{\text{energy} - C}{\sigma}\right)^2\right) \tag{4.6}$$

was fit to the strongest peaks in each of the four crystals using approximately 20 bins per keV of energy. The constant offset O, slope of the background L, Gaussian amplitude A, centroid C, and width σ are all free parameters. We plotted the resulting values of σ versus gamma energy and fitted Eq. (4.5) to the data, resulting in Fig. 4.14. The fit values of a and b are shown in Table. 4.5.1.

4.5.2 The Peak Fitter

With the width of any given peak now constrained by the energy of the peak itself, we turn our attention to the peak fitter. All peaks are fit with a linear background and fit windows of ±20 keV. If there is more than one peak within this window, the results must be more closely fit manually. In some cases, a neutron recoil creates a peak in the spectrum that results in a more "sawtooth" shaped background than Gaussian. Unfortunately, there are very few peaks in a background spectrum that are not within 20 keV of another strong feature. While the peak fitter is not very useful for analyzing a background spectrum, it can still be used for reduced datasets or when a strong source is present inside the shield.

The peak fitter algorithm uses the fit equation

$$Fit = c_1 + c_2 \cdot \text{energy} + \sqrt{c_3^2} \exp\left[-\frac{1}{2}\left(\frac{\text{energy} - c_4}{\sqrt{a^2 + b^2\,\text{energy}}}\right)^2\right] \tag{4.7}$$

where a and b are given by Table 4.5.1, and the free fit variables are c_1, c_2, c_3, and c_4.

The initial values will change depending on the first-order shape of the spectrum. In the case of the 42-hour background dataset, c_1 is very roughly set to assume that the continuum background is linear with a y-intercept of 2000 and a slope of -0.64 with respect to the energy, while c_2 is given a starting value of 0. The starting value of c_3 is set to the bin height at the center of the fit window less c_1, and the seemingly unnecessary construction of $\sqrt{c_3^2}$ is to avoid negative peaks (the fit function does not properly handle absolute values). The initial c_4 is set to the center of the fit window itself. The fitter then steps over every bin from 40 keV to 3000 keV. The background at the peak centroid is found using the equation

$$\text{background per bin} = c_1 + c_2 \cdot c_4$$

The area of a peak is found using the standard Gaussian area function

$$\text{peak area} = \sqrt{2\pi}\, c_3\, \sqrt{a^2 + b^2\, c_4} \tag{4.8}$$

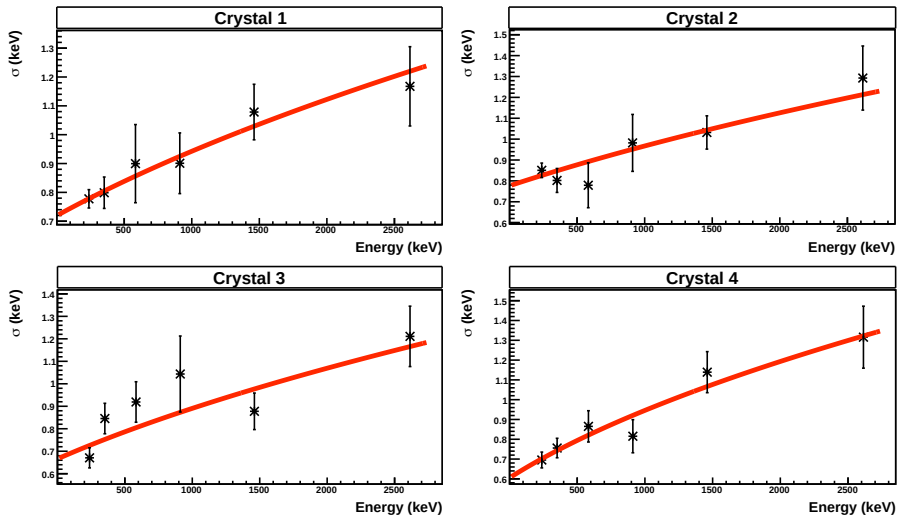

Figure 4.14: CLOVER peak width fit. The energy error bars are too small to be seen on this scale. The fit values are given in Table 4.5.1. The χ^2 for crystals 1 through 4 were 0.57, 2.61, 7.65, and 2.48, respectively, each with 4 degrees of freedom. The corresponding P-values are 0.97, 0.63, 0.11, and 0.65.

Table 4.8: CLOVER peak width parameters. The width of the peaks is roughly 1 keV. Crystal 3 has the best overall resolution, while crystal 2 has the highest y-intercept, indicating a heightened noise level in the electronics.

Crystal	a	b
1	0.719 ± 0.040	0.0193 ± 0.0027
2	0.776 ± 0.040	0.0182 ± 0.0029
3	0.666 ± 0.051	0.0187 ± 0.0027
4	0.605 ± 0.051	0.0230 ± 0.0025

This area must be normalized to the histogram bin width and energy scale. For example, if the horizontal energy scale is in keV and there are 5 bins per keV, the area as given by this equation must be multiplied by 5. The uncertainties in the peak areas are those returned by the ROOT fitting routine.

To calculate the significance of a peak, the background fit is integrated around the peak, with centroid $\pm 2.5\sigma$ being the integration limits. Integrating a Gaussian curve over $\pm 2.5\sigma$ will give 98.8% of the peak area, so the area of the Gaussian as given by Eq. (4.8) must be reduced by this same factor. To calculate significance above background then, the suppressed peak area is divided by the square root of the integrated background:

$$\text{significance} = \frac{0.988\,\sqrt{2\pi}\,c_3\,\sigma}{\sqrt{\int_{c_4-2.5\sigma}^{c_4+2.5\sigma}(c_1+c_2x)\,dx}} \tag{4.9}$$

We also employed two more tweaks to the peak finder. Only those peaks with a significance of 3σ or greater are reported. Also, the centroid of the peak must be within 3 keV of the center of the fit window. This last requirement removes spurious peaks of insensibly large area (and therefore significance) at the very edge or even outside of the fit window.

4.5.3 Background spectrum and fit peaks

With the peak fitting algorithm in place, we can now go about the task of identifying peaks in the background spectrum. To reiterate what was stated in Section 4.5.2, the peak fitter was used on the background data, but the results were only used as a guide. All peak measurements in this section were performed manually, and the manual fits allowed for peaks with significance less than 3σ.

To identify background radiation, we had to compromise between resolution and statistics. To emphasize statistics, we would accept all events, regardless of how many crystals were hit in the event and which crystals had the deposited energy. To emphasize resolution, we would accept events where only a specific crystal (e.g., crystal 3) registered energy deposition, and no others. The compromise, then, was to use the combined histograms when only a single crystal registered an energy deposition. Because we combined the data from all four crystals, however, we had to re-measure the peak widths as a function of energy. Using the combined data, we get values for a and b of (see Eq. 4.5)

$$\begin{aligned} a &= 0.740 \pm 0.014 \\ b &= 0.0186 \pm 0.0011 \end{aligned} \tag{4.10}$$

Table 4.9 shows information about the peaks, including the peak source, the published gamma energies, and relative intensities of the lines. Figs. 4.15, 4.16, and 4.17 shows the background spectrum with peaks from Table 4.9 labeled.

A few peaks with significance less than 4σ were included in Table 4.9. These lines were included in the table because they are related to known existing lines (e.g., the presence of the 1173 keV line from ^{60}Co implies the existence of the coincident line at 1332 keV). In addition to these related lines are sub-threshold lines linked to known processes, i.e., trace ^{137}Cs contamination, neutron capture on ^{73}Ge, and inelastic nucleon recoils on ^{27}Al.

In addition to the Gaussian fits, there are a number of peaks that have a sawtooth shape rather than a Gaussian shape. The clearest example of this sawtooth shape is the 692 keV peak from ^{72}Ge(n,n'e) reactions. This sawtooth pattern derives from a nuclear recoil from the fast neutron collisions [84]. These sawtooth-shaped peaks were fit using methods outlined in the next section. If a Gaussian peak and neutron recoil peak are related to the same energy state, only the area of the Gaussian was recorded in Table 4.9. For the 692 keV peak, however, there is no associated Gaussian, and the peak area comes from fitting a sawtooth shape to the feature.

Table 4.9: Background peaks of the CLOVER detector. Peak energies were found using a peak fitter as a guide, but then manually fit (see text for further details). The relative intensities are comparable only between peaks derived from the same radioisotope. Entries grouped together all apply to a single fit energy peak.

Fit E (keV)	Peak Counts	Peak Uncer.	Back-ground	Sig. (σ)	Source	Pub E (keV)	Rel. Int.
24.1	1108.3	107.0	11307.9	10.30	^{71m}Ge	23.4	0.48
46.6	4006.7	93.9	4654.1	58.03	^{210}Pb	46.5	4.3
53.7	2028.7	82.2	4891.9	28.66	^{75m}Ge	53.4	
63.5	3389.2	101.5	6093.3	42.90	^{234}Th	63.3	4.8
66.7	536.7	91.8	6560.6	6.55	^{75m}Ge sum peak	66.7	
72.9	4705.7	123.3	6979.4	55.65	Pb X-Ray	72.8	
75.1	11646.4	154.9	6843.2	139.10	Pb X-Ray	75.0	
77.3	6108.7	126.7	6666.7	73.92	^{115}In(n, γ)	76.8	
84.8	4106.1	143.8	6356.1	50.89	Pb X-Rays	84.5 84.9	
87.3	2661.4	132.8	6563.1	32.46	Pb X-Rays	87.2 87.4 87.9	
90.2	405.0	167.0	6208.9	5.08			
92.8	5711.0	139.7	5497.1	76.10	^{234}Th	92.4 92.8	2.8 2.8
98.7	318.0	75.4	4513.7	4.68			
110.0	752.4	66.0	4336.1	11.29	^{19}F(n, X)	109.9	
112.7	450.9	62.5	4300.1	6.79			
129.2	413.3	63.6	4071.6	6.40	^{228}Ac	129.1	2.45
139.7	1979.2	76.0	4009.3	30.88	^{75m}Ge	139.7	39.0
143.7	687.2	64.3	3996.7	10.74	^{230}Th	143.9	0.048
162.9	716.7	64.3	3870.3	11.38	^{115}In(n, γ)	162.4	5.1
185.9	3494.7	83.8	3852.0	55.63	^{226}Ra	186.2	3.58
198.3	2281.6	75.2	3780.0	36.66	^{71m}Ge	198.4	
209.4	524.2	59.6	3590.7	8.64	^{228}Ac	209.3	3.9
238.7	10099.3	116.5	3223.9	175.73	^{212}Pb	238.6	43.3

Continued on next page

Table 4.9 – continued from previous page

Fit E (keV)	Peak Counts	Peak Uncer.	Back-ground	Sig. (σ)	Source	Pub E (keV)	Rel. Int.
241.6	1489.4	66.0	3203.9	26.00	^{214}Pb	242.0	7.4
270.0	518.3	52.6	2891.8	9.52	^{228}Ac	270.2	3.5
295.4	1997.4	66.4	2801.0	37.29	^{214}Pb	295.2	19.3
300.4	427.2	51.3	2774.2	8.01	^{212}Pb	300.1	3.3
327.9	426.6	49.9	2602.6	8.26	^{228}Ac	328.0	3.0
338.4	1338.2	59.1	2530.2	26.28	^{228}Ac	338.3	11.3
352.0	3311.3	74.9	2432.6	66.33	^{214}Pb	351.9	37.6
412.1	200.7	41.9	2049.8	4.38	^{198}Au	411.8	96
416.8	226.6	41.7	2026.7	4.97	^{116m}In	416.9	27.7
463.3	234.5	42.0	1851.9	5.38	^{228}Ac	463.0	4.4
511.0	4782.0	80.5	2008.9	105.41	^{208}Tl Ann. γ	510.8 511.0	22.6
537.2	178.7	37.1	1532.0	4.51	^{206}Pb(n, n'γ)	537.5	
569.9	377.7	42.5	1713.2	9.02	^{70}Ge(n, n'γ)	569.7	0.5
583.2	2213.4	61.3	1615.1	54.41	^{208}Tl	583.2	84.5
595.9	921.6	140.0	1426.1	24.11	^{74}Ge(n, n'γ)	595.8	
597.4	4022.3	301.6	15036.5	32.41	^{74}Ge(n, n'γ)	595.8	
609.3	1944.1	62.3	1383.1	51.65	^{70}Ge(n, n'γ) ^{73}Ge(n, γ) ^{214}Bi	608.3 608.4 609.3	46.1
661.6	217.8	37.4	1385.0	5.78	^{137}Cs	661.7	85.1
692.4	3222.4	173.8	5429.8	43.21	^{72}Ge(n, n'e)	692.0	
727.2	555.6	40.4	577.4	22.84	^{212}Bi	727.3	6.6
767.9	202.1	33.6	1165.6	5.85	^{214}Bi	768.4	4.9
771.8	159.2	32.9	1160.5	4.62			
785.8	196.4	33.0	1110.1	5.83	^{212}Bi	785.4	1.1
794.7	263.4	33.9	1099.9	7.85	^{228}Ac	794.9	4.3
803.1	503.8	37.4	1090.0	15.08	^{206}Pb(n, n'γ)	803.1	
834.1	2207.6	289.1	11116.3	20.69	^{72}Ge(n, n'γ)	834.4	
860.8	327.6	36.3	951.7	10.49	^{208}Tl	860.6	12.4
881.0	129.7	31.3	929.8	4.20	^{206}Pb(n, n'γ)	881.0	
898.6	201.0	31.1	982.2	6.34	^{207}Pb(n, n'γ)	897.8	

Continued on next page

Table 4.9 – continued from previous page

Fit E (keV)	Peak Counts	Peak Uncer.	Back-ground	Sig. (σ)	Source	Pub E (keV)	Rel. Int.
911.2	1708.3	50.8	943.1	54.96	^{228}Ac	911.2	25.8
933.8	100.7	29.3	900.9	3.32	^{214}Bi	934.1	3.0
964.8	277.6	31.3	865.8	9.32	^{228}Ac	964.8	5.0
969.0	1027.1	42.3	859.3	34.62	^{228}Ac	969.0	15.8
986.9	122.7	28.1	831.8	4.20			
1001.5	288.4	30.9	816.8	9.97	^{223m}Pa	1001.0	0.8
1014.4	201.4	29.0	806.9	7.01	^{27}Al(n, n')	1014.4	
1063.8	120.7	27.8	844.2	4.10	^{207}Pb(n, n'γ)	1063.7	
1096.9	228.6	29.0	771.0	8.14	^{116m}In	1097.3	56.2
1120.4	509.7	33.7	752.3	18.36	^{214}Bi	1120.3	15.1
1173.4	198.6	27.9	669.9	7.58	^{60}Co	1173.2	100.0
1238.5	203.1	27.6	680.0	7.69	^{214}Bi	1238.1	5.8
1293.4	215.1	26.0	558.5	8.99	^{116m}In	1293.6	84.4
1332.5	89.1	22.7	529.8	3.83	^{60}Co	1332.5	100.0
1377.9	159.6	24.0	492.7	7.10	^{214}Bi	1377.7	4.0
1460.8	3480.4	62.8	430.9	165.66	^{40}K	1460.8	11.0
1509.0	129.9	20.9	373.3	6.64	^{214}Bi	1509.2	2.1
1588.0	179.4	21.7	336.3	9.66	^{228}Ac	1588.2	3.2
1592.4	103.3	19.5	336.0	5.57	^{208}Tl DEP	1592.5	
1620.5	87.3	19.2	338.8	4.68	^{212}Bi	1620.5	1.5
1729.7	142.8	19.4	284.9	8.36	^{214}Bi	1729.6	2.9
1764.5	714.2	31.2	260.9	43.69	^{214}Bi	1764.5	15.4
1778.7	64.7	16.5	249.3	4.05	^{28}Al	1778.9	100
1805.8	61.6	16.1	241.0	3.92			
1847.0	71.5	16.3	242.1	4.54	^{214}Bi	1847.4	2.1
2103.4	142.5	18.3	232.0	9.24	^{208}Tl SEP	2103.5	
2203.8	201.2	19.5	201.4	14.01	$\left\{ \begin{array}{l} ^{76}\text{Ge(n, n'}\gamma\text{)} \\ ^{214}\text{Bi} \end{array} \right.$	$\left\{ \begin{array}{l} 2203.8 \\ 2204.2 \end{array} \right.$	$\left\{ \begin{array}{l} \\ 5.1 \end{array} \right.$
2447.6	56.1	13.5	144.9	4.61	^{214}Bi	2447.9	1.6
2614.4	1723.6	42.9	116.5	157.81	^{208}Tl	2614.5	99.0

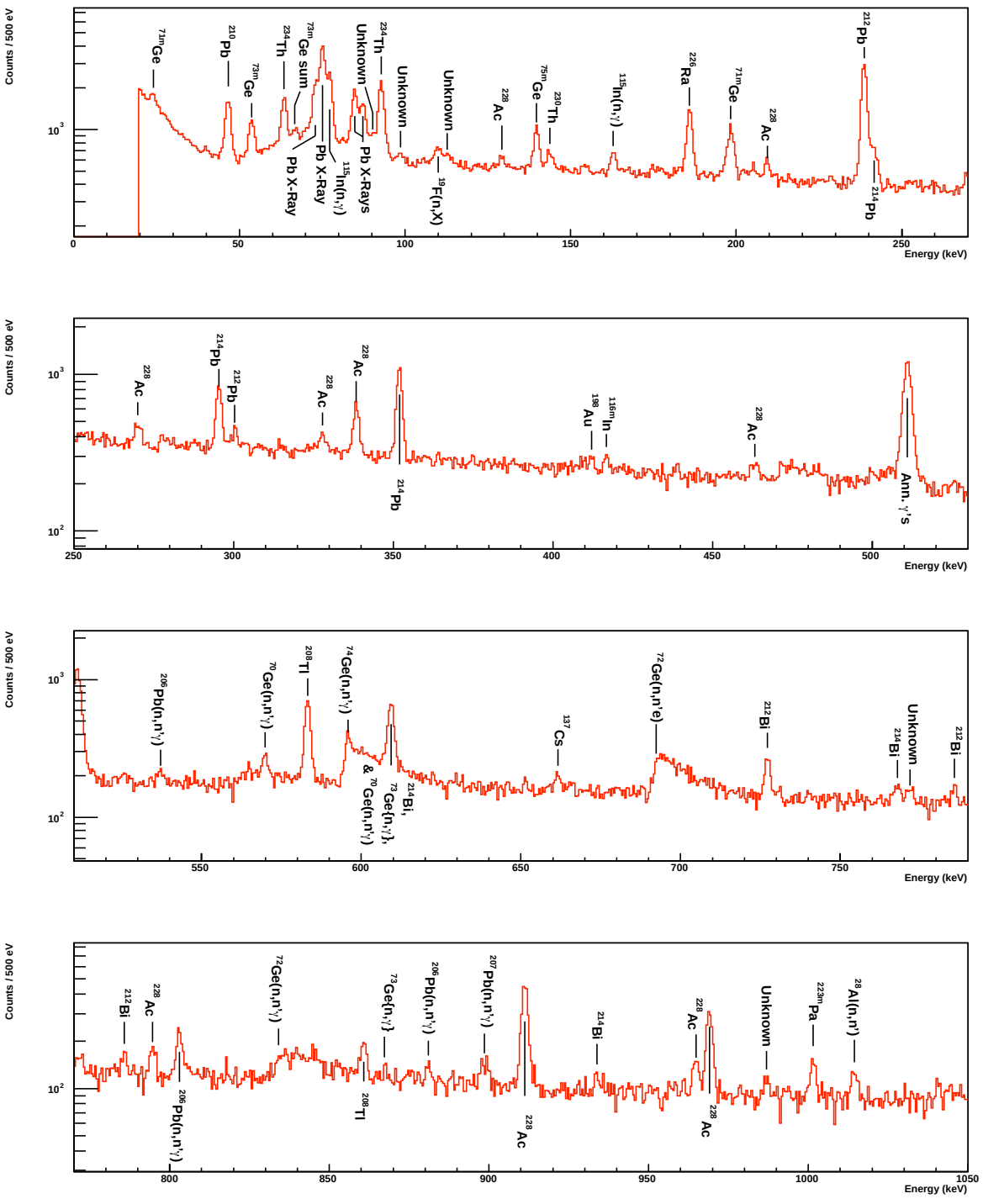

Figure 4.15: CLOVER background spectrum (0-1000 keV). This spectrum is based on 42 hours of background data (33.8 hours of live time) with the CLOVER in a 4" lead shield. Only data from crystal 3 are shown.

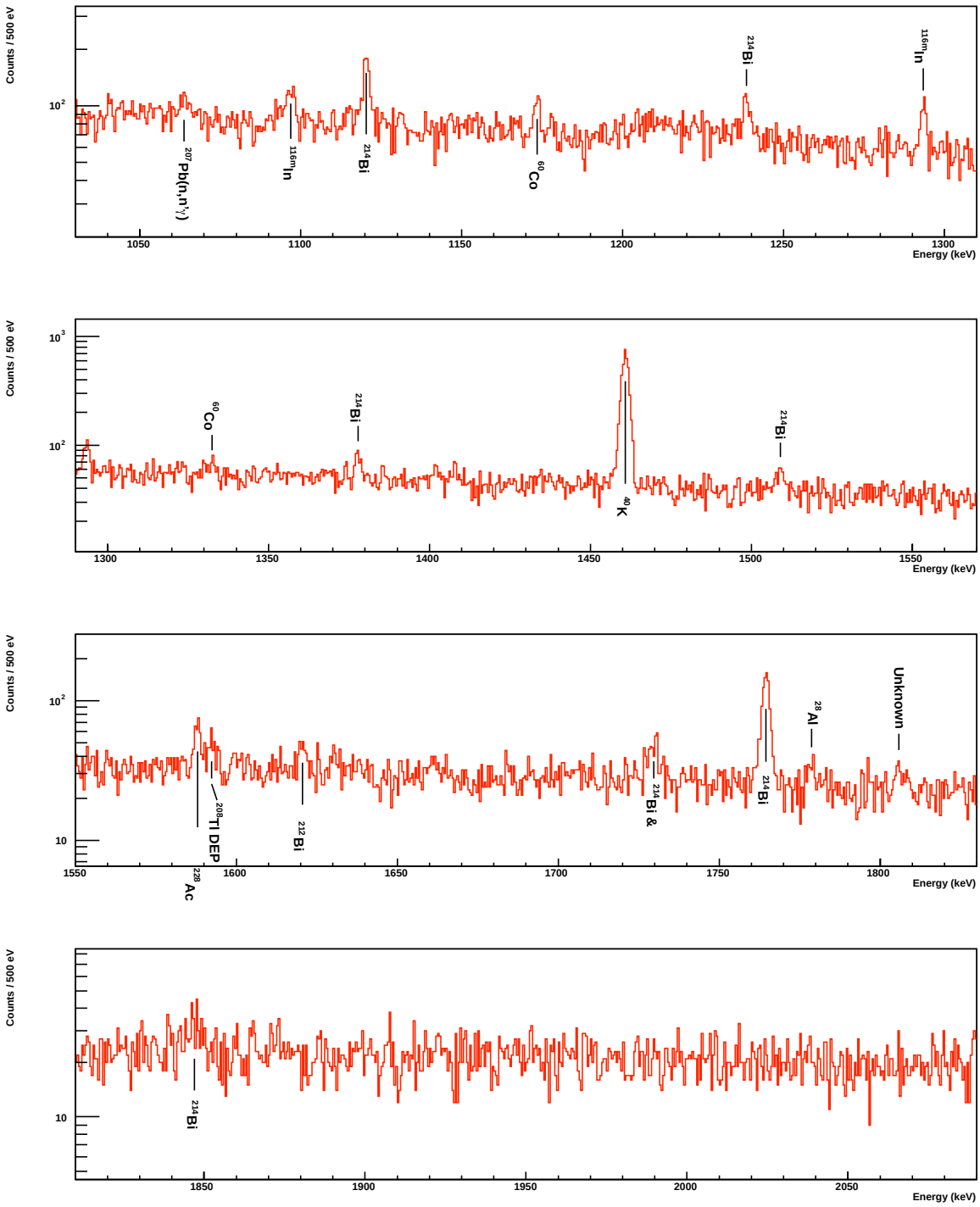

Figure 4.16: CLOVER background spectrum (1000-2000 keV). This spectrum is based on 42 hours of background data (33.8 hours of live time) with the CLOVER in a 4" lead shield. Only data from crystal 3 are shown.

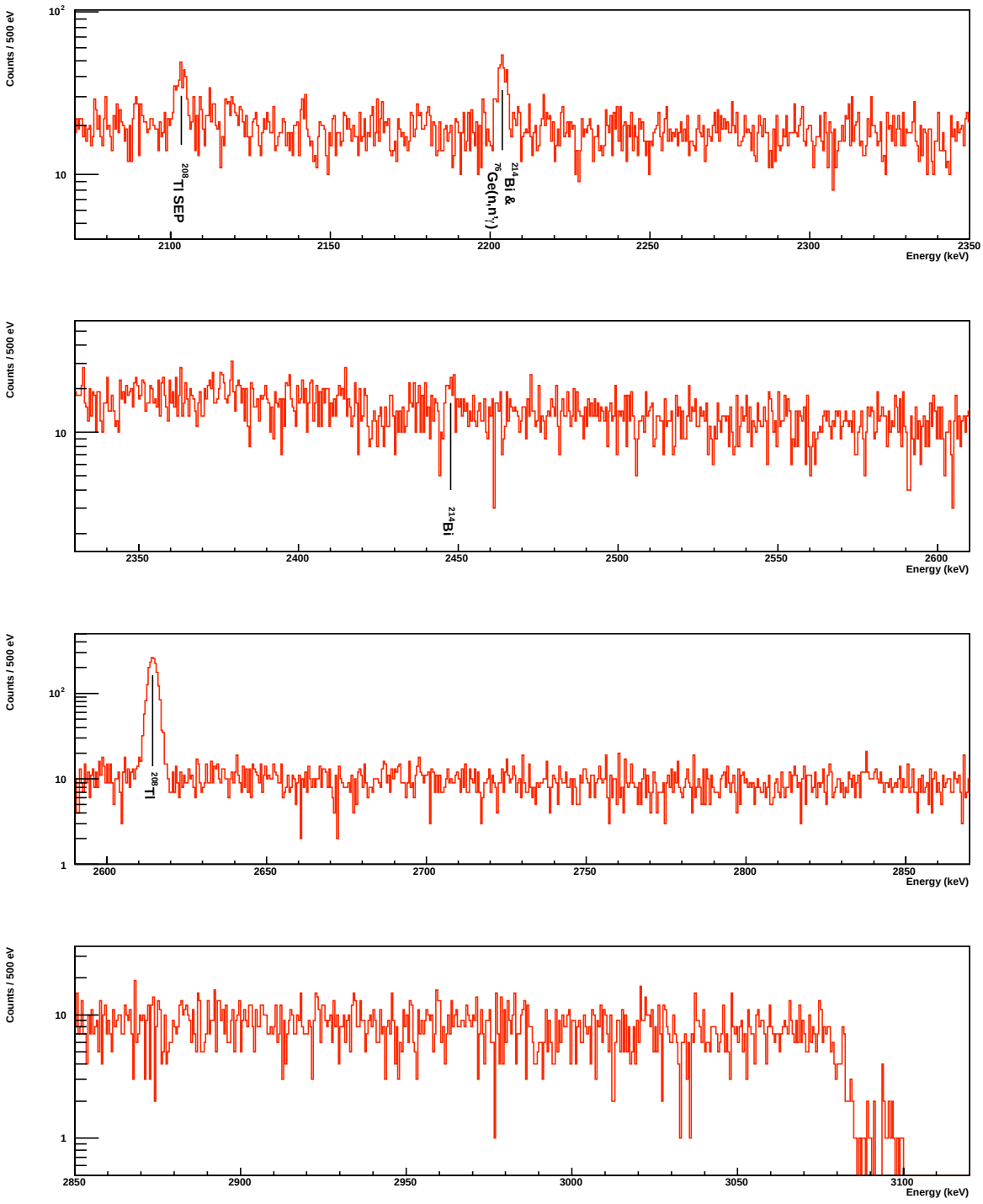

Figure 4.17: CLOVER background spectrum (2000-3000 keV). This spectrum is based on 42 hours of background data (33.8 hours of live time) with the CLOVER in a 4" lead shield. Only data from crystal 3 are shown.

4.5.4 Verification of peak identification

The peaks in the background spectrum were checked for consistency against published intensities [89] and the measured relative efficiencies. By normalizing a peak area by both the relative intensity of the gamma and the relative efficiency as measured in Section 4.4, we can generate a table of augmented peak areas that would ideally all take on the same value within any given isotope. We then normalized these augmented peak areas by the first such value within an isotope. The results are shown in Table 4.10.

Table 4.10: Peak verification in the background spectrum. By appropriately normalizing the peak areas, they should all take on the same value within any given isotope. The last column shows the ratio of the normalized peak areas to the area of the lowest-energy peak in the isotope group. The absolute uncertainties in the last place of any value are shown in parenthesis. See the text for more details.

Isotope	Energy (keV)	Normalized Area	Ratio
^{228}Ac	209.3	132(24)	1.00(25)
	270.2	156(36)	1.18(29)
	328	159(29)	1.20(31)
	338.3	134(19)	1.01(23)
	463	69(15)	0.52(15)
	794.9	110(19)	0.83(21)
	911.2	133(16)	1.00(22)
	964.8	117(19)	0.88(21)
	969	138(17)	1.04(22)
	1588.2	190(29)	1.43(34)
^{208}Tl	583.2	38(5)	1.00(18)
	860.6	51(8)	1.32(27)
	2614.5	92(5)	2.39(34)
^{214}Bi	768.4	73(15)	1.00(18)
	934.1	69(22)	0.95(36)
	1120.3	81(10)	1.12(27)
	1377.7	117(21)	1.62(44)
	1764.5	174(16)	2.40(54)
	1847.4	134(35)	1.85(61)
^{212}Bi	727.3	143(20)	1.00(20)
	785.4	319(66)	2.23(56)

Continued on next page

Table 4.10 – continued from previous page

Isotope	Energy (keV)	Normalized Area	Ratio
^{60}Co	1173.2	5(1)	1.00(25)
	1332.5	3(1)	0.51(16)
^{116m}In	416.9	10(2)	1.00(33)
	1097.3	10(2)	0.95(27)
	1293.6	7(2)	0.70(19)
^{212}Pb	238.6	237(32)	1.00(19)
	300.1	142(26)	0.60(13)
^{214}Pb	242	205(29)	1.00(20)
	295.2	112(16)	0.55(11)
	351.9	101(14)	0.50(10)

Most of the ratios turned out to be unity within uncertainties. In a few interesting cases, the discrepancies can be explained. For instance, in the case of the excess counts in the 2614 keV line in the ^{208}Tl group, we know that fast neutron inelastic recoils off ^{208}Pb will result in the same energy gamma, giving us excess counts in the peak.

A few discrepancies remain. There is an excess of counts in the 1765 keV line from ^{214}Bi, the 785 keV line from ^{212}Bi, and the 242 keV line from ^{214}Pb. This would seem to indicate that perhaps there are other decays that are contributing to those peak areas. There is an unexplained deficiency of the counts in the 463 keV line from ^{228}Ac.

The fact that most of the lines are internally consistent, and even the discrepancies are still within a factor of roughly two of the expected value, is indicative of the robustness of the foregoing calibrations and fitting.

4.5.5 Fast neutron rate

One feature of the background spectrum that will have increased relevance during the neutron activation of the CLOVER detector is the intrinsic backgrounds from fast neutrons. Škoro et al. [90] have developed a method for measuring a fast neutron flux using a high purity germanium detector. We utilized their method here.

The relevant equation is from page 334 of [90]:

$$\Phi = k\frac{I}{V} \tag{4.11}$$

where Φ is the flux in neutrons / s $\cdot$ cm^2 and V is the volume of the germanium detector in cm^3.

k is a constant ratio set by [90] to 900 ± 150 cm. Finally, I is the intensity of the broad 692 keV ^{72}Ge(n,n'γ) peak in Hz. The total volume of the detectors, (566.8 ± 0.4) cm^3, is obtained using the masses of the individual crystals (see Table 4.1).

The only unknown term is I, the spectral intensity of the 692 keV peak. To determine the area of the peak at 692 keV peak the following fit equation was used

$$\frac{dN}{dE} = c_0 \frac{\exp\left[-(\text{energy} - c_1)/c_2\right]}{1 + \exp\left[-(\text{energy} - c_1)/c_3\right]} \tag{4.12}$$

where the c_n terms are free parameters in the fit. The numerator is an exponential fit to the high-energy tail of the 692 keV peak, and the denominator is a smooth step function with the strength of the step set by c_3. In addition to Eq. (4.12), the fit included a quadratic background and two Gaussians centered on 680 keV and 727 keV (the offset, linear, and quadratic were all free parameters, as were the parameters associated with the two Gaussian peaks).

The fit ended up having a χ^2 / D.O.F. of 170.2 / 170 (P-value = 0.482) with the following fit values:

$$c_0 = 202.63 \pm 10.47$$
$$c_1 = 692.15 \pm 0.21$$
$$c_2 = 10.68 \pm 0.67$$
$$c_3 = 0.78 \pm 0.15$$

The fit is shown in Fig. 4.18.

The uncertainties in the fit values were numerically propagated through the area calculation using the appropriate entries from the covariance fit matrix. The range of integration was performed from $[c_1 - 2.5(\text{peak width at } c_1)]$ to $[c_1 + 5c_2]$. Integrating out five "attenuation lengths" gives an area 99.3% the area if the integration were performed out to infinity. We use this cutoff in the integration to make possible a consistent estimate of the background underneath the peak (i.e., we integrate the background counts in the same range). Another factor to take into account is the binning. Because there are 2 bins per keV, and the x-scale is in keV, we have to multiply the results of the integrations by 2.

The peak area is 4306 ± 221. This measured 692 keV peak area is different from the one shown in Table 4.9 because in the current case the spectrum did not exclude multi-crystal events. Fast neutrons may interact more than once in the detector, and cutting on a single-crystal event would have incorrectly attenuated the flux. Normalizing this peak count by the live time puts the value of

I at (35.4 ± 1.8) 10^{-3} Hz. Finally, with all three terms in place, the flux can be calculated:

$$\begin{aligned}\Phi &= (900 \pm 150 \text{ cm})\frac{(35.9 \pm 1.8)\ 10^{-3} \text{ Hz}}{(566.8 \pm 0.4) \text{ cm}^3} \\ &= (57.0 \pm 9.9)\ 10^{-3} \text{ neutrons / s} \cdot \text{cm}^2 \end{aligned} \tag{4.13}$$

The uncertainty in the flux ends up being 17.4%.

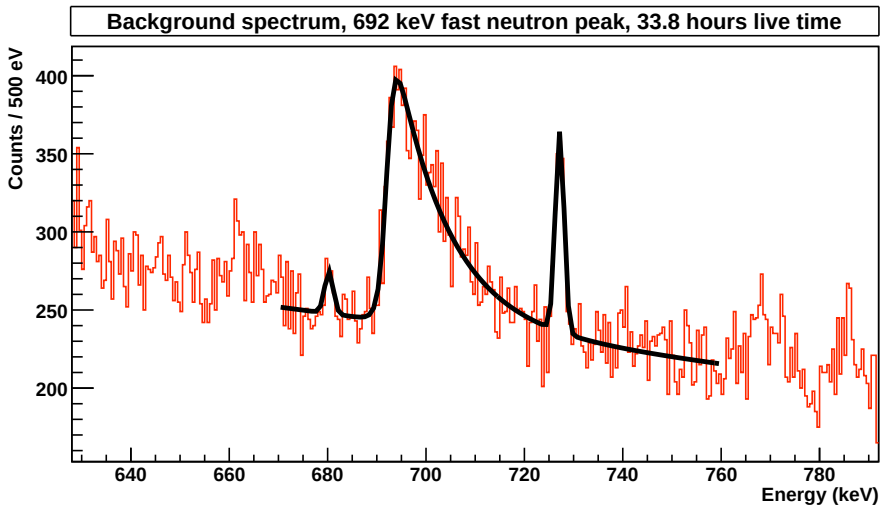

Figure 4.18: Background 692 keV neutron recoil peak. This is a zoom in on the 42 hours of background data (33.75 hours of live time) shown earlier. The χ^2 / D.O.F. = 170.2 / 170.

Chapter 5

CLOVER ACTIVATION

The natural germanium of the CLOVER was activated by moderating neutrons from an AmBe source. There were concerns, however, regarding the effects of fast neutrons on the detector. This section is concerned with finding a compromise between obtaining quality data and protecting the detector from damage.

5.1 Background and Activation Spectra

Previous studies [85][88] have determined that a fast neutron (~1-10 MeV) flux can degrade the resolution of a germanium diode detector over time, requiring an annealing procedure to restore the quality of the resolution. Based on these studies we needed to keep the total fast neutron fluence on the CLOVER detector to less than 10^8 n/cm^2. Our first activation was therefore a somewhat conservative attempt, with the primary goals being to measure both the fast and thermal neutron fluxes.

We used three bricks of polyethylene to moderate the neutrons, each 2" thick. We wanted to measure the activity of the AmBe source *in situ*, which required a 2" lead brick is to reduce the high-intensity lower-energy gamma activity coming from the source. This put the AmBe source approximately eight inches (~20 cm) away from the side of the CLOVER detector. Making a very conservative estimate of no neutron moderation, the fluence of fast neutrons at the CLOVER from our AmBe source is 12.9 neutrons / cm^2· s. With this geometry, the CLOVER can be exposed to the AmBe source for approximately three months before reaching the 10^8 n/cm^2 "danger fluence". If the germanium detector suffers from fast neutron damage, it would show up in the form of degraded energy resolution. It could be shipped back to the manufacturer to undergo an annealing procedure to restore most of the resolution, but we wanted to avoid the detector down time if possible.

5.1.1 Background spectrum with local polyethylene

We took data for 16.1 hours (live time of 15.3 hours) with the six inches polyethylene moderator in place but without the AmBe source to catalog any changes in the background spectrum. In addition to the lines enumerated in Table 4.9, we note the addition of a strong line that fits to 2223.2 keV. The identification of this line is a prompt gamma from neutron capture on hydrogen in the polyethylene. There are other lines associated with neutron capture on various isotopes that will be covered in

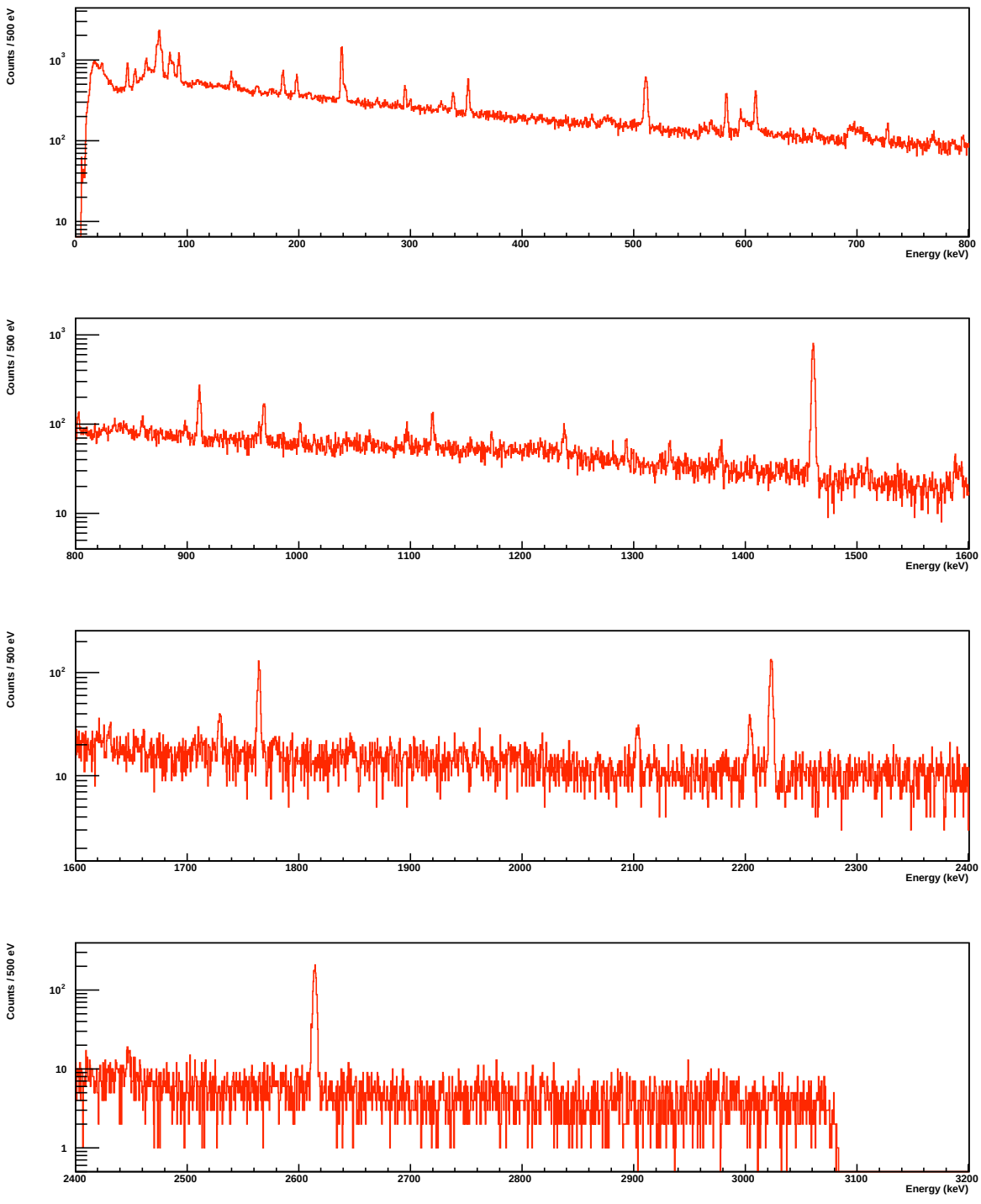

Figure 5.1: CLOVER background spectrum with polyethylene. There is a 2223 keV line not present in the basic background spectrum (see Fig. 4.17) associated with neutron capture on hydrogen.

more detail later in this section.

5.1.2 Activation spectrum

Keeping in mind our desire to be conservative in exposing the CLOVER to fast neutrons, and notwithstanding the conservative estimates made previously, we wanted to minimize the time-integrated fast neutron flux. Unfortunately, the DAQ system did not allow us to set the data collection time, but rather the total number of spills. We made a few quick test measurements to determine the data rate, and activated the Clover detector for 520.1 minutes. During this neutron exposure we left the AmBe source in place, and obtained eight data sets, each approximately one hour. The resulting live time over all eight data sets was 296.2 minutes. Table 5.1 is a catalog of the peaks with the AmBe source in place, and the corresponding spectrum is shown in Figures 5.2, 5.3, and 5.4.

To clearly see the peaks resulting only from activation, we subtracted the time-normalized background spectrum with the polyethylene moderator in place from the time-normalized activation spectrum. The result is shown in Fig. 5.5. It is clear that some of the background-associated lines at, for instance, 238 keV and 1460 keV, have been greatly attenuated.

Table 5.1: Activation peaks of the CLOVER detector. Peak energies were found using a peak fitter and then manually fit (see Section 4.5.3 for details). Entries grouped together all apply to a single fit energy peak. Unlike Table 4.9, there is no relative intensity column because the peaks derive mostly from inelastic neutron scatters and not nuclear decays.

Fit E (keV)	Peak Counts	Peak Uncer.	Back-ground	Sig. (σ)	Source	Pub E (keV)
23.8	7006.9	269.9	65598.1	27.03	^{71m}Ge	23.4
53.6	23146.5	215.6	22780.2	151.52	^{73}Ge(n, n'γ)	53.4
66.6	7650.8	212.9	30819.2	43.06	^{75m}Ge sum peak	66.1
70.3	3770.2	220.3	28162.2	22.20	Unknown	
73.0	10432.3	221.4	28364.9	61.20	Pb X-Ray	72.8
75.1	16793.7	231.2	26759.7	101.43	Pb X-Ray	75.0
85.0	8098.7	182.7	20257.8	56.22	Pb X-Rays	84.5 84.9
87.3	2288.0	154.8	19343.6	16.25	Pb X-Rays	87.2 87.4 87.9

Continued on next page

Table 5.1 – continued from previous page

Fit E (keV)	Peak Counts	Peak Uncer.	Back-ground	Sig. (σ)	Source	Pub E (keV)
92.8	797.0	133.9	17448.1	5.96	^{234}Th	92.4 92.8
96.2	1257.9	129.3	17151.3	9.49	^{115}In(n, γ)	96.0
110.1	4940.7	163.0	17055.4	37.38	^{19}F(n, X)	109.9
112.1	948.3	143.8	17034.8	7.18	Unknown	
139.8	23952.0	198.5	16901.6	182.03	^{75m}Ge	139.7
159.5	1112.1	118.7	15667.5	8.78	Unknown	
162.3	10673.8	157.7	15635.0	84.34	^{115}In(n, γ)	162.4
175.1	4376.7	140.7	16496.4	33.67	^{71m}Ge	175.0
186.4	2022.5	128.1	16484.8	15.56	^{115}In(n, γ)	186.2
198.3	22988.7	195.1	16569.9	176.45	^{71m}Ge	198.4
238.6	1612.0	116.7	14763.6	13.11	^{212}Pb	238.6
253.1	3610.1	124.4	14461.4	29.66	^{74}Ge(n, γ)	253.0
272.7	769.1	105.5	13771.4	6.48	^{115}In(n, γ)	273.0
297.8	2096.5	129.1	13479.9	17.84	^{73}Ge(n, n'γ)	297.3
326.1	3634.7	117.0	12718.3	31.84	^{73}Ge(n, n'γ)	325.7
416.9	3532.7	105.2	9426.0	35.95	^{116m}In	416.9
470-485	N/A	N/A	N/A	N/A	A big mess	N/A
492.8	570.7	91.5	8232.5	6.21	^{115}In(n, n'γ)	492.4
500.1	3627.7	109.9	8416.0	39.07	^{70}Ge(n, γ)	499.9
510.9	11168.2	84.5	11515.2	102.83	Ann. γ	511.0
516.7	592.6	40.4	10061.71	5.84	^{206}Pb(n, n'γ)	516.2
537.5	1607.9	85.3	7027.6	18.95	^{206}Pb(n, n'γ)	537.5
562.3	3054.7	189.5	109532.5	9.12	^{76}Ge(n, n'γ)	562.9
569.7	4073.5	123.5	6486.7	49.97	^{207}Pb(n, n'γ)	569.7
574.9	604.2	88.9	6451.4	7.43	^{74}Ge(n, γ)	574.8
583.1	2709.4	104.3	6304.5	33.71	^{208}Pb(n, n'γ)	583.2
596.0	13297.5	156.2	7398.1	152.74	^{74}Ge(n, n'γ)	595.8
597.5	14852.0	233.9	86698.9	49.84	^{74}Ge(n, n'γ)	595.8
608.5	1403.3	105.3	7081.0	16.48	^{70}Ge(n, n'γ) ^{73}Ge(n, γ)	608.3 608.4
657.7	351.3	71.9	6285.0	4.38	^{206}Ge(n, n'γ)	657.2

Continued on next page

Table 5.1 – continued from previous page

Fit E (keV)	Peak Counts	Peak Uncer.	Back-ground	Sig. (σ)	Source	Pub E (keV)
663.5	708.6	74.1	6185.6	8.90	^{206}Pb(n, n'γ)	663.8
691.9	12728.2	211.5	55735.9	53.27	^{72}Ge(n, n'e)	691.4
698.8	689.2	138.7	10872.5	6.53	Unknown	
701.3	889.0	129.0	10825.6	8.44	^{74}Ge(n, γ)	701.5
708.1	1377.7	92.4	5627.4	18.14	^{70}Ge(n, γ)	708.2
747.1	342.8	67.9	5209.0	4.69	^{70}Ge(n, γ)	747.3
763.5	301.3	65.3	5129.7	4.16	^{73}Ge(n, n'γ)	764.1
787.8	703.7	68.2	5050.9	9.78	^{70}Ge(n, γ)	788.7
802.9	8681.6	115.4	4891.6	122.64	^{206}Pb(n, n'γ)	803.1
807.9	357.9	64.6	4839.9	5.08	^{70}Ge(n, γ)	808.3
818.8	463.7	65.4	4726.0	6.66	^{116m}In	818.7
832.6	16012.7	645.7	53838.4	68.18	^{72}Ge(n, n'γ)	834.4
834.1	424.8	138.8	4336.9	6.37	^{72}Ge(n, n'γ)	834.4
843.6	1079.3	91.6	4167.5	16.52	^{27}Al(n, n'γ)	843.7
847.1	622.1	82.8	4105.4	9.59	^{76}Ge(n, n'γ)	847.2
860.7	647.3	73.3	4489.5	9.55	^{76}Ge(n, γ)	861.4
868.0	2019.0	81.7	4463.8	29.86	^{74}Ge(n, n'γ)	867.9
880.9	1579.5	73.5	4474.2	23.33	^{206}Pb(n, n'γ)	881.0
898.0	2179.3	76.8	4575.5	31.83	^{207}Pb(n, n'γ)	897.8
961.4	359.6	56.7	4057.2	5.58	^{74}Ge(n, n'γ)	961.1
982.0	358.7	58.3	3963.0	5.63	Unknown	
1014.4	1668.9	68.7	3807.6	26.72	^{27}Al(n, n')	1014.4
1039.5	7199.7	358.3	36778.4	37.09	^{70}Ge(n, n'γ)	1039.5
1063.6	1363.9	68.8	3459.4	22.91	^{207}Pb(n, n'γ)	1063.7
1097.0	4329.1	87.5	3726.1	70.07	^{116m}In	1097.3
1100.6	445.7	58.3	3707.7	7.23	^{74}Ge(n, n'γ)	1101.3
1139.3	578.5	58.0	3502.8	9.66	^{73}Ge(n, γ)	1138.8
1165.0	612.4	57.4	3326.8	10.49	^{72}Ge(n, γ)	
1196.3	10318.4	702.8	60739.7	41.36	Unknown	
1201.1	1947.1	81.3	3181.64	34.10	n(p, d)γ DEP	1201.2
1204.1	756.6	70.5	3173.1	13.27	^{74}Ge(n, n'γ)	1204.2
1293.5	4374.2	84.4	3181.2	76.62	^{116m}In	1293.6

Continued on next page

Table 5.1 – continued from previous page

Fit E (keV)	Peak Counts	Peak Uncer.	Back-ground	Sig. (σ)	Source	Pub E (keV)
1298.5	766.8	56.9	3162.8	13.47	^{70}Ge(n, γ)	1298.7
1378.3	396.8	81.5	2968.1	7.20	^{70}Ge(n, γ)	1379.0
1380.3	366.3	81.6	2963.2	6.65	Unknown	
1413.0	265.7	50.3	2947.7	4.83	Unknown	
1433.0	228.3	50.7	2953.9	4.15	^{206}Pb(n, n'γ)	1433.5
1436.4	277.1	51.3	2955.0	5.04	Unknown	
1460.8	792.9	60.3	3003.6	14.29	^{40}K	1460.8
1463.8	715.9	63.0	3015.4	12.88	^{72}Ge(n, n'γ)	1464.0
1466.6	330.7	57.6	3026.5	5.94	Unknown	
1507.8	587.9	54.8	3008.7	10.59	^{116m}In	1507.7
1592.3	701.9	54.9	2872.3	12.94	^{208}Pb(n, n'γ) DEP	1592.6
1704.4	333.5	52.6	3046.1	5.97	Unknown	
1712.0	3591.3	80.5	3100.8	63.72	n(p, d)γ SEP	1712.2
1726.1	223.4	51.6	3051.4	4.00	^{207}Pb(n,n'γ)	1725.7
1769.9	342.7	51.8	3003.6	6.18	^{207}Pb(n,n'γ)	1770.2
1778.7	1336.7	61.8	3008.2	24.08	^{28}Al	1779.0
1844.5	468.7	53.5	3042.0	8.40	^{206}Pb(n, n'γ)	1844.5
1950.9	264.9	53.4	3647.6	4.33	Unknown	
2092.3	346.4	45.5	2193.8	7.31	^{207}Pb(n, n'γ)	2092.7
2103.3	813.3	50.0	2077.1	17.63	^{208}Pb(n, n'γ) SEP	2103.5
2111.9	531.9	45.8	1984.6	11.80	^{116m}In	2112.3
2223.1	62987.2	254.2	1617.4	1547.38	n(p, d)γ	2223.2
2390.7	256.5	35.8	1300.5	7.03	^{116m}In	2112.3
2614.3	8164.0	95.7	1005.9	254.33	^{208}Pb(n, n'γ)	2614.5
2649.8	157.6	30.7	966.4	5.01	Unknown	

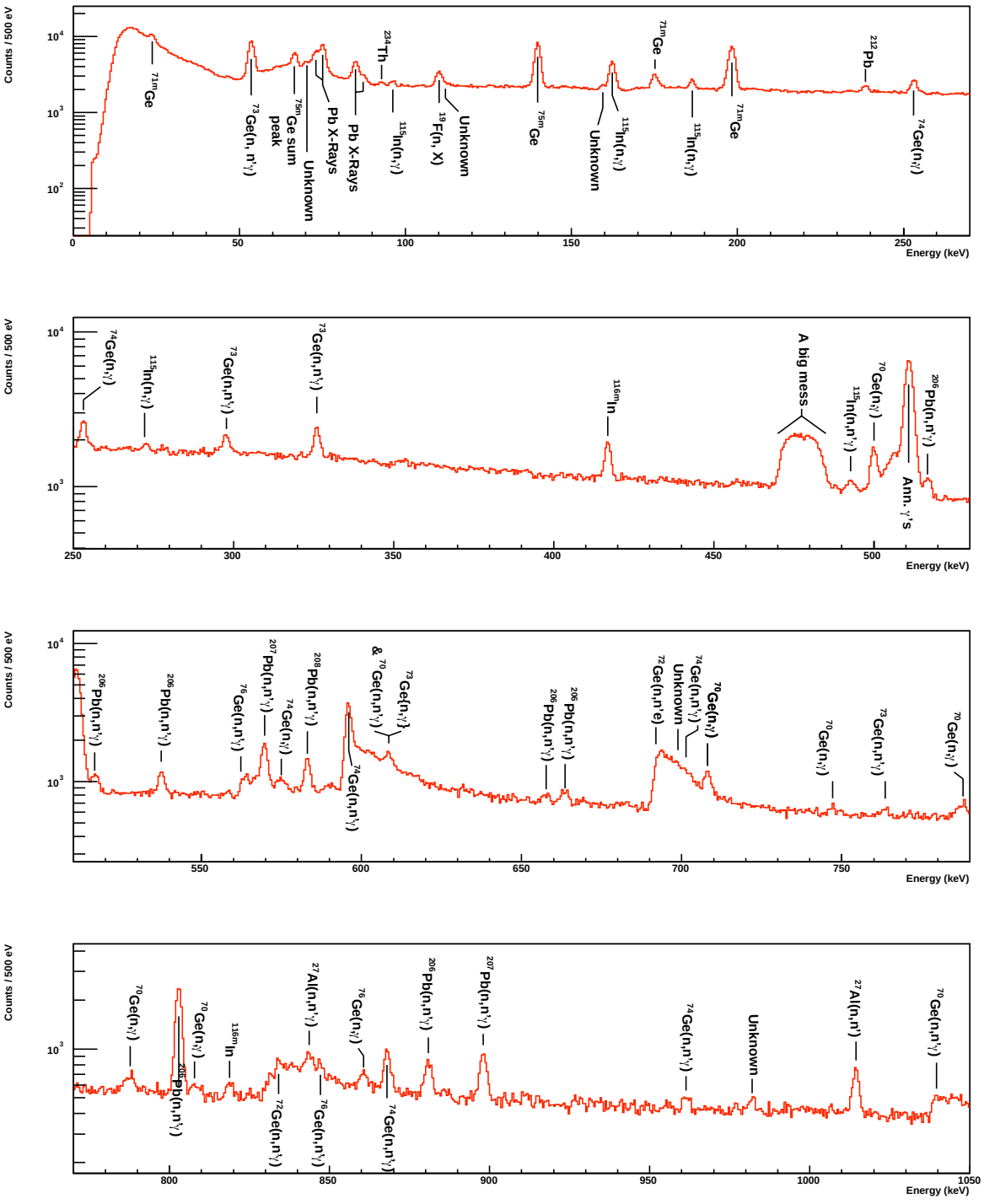

Figure 5.2: CLOVER activation spectrum (0-1000 keV). This spectrum is based on 520.1 minutes of activation data (live time of 296.2 minutes) with the CLOVER in a 4" lead shield and moderating the neutrons through 6" of polyethylene.

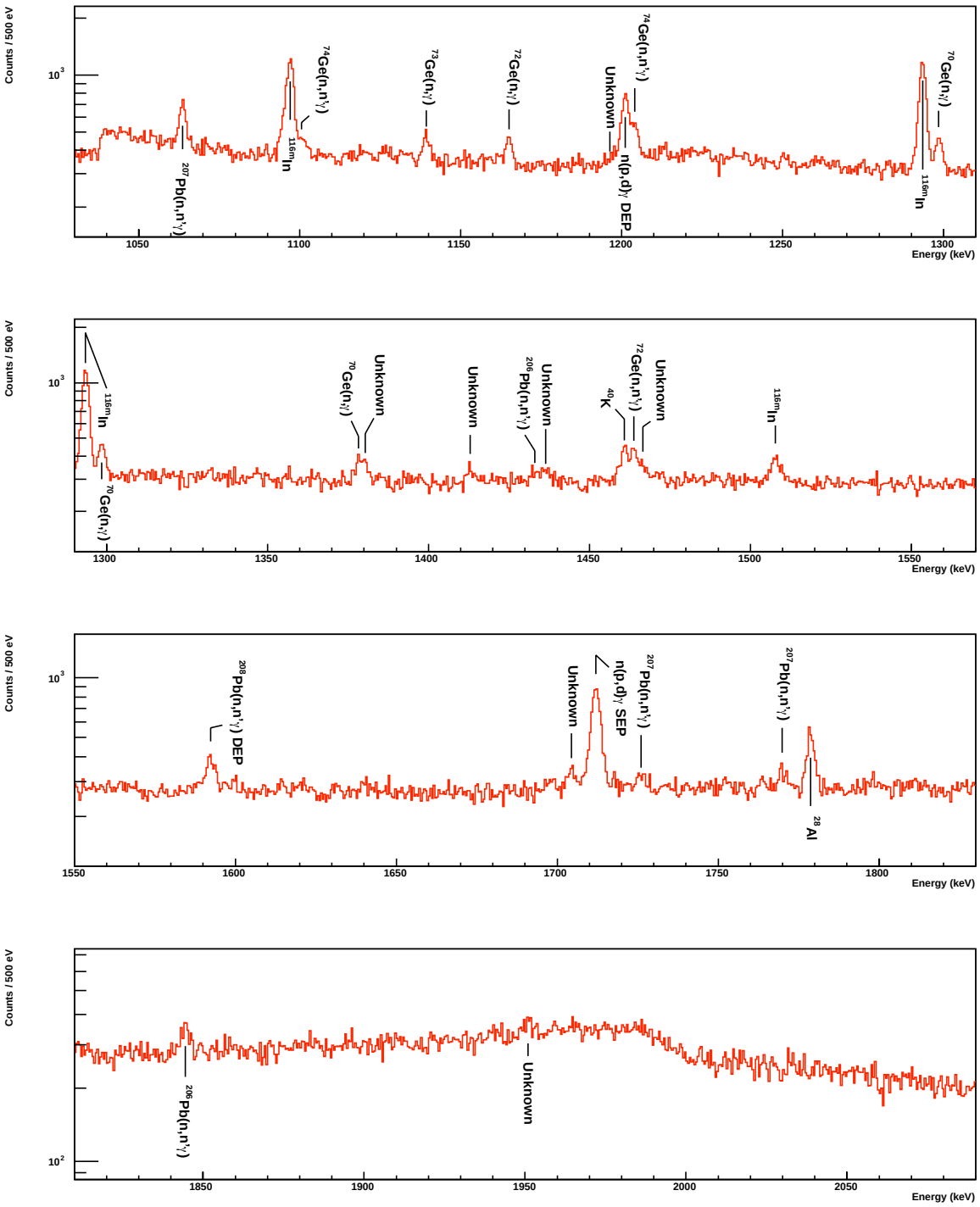

Figure 5.3: CLOVER activation spectrum (1000-2000 keV). This spectrum is based on 520.1 minutes of activation data (live time of 296.2 minutes) with the CLOVER in a 4" lead shield and moderating the neutrons through 6" of polyethylene.

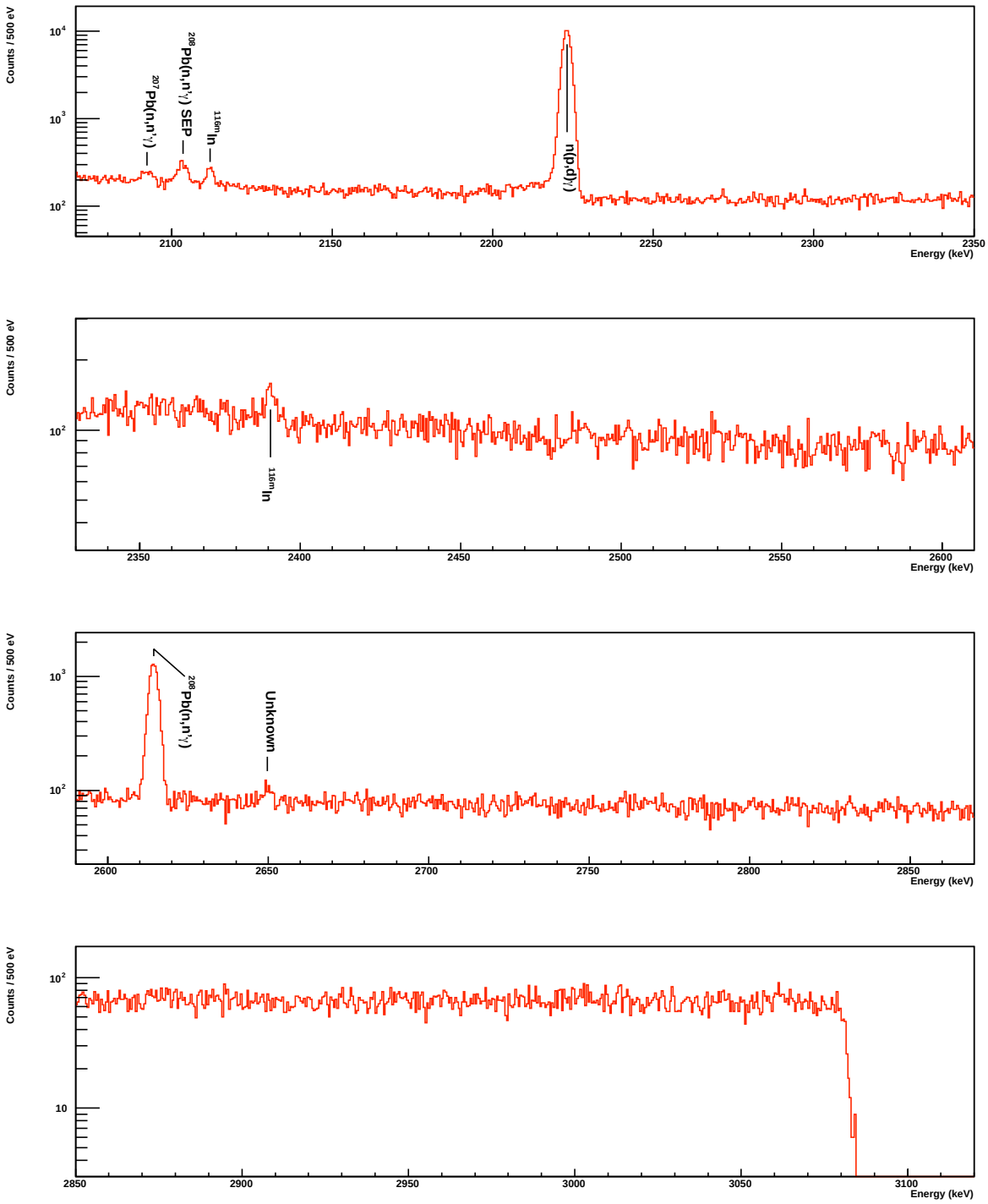

Figure 5.4: CLOVER activation spectrum (2000-3000 keV). This spectrum is based on 520.1 minutes of activation data (live time of 296.2 minutes) with the CLOVER in a 4" lead shield and moderating the neutrons through 6" of polyethylene.

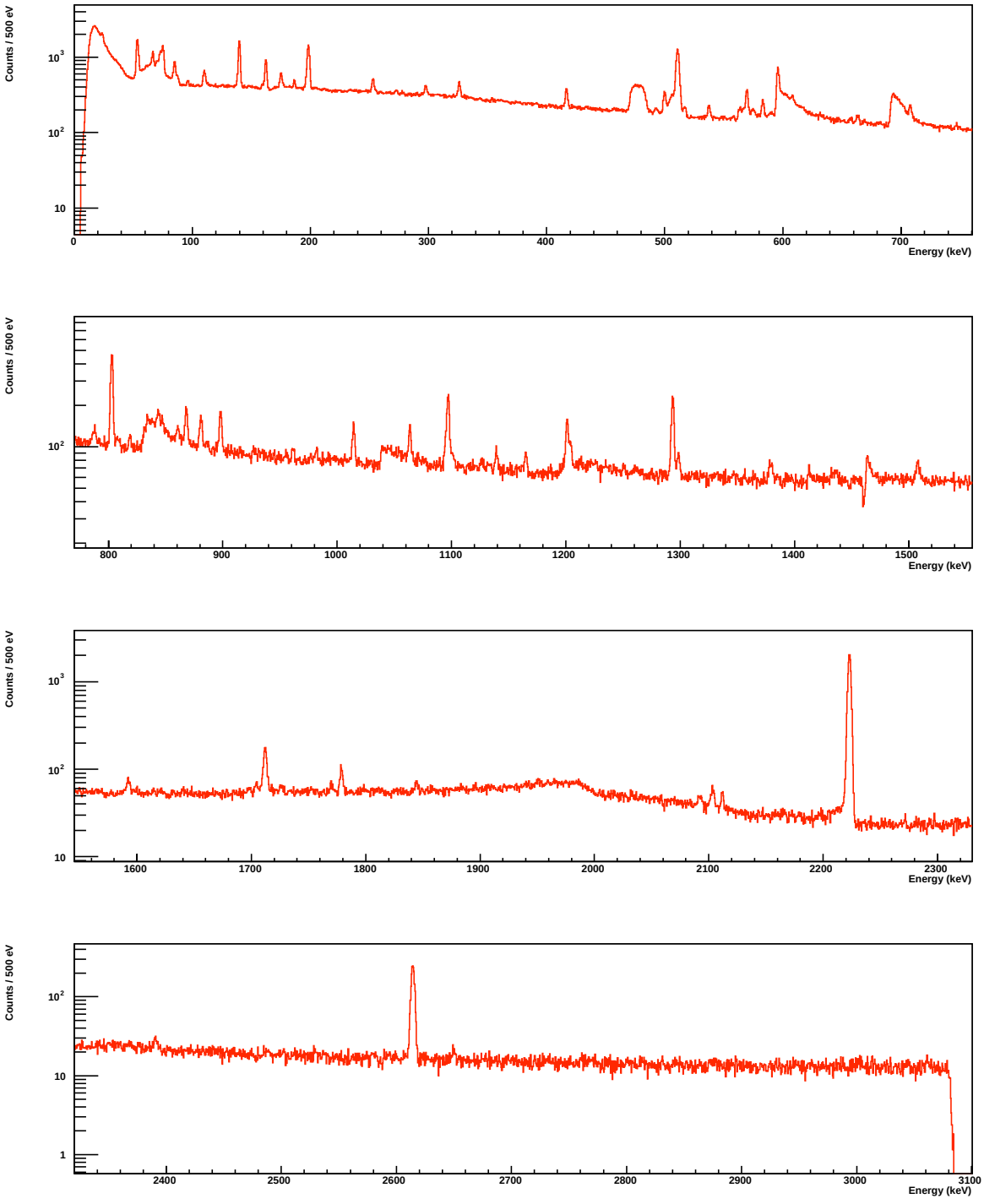

Figure 5.5: CLOVER background-subtracted activation spectrum. Lines not associated with the AmBe source are greatly reduced.

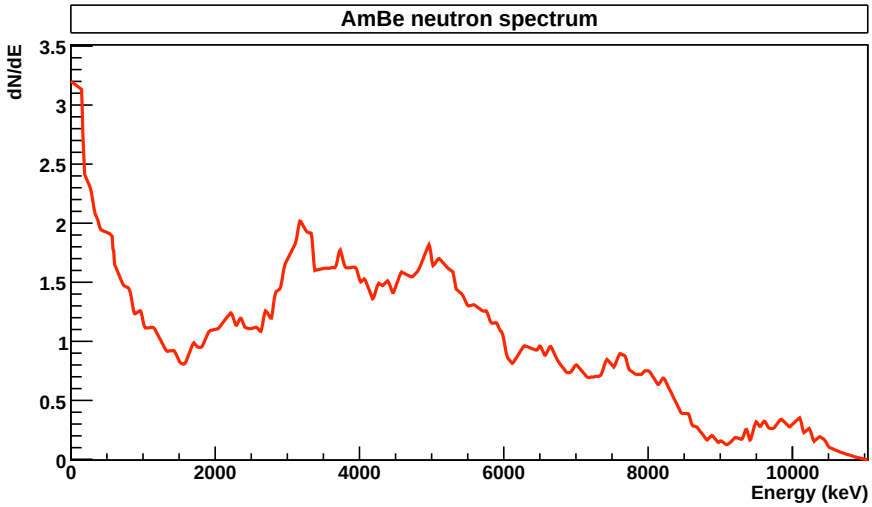

Figure 5.6: AmBe neutron spectrum. The data is digitzed from a graph in March *et al.* [86]. The spectrum is normalized, so it can be used directly as a probability distribution function.

5.1.3 The AmBe Source and effects of shielding

The neutron flux measurement in the previous section only incorporated the AmBe neutrons that are above reaction threshold, i.e., above 692 keV. The total neutron flux coming from the AmBe source can be measured once we know the shape of the AmBe neutron spectrum.

The source is 30 mCi in the americium, and the full-spectrum neutron rate is (6.487 ± 0.045) 10^4 Hz[1]. The rate is normalized to 12:00 GMT on 22 May 1987, and allowing for the 433-year halflife of ^{241}Am, the activity of the source at the time of the experiment was (6.230 ± 0.043) 10^4 Hz.

Marsh, Thomas, and Burke performed a high-resolution measurement of the neutron spectrum from an AmBe source [86]. The data from the high-resolution AmBe spectrum was digitized and is shown in Fig. 5.6. Only neutrons with energy greater than 692 keV contributed to the inelastic scattering peak shown in Fig. 5.7, which from the Marsh *et al.* data is (88.74 ± 0.89)% of the AmBe neutron spectrum, where the uncertainty is an estimate based on the resolution of the digitization. If there were no lead or moderator between the source and the detector, assuming the source is 20 cm away from the CLOVER, there would be a flux of (11.00 ± 0.08) neutrons / s · cm^2 above 692 keV.

[1]The source manufacturer is Amersham, and the neutron rate was measured at the Nuclear Physics Laboratory at Teddington. The uncertainty of 0.7% has a CL of 95%.

Thus the two inches of lead shielding and six inches of moderator reduced the neutron flux to (21.0 ± 3.5)% of the unmoderated neutron flux.

Given the reduction in the fast neutron flux, the CLOVER can be exposed to the source in this shield and moderator geometry for about 16 months before entering the damage region. The exposure, including testing and preliminary measurements, has been roughly 12 hours.

5.2 Fast AmBe Neutron Flux

We fit Eq. (4.12) plus five Gaussians centered near 699, 701, 708, 739, and 747 keV to the same region as used in section 4.5.5. The 739 keV peak was not listed in Table 5.1 because it has a significance of only 3.8σ, although it had to be included in the current fit to allow for a reasonable goodness-of-fit parameter. The fit had the following results (see Fig. 5.7):

$$c_0 = 1398.67 \pm 25.40$$
$$c_1 = 691.775 \pm 0.047$$
$$c_2 = 9.712 \pm 0.254$$
$$c_3 = 0.523 \pm 0.032$$

Normalizing the resulting integral by the bin width and using the same error analysis procedure as in Section 4.5.5 gives a peak area of 26007 ± 453. The uncertainty was calculated in the same manner as described in Section 4.5.5. With a livetime of 296.2 minutes, the 692 keV peak intensity was (1.463 ± 0.025) Hz. Plugging these values into Eq. (4.11) gives a final flux of

$$\begin{aligned}\Phi &= (900 \pm 150 \text{ cm})\frac{(1.463 \pm 0.025) \text{ Hz}}{(566.8 \pm 0.4) \text{ cm}^3} \\ &= (2.323 \pm 0.389) \text{ neutrons / s} \cdot \text{cm}^2\end{aligned}$$

To calculate the activity relative to background, we simply used the ratio of 692 keV peak intensities, thereby eliminating the largest source of error (the k term in Eq. (4.11)). The fast neutron flux during activation was (25.7 ± 1.4) times the room background fast neutron flux (see Section 4.5.5). Finally, we subtracted the background rate from the activation rate to measure the AmBe-related flux:

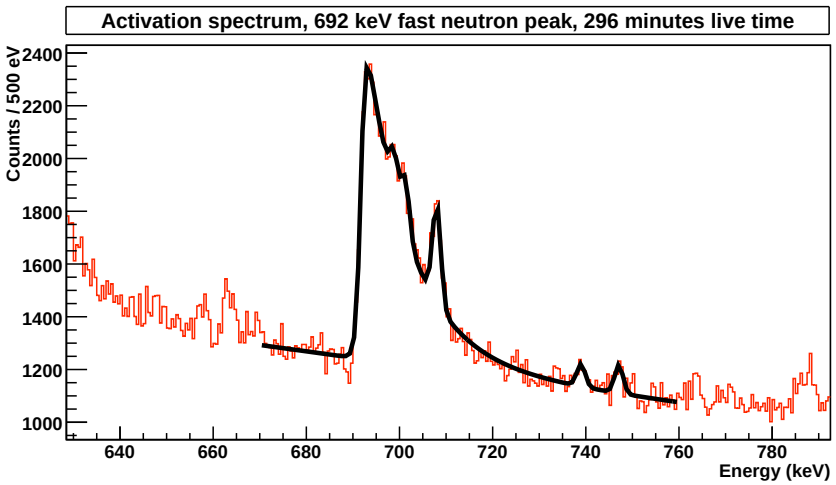

Figure 5.7: 692 keV fast neutron peak during activation. There are five Gaussians in the fit region at 699, 701, 708, 739, and 747 keV. The continuum and Gaussian background parameters were free parameters in the fit. Because of the limit in the number of allowed free parameters, three of the Gaussian curves were fit individually and their characteristics made an explicit part of the fit formula. The resulting fit has a χ^2 / D.O.F. of 180.7 / 170, P-value = 0.272.

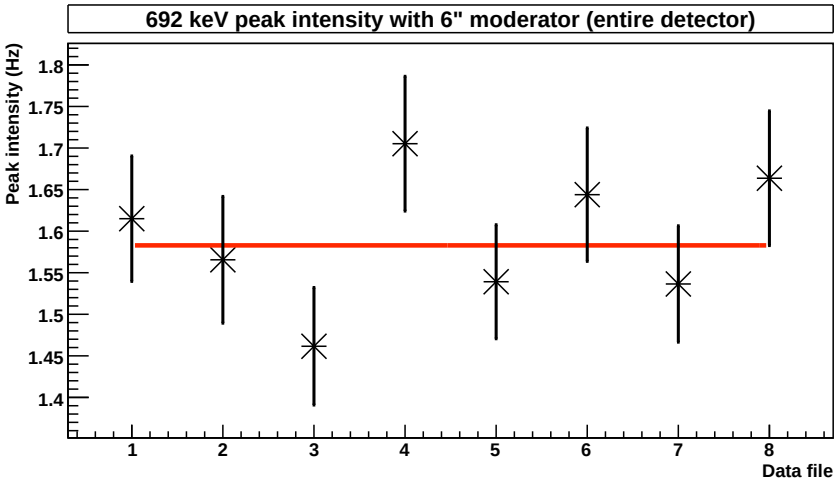

Figure 5.8: 692 keV peak intensity reproducibility. The AmBe source was not disturbed during the activation run, so we expect the peak intensity to be constant across all eight data files. The χ^2 / D.O.F. = 7.88 / 7 (P-value = 0.34).

$$\Phi_{AmBe} = (900 \pm 150 \text{ cm}) \frac{(1.406 \pm 0.025) \text{ Hz}}{(566.8 \pm 0.4) \text{ cm}^3}$$
$$\Phi_{AmBe} = (2.233 \pm 0.374) \text{ neutrons / s} \cdot \text{cm}^2 \quad (5.1)$$

We now measure the reproducibility of the 692 keV peak intensity using the eight individual data files in the 6" activation data set. Because the AmBe source was not moved during this activation, we would expect the 692 keV peak intensity to remain constant. Fig. 5.8 shows the 692 keV peak intensity for the eight files, with a constant fit. Given a χ^2 / NDF of 7.88 / 7, we conclude that it is very reasonable to fit a constant value to the 692 keV peak intensity for these eight data files.

5.3 Thermal Neutron Flux

The thermal neutron flux can be measured by looking for the decay of the ^{75m}Ge isomer, using a method described by Škoro *et al.* [90]. A thermal neutron captures on ^{74}Ge to this isomeric state with a cross section of σ_{th} (^{75m}Ge) = 170 ± 30 mb [87]. ^{75m}Ge decays with a 99.970% branching ratio to ^{75}Ge, a transition with a Q value of 139.7 kev. This decay proceeds via both internal conversion and gamma emission, at a ratio of $\alpha_{ICC} = 1.62 \pm 0.05$ [91]. ^{75m}Ge has a half life of 47.7 seconds, and thus the total event rate is quickly obtained. The difference in the final number of decays over 520 minutes assuming a constant decay rate versus an asymptotically increasing decay rate differs by just 0.2%. This difference will be disregarded.

5.3.1 Extracting the flux

The equation from Škoro *et al.* that relates the intensity of the 139.7 keV peak to the thermal neutron flux is

$$\Phi_{th} = \frac{I_{139.7}}{N(^{74}Ge)\frac{\epsilon^{\gamma}_{139.7}+\alpha_{ICC}}{1+\alpha_{ICC}}\sigma_{th}(^{75m}Ge)} \quad (5.2)$$

where Φ_{th} is the total thermal neutron flux, $I_{139.7}$ is the intensity of the 139.7 keV peak, N(^{74m}Ge) is the number of ^{74}Ge atoms, $\epsilon^{\gamma}_{139.7}$ is the detector's photopeak efficiency for a 139.7 keV gamma. Note that the observation efficiency of the internal conversion electrons is assumed to be 100%. In reality, some of the internal conversion electrons will either escape the crystal or deposit energy inside a dead layer. This effect is assumed to be small compared to the uncertainty in the neutron capture cross section, and will be neglected.

The number of ^{74}Ge atoms within a mass of natural germanium can be expressed as a function of the volume of the germanium:

$$N\left(^{74}Ge\right) = V[\mathrm{cm}^3]\ \left(1.601 \times 10^{22}\right) \tag{5.3}$$

where V is the volume of the natural germanium in cm^3. Škoro *et al.* also express $\epsilon^{\gamma}_{139.7}$ as a function of the volume of the germanium:

$$\epsilon^{\gamma}_{139.7} \simeq 1 - \frac{1 - \exp(-V^{1/3})}{V^{1/3}} \tag{5.4}$$

where as before, V is the volume of the detector expressed in cm^3. Plugging Eqs. (5.3) and (5.4) into Eq. (5.2) gives

$$\Phi_{th} = 980 \frac{I_{139.7}}{V\left(2.6 - \frac{1-\exp(-V^{1/3})}{V^{1/3}}\right)} \tag{5.5}$$

where, once again, the volume V is expressed as cm^3. Škoro *et al.* estimate the final uncertainty in the thermal neutron flux measurement to be 30%.

The ultimate goal of the current study, however, is not necessarily to determine the thermal neutron flux, but to determine the number of ^{77}Ge decays in the final data set. To this end, we only need to calculate the ratio of neutron captures on ^{74}Ge to ^{76}Ge. The uncertainty in this ratio will be less than the 30% uncertainty estimated by Škoro *et al*. For now, though, we complete the study of the neutron flux, and will in Section 6.1.4 make the switch to using just the capture ratio with its lower relative uncertainty.

5.3.2 The thermal neutron flux through the CLOVER crystals

The volume of each crystal can be obtained from its mass (see Table 4.1), and is about 141.6 cm^3 each, giving a photopeak efficiency for a 139.7 keV gamma of 80.9%, which the authors of [90] claim is accurate to 10%. The efficiency is added to α_{ICC} to obtain a factor of 2.41.

To test the efficiency approximation, we used the MaGe[2] Monte Carlo simulation framework to simulate one million 140-keV gamma rays spread homogeneously throughout crystal 1. 75% of the gammas deposited full energy within the crystal, which is within the 10% uncertainty predicted by Škoro *et al.*. Adding this value to α_{ICC} gives a factor of 2.35, and thus the efficiency approximation suppresses the Φ_{th} by 2.5% relative to the calculated flux.

Because part of the goal of the present work is to experimentally evaluate the accuracy of the simulation, the $\epsilon^{\gamma}_{139.7}$ approximation, with an assumed uncertainty of 10%, will be used to measure the thermal neutron flux.

---

[2]MaGe is covered in detail in Chapter 7

Since ^{75m}Ge has a half life of 48 s, the ^{75m}Ge decays should not be individually correlated with any other events depositing energy in the CLOVER. The area of this peak should therefore be independent of whether the single-crystal or multi-crystal histograms are used. Indeed, this is what we observed, with the peak area sum of all four crystals being 23900 ± 200 for the single-crystal events, and 24000 ± 240 for the multi-crystal events. Because of the better resolution, we therefore decide to measure the 140 keV peak using the single-crystal events.

The thermal neutron flux through the individual CLOVER crystals was also measured. In the case of the individual crystals, the mass is taken to be 754 grams, giving a volume of 141.6 cm^3.

There is a complication, though, in analyzing the neutron flux through individual crystals–140 keV gammas may exit one crystal and enter another, adding to the counts in the ^{75m}Ge peak. This serves to double-count some of the neutrons flowing through the crystals. We therefore want to answer the question, of all the counts in the 140 keV peak in any given crystal, how many originated within the crystal itself?

To answer this question, we re-used the data from the Monte Carlo simulation mentioned above. Of those one million simulated primary gamma events, 750,000 contributed to the 140 keV peak in crystal 1, 21,000 in crystals 2 and 4, and 5500 in crystal 3. The remaining gamma rays either escaped the detector entirely or only added to the continuum below 140 keV.

With these efficiencies in hand, we can write down a matrix equation for how many counts we would expect to observe in any given crystal, given how many decays actually occurred in each crystal:

$$\begin{pmatrix} ob_1 \\ ob_2 \\ ob_3 \\ ob_4 \end{pmatrix} = \frac{\alpha_{ICC}}{1+\alpha_{ICC}} \begin{pmatrix} a_1 \\ a_2 \\ a_3 \\ a_4 \end{pmatrix} + \frac{1}{1+\alpha_{ICC}} \begin{pmatrix} \epsilon_1 & \epsilon_4 & \epsilon_3 & \epsilon_2 \\ \epsilon_2 & \epsilon_1 & \epsilon_4 & \epsilon_3 \\ \epsilon_3 & \epsilon_2 & \epsilon_1 & \epsilon_4 \\ \epsilon_4 & \epsilon_3 & \epsilon_2 & \epsilon_1 \end{pmatrix} \begin{pmatrix} a_1 \\ a_2 \\ a_3 \\ a_4 \end{pmatrix} \tag{5.6}$$

where a_n is the actual number of ^{75m}Ge decays in crystal n, ob_n is the observed number of 140 keV energy depositions in crystal n, and the efficiency values ϵ_n are defined according the simulation results:

$$\epsilon_1 = 7.5 \times 10^{-1}$$
$$\epsilon_2 = 2.1 \times 10^{-2}$$
$$\epsilon_3 = 5.5 \times 10^{-3}$$
$$\epsilon_4 = 2.1 \times 10^{-2}$$

To understand Eq. (5.6), we have a proportion of ^{75m}Ge decays proceeding via internal conversion, and the observation efficiency of these decays is assumed to be 100%. These internal conversions are represented in the first term on the right of Eq. (5.6). We then have a proportion of ^{75m}Ge

decays proceeding via gamma emission, represented by the second term. The cyclic permutation of the ϵ_n values is due to the four-fold symmetry of the CLOVER construction.

After collecting like terms on the right, the matrix in Eq. (5.6) is inverted to obtain the actual number of ^{75m}Ge decays based on the observed peak areas of the four crystals:

$$\begin{pmatrix} a_1 \\ a_2 \\ a_3 \\ a_4 \end{pmatrix} = \begin{pmatrix} \delta_1 & \delta_4 & \delta_3 & \delta_2 \\ \delta_2 & \delta_1 & \delta_4 & \delta_3 \\ \delta_3 & \delta_2 & \delta_1 & \delta_4 \\ \delta_4 & \delta_3 & \delta_2 & \delta_1 \end{pmatrix} \begin{pmatrix} ob_1 \\ ob_2 \\ ob_3 \\ ob_4 \end{pmatrix} \tag{5.7}$$

where now the δ_n values are given by

$$\begin{aligned} \delta_1 &= 1.1 \\ \delta_2 &= -9.8 \times 10^{-3} \\ \delta_3 &= -2.4 \times 10^{-3} \\ \delta_4 &= -9.8 \times 10^{-3} \end{aligned}$$

We then answer the question, given a known number of ^{75m}Ge decays in any given crystal, how many 140 keV energy depositions remain within that crystal. The answer is the matrix equation

$$\begin{pmatrix} c_1 \\ c_2 \\ c_3 \\ c_4 \end{pmatrix} = \left(\frac{\alpha_{ICC}}{1+\alpha_{ICC}} + \frac{1}{1+\alpha_{ICC}} \right) \begin{pmatrix} a_1 \\ a_2 \\ a_3 \\ a_4 \end{pmatrix} \tag{5.8}$$

Finally, we substitute Eq. (5.7) into Eq. (5.8) to obtain

$$\begin{pmatrix} c_1 \\ c_2 \\ c_3 \\ c_4 \end{pmatrix} = \begin{pmatrix} \phi_1 & \phi_4 & \phi_3 & \phi_2 \\ \phi_2 & \phi_1 & \phi_4 & \phi_3 \\ \phi_3 & \phi_2 & \phi_1 & \phi_4 \\ \phi_4 & \phi_3 & \phi_2 & \phi_1 \end{pmatrix} \begin{pmatrix} ob_1 \\ ob_2 \\ ob_3 \\ ob_4 \end{pmatrix} \tag{5.9}$$

where the ϕ_n values are given by

$$\begin{aligned} \phi_1 &= 1.0 \\ \phi_2 &= -8.9 \times 10^{-3} \\ \phi_3 &= -2.2 \times 10^{-3} \\ \phi_4 &= -8.9 \times 10^{-3} \end{aligned}$$

What Eq. (5.9) tells us is that given an equal number of counts in the 140 keV peak in all four crystals, the thermal neutron flux through any one crystal would have been erroneously augmented by just a few percent, which may be negligible given the 30% uncertainty in determining the thermal neutron flux. We have two comments on this consideration. One, since the AmBe source is placed closest to crystals 3 and 4, we do not expect the 140 keV peaks in each crystal to be the same size, making this matrix correction more substantial for crystals 1 and 2 than 3 and 4. Two, while the current uncertainty may be 30%, this procedure can be applied to any array of germanium crystals for processes with a much smaller uncertainty, perhaps making this count separation procedure more relevant.

Using the foregoing method, we measured the thermal neutron flux through the individual CLOVER crystals. Table 5.2 shows the results.

Table 5.2: Thermal neutron fluxes through individual crystals with 6" of moderator. The live time was 296.2 minutes. The peak areas were normalized by the run time and the resulting intensities entered into Eq. (5.9) and then Eq. (5.5) to obtain the last column. The statistical uncertainties are far smaller than the estimated 30% uncertainty in the method, thus the uncertainties in the reported fluxes are simply taken to be 30%.

Crystal	Peak area	Flux ($n / cm^2 \cdot s$)
1	4446 ± 83	0.94 ± 0.28
2	5263 ± 89	1.12 ± 0.34
3	8074 ± 122	1.73 ± 0.52
4	6189 ± 104	1.32 ± 0.40

As we might expect, the thermal neutron flux through the crystals nearest to the AmBe source, crystals 3 and 4, is higher than the flux through the far crystals 1 and 2. There is a second smaller effect, though, deriving from the fact that the AmBe source is closer to the physical height of crystals 2 and 3 and 1 and 4, leading to a further flux difference between the four crystals (skip ahead to Fig. 6.1 to see a photo of the activation setup with 4" of polyethylene moderator instead of 6"). The average thermal neutron flux was determined to be (1.28 ± 0.20) $n / cm^2 \cdot s$.

Crystal separation material

There is material in the CLOVER detector used to physically separate the crystals from each other. The identity and geometry of this separator is a proprietary engineering detail, though we may use the thermal neutron flux measurements to determine the nature of the material.

With 6" of neutron moderator, the AmBe source sits approximately 20 cm from crystal 3 and 25 cm from crystal 2. Thus we can expect the thermal neutron flux through crystal 2 to be $(20/25)^2$ =

64% that of the thermal neutron flux through crystal 3 given the increased distance from the source. The close crystals, though, are themselves absorbing 28% of the neutrons that stream through them (see Appendix B). We would therefore expect the flux through crystal 2 to be 46% of the flux through crystal 1. Table 5.2 shows that the ratio is 0.65 ± 0.28. While this flux ratio is in agreement with prediction, the size of the uncertainty makes a more sensitive test impossible at this point.

Because of the large error bars, and the fact that the flux through crystal 2 is actually larger than expected, it is difficult to say anything definite about the nature of the crystal separator. The strongest statement that can be made is that the separator is most likely not made of a material with a very high thermal neutron capture cross section.

Systematic analysis of peak intensity

We create a plot of the 140 keV peak intensity for each of the eight datasets making up this data run. This graph is comparable to Fig. 5.8, except relevant to the thermal neutron flux rather than the fast neutron flux. We compare the intensities of the 140 keV peaks for each of the eight individual data files comprising this activation data set. Because the AmBe source was left in place during the entire activation, we would expect the peak intensities to be constant. We add the peak intensities for all four crystals for each data set. This analysis sets an expectation for later comparisons when the AmBe source was replaced between each activation. Fig. 5.9 shows the results. As with Fig. 5.8, a linear fit to the peak intensities is reasonable.

5.4 Cooldown Analysis

Before analyzing specific peaks and signals in the CLOVER data, the cooldown spectrum must have its peaks identified and categorized. The known bulk materials present were germanium, aluminum, lead, and polyethylene. Neutron activation indicated significant amounts of indium and manganese, and these materials might have an impact on the thermal neutron flux measurement.

5.4.1 Background and Activation Spectra

After the 520 minutes of neutron activation, cooldown data were taken for 58.1 hours (52.25 hours of live time). Table 5.3 is a catalog of the peaks, and the resulting spectrum is shown in Figures 5.10, 5.11, and 5.12. The peaks that are not identified in Figs. 4.15, 4.16, and 4.17 are identified in Table 5.3.

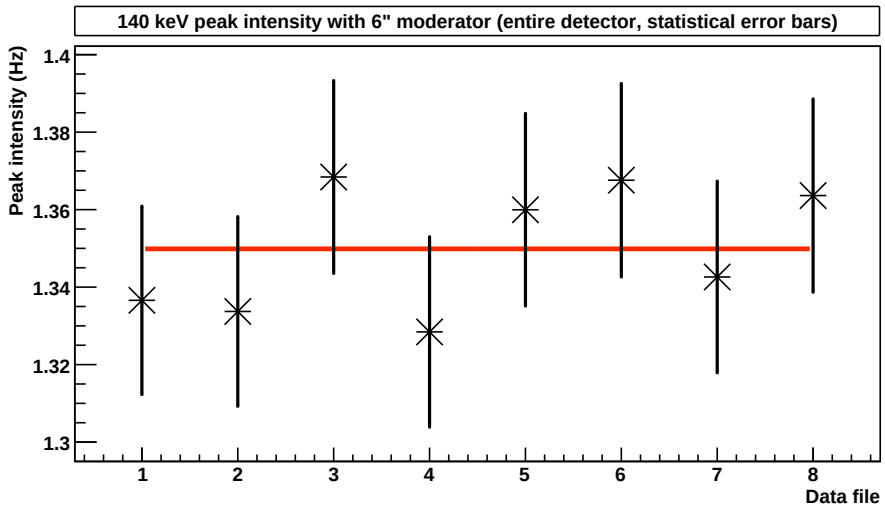

Figure 5.9: 139.7 keV peak intensity systematics. The error bars in this graph are statistical, and fitting a constant value to them results in a χ^2 / NDF of 3.13 / 7 (P-value = 0.87).

Table 5.3: New cooldown peaks of the CLOVER detector. Most peaks are found in the background spectrum as well (Figs. 4.15, 4.16, and 4.17).

Fit E (keV)	Peak Counts	Peak Uncer.	Back-ground	Sig. (σ)	Source	Pub E (keV)
253.0	371.1	76.4	6973.4	4.39	Unknown	
325.7	431.2	76.6	5627.8	5.68	Unknown	
807.5	226.7	46.7	2122.5	4.86	Unknown	
818.8	219.9	45.3	2157.9	4.68	^{116m}In	818.7
846.7	286.4	70.2	2152.1	6.10	^{56}Mn	846.8
1155.2	133.7	35.1	1358.0	3.58	Unknown	
1630.5	167.2	25.9	618.8	6.64	Unknown	
1712.0	188.0	25.3	577.4	7.73	Unknown	
2112.4	245.1	24.2	420.6	11.81	^{116m}In	2112.3
2118.6	107.9	21.0	416.7	5.22	Unknown	
2390.6	94.5	19.0	337.6	5.08	Unknown	

5.4.2 Indium and Manganese in the CLOVER

In addition to the known bulk materials near the CLOVER crystals, there is indium and manganese as well. The amounts of these materials will affect later analyses, so we categorized their levels.

The presence of indium

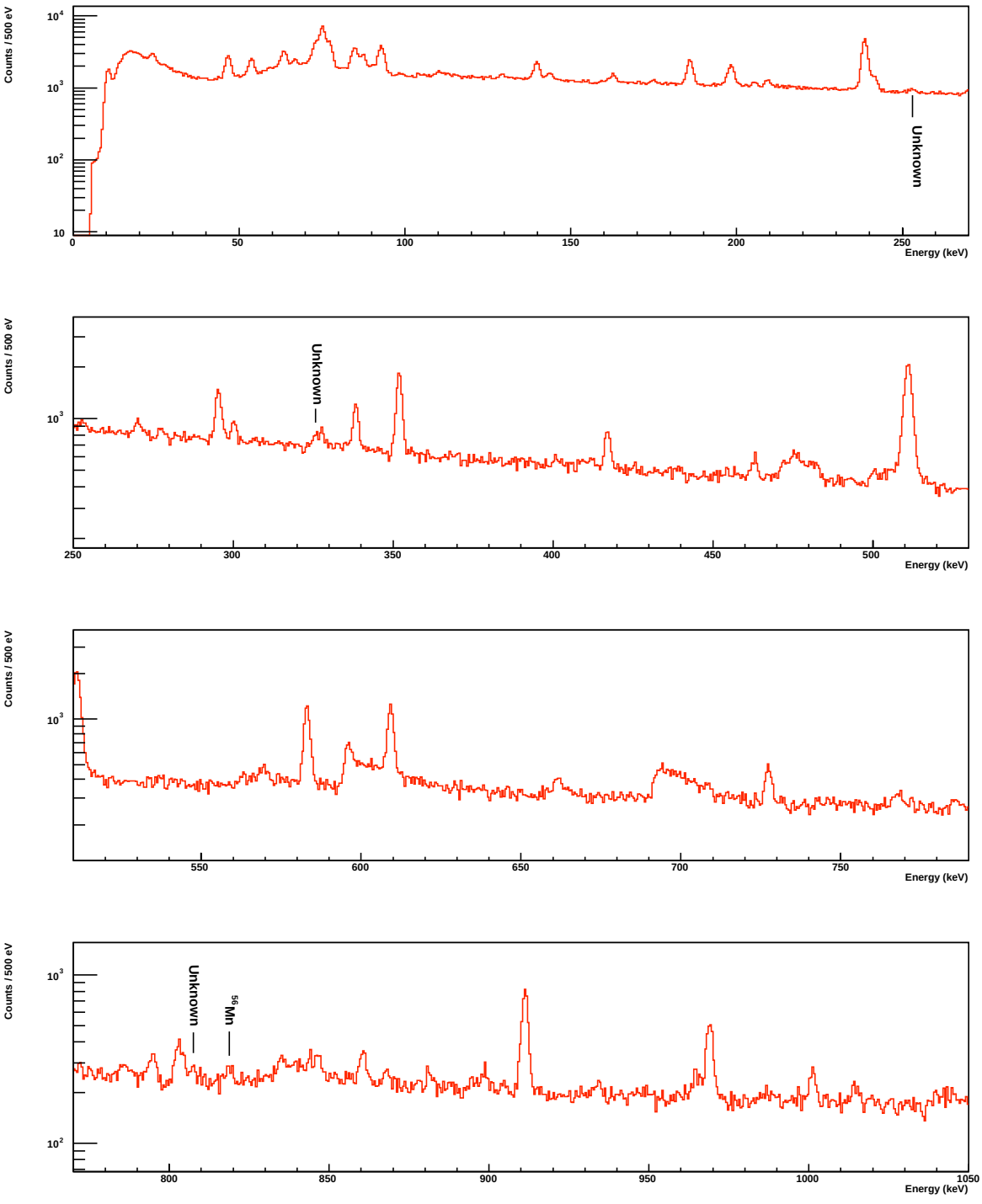

Figure 5.10: CLOVER cooldown spectrum (0-1000 keV). This spectrum is based on 58.3 hours of cooldown data with the CLOVER in a 4" lead shield and with 6" of polyethylene present. See Fig. 4.15 for a list of peak identifications not shown here.

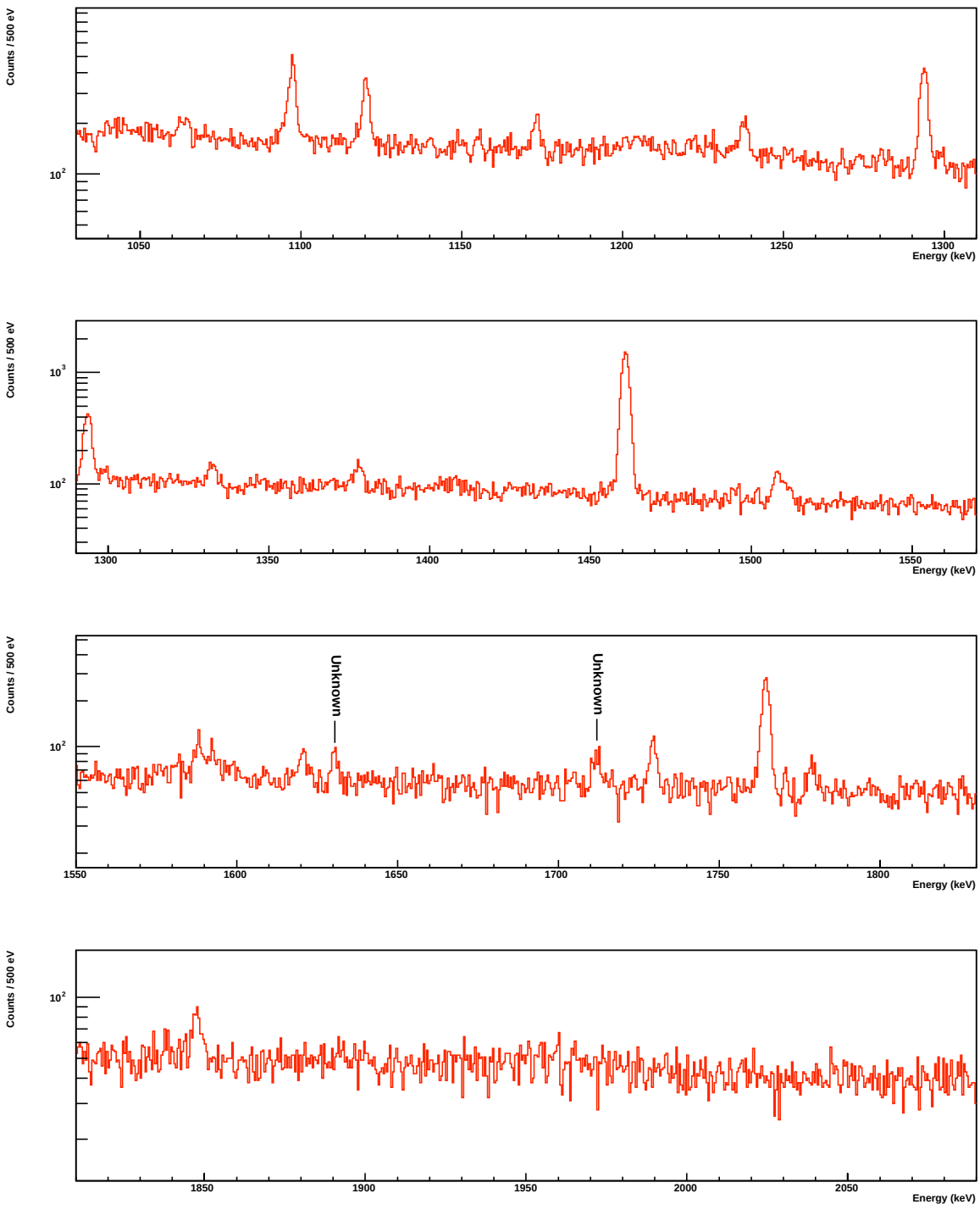

Figure 5.11: CLOVER cooldown spectrum (1000-2000 keV). This spectrum is based on 58.3 hours of cooldown data with the CLOVER in a 4" lead shield and with 6" of polyethylene present. See Fig. 4.16 for a list of peak identifications not shown here.

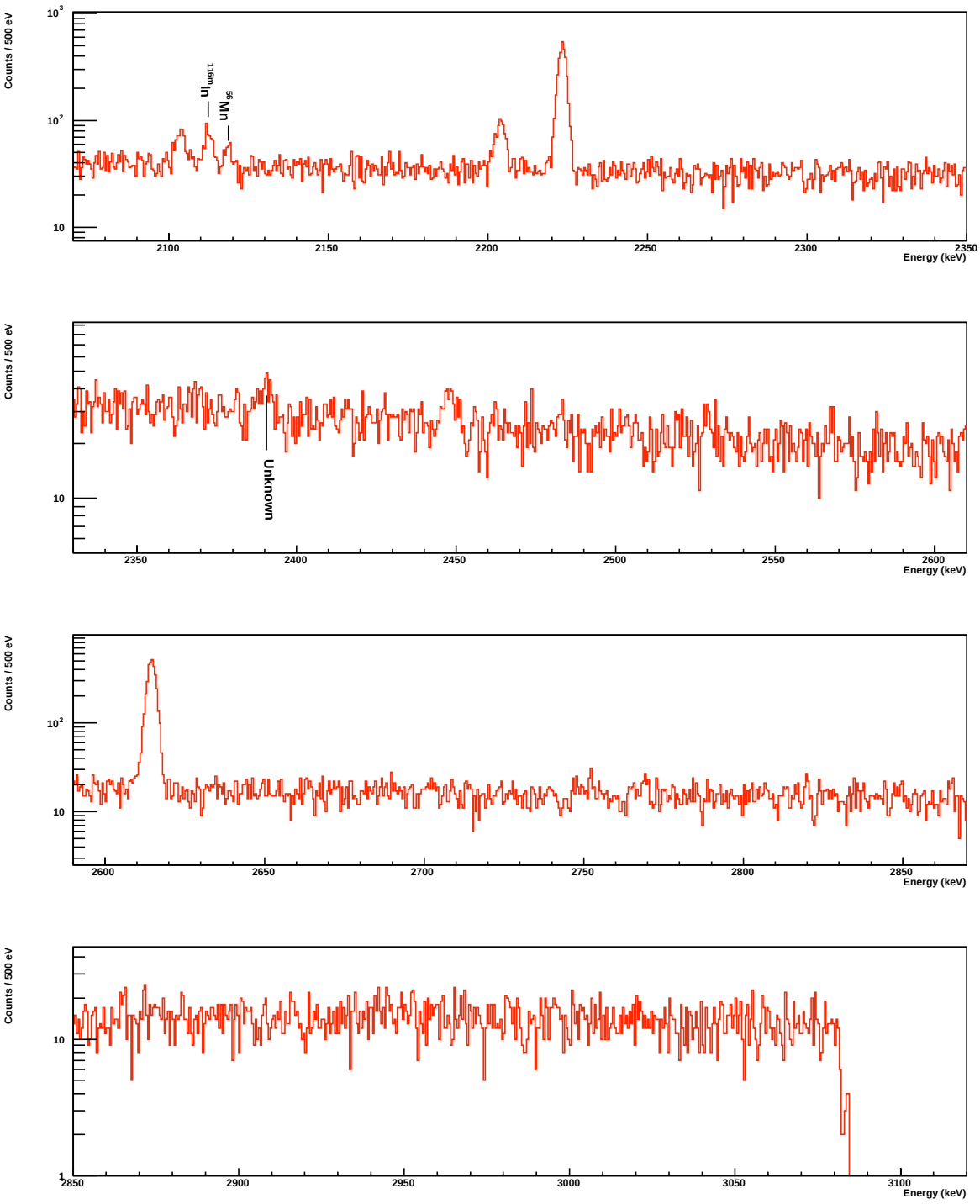

Figure 5.12: CLOVER cooldown spectrum (2000-3000 keV). This spectrum is based on 58.3 hours of cooldown data with the CLOVER in a 4" lead shield and with 6" of polyethylene present. See Fig. 4.17 for a list of peak identifications not shown here.

Table 5.4: Properties of natural indium. Natural abundances and cross-sections come from [87]. The thermal neutron capture cross section for natural indium is (271.5 ± 7.7) barns.

Isotope	Natural Abundance	Thermal neutron capture cross-section (b)	Percentage of neutron captures relative to natural germanium
^{113}In	4.29(5)%	15.1(13)	(0.238 ± 0.0218)%
^{115}In	95.71(5)%	283(8)	(99.76 ± 3.98)%

Table 5.5: Strongest ^{116m}In lines. The third and fourth columns are based on measured peak areas from the cooldown dataset. The last column is obtained via the same method as described in Section 4.5.4.

γ Energy (keV)	Rel. Int. (%)	Peak Area (counts)	Normalized Peak Area Ratio (counts)
416.86(3)	27.7(12)	2051(93)	1.00(20)
818.718(21)	11.5(4)	438(70)	0.77(19)
1097.326(22)	56.2(11)	2264(69)	1.04(19)
1293.558(15)	84.4(17)	2613(67)	0.94(17)
2112.312(22)	15.5(4)	364(33)	1.14(21)

constant. The decay constant fits to (52.8 ± 1.9) minutes, in good agreement with the accepted half life of ^{116m}In of 54.3 minutes.

With the strongest ^{116m}In lines present in the cooldown spectrum, and the good agreement of the half life measurment, the evidence for the presence of indium in the CLOVER is solid. How indium is used in the CLOVER construction, however, is proprietary and the manufacturer will divulge neither the placement nor the overall mass.

The presence of manganese

There is only one natural occuring isotope of manganese, ^{55}Mn, with a thermal neutron capture of 13.36(5) barns. The resulting isotope, ^{56}Mn, has a half life of 2.58 hours. Table 5.6 shows the strongest ^{56}Mn lines.

Unfortunately, only the strongest of these lines was observed in the cooldown spectrum. It is unsurprising that the other lines were not visible, because not only were the peaks less intense, but the photopeak efficiency at the higher energies also conspired to keep peaks below statistical significance.

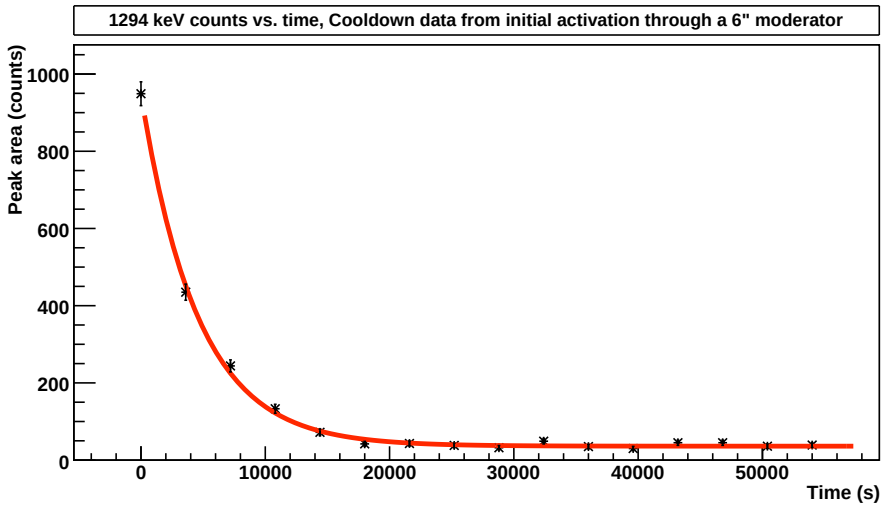

Figure 5.13: Decay of ^{116m}In in the cooldown data. The decay constant fits to (52.8 ± 1.9) minutes, in agreement with the accepted value of 54.3 minutes. The χ^2 / D.O.F. = 15.7 / 13 (P-value = 0.266).

Repeating the half life measurement of the 847 keV peak (see Fig. 5.14), the half life turned out to be (2.02 ± 0.30) hours, or 1.9 σ from the accepted value.

While the statistics would need to be improved to obtain a more confident determination of the presence of manganese, the corroborating evidence of peak presence and decay constant provide a strong hint. Confirming measurements will be made in the next chapter when increased statistics are available.

Table 5.6: Strongest ^{56}Mn lines. Peak areas are not compared because in the current dataset, only the 847 keV line was observed.

γ Energy (keV)	Rel. Int. (%)
846.771(5)	98.9(3)
1810.772(17)	27.2(8)
2113.123(10)	14.3(4)

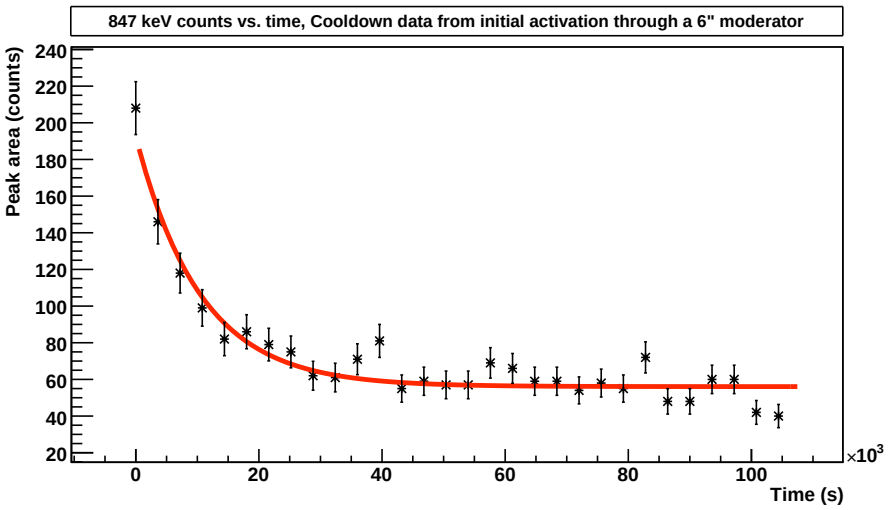

Figure 5.14: Decay of ^{56}Mn in the cooldown data. The decay constant fits to (2.02 ± 0.30) hours. The χ^2 / D.O.F. = 34.2 / 27 (P-value = 0.160).

Chapter 6

EXPERIMENTAL RESULTS

With the CLOVER fully characterized, one polyethylene brick was removed, leading to a greater thermal neutron flux both because the AmBe source was now closer to the CLOVER and fewer neutrons were captured in the wax[1]. With this higher flux, the CLOVER was put through a series of activation and cooldown cycles, and from those cooldown datasets the efficiency of observing the surrogate excited-state double-beta decay signal was extracted.

6.1 Production Activation and Cooldown

For production datataking, we determined the activation/cooldown cycle timing and subsequently went through sixteen such cycles. For each activation we measured the fast and thermal neutron fluxes. From the intensity of the ^{75m}Ge decays we extrapolated the total number of ^{77}Ge events in the dataset.

6.1.1 Experimental setup

Using the six inches of moderator in the previous chapter was a conservative choice made for testing purposes. Removing a single polyethylene brick would increase the fast neutron flux by approximately a factor of (4 bricks / 3 bricks)^2 = 1.8, a level deemed safe for the CLOVER with modest exposure. Fig. 6.1 shows a photograph of the set up with the front part of the shield removed to show the relationship between the AmBe source, the polyethylene moderator, and the CLOVER detector.

6.1.2 Optimizing the cycle period

We determined the optimal cycle time in the following way. Assume that the activation and cooldown times are equal, and represented by t. At the end of a single activation period, the ^{77}Ge signal will be at $(1 - 2^{-t/\tau})$ of maximum, where τ is the half-life of the isotope in question. Integrating the signal during the cooldown period, starting at this fraction of maximum, gives

$$\text{Single cycle integrated signal} = \tau\, 4^{-t/\tau}(1 - 2^{t/\tau})^2$$

[1]We do not *a priori* expect the relative increase in the fast neutron flux to be equal to the relative increase in the thermal neutron flux

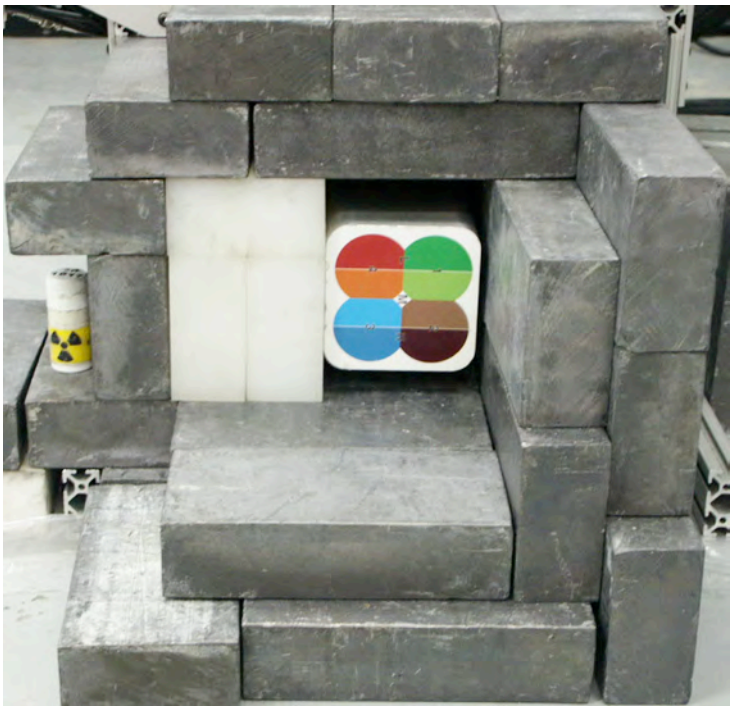

Figure 6.1: Activating the CLOVER Detector. The CLOVER detector is in the middle of the photo, with a colored sticker showing the approximate locations of the four internal crystals. The white bricks to the left of the CLOVER are the polyethylene moderator, and the AmBe source is on the far left.

If there is a total time limit on the number of activation/cooldown cycles of T, the number of cycles that can be fit in is $T/2t$. We can therefore find the optimal activation by looking for a maximum in the equation

$$\text{Total integrated signal} \sim \frac{4^{-t/\tau}}{t}(1 - 2^{t/\tau})^2 \tag{6.1}$$

where all normalization constants have been dropped. This equation is plotted in Fig. 6.2.

The optimal t is 2.07 τ. For ^{77}Ge, τ = 11.30 hours, putting a fully-optimized activation/cooldown cycle at 46.7 hours—activate for 23.4 hours, then take cooldown data for 23.4 hours. We wanted to obtain data more often than once every two days, however, to discover any problems with the ongoing procedure and reduce the risk of lost time. Taking into account human considerations of a regular schedule, we decided to halve the activation/cooldown cycle, and activate for 12 hours and obtain data for 12 hours.

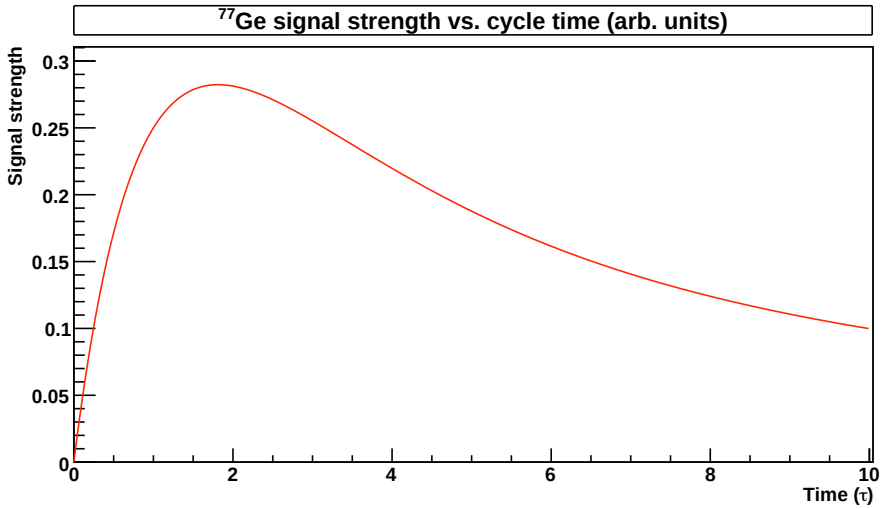

Figure 6.2: ^{77}Ge cycle optimization. This graph shows that the optimal activation/cooldown cycle time is 2.07 τ individually for activation and cooldown (4.14 τ for the complete cycle). Our complete cycle time was 24 hours, reducing the ^{77}Ge signal to 91.2% of maximum.

Using the values of 12/11.3 and 11.3 for t and τ respectively in Eq. (6.1) gives an integral of 0.256. Using the optimal value for t of 2.07 τ gives an integral of 0.280. Thus with this shorter activation/cooldown cycle time, the ^{77}Ge signal efficiency was at 91.2% of maximum.

6.1.3 Fast neutron flux

With the cycle time determined, we embarked on a series of 16 activation/cooldown cycles with the 4" moderator. The start and stop times are shown in Appendix C.

For each of the 16 activation datasets we measured the intensity of the 692 keV fast neutron peak using the fit equation described in Section 5.2. Fig. 6.3 shows the peak intensity for each of the data runs.

Turning the 692 keV peak intensity into a fast neutron flux (see Section 4.5.5) and integrating over the activation times for each individual data run gives a total fast neutron fluence of $(8.2 \pm 0.4) \times 10^5$ n / cm^2, well below the 10^8 n / cm^2 danger region.

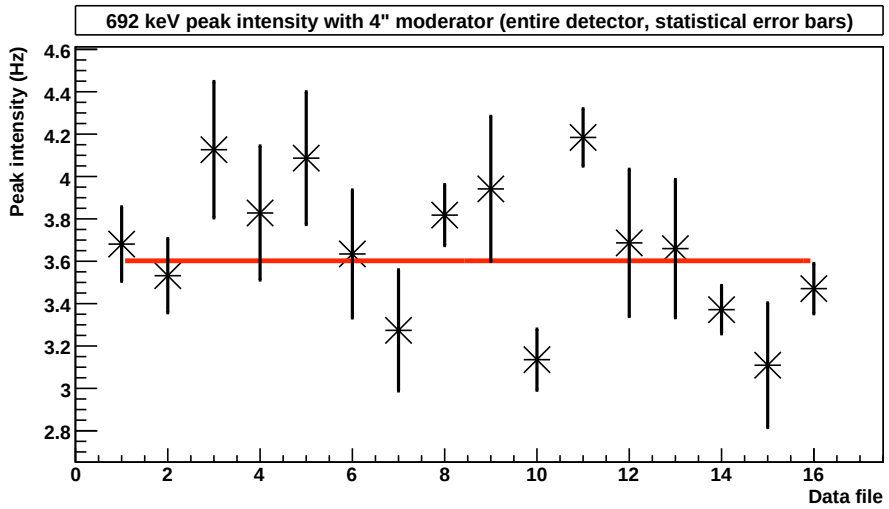

Figure 6.3: 692-keV peak intensity through 4" moderator. Fitting a constant peak intensity through all 16 runs results in a χ^2 / D.O.F. = 47.8 / 15 (P-value = 2.8e-5). Compare to Fig. 5.8.

6.1.4 ^{77}Ge creation rate

We also measure the intensity of the 140 keV peak from the decay of ^{75m}Ge. Ordinarily, this peak would be used to calculate the thermal neutron flux. In the present case, however, the goal is not to measure the thermal neutron flux *per se*, but rather to calculate the number of ^{77}Ge decays in the cooldown datasets. Once we have the ^{75m}Ge creation rate, we can multiply by the ratio of the appropriate thermal neutron capture cross sections and relative abundances of ^{74}Ge and ^{76}Ge to obtain the ^{77}Ge creation rate. In this way, the proprietary construction details do not increase the uncertainty in the rates.

^{76}Ge has a thermal neutron capture cross section to ^{77}Ge of (0.06 ± 0.01) barns. ^{76}Ge also has a capture cross section to ^{77m}Ge of (0.10 ± 0.01) barns. ^{77m}Ge decays via internal transition (half life = 52.9 s) to ^{77}Ge, with a branching ratio of 19%. The other 81% of the time it beta decays to ^{77}As without passing through the triple-coincidence branches currently under study. Thus (49 ± 7)% of all neutron captures on ^{76}Ge result in a ground-state ^{77}Ge nucleus.

$$\frac{^{77}\text{Ge creation rate}}{^{75m}\text{Ge creation rate}} = \left(\frac{(0.49 \pm 0.07)(160 \pm 14)\text{ mb}}{170 \pm 30\text{ mb}}\right)\left(\frac{7.61 \pm 0.38\%}{36.28 \pm 0.73\%}\right)$$
$$= 0.097 \pm 0.024 \tag{6.2}$$

Note that the uncertainty in this ratio is about 25%. This will set the lower limit for the systematic uncertainty in the number of ^{77}Ge decays present in the dataset.

Similar to the process in Section 5.3.2, we compare the intensity of the 140 keV peak from run to run in the 4" polyethylene configuration. Fig. 6.4 shows the results. The manufacturer of the AmBe source confirmed that the neutrons are not emitted isotropically. We questioned whether the spread in values derives from this anisotropy. Unfortunately, if this were the case then a run with a particularly high (or low) fast neutron flux would also have a particularly high (or low) thermal neutron flux. Comparing Figs. 6.3 and 6.4, we see this is not necessarily the case.

A separate experiment with controlled rotation of the AmBe source was not performed. It is possible that there may be another systematic effect that alters the fast and thermal neutron fluxes, although without a controlled experiment to measure the degree of anisotropy in the neutron emission, it cannot be completely ruled out.

^{77}*Ge tally*

With the 140 keV peak intensity measured for each activation run, and the creation rate of ^{77}Ge nuclei thereby extrapolated, we can calculate the overall rate of ^{77}Ge decays during both activation and cooldown. We assumed an asymptotic rise in the ^{77}Ge event rate during activation based on its half life, and an exponential fall in the event rate during cooldown data taking. Fig. 6.5 shows the rate curves.

By integrating over the times during which cooldown data were being taken (the shaded regions of Fig. 6.5), we predicted the number of ^{77}Ge decays. Because of the presence of ^{116m}In, we applied a time cut by removing the first part of every cooldown dataset. We do not know *a priori* the optimal time to wait for the ^{116m}In to decay—if the time cut is too small we have a significant ^{116m}In background, but if the time cut is too large the statistics are too low and the uncertainty on the coincidence peak areas will correspondingly be very large.

We therefore decided to measure the significance of the coincidence peaks using 11 different time cuts of 0, 1, 2, 3, 4, 5, 6, 7, 8, 9, and 10 hours. We then use the time cut that gives the greatest coincidence peak significance. The number of ^{77}Ge decays in the final data set will of course depend on what time cut was used. Table 6.1 shows the number of expected ^{77}Ge decays for each early time cut as well as the total integrated time of all cooldown data sets.

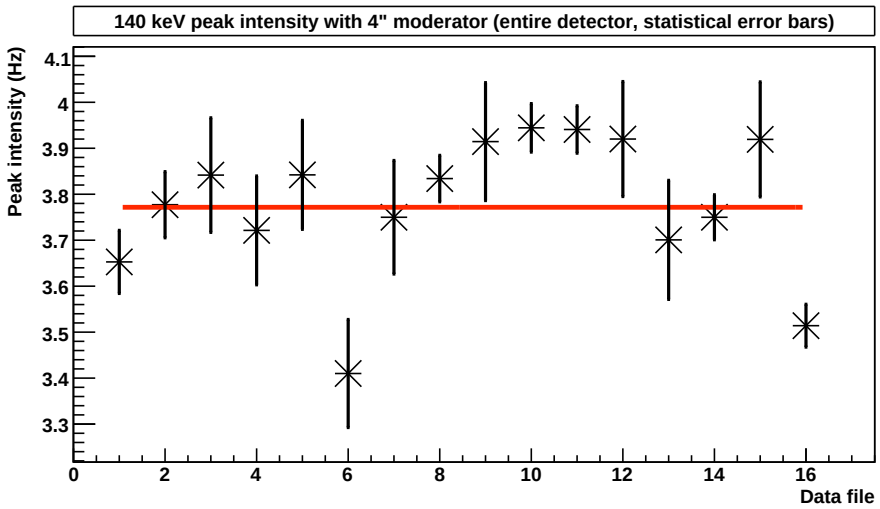

Figure 6.4: 140-keV peak intensity through 4" moderator. A constant peak intensity through all 16 runs results in a χ^2 / D.O.F. = 71.6 / 15 (P-value = 10^{-9}). This quality of fit should be compared to that of Fig. 5.9. The statistical uncertainty in the peak intensity is between 1% and 3% depending on the dataset.

6.2 Cross talk between the CLOVER Crystals

An issue that emerged during the coincidence studies is that of cross talk between the crystals. Cross talk is seen in the CLOVER as a suppression of reported energy in a crystal. Among other mechanisms, the cross talk can depend on either the energy deposition or the number of crystals hit. To study the energy dependence, we hold the number of crystals hit constant, and vice versa.

While the presence of indium in the CLOVER has been a sometimes difficult issue to work with, we can use the ^{116m}In signal to study the crosstalk. The 417 keV gamma ray from ^{116m}In can occur in coincidence with 818, 1294, and 2112 keV gamma rays. To study the energy dependence, we require exactly two crystals be hit. We further require one of those two crystals have an energy deposition at one of the coincidence energies, and we fit a Gaussian curve to the nominal 417 keV peak. Fig. 6.6 shows the resulting histogram. The figure clearly shows the 417 keV peak centroid increasingly suppressed with increasing coincidence energies. Fig. 6.6 includes the spectrum from single-energy depositions as a reference.

We next characterize the dependence of the crosstalk on the number of crystals hit. We use all three coincidence energies (818, 1294, and 2112 keV) to perform three separate analyses. In each analysis we require two, three, and four crystals be hit. For the two-crystal cut, one of the crystals

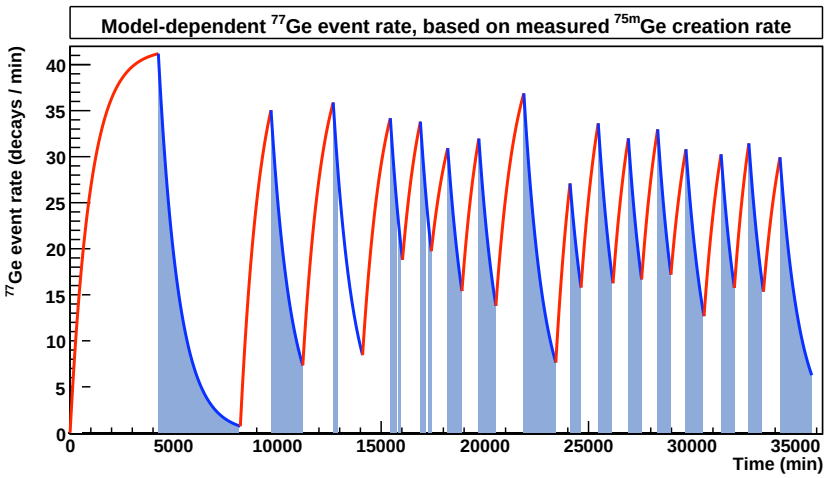

Figure 6.5: Estimated ^{77}Ge rate during activation and cooldown cycles. The solid red and blue lines show the rate of ^{77}Ge events in the CLOVER detector based on the measured thermal neutron flux and extrapolated number of neutron captures on ^{76}Ge nuclei. The shaded-to-zero areas show when data was being taken. Integrating the blue areas gives the total number of ^{77}Ge decays in the CLOVER detector.

Table 6.1: Number of ^{77}Ge decays. We eliminated the first zero through ten hours from each individual decay data set. The systematic uncertainty in the number of decays is 25% (see Eq. (6.2) and accompanying text.

Time cut (hours)	Number of ^{77}Ge decays	Integrated time (m)
0	285527	15272
1	254561	14327
2	224950	13376
3	197102	12407
4	172025	11485
5	150824	10652
6	132213	9872
7	112765	9008
8	93837.0	8116
9	78235.6	7341
10	64604.7	6621

must have an 818 keV energy deposition. For the three-crystal cut, two of the crystals have to sum to 818 keV, and for the four-crystal cut, three of the crystals have to sum to 818 keV. For each number-crystal cut, we histogram the energies in the remaining crystal, and, as before, fit a Gaussian curve to the nominal 417 keV peak. We repeated the procedure for the 1294 and 2112 keV coincidence energies as well. The results are shown in Fig. 6.7 and Table 6.2. Based on these measurements, we conclude the crosstalk is not dependent on the number of crystals hit.

Traditionally, the cross talk issue is an intricate one, though we have demonstrated that in the CLOVER detector it is dependent on total energy deposition and independent of the number of crystals hit. Even though the relationships may be analyzed phenomenologically, there are a number of potential sources of the cross talk, including crystal coupling, capacitive pickup, ground loops, and image charges (and this list is by no means complete). Digitization of the full pulse from all four crystals for every event, independent of the number of crystals with energy deposition, may help in understanding this issue.

Because of the unknown model of the source of cross talk, rather than attempting to predict the behavior at various coincident energies we decided to simply measure the centroids of coincidence peaks and reanalyze the coincidence data centered on those suppressed energies. We kept the coincidence window at ± 2 keV.

6.3 Verification of ^{77}Ge Signal

We analyzed the cooldown data sets to verify the presence of ^{77}Ge. 15.3% of ^{77}Ge decays are to the 475 keV energy level of ^{77}As (see Fig. 3.5 or Appendix A). This energy level has a half life of 114 μs. This excited ^{77}As nucleus then decays 97% of the time via two coincidence gamma rays at 211 keV and 264 keV (the other 3% is a decay directly to the ground state). This long-lived state leads to two possible methods for verifying the ^{77}Ge signal. In the first method, the long half life of this level means the vast majority of these decays will not have the beta particle coincident with the two subsequent cascade gammas. As a result, there is a much greater chance of observing a 211 keV energy deposition in one crystal and a 264 keV energy deposition in another. In the second method, a histogram of the energy depositions immediately preceding the coincidence event should give a beta spectrum with the correct endpoint energy.

6.3.1 ^{77}Ge verification with coincidences

Utilizing no time cut (i.e., incorporating all of the cooldown data) and requiring exactly two crystals have an energy deposition, we plotted two histograms. One spectrum is of energy depositions coincident with 211 keV, and the other is of 264 keV coincidences. If there is a significant ^{77}Ge presence, there will be a large 264 keV peak in the 211 keV coincidences histogram, and vice versa.

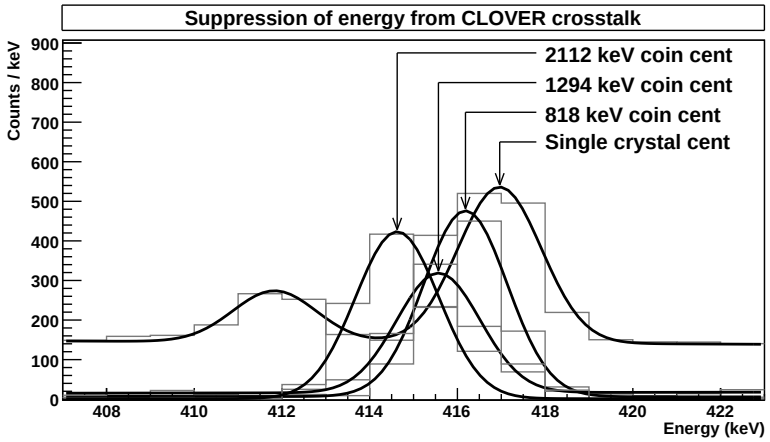

Figure 6.6: Coincidence energy effect on peak centroids. Except for the single-crystal curve, the coincidence curves require exactly two crystals have an energy deposition. The 818 keV coincident centroid is at 416.18(3) keV, the 1294 keV coincident centroid is at 415.57(4) keV, and the 2112 coincident centroid is at 414.63(3) keV. The single-crystal curve, with a centroid at 416.97(4) keV, is included for reference. The single-crystal curve is attenuated by a factor of 500 for easier comparison between peak heights.

Table 6.2: Crystal multiplicity effect on peak centroids. The centroids remain unchanged within any given coincidence energy, showing that the number of crystals hit has no effect on the crosstalk energy suppression. These centroids correspond to the curves shown in Fig. 6.7.

	818 keV coin.	1294 keV coin.	2112 kev coin.
2-crystal	416.18(3)	415.57(4)	414.63(3)
3-crystal	416.12(8)	415.63(8)	414.71(8)
4-crystal	415.6(5)	415.9(3)	415.0(5)

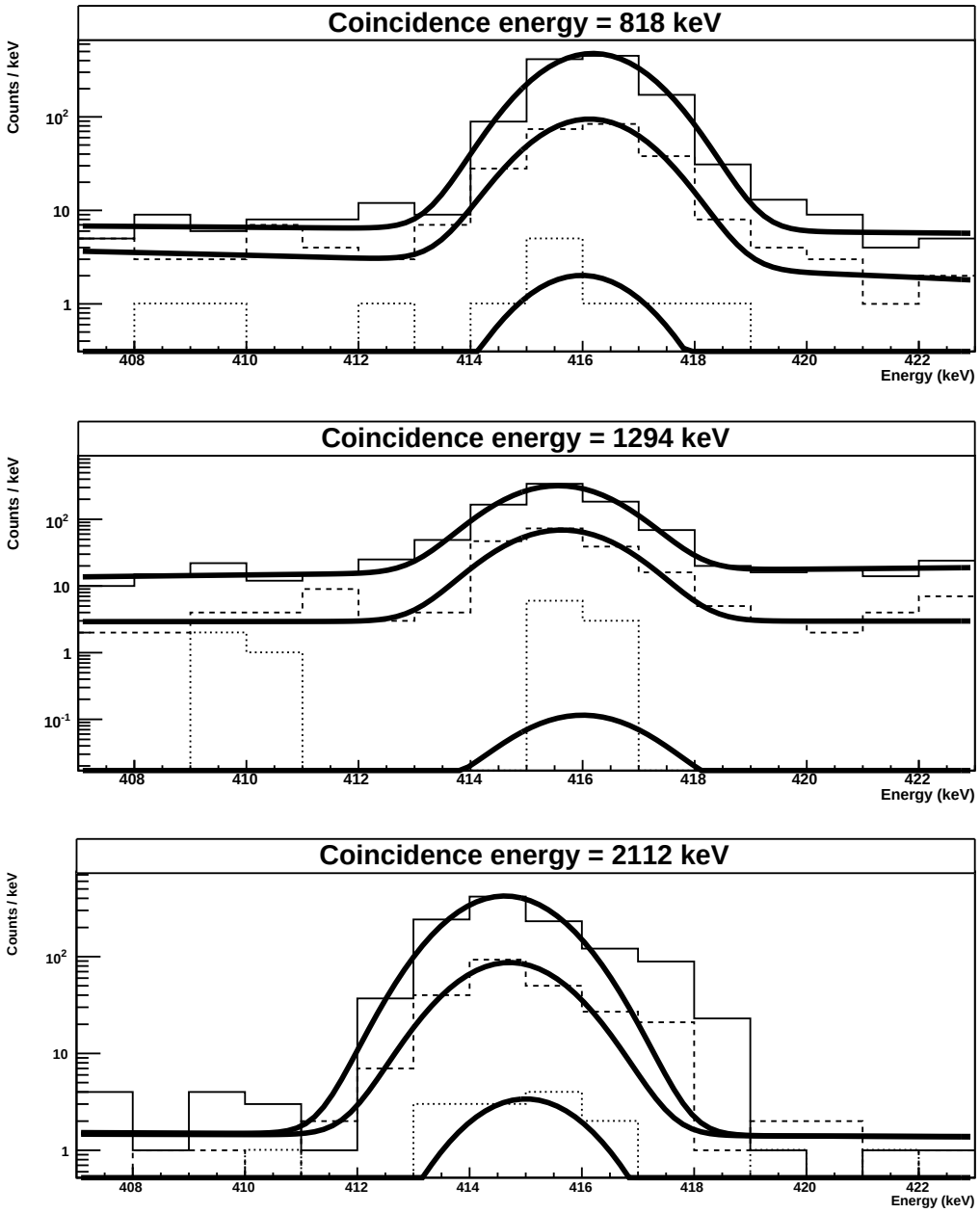

Figure 6.7: Crystal multiplicity effect on peak centroids. The top curve for each of the three graphs (coincidence energy 818, 1294, and 2112 keV) shows the two-crystal cut. The middle curve is the three-crystal cut and the bottom curve in each of the three graphs is the four-crystal cut. Although the statistics for the four-crystal cuts are too low to reliably fit a Gaussian curve, it is included for comparison. See Table 6.2 for the centroid values. The source of excess counts on the high side of the 2112-coincidence curves is unknown.

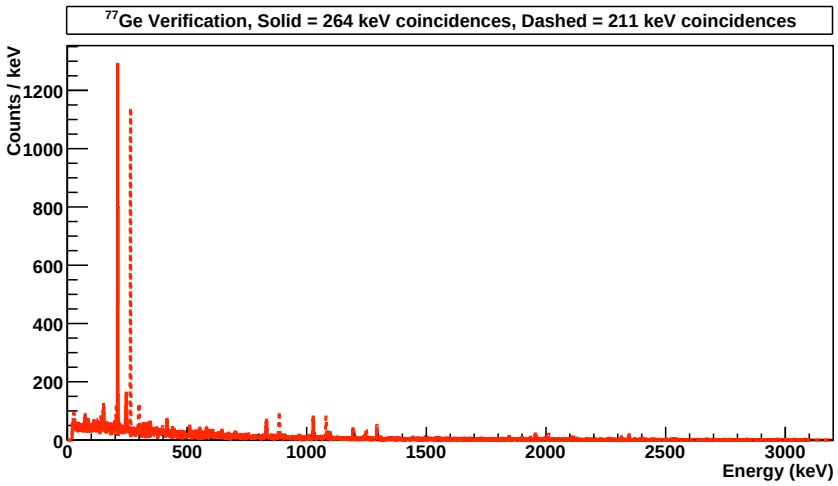

Figure 6.8: Verification of ^{77}Ge signal with coincidences. The strongest lines in the spectra are the respective coincidence partners. The minor lines in the spectra are attributed to Compton scatters from the stronger lines in the raw spectrum, e.g. ^{116m}In, ^{208}Tl, ^{40}K. Because the coincidence energies involved are lower than those from ^{116m}In, the suppression was lower than that shown in Fig. 6.6.

We used this coincidence to test the cross talk. We performed the coincidence study using the published gamma ray energies of 211.03 and 264.44 keV with a window of ± 2 keV. The centroid of the resulting 211 keV peak was 210.70(2) keV, and the area 2533(53) counts. The centroid of the 264 keV peak was 264.04(2) keV, and the area was 2592(53) counts.

The analysis was performed using the fit centroids ± 2 keV. The centroid of the 211 keV peak remained at 210.70(2) keV, and the area was 2545(54) counts. For the 264 keV peak the centroid was once again 264.04(2) keV, and the area was 2580(53) counts. The peak areas were not appreciably different whether using the published energy or the suppressed energy. The difference between the sets of energies (published and suppressed) was roughly one sixth the FWHM of the peaks (see Section 4.5.1), so we would not necessarily expect a dramatic effect in the area of the peaks.

The results of the analysis with the shifted centroids are plotted in Fig. 6.8, and demonstrate the presence of ^{77}Ge.

6.3.2 ^{77}Ge verification with the beta spectrum

Utilizing this same 475 keV energy level, the energy of the events previous to the 211 / 264 keV coincidence are shown in Fig. 6.9. There were three requirements for any given previous event:

it must have been the event immediately preceding the coincidence event, there must have been exactly one crystal with an energy deposition, and the preceding event must have occurred within three half lives of the 475 keV energy level (i.e., $3 \times 114\,\mu s = 342\,\mu s$). As the average time between all events is 0.1 seconds, the effect of accidental events should be small. There were 1599 events that met all three criteria.

As a test to make sure Fig. 6.9 is not simply an accidental background spectrum, we created a histogram of events immediately following rather than immediately preceding the 211 / 264 keV coincidence. The other requirements (the time cut and the single-crystal deposition) remained the same. Fig. 6.10 shows the result, which follows a basic background continuum much more closely than Fig. 6.9. We created a Kurie plot from the beta spectrum, shown in Fig. 6.11. The data supports the claim that the observed decays are consistent with beta decay from ^{77}Ge.

There is a source-associated background to this beta spectrum and its associated Kurie plot. Referring to Appendix A, we note it is possible for ^{77}Ge to decay to an energy level above 475 keV, with a subsequent transition to the 475 keV energy level. The total branching ratio for all such transitions is 16.5%. This should be compared to the branching ratio of a decay directly to the 475 keV energy level of 15.3%.

The backgrounds derive primarily from two transitions: 1189.8 → 475 keV (7.17%) and 1560.6 → 475 keV (6.05%).These two backgrounds involve 715 keV and 1086 keV energy gamma rays respectively, and the single-crystal cut should suppress these backgrounds. A Monte Carlo simulation would have to be run to determine the full effects of these backgrounds. Regardless, the purpose of this beta-spectrum exercise was to verify the presence of ^{77}Ge, and the differing spectra of Figs. 6.9 and 6.10 combined with the fit of Fig. 6.11 demonstrates this presence.

6.4 Coincidence Results

With the presence of ^{77}Ge confirmed, we finally turned our attention to measuring the efficiency of observing the ^{77}Ge triple coincidence that mimics the ^{76}Ge double beta decay to the first excited 0^+ state of ^{76}As.

As a reminder, the coincidences we looked for come from the 631.8 keV energy level, and are 367.40 / 264.44 keV and 416.33 / 215.50 keV. Unfortunately, both of these coincidences have backgrounds in the decays of ^{75}Ge (at 264.66 keV) and ^{116m}In (at 416.86 keV), respectively. We may be able to reduce these backgrounds by eliminating the first portion of every cooldown data set. To this end, we removed the first 0 through 10 hours of data from every cooldown data set (i.e., the 0-hour cut contained all the data, the 1-hour cut contained all but the first hour from every data set, and so on). We then calculated the significance of the coincidence peaks for every time cut. The time cut we used for the final analysis was the one that resulted in the peak with the greatest significance. Because the backgrounds are not the same for all four coincidence peaks, we had to

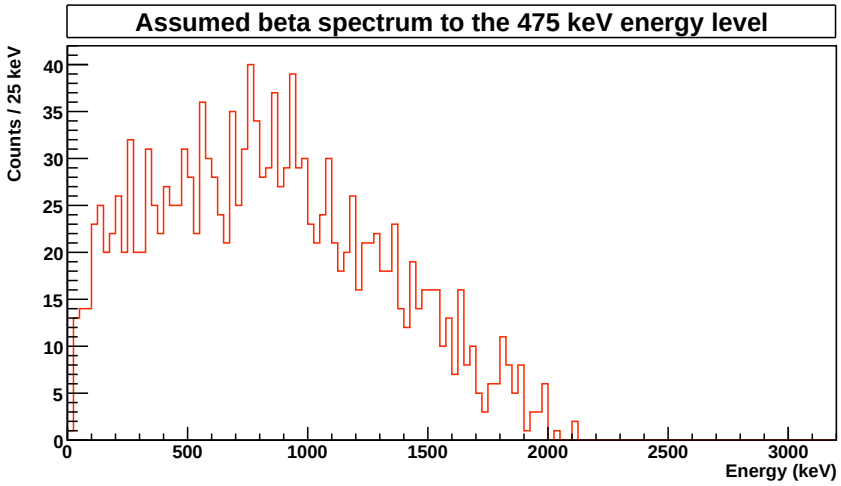

Figure 6.9: Verification of ^{77}Ge signal with beta spectrum analysis. The events in the spectrum precede a 211/264 keV coincidence. According to the partial decay spectrum shown in Fig. 3.5, this beta spectrum should have an end point energy of 2227 keV. Fig. 6.11 shows the accompanying Kurie plot.

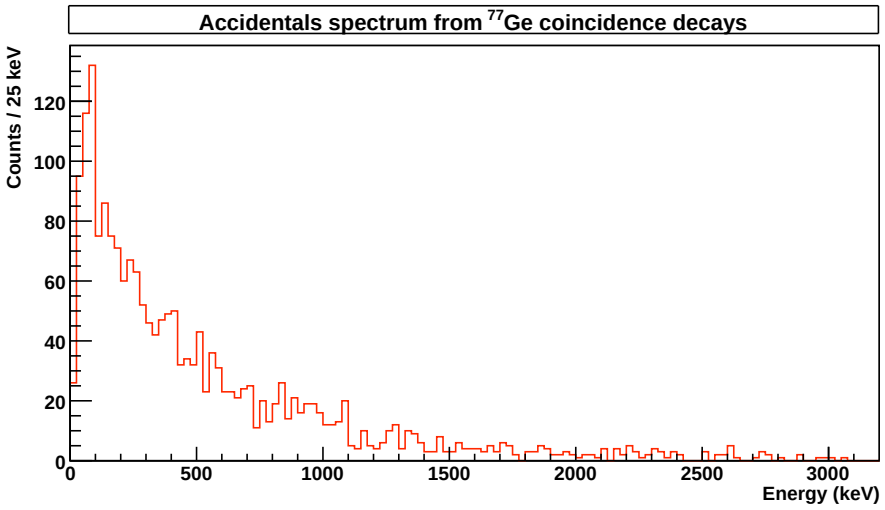

Figure 6.10: Accidental ^{77}Ge-coincidence events. This figure shows a clear deviation from Fig. 6.9, supporting the interpretation of Fig. 6.9 as a beta spectrum from ^{77}Ge. See text for further details.

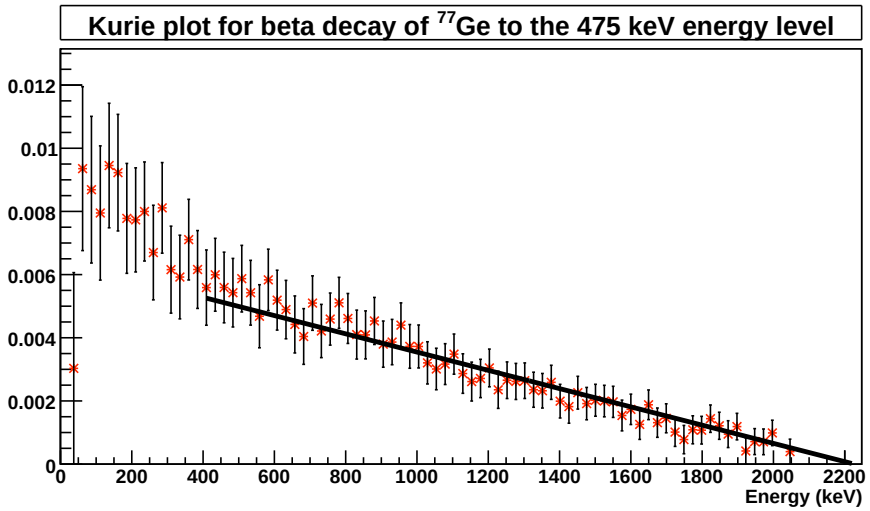

Figure 6.11: Kurie plot of ^{77}Ge beta spectrum. The points are experimental, and the line is a best fit to the data with the end point locked at 2227 keV. The fit runs from 400 keV to 2250 keV, and has a χ^2 / D.O.F = 21.42 / 72.

allow for different time cuts for each peak.

We also had to take into account the crosstalk between the CLOVER crystals. As described at the end of Section 6.2, we perform the analysis with the published energies, measure the suppressed centroids, and reanalyze with the new energies.

6.4.1 The 367.40 / 264.4 keV coincidence

Coincidences with published energies

We plotted a set of eleven histograms of events coincident with either a (264.44 ± 2) keV or (367.40 ± 2) keV energy deposition after eliminating the first zero through ten hours of data from each individual data set. We also required exactly three crystals have an energy deposition. For each of these 2 × 11 data sets, we measured the centroid, significance, area, and background around the coincidence peak, with the results shown in Tables 6.3 and 6.4.

Coincidences with suppressed energies

What then is the effect of searching for coincidences centered on the suppressed centroids? We reanalyzed the data, looking for coincidences at the centroid averages of (262.81 ± 2) keV and

Table 6.3: Significance of the 367 keV peak using the published value of the 264 keV coincidence. We eliminated the first zero through ten hours from each individual decay data set. The bold line indicates the time cut that results in the greatest peak significance. See text for further explanation.

Time cut (hours)	Centroid	Significance	Peak area	Background / bin
0	**366.09**	**6.32** σ	**40.93 ± 9.02**	**8.40**
1	366.12	6.06 σ	36.47 ± 8.48	7.25
2	366.06	5.95 σ	33.90 ± 8.11	6.49
3	365.90	5.11 σ	27.17 ± 7.38	5.66
4	365.80	4.39 σ	22.70 ± 6.91	5.34
5	365.84	4.04 σ	20.12 ± 6.60	4.95
6	365.97	4.93 σ	21.78 ± 6.39	3.91
7	365.54	4.66 σ	18.66 ± 5.85	3.21
8	365.68	4.28 σ	15.78 ± 5.40	2.72
9	365.62	4.41 σ	15.67 ± 5.29	2.52
10	365.52	3.95 σ	13.21 ± 4.85	2.24

Table 6.4: Significance of the 264 keV peak using the published value of the 367 keV coincidence. We eliminated the first zero through ten hours from each individual decay data set. The bold line indicates the time cut that results in the greatest peak significance. See text for further explanation.

Time cut (hours)	Centroid	Significance	Peak area	Background / bin
0	262.81	6.81 σ	44.15 ± 9.30	8.41
1	**262.76**	**6.92** σ	**41.30 ± 8.88**	**7.13**
2	262.83	6.90 σ	39.17 ± 8.58	6.45
3	262.71	6.69 σ	35.14 ± 8.10	5.51
4	262.73	6.44 σ	31.57 ± 7.61	4.80
5	262.66	6.68 σ	29.93 ± 7.29	4.01
6	262.72	6.22 σ	27.30 ± 7.05	3.85
7	262.66	4.91 σ	20.78 ± 6.27	3.58
8	262.79	4.44 σ	18.19 ± 5.99	3.35
9	262.13	3.24 σ	12.18 ± 5.35	2.82
10	263.13	2.80 σ	10.28 ± 5.00	2.70

(365.83 ± 2) keV. The results are shown in Tables 6.5 and 6.6.

The consistent increase in peak significances in going from the published to measured energy centroids demonstrates the validity of the energy-suppressed search windows. Figures 6.12 and 6.13 show the peak fits in the raw (upper, dashed curve), coincidence (middle, solid curve), three-crystal (middle, dashed curve), and optimal time-cut (lower, solid curve) spectra for the two coincidence peaks under consideration.

In Fig. 6.13, there is a sizeable 264 keV peak in the raw spectrum, indicating a potential background in the coincidence spectrum. Unfortunately, this 264 keV peak is assumed to come from, at least in part, ^{75}Ge, and there are no other peaks in the ^{75}Ge spectrum that would allow background subtraction from the coincidence spectrum. For this reason, the area of the 367 keV peak in the 264 keV coincidence spectrum will be used to determine the efficiency of observing this 264 / 367 keV coincidence.

Also in Fig. 6.13, there is a peak near 270 keV in the upper two curves. This peak most likely comes from the decay of ^{77}As, created from the decay of ^{77}Ge. ^{77}As has a 368.7 / 270.8 keV gamma coincidence.

With a one-hour time cut, the total number of ^{77}Ge events is 255000 ± 64000. The area of the 367 keV peak was 58.30 ± 9.59 counts, giving an efficiency for observing this decay of

$$\text{Efficiency for observing the } ^{77}\text{Ge 264 / 367 keV coincidence} = (0.0229 \pm 0.0069)\%. \qquad (6.3)$$

6.4.2 The 416.33 / 215.50 keV coincidence

Coincidences with published energies

We plotted another set of 2 × 11 histograms similar to those in the previous section, and again required exactly three crystals have an energy deposition. We searched for coincidences using the published gamma ray energies ± 2 keV. We then measured the significance of the nominal 416 and 215 keV peaks, with the results shown in Tables 6.7 and 6.8.

Deciding what suppressed energy to use for the 416 keV coincidence is not as simple as taking the average. The ^{116m}In background to the 416 keV coincidences is stronger than the ^{75}Ge background to the 264 keV coincidences because the 417 keV gamma are always coincident with at least two other particles, making the three-crystal cut less effective. We therefore decided to allow the ^{116m}In to decay a bit. Based on Table 6.8, we would use a time cut of either 3 or 4 hours. Looking ahead to Table 6.10, we decided to use a three-hour time cut to measure the suppressed energy. The average of these centroids is (415.00 ± 0.42) keV. We used a simple average of the eleven centroid measurements of the 215 keV gamma: (213.62 ± 0.21) keV.

Table 6.5: Significance of the 367 keV peak using the energy-suppressed value of the 264 keV coincidence. The "264" keV coincidence was actually (262.81 ± 2) keV. The bold line indicates the time cut that results in the greatest peak significance. See text for further explanation.

Time cut (hours)	Centroid	Significance	Peak area	Background / bin
0	365.83	9.82 σ	61.53 ± 10.08	7.86
1	**365.81**	**10.34** σ	**58.68 ± 9.59**	**6.44**
2	365.80	10.11 σ	53.98 ± 9.12	5.70
3	365.78	9.45 σ	47.80 ± 8.58	5.12
4	365.58	8.28 σ	40.32 ± 8.04	4.74
5	365.70	7.94 σ	36.67 ± 7.73	4.27
6	365.76	9.11 σ	37.12 ± 7.43	3.32
7	365.63	8.72 σ	32.26 ± 6.88	2.74
8	365.68	7.81 σ	27.95 ± 6.47	2.56
9	365.48	5.71 σ	20.43 ± 5.73	2.56
10	365.51	4.70 σ	16.46 ± 5.28	2.45

Table 6.6: Significance of the 264 keV peak using the energy-suppressed value of the 367 keV coincidence. The "367" keV coincidence was actually (365.83 ± 2) keV. The bold line indicates the time cut that results in the greatest peak significance. See text for further explanation.

Time cut (hours)	Centroid	Significance	Peak area	Background / bin
0	262.86	9.01 σ	60.93 ± 10.19	9.15
1	262.75	8.74 σ	55.60 ± 9.70	8.09
2	262.81	8.88 σ	52.73 ± 9.32	7.05
3	**262.75**	**9.76** σ	**51.10 ± 8.84**	**5.48**
4	262.70	8.61 σ	44.39 ± 8.37	5.31
5	262.67	7.76 σ	38.46 ± 7.92	4.91
6	262.68	7.36 σ	35.51 ± 7.67	4.65
7	262.63	5.88 σ	27.70 ± 6.97	4.44
8	262.76	4.79 σ	21.97 ± 6.44	4.21
9	263.10	4.10 σ	17.05 ± 5.83	3.46
10	263.21	3.63 σ	14.28 ± 5.41	3.10

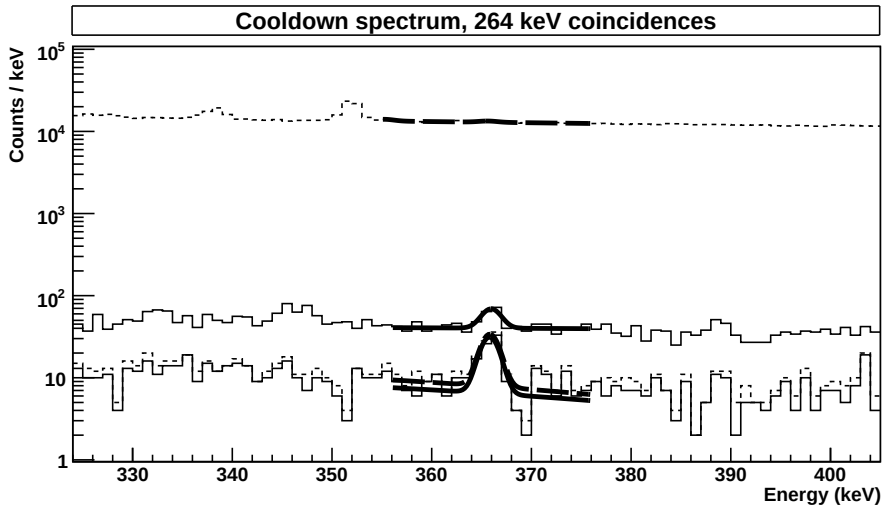

Figure 6.12: 367 keV region in the 264 keV coincidence spectrum. The significances of the peaks are 4.28 σ (upper dashed), 4.94 σ (middle solid), 9.82 σ (middle dashed), 10.34 σ (lower solid). See the text for details.

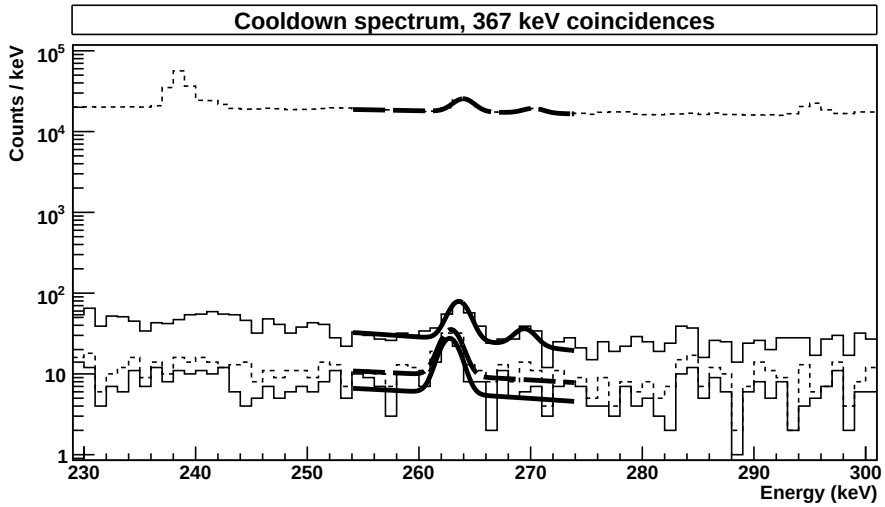

Figure 6.13: 264 keV region in the 367 keV coincidence spectrum. The significances of the peaks are 59.5 σ (upper dashed), 11.3 σ (middle solid), 9.01 σ (middle dashed), 9.76 σ (lower solid). See the text for details.

Table 6.7: Significance of the 416 keV peak using the published value of the 215 keV coincidence. We eliminated the first zero through ten hours from each individual decay data set. The bold line indicates the time cut that results in the greatest peak significance. See text for further explanation.

Time cut (hours)	Centroid	Significance	Peak area	Background / bin
0	**415.57**	**8.05** σ	**61.37 ± 10.78**	**11.63**
1	415.41	5.98 σ	41.78 ± 9.31	9.76
2	415.47	5.35 σ	35.22 ± 8.67	8.67
3	415.42	4.77 σ	30.45 ± 8.14	8.14
4	415.30	3.86 σ	23.58 ± 7.46	7.46
5	415.52	2.87 σ	16.73 ± 6.78	6.78
6	415.09	2.11 σ	11.78 ± 6.26	6.26
7	414.86	2.10 σ	11.60 ± 6.12	6.12
8	414.79	2.40 σ	13.12 ± 5.98	5.98
9	414.76	2.52 σ	13.42 ± 5.67	5.67
10	414.24	2.14 σ	11.09 ± 5.37	5.37

Table 6.8: Significance of the 215 keV peak using the published value of the 416 keV coincidence. We eliminated the first zero through ten hours from each individual decay data set. The bold line indicates the time cut that results in the greatest peak significance. See text for further explanation.

Time cut (hours)	Centroid	Significance	Peak area	Background / bin
0	213.86	5.73 σ	53.17 ± 11.19	17.22
1	213.81	7.12 σ	52.77 ± 9.99	10.99
2	213.74	6.94 σ	45.51 ± 9.06	8.60
3	213.76	7.77 σ	45.68 ± 8.69	6.92
4	**213.72**	**7.78** σ	**41.45 ± 8.08**	**5.67**
5	213.48	7.29 σ	36.48 ± 7.53	5.01
6	213.37	6.22 σ	28.94 ± 6.83	4.33
7	213.67	5.59 σ	24.66 ± 6.44	3.89
8	213.69	5.29 σ	22.58 ± 6.23	3.65
9	213.57	6.20 σ	23.96 ± 6.14	2.99
10	213.15	5.47 σ	19.80 ± 5.53	2.62

Coincidences with suppressed energies

Reanalyzing the data with the suppressed energies results in Tables 6.9 and 6.10. Here the effects of the 416 keV background from ^{116m}In are shown. There is no gamma line near 215 keV in the decay spectrum of ^{116m}In, so events from the decay of this isotope will only contribute to the background around 215 keV. By letting this very strong indium signal decay away, the background around the 215 keV peak is reduced faster than the peak area drops, increasing the peak's significance, with the maximum occurring at a time cut of three hours. Fig. 6.15 shows the raw (upper, dashed curve), 416 keV coincident (upper, solid curve), three-crystal cut (lower, dashed curve), and three-hour cut (lower, solid curve) spectra. For the sake of completeness, Fig. 6.14 shows the raw (upper, dashed), 215 keV coincident (solid curve), and three-crystal cut (lower, dashed curve) spectra. There is no time cut in Fig. 6.14 because all time cuts serve to reduce the significance of the peak.

Similar to the previous 264 / 367 keV coincidence, we do not use the 416 keV peak in the 215 keV coincidence spectrum to measure the efficiency of observing this ^{77}Ge decay. In this case it is because of the very strong ^{116m}In background. With a three-hour time cut, the total number of ^{77}Ge events is 197000 ± 49000. The area of the 215 keV peak was 50.04 ± 9.28 counts, giving an efficiency for observing this event of

$$\text{Efficiency for observing the } ^{77}\text{Ge 215 / 416 keV coincidence} = (0.0254 \pm 0.0079)\%. \qquad (6.4)$$

Table 6.9: Significance of the 416 keV peak using the suppressed value of the 215 keV coincidence. We eliminated the first zero through ten hours from each individual decay data set. The bold line indicates the time cut that results in the greatest peak significance. See text for further explanation.

Time cut (hours)	Centroid	Significance	Peak area	Background / bin
0	**415.43**	**13.37** σ	**94.29 ± 11.87**	**9.94**
1	415.25	10.54 σ	70.17 ± 10.57	8.87
2	415.25	9.83 σ	59.97 ± 9.69	7.44
3	415.23	9.70 σ	55.38 ± 9.21	6.52
4	415.18	8.64 σ	48.56 ± 8.80	6.32
5	415.30	6.93 σ	37.68 ± 8.01	5.92
6	414.95	6.17 σ	31.84 ± 7.56	5.33
7	415.02	5.53 σ	27.89 ± 7.15	5.09
8	414.96	5.40 σ	25.67 ± 6.86	4.52
9	414.91	6.09 σ	26.13 ± 6.65	3.68
10	414.58	5.70 σ	21.58 ± 6.00	2.87

Table 6.10: Significance of the 215 keV peak using the suppressed value of the 416 keV coincidence. We eliminated the first zero through ten hours from each individual decay data set. The bold line indicates the time cut that results in the greatest peak significance. See text for further explanation.

Time cut (hours)	Centroid	Significance	Peak area	Background / bin
0	213.80	6.10 σ	58.21 ± 11.65	18.23
1	213.83	7.11 σ	55.59 ± 10.40	12.24
2	213.83	7.42 σ	51.75 ± 9.69	9.73
3	**213.83**	**7.79** σ	**50.04 ± 9.28**	**8.25**
4	213.88	7.43 σ	44.35 ± 8.65	7.13
5	213.78	6.01 σ	33.75 ± 7.71	6.30
6	213.70	5.01 σ	26.71 ± 7.06	5.68
7	213.87	5.22 σ	26.13 ± 6.85	5.01
8	214.05	5.40 σ	25.23 ± 6.66	4.36
9	214.02	5.48 σ	24.50 ± 6.50	4.00
10	213.85	4.61 σ	19.13 ± 5.78	3.44

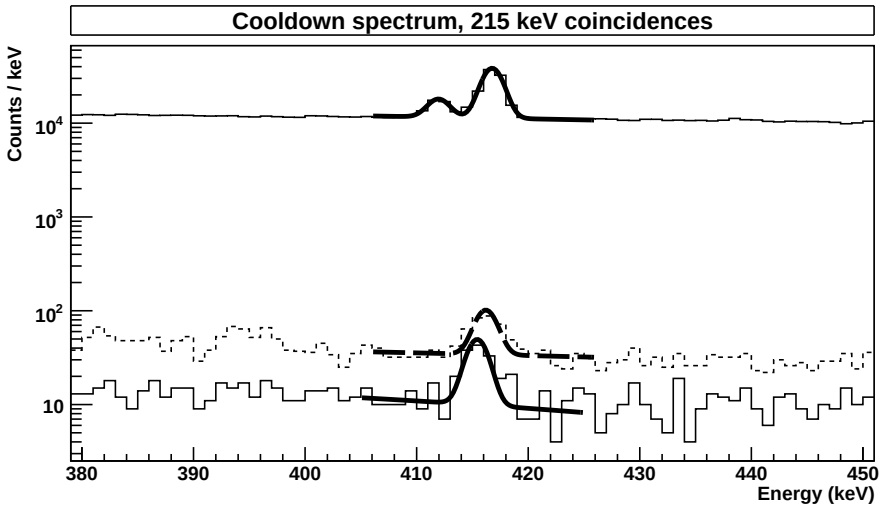

Figure 6.14: 416 keV region in the 215 keV coincidence spectrum. The significance of the peaks are 266.7 σ (top solid), 11.47 σ (middle, dashed), 13.37 σ (bottom solid). See text for details.

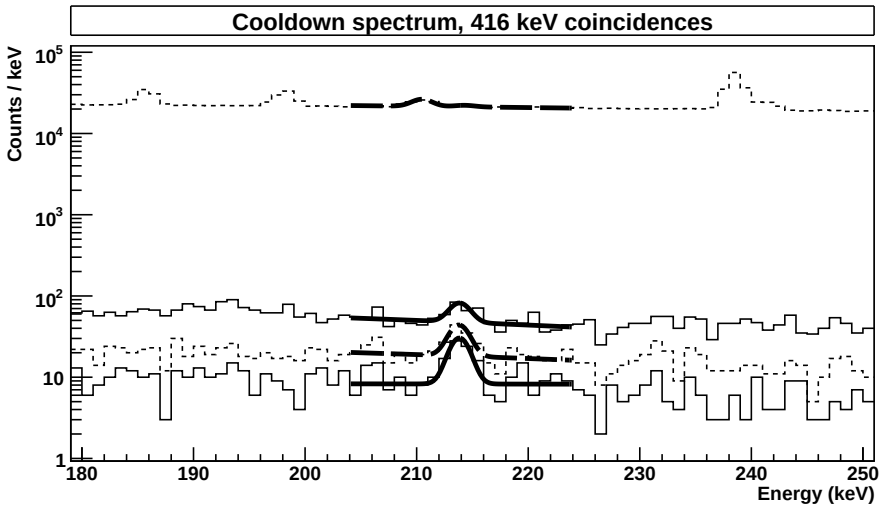

Figure 6.15: 215 keV region in the 416 keV coincidence spectrum. The significance of the peaks are 7.29 σ (upper dashed), 5.24 σ (upper solid), 6.10 σ (lower dashed), 7.79 σ (lower solid). See text for details.

Chapter 7

PERFORMANCE OF THE MAGE SIMULATION FRAMEWORK

With the efficiency for observing the triple coincidences from ^{77}Ge experimentally measured, what is the Monte Carlo prediction? To answer this question, we use the Monte Carlo simulation framework under development by both the Majorana [74] and GERDA [95] collaborations. This frameworks gets its name from the two collaborations, and is called MaGe.

7.1 MaGe: The Majorana/GERDA simulation package

MaGe is a Monte Carlo simulation framework based on the GEANT4 [93] simulation and ROOT [81] analysis packages. The framework utilizes the fact that GEANT4 and ROOT are written in C++, allowing for a powerful, extensible, and scalable object-oriented approach to the simulations. Given the similarities between the Majorana and GERDA experiments, the collaborations decided to avoid duplication of efforts and contribute mutually-useable code for physics processes and event generators while also allowing very simple control over detector-specific details.

The structure of MaGe consists of an overall "run manager" that handles the various subsystems in the framework. The basic structure is shown in Fig. 7.1. Where possible, C++ objects inherit from virtual objects to ensure compatibility with the existing structure. When the conventions are followed it is very easy to write a macro command file and run a previous simulation with a new detector or new output scheme. MaGe includes online help within the simulation that lists and describes the available options.

Code examples of the MaGe simulation framework can be found in Appendix D.

7.1.1 The database subsystem

The database within MaGe is based on the open-source relational database PostgresQL [94]. The primary database is maintained at Lawrence Berkeley National Laboratory, with regularly-updated local implementations running at other sites. Part of the goal behind MaGe was to make the simulation as scalable as possible. With an eye toward simulating a modular detector displaying great redundancy in design, the database acts as a repository for information about the specific parts of any given detector.

Take the CLOVER detector as an example. It is made up of four individual germanium crystals, each of which is very close, though not identical, in size. There is a separate database line for

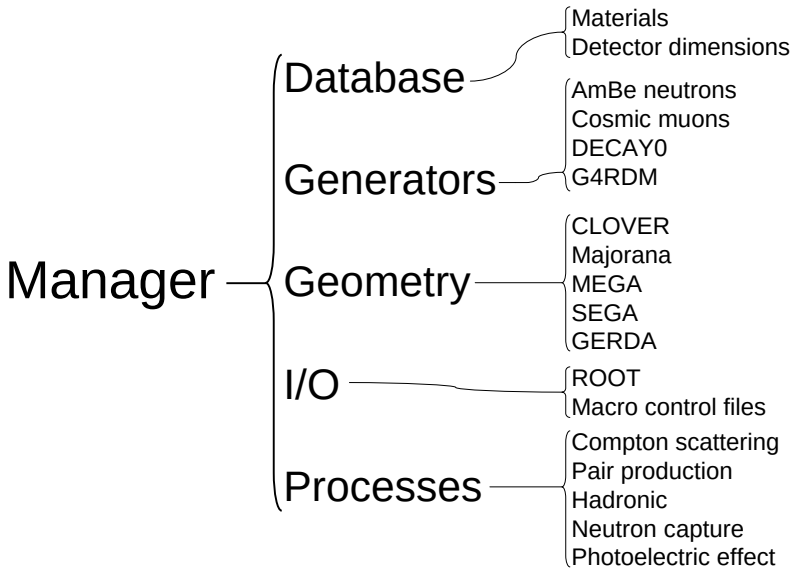

Figure 7.1: Structure of the MaGe framework. What is shown here is not a full list of the subsystem parts, but is simply representative of which subsystems govern which aspects of the simulation.

each individual crystal detailing its dimensions, dead layer thicknesses, and so on. The database is extendable, so we may add more information to the crystal database entries, such as crystal orientation for pulse shape processing, without disrupting legacy code or macro files.

There is a database entry for the CLOVER detector itself as well. This CLOVER entry includes not only the CLOVER dimensions, but the serial numbers of the individual crystals. If one of the actual crystals ever becomes damaged and a new crystal put in its place, no MaGe code would need to be rewritten or even recompiled to reflect this change. Rather, a database entry for the new crystal would be created, and the CLOVER's list of crystal serial numbers would be updated.

This database also contains materials information. A material in this case can be defined as either a single element with a specified A, Z, density, state, temperature, and pressure, or it can be built up of component isotopes. Building a material out of isotopes can allow for the creation of, for instance, polyethylene (comprised of H and C atoms) or germanium with various isotopic abundances. As currently envisioned, the Majorana experiment will be using crystals enriched to 86% ^{76}Ge, 14% ^{74}Ge, and trace amounts of other isotopes. If a new enrichment process is created by which the isotopic abundances change, only the database needs to be updated. As with the case of a swapped crystal, no MaGe code would need to be rewritten or recompiled.

There is no limit to the information that might be contained within the database. Some types of simulation control might be better handled by the macro file or a new C++ object, but use of the database can minimize the work necessary to run a new simulation, and that can improve the quality control of MaGe.

In addition, there may be future development of MaGe that would be greatly simplified by using a database. For instance, while GEANT4 has the ability to generate images of detector geometries, there may be a different visualization package the collaboration decides to use in the future. If the detector geometry were hardcoded into MaGe, those values would have to be manually extracted and re-entered in the visualization package. If there were a alteration to the geometry, changes would have to be made in multiple locations, increasing the risk of errors being made. As it is, a single change made in the database will be reflected in subsequent simulations, the visualization, and any other future packages.

7.1.2 The generators subsystem

Within MaGe, the generator is that part of the code that creates primary particles with an energy and initial direction. The starting location of those primary particles is specified next, and the particles are then handed off to other GEANT4 code for transport and interaction. The generators included in the MaGe simulation are drawn from a number of sources. The macro file contains the command that specifies which generator is used. MaGe uses generators distributed as part of GEANT4, generators developed by the collaboration, and generators developed by third parties. In this section we give an example of each.

The GEANT4 Radioactive Decay Manager (G4RDM)

The G4RDM is distributed as part of the GEANT4 package, and creates alphas, betas, and gammas in proportions and energies based on the Evaluated Nuclear Structure Data File (ENSDF) database [96]. ENSDF is updated on a continual basis, and as of February 17^{th}, 2006, it contained 15641 datasets for 2979 nuclides.

In the G4RDM, an isotope is placed at a specific location with an initial momentum. That isotope is allowed to propagate and, if unstable, to decay to progeny specified in ENSDF. The progeny are also propagated and allowed to decay. Thus the G4RDM is very useful when simulating the backgrounds from decay chains, such as ^{238}U and ^{232}Th.

The AmBe neutron generator

The MaGe development team built a generator for neutrons produced by an americium-berilliyum (AmBe) source. To build this generator, an experimentally-measured spectrum of AmBe neutrons

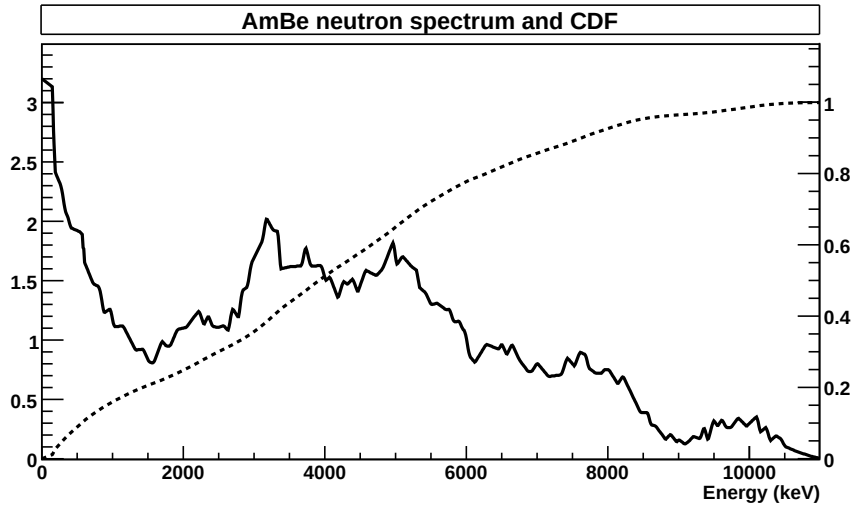

Figure 7.2: Spectrum and CDF of AmBe neutrons. The CDF (dotted line) was created from the normalized spectrum. The CDF uses the vertical scale on the right side. The spectrum (solid line) is the same as that shown in Fig. 5.6. AmBe neutron spectrum from Marsh *et al.* [86].

was digitized and normalized, and a cumulative distribution function (CDF) created from the normalized spectrum. Fig. 7.2 shows the normalized spectrum and CDF.

To select a neutron energy in the AmBe generator, a random number is generated uniform between 0 and 1. A linear interpolation between consecutive energy values corresponding to the CDF values immediately below and above the random number is performed, and the result is used as the energy of the generated neutron. The initial direction of an AmBe neutron is random.

Decay0

The Decay0 [97] generator was created by Ponkratenko, Tretyak, and Zdesenko, and is used to create double-beta decay events of any of 21 isotopes. Decays of ^{76}Ge may proceed to the 0^+_0 (i.e., ground) state, or the excited 2^+_1, 0^+_1, or 2^+_2 states of ^{76}Se. If the decay is to an excited state, Decay0 will also generate the cascade gammas. The energies of the beta particles are calculated separately. Decay0 then creates a table of events with particle type, initial 3-momentum, and time since previous particle emission. These Decay0 events were written to a file, which MaGe then parses to instantiate the event.

7.1.3 Positioning the primary particles

Once the primary particles were identified, they had to be placed into the simulation. This was done in several ways, depending on the simulation. For instance, simulating a radioactive source would require all the primary particles be generated at a specific point. Calculating the effects of contamination spread homogeneously throughout a specific part would require a volume "position sampler" that randomly distributes events evenly throughout a defined volume. Using a collomated source or a laser would require the primary particles be distributed in a narrow opening cone from a single source. Finally, to allow for contaminants that drift onto the various parts of the actual detector, there is a separate "surface sampler" that returns the coordinates on the surfaces of the detector objects.

Thus depending on the situation, primary particles can be positioned anywhere and with any initial direction as specified by the actual physical setup that is being simulated.

7.1.4 The geometry subsystem

As explained in Section 7.1.1, detector dimensions and materials are stored in the database. The geometry subsystem reads in those values and builds the detector, referencing the parameter names virtually exclusively. This is what allows a detector parts to be "swapped out" in the simulation without requiring a recompile. An example of how a detector is built within MaGe is shown in Appendix D.2.

7.1.5 The I/O subsystem

Simulation control is provided via a macro input file, and the G4Messenger class is used to read in those macro command lines. The G4Messenger class provides a framework so that any class within GEANT4 (geometry, generators, physics processes, and so on) can be controlled without a recompilation. A typical macro file is shown with explanation in Appendix D.3.

Anticipating using the ROOT framework to analyze both the simulation and experimental data, MaGe outputs the results into tree objects in ROOT-formatted files. The output files are, unsurprisingly, inherently connected to the detector geometry. A separate ROOT output scheme must therefore be defined for every distinct detector geometry class, although object-oriented programming allows for code re-use. Different output schemes can store varying levels of information. For example, with the CLOVER detector the total energy deposited in a crystal may be recorded, or every individual energy deposition within a crystal may be recorded for offline segmentation or pulse shape analysis. Each output scheme is available at run time via the macro command file.

7.1.6 The processes subsystem

The final complex subsystem within MaGe is the processes subsystem, also known as the "physics lists", which is based on the code distributed as part of GEANT4. The processes allow for various kind of physical interactions. For example, gamma rays may interact via, among other processes, Compton or Rayleigh scattering, photoelectric effect, e^+e^- conversion, and so on.

Most of the anticipated radiation in the Majorana and GERDA experimental halls comes from nuclear decays. The simulation therefore includes the ability to handle alphas, betas, and gammas from the lower limit of GEANT4 electromagnetic interaction energy (250 eV) up to roughly 10 MeV. At the same time, cosmic rays can create backgrounds in the $0\nu\beta\beta$ region of interest, and spallation neutrons may be absorbed by stable nuclei, emitting prompt gammas and inducing further decays in the now-unstable nucleus. The Majorana and GERDA experiments therefore also have to be able to simulate the effects of muons up to 1 TeV in energy, as well as neutrons from thermal energies up to 1 GeV.

These wide ranges of energies, particles, and interactions call for a very comprehensive physics lists. The MaGe process list therefore draws on two lists that are distributed with the GEANT4 package: the underground physics list and the QGSP_HP hadronic physics list. The former list is intended primarily for low-background experiments, as it is comprised of separate low-energy[1] models for electromagnetic interactions. The QGSP list is used for high-energy penetration shielding, and is therefore suited to simulating cosmic rays. The QGSP_HP list is a high-precision version of the QGSP list that uses data tables for neutron interactions from thermal energies up to about 20 MeV. These neutron data tables are also available from the GEANT4 collaboration web pages. These two lists were merged line by line to create a single list that contained all the interactions present in both lists.

Even when performing high-precision simulations, however, it makes no sense to simulate events down to the keV energies in, for instance, the bulk of a lead shield. The lead is not instrumented, and as long as the simulation correctly predicts the energy attenuation of various particles going through the lead shield, we are not so concerned with where precisely in the lead shield the particles lost their energy. MaGe uses GEANT4's ability to set what is known as the "energy cutoff" to different values depending on what volume a particle is traveling through. The energy cutoff is the energy below which secondary particles are not created. The energy cutoff can be set separately for different particles and detector regions.

The energy cutoff is actually set as a length, which is equal to the attenuation length of a particle with a specific energy moving through a specific medium. As may be obvious, there is no single equation that transforms the cutoff length to an energy, as it depends on what physics processes are

[1] "Low-energy" in this case means between 250 eV and 3 GeV.

included in the simulation. For the MaGe physics list, Table 7.1 shows the equivalent energies for various particles traversing various materials. In certain situations, secondary particles are created even if the parent particle was below the cutoff energy. One such situation is if the particle is within the cutoff length of a material boundary, as there may be an active volume on the other side of that boundary. Another situation is if the particle can decay or be captured, creating other particles with energy that may be above the cutoff, e.g., positrons may have a kinetic energy below the cutoff, but when they annihilate the resulting gammas may be above the cutoff length; in this case, the positrons are still created.

We still have to decide what cutoff length to use. In germanium, a 1 MeV beta particle will travel on the order of 1 mm. We therefore decide to set the cutoff length to an order of magnitude than this typical beta track length, or 100 μm.

Table 7.1: Energy cutoff values in MaGe. The cutoff parameter is set as a length, which is then converted to an energy for any combination of particle and material. The cutoff energy is the energy below which secondary particles are not created. In this example, the cutoff length was set to 100 μm for all three particles. Energies are in keV.

Particle	Vacuum	Air	Aluminum	Germanium	Indium	Gold
Gamma	0.990	0.990	2.3	5.9	11.1	40.3
Electron	0.990	0.990	129.7	172.1	199.5	347.1
Positron	0.990	0.990	128.1	167.9	192.3	334.6

7.2 The MaGe CLOVER Detector

The LANL CLOVER geometry was entered into the MaGe simulation. Many of the construction details come from the manufacturer, including the specific crystal dimensions, the cryostat dimensions, the characteristics of the crystal dead layers, and the material used for the inner contacts. Unfortunately, there are also proprietary engineering specifications that the manufacturer will not divulge. One such detail is the shape of the cold plates, although the material is known to be aluminum and the thickness 1 cm. Another missing detail is the method by which the crystals are held together. Fig. 7.3 shows the CLOVER crystals as programmed into MaGe. Visible are the crystals, crystal separator, and coldplates.

7.2.1 ^{77}Ge coincidence simulations

To simulate the CLOVER response to ^{77}Ge decays, the G4RDM event generator and volume position sampler were used to homogeneously distribute ^{77}Ge decays throughout crystal 1. Fig. 7.4

Table 7.2: ^{77}Ge simulation coincidence results. The top line of each of the four sections shows the area and significance of the coincidence energy in the raw spectrum. The middle line of each section shows the same values but with the coincidence applied. The bottom line of each section shows the area and significance of the coincidence peak when requiring exactly three crystals register energy deposition.

Coincidence	Curve	Coin. energy	Area	BG / bin	Sig. (σ)	Efficiency
264 keV	Raw	367.4	49912 ± 275	5112	312	
	264 keV coin.	367.5	2061 ± 51	104	90.4	
	3-crystal	367.5	1958 ± 47	42	135	0.0196(5)%
367 keV	Raw	264.4	219395 ± 505	6219	1244	
	367 keV coin.	264.4	2360 ± 51	33	184	
	3-crystal	264.4	2045 ± 47	20	205	0.0205(5)%
215 keV	Raw	416.3	73748 ± 323	4955	469	
	215 keV coin.	416.3	2932 ± 57	60	169	
	3-crystal	416.3	2705 ± 53	23	252	0.0271(5)%
416 keV	Raw	215.5	109244 ± 389	8518	529	
	416 keV coin.	215.5	2928 ± 57	52	182	
	3-crystal	215.5	2638 ± 53	31	212	0.0264(5)%

shows the detector response in the four crystals.

With the ^{77}Ge events simulated, we calculated the area and significance of the coincidences that were measured in the experimental data at the end of Section 6.4. Figs. 7.5 through 7.8 show the 264 keV, 367 keV, 215 keV, and 416 keV coincidences, respectively. The area and significance of the Gaussian peaks, along with the background under the peaks, are shown in Table 7.2.

7.2.2 Comparison to experiment

In the previous chapter, we measured the experimental efficiency of observing a triple coincidence of ^{77}Ge. There were two possible decay chains to analyze. One chain involved a triple coincidence between a beta particle and two gammas at 264 and 367 keV (observation efficiency (0.0229 ± 0.0069)%, see Eq. (6.3)). The other chain involved a triple coincidence between a beta particle and two gammas at 215 and 416 keV (observation efficiency (0.0254 ± 0.0079)%, see Eq. (6.4)).

Using MaGe, we predicted efficiencies of (0.0196 ± 0.0005)% and (0.0264 ± 0.0005)%. By taking ratios of the experimental and simulation efficiencies, we may evaluate the accuracy of the simulation. We have the following ratio for the 264 / 367 coincidence:

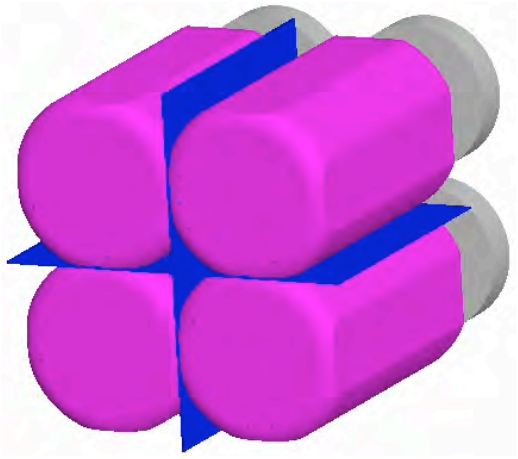

Figure 7.3: The MaGe CLOVER. The germanium crystals are shown in purple, the crystal separator in blue, and the coldplates in grey.

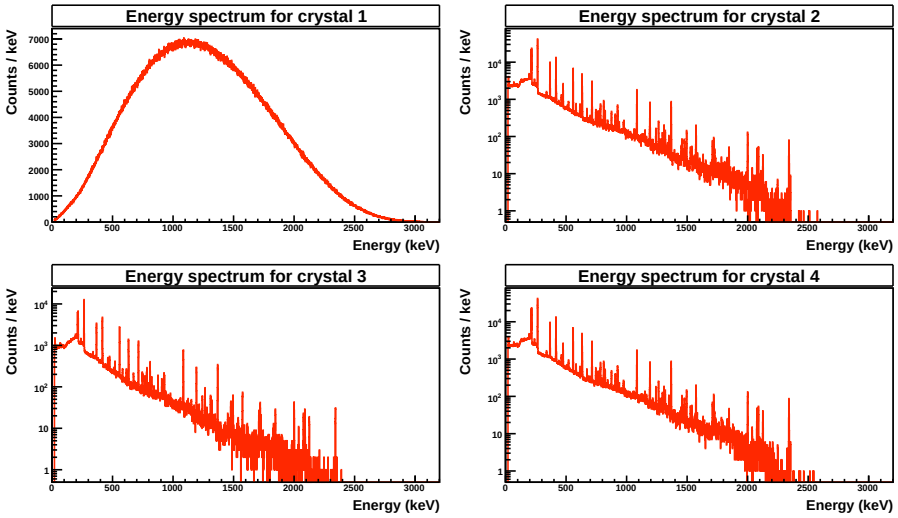

Figure 7.4: ^{77}Ge simulated events. 10 million events were simulated in the MaGe CLOVER, with events evenly distributed throughout crystal 1. The range of the simulated data was chosen to match that of the CLOVER detector DAQ software. The spectrum in crystal 1 is smooth because the energy of the beta particle, which has a smooth spectrum, was always added to any energy deposited by any gamma rays, washing out any sharply-defined features in the final spectrum of crystal 1. The sharp lines seen in crystals 2, 3, and 4 are listed in Table A.1.

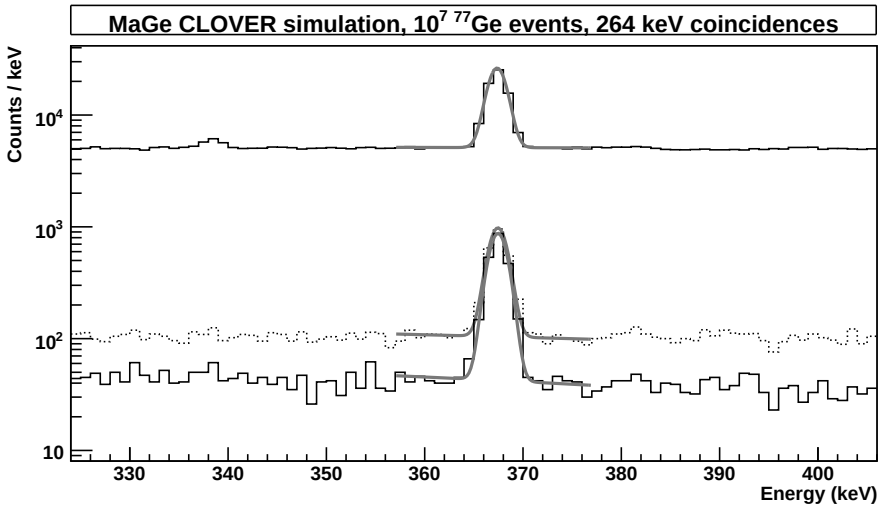

Figure 7.5: 264 keV coincidence simulation curves. The top solid line is the raw spectrum, the center, dotted line is with 264 keV coincidences, and the bottom solid line adds a 3-crystal cut to the coincidence cut. Compare to Fig. 6.12.

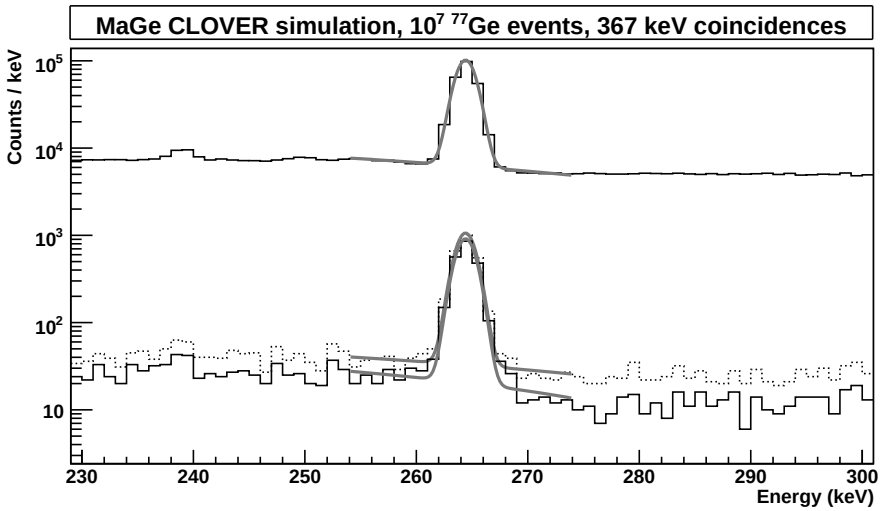

Figure 7.6: 367 keV coincidence simulation curves. The top solid line is the raw spectrum, the center, dotted line is with 367 keV coincidences, and the bottom solid line adds a 3-crystal cut to the coincidence cut. Compare to Fig. 6.13.

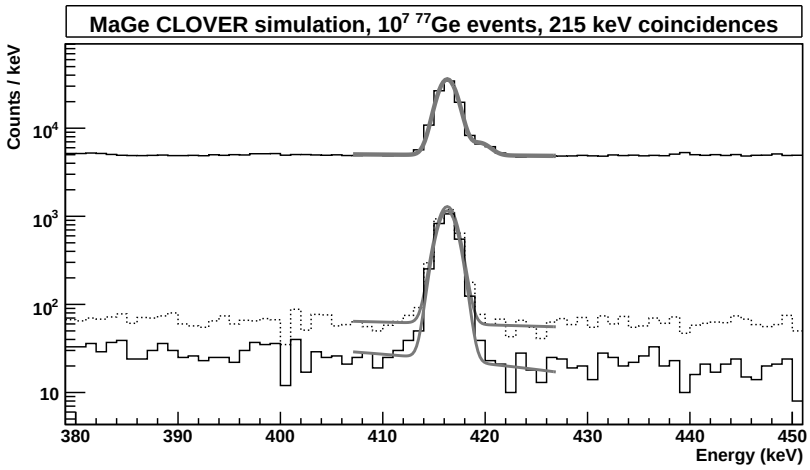

Figure 7.7: 215 keV coincidence simulation curves. The top solid line is the raw spectrum, the center, dotted line is with 215 keV coincidences, and the bottom solid line adds a 3-crystal cut to the coincidence cut. Compare to Fig. 6.14. In the top curve, there are two lines present at 416.3 and 419.8 keV.

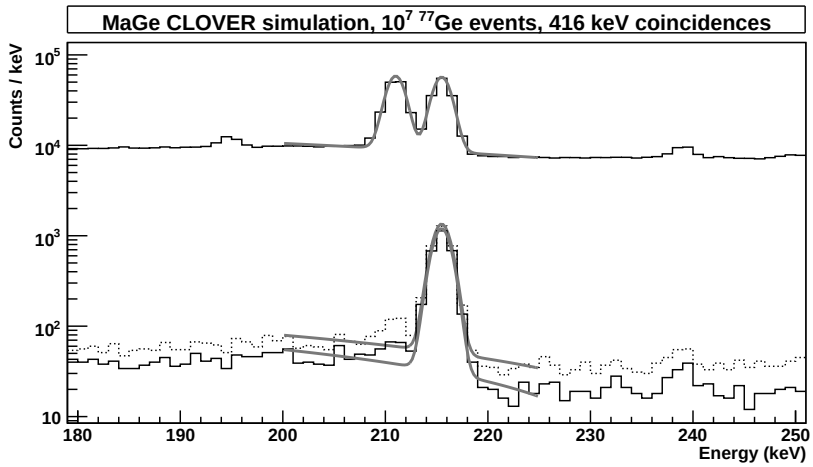

Figure 7.8: 416 keV coincidence simulation curves. The top solid line is the raw spectrum, the center, dotted line is with 416 keV coincidences, and the bottom solid line adds a 3-crystal cut to the coincidence cut. Compare to Fig. 6.15. There are two strong peaks in the top curve because both 211 and 215 keV gamma rays are strong lines in the ^{77}Ge spectrum (see Table A.1).

Table 7.3: ^{77}Ge coincidence uncertainty details. If we took six times as much data, the uncertainty in the experimental peak areas would drop to around 5%, but before then the uncertainties would be dominated by the thermal neutron capture cross sections and natural abundances uncertainties. Where two numbers are reported separated by a comma, the first number refers to the 264 / 367 keV coincidence, and the second to the 215 / 416 keV coincidence.

Source	Uncertainty	Totals
α_{ICC}	3%	Systematic: 27.0%
^{74}Ge $\rightarrow$ ^{75m}Ge cross section	17.6%	
^{76}Ge $\rightarrow$ ^{77}Ge cross section	10.0%	
^{76}Ge $\rightarrow$ ^{77m}Ge cross section	16.7%	
^{74}Ge natural abundance	2.0%	
^{76}Ge natural abundance	5.0%	
140 keV peak intensity (exp.)	1.2 – 3.1%	Statistical: 17%, 19%
Coincidence peak areas (exp.)	16%, 19%	
Coincidence peak areas (sim.)	2.6%, 1.9%	

$$\begin{aligned}\text{Ratio} &= \frac{\text{measured efficiency for 264 / 367 keV coincidence}}{\text{simulated efficiency for 264 / 367 keV coincidence}} \\ &= \frac{0.0229 \pm 0.0069}{0.0196 \pm 0.0005} \qquad (7.1) \\ &= 1.17 \pm 0.35 \qquad (7.2)\end{aligned}$$

The experimental and simulation results are separated by 0.49σ. As for the 215 / 416 coincidence, we have

$$\begin{aligned}\text{Ratio} &= \frac{\text{measured efficiency for 215 / 416 keV coincidence}}{\text{simulated efficiency for 215 / 416 keV coincidence}} \\ &= \frac{0.0254 \pm 0.0079}{0.0264 \pm 0.0005} \qquad (7.3) \\ &= 0.96 \pm 0.30 \qquad (7.4)\end{aligned}$$

In this second coincidence the ratio between experimental and simulation results is only 0.13σ from unity.

7.3 Evaluation of simulation

We conclude the MaGe simulation is an accurate representation of the CLOVER detector. With these results, we may use MaGe to predict the efficiency of a Majorana module to an ES2$\nu\beta\beta$ decay from ^{76}Ge with confidence in obtaining results to within 1σ.

With the experimental and simulation results compared, we show a breakdown of the sources of uncertainty in the ratios in Table 7.3. From this table we see that the uncertainty is dominated by the systematics. To reduce the systematic uncertainty would require more accurate measurements of the thermal neutron capture cross sections of ^{74}Ge and ^{76}Ge.

Chapter 8

APPLYING MAGE TO THE MAJORANA EXPERIMENT

The MaGe simulation framework is applied to a 60 kg Majorana module. The simulations not only provide measurements of signal sensitivity, but measurements of background levels as well. While MaGe must eventually incorporate every observable form of electromagnetic, muon, and hadronic interactions, this chapter focuses only on electromagnetic interactions, and backgrounds due to nuclear decay.

8.1 The Majorana Detector

Before describing the simulations of the Majorana detector, we describe the detector itself. A basic description of the Majorana experiment was provided at the end of Chapter 1, and here we go into a bit more detail.

Since Klapdor-Kleingrothaus *et al.* published a claim of observation for $0\nu\beta\beta$ decay of ^{76}Ge [48] [55], it behooves any germanium-based search for $0\nu\beta\beta$ decay to verify or refute the measurement. In light of this, the stated goals of the Majorana experiment are to:

1. Probe the quasi-degenerate neutrino mass region above 100 meV.
2. Demonstrate that backgrounds, at or below 1 count/ton/year in the $0\nu\beta\beta$-decay peak 4-keV region of interest (1 count/ROI/t-y), can be achieved that would justify scaling up to a 1 ton or larger mass detector.
3. Definitively test the Klapdor-Kleingrothaus claim to have observed $0\nu\beta\beta$ decay in ^{76}Ge in the mass region around 400 meV.

Taken together, these goals drove the design of the detector array. It had to have an adequate active mass, as well as be modular so that if the background reduction can be demonstrated, scaling to a larger experiment is "simply" a matter of constructing more modules. Majorana is proposed as a 1-, 2-, or 3-module experiment, with each module being approximately 60 kg of germanium, enriched to 86% ^{76}Ge. Fig. 8.1 shows a cutaway view of the 2-module design inside a shield. Figs. 8.2 show the crystal arrangement inside a module. The crystals measure 7 cm high and 6.2 cm in diameter, with a hollow core 6 cm high and 0.8 cm in diameter. The crystals may be segmented to allow for greater distinction between multi-site and single-site events. The exact segmentation scheme is not yet decided upon, but the highest degree of segmentation under consideration is 6 ϕ

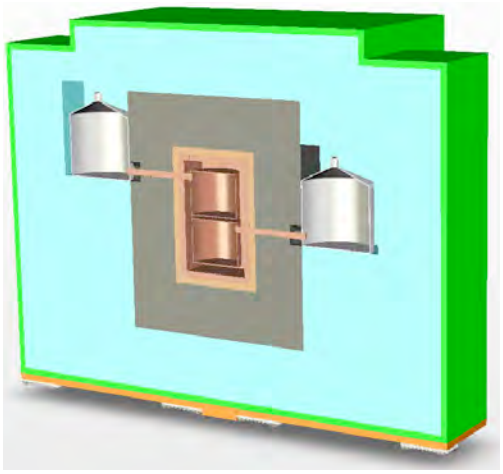

Figure 8.1: Potential 2-module design of the Majorana detector. This design is modular to allow for the inclusion of additional active mass. Each module in this design contains 19 columns of three crystals, each 1.1 kg. The total mass is roughly 120 kg, 86% of which is ^{76}Ge. The final apparatus will stand between two and three meters high.

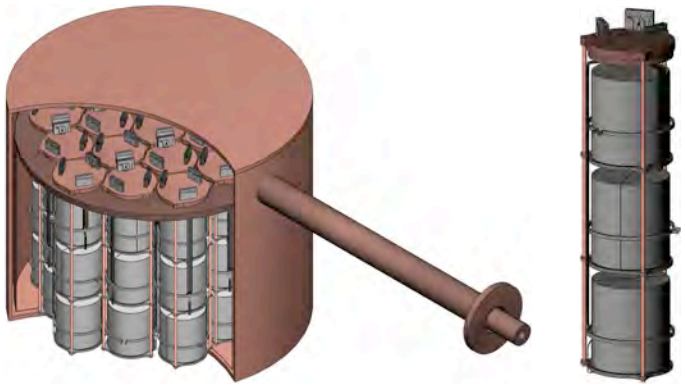

(a) M120 module (b) M120 string

Figure 8.2: Single Majorana module and string. These renderings show the 19 columns of three-crystal strings as well as the cryostat, coldplates, and coldfinger. The three front end electronic boards at the top of each string are held by the ”stringer lid”, from which the crystals also hang. Each string is supported by the ”stringer mount plate”.

segments ("pie wedges") × 6 z segments ("hockey pucks"). Fig. 8.3 shows some of the possible segmentation schemes.

The background reduction techniques of germanium detectors has improved since the Heidelberg-Moscow experiment. These techniques include radiologically cleaner electroforming of copper parts, better materials screening, reducing cosmogenic activation by fabricating the detector components deep underground, segmentation, and improved pulse shape discrimination. If Majorana is able to achieve the background reduction goals, and Klapdor-Kleingrothaus *et al.* accurately measured the $0\nu\beta\beta$ half life of ^{76}Ge, the double-beta signal as seen by a 2-module detector will be very strong. Fig. 8.4 shows the size of the predicted peak after 4.5 years of running. The proposed detector is sensitive enough to confirm the signal reported by Klapdor-Kleingrothaus *et al.* [55].

8.2 Excited state double-beta decay sensitivity

The sensitivity of a Majorana module detector to excited state $2\nu\beta\beta$ decays depends directly on the efficiency for observing the decay. Given the modularity of the design, the efficiency is calculated using Monte Carlo techniques for an individual 57-crystal module. This provides a conservative estimate on the efficiency of observing the decays, as running two modules in tandem can only increase the efficiency.

8.2.1 Calculating the Majorana module ES$2\nu\beta\beta$ efficiency

A geometry of a Majorana module was entered into the MaGe simulation, and a visualization of the simulation geometry is shown in Fig. 8.5. To calculate the ES$2\nu\beta\beta$ efficiency, we used the DECAY0 event generator, based on the DECAY4 code [97]. DECAY0 uses the ENSDF [96] data tables to obtain endpoint and cascade gamma energies as well as determine relative angles between the decay particles. It allows for double-beta decay in various modes, including either zero or non-zero neutrino mass, right-handed currents, and decays to 0^+ and 2^+ states of the final nucleus. The beta spectra incorporate the Fermi function. Fig. 8.6 shows the spectra of the individual beta particles in the ES$\beta\beta$ decay of ^{76}Ge as well as the summed beta energy for ES$2\nu\beta\beta$ decays. A trial simulation with 10,000 events homogeneously distributed through crystal L0C1 was run, and the location of energy depositions recorded. Fig. 8.7 is a projection of the hit locations onto the XY-plane.

The signal observation efficiency was calculated for each unique crystal location in a module, of which there are twelve[1]. For each of these twelve crystals 1 million DECAY0 ES$2\nu\beta\beta$ events were generated. The results of the analysis were then averaged over the the 12 unique positions, weighted by that position's multiplicity. That is to say, the efficiency of the total detector was determined using the equation

[1]There are four unique crystal positions (e.g., crystals 0, 1, 7, and 8) in each of three layers.

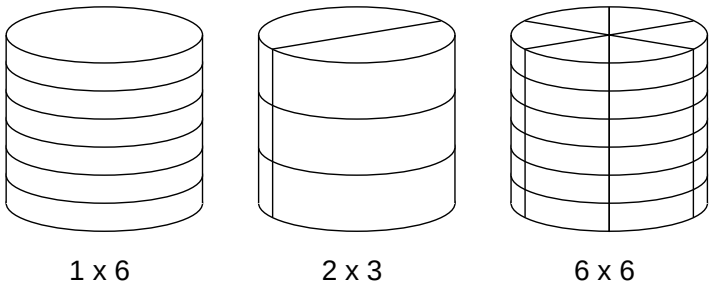

Figure 8.3: Possible Majorana crystal segmentation schemes. The segmentation increases detector granularity, which helps to distinguish multi-site from single-site events.

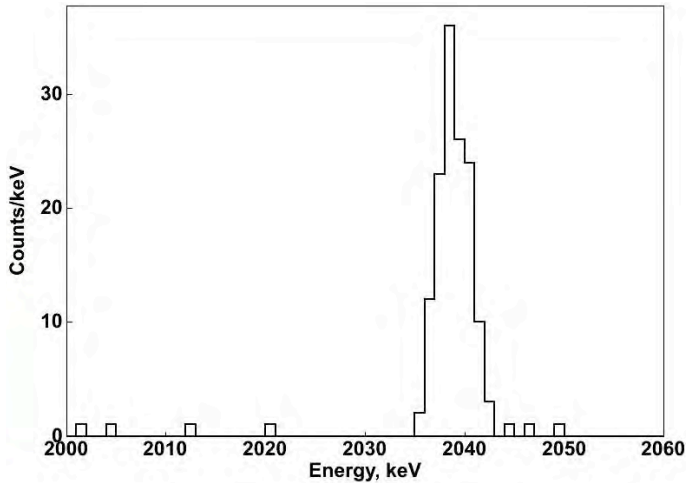

Figure 8.4: Predicted Majorana $0\nu\beta\beta$ signal assuming $T^{0\nu}_{1/2} = 1.19 \times 10^{25}$ years. (this half life is the value observed by Klapdor-Kleingrothaus *et al.* [55]). This figure represents the signal from two 60-kg Majorana modules running for 4.5 years. The graph shown is the simulated spectrum after analysis cuts.

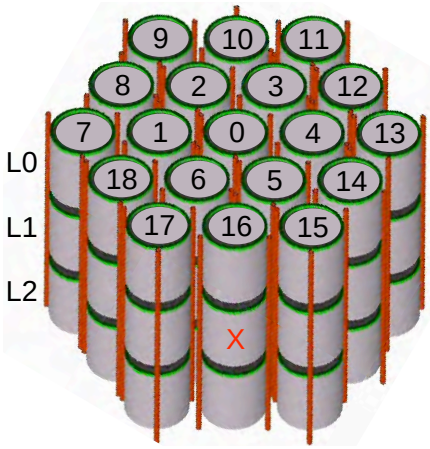

Figure 8.5: MaGe geometry of Majorana module. The crystals, crystal plates, and side copper support rods are visible. The support structure, cryostat, and front-end electronics boards are present in the simulation but omitted in this figure for clarity. The crystals can be uniquely identified by the number and layer, e.g., L1C16 is the center crystal in the front face of the hexagon, middle layer (marked with a red X). Compare to Fig. 8.2(a).

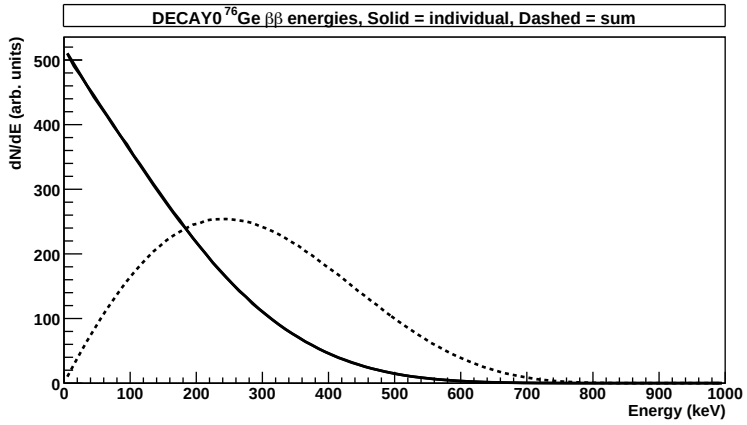

Figure 8.6: DECAY0 beta spectra. The solid curve is for a single beta particle, and the dashed curve is the sum energy. The endpoint energy is 917 keV. The strong effects of the Fermi function are seen in the relatively high probability in the low-energy range of the single-beta spectrum. Compare the solid curves to Fig. 2.3.

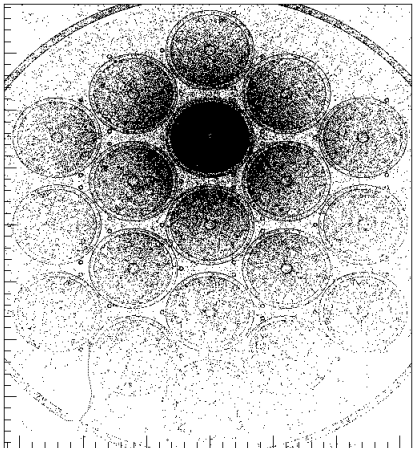

Figure 8.7: Energy depositions in a Majorana module. This figure shows a projection onto the XY-plane of all energy depositions resulting from 10,000 ES2$\nu\beta\beta$ decays spread homogenously throughout crystal L0C1. Hits are visible on the crystals, crystal plates, copper support tubes, and cryostat wall. The scales on both axes are in centimeters.

$$\text{Total module efficency} = \frac{1}{57}\left(\sum_{x} \text{Efficiency from crystals LxC0} + 6 \times \sum_{x,y} \text{Efficiency from crystals LxCy}\right) \tag{8.1}$$

where x takes on the values 0, 1, and 2, and y takes on the values 1, 7, and 8.

There are two ways we can look for excited-state decays. One is by taking advantage of the triple coincidence and requiring a "strict" three-crystal (or three-segment) cut, as was done in the case of ^{77}Ge in Chapter 6. In this strict analysis, we require that one crystal or segment have an energy deposition of 559 ± 2 keV and another a deposition of 563 ± 2 keV. The third energy deposition is presumably the energy from the beta particle, and is therefore allowed to range up to 917 keV.

A second analysis method involves relaxing the requirement that exactly three crystals or segments be hit, and performing the analysis based solely on the amount of energy deposited (this method will be referred to as the "relaxed" analysis). For an ES2$\nu\beta\beta$ decay wholly contained within the detector, the total energy will of course fall along a spectrum from 1122 to 2039 keV. We can take advantage of the fact that the two beta particles are unlikely to leave the crystal or segment in which the decay occurred by systematically removing the energy from one crystal or other from the

Table 8.1: ES2$\nu\beta\beta$ observation efficiency. For this analysis, n-hit was required to be exactly 3. The unsegmented scheme is here referred to as "1×1" segmentation.

Segmentation	Strict analysis	Relaxed analysis
1×1	0.916(10)%	2.39(2)%
2×3	0.945(10)%	7.29(3)%
6×6	0.575(6)%	12.18(3)%

total. If the remaining energy adds to 1122 keV, we interpret that event as an ES2$\nu\beta\beta$ decay. This method can of course be expanded to a segmented analysis.

Because the segmentation scheme has not yet been decided upon, we perform the analysis on three segmentation schemes. One scheme assumes no segmentation (or 1×1 segmentation), one scheme assumes a modest segmentation of 2×3, and the last scheme assumes the highest segmentation under consideration, 6×6.

In hopes of improving the signal-to-background ratio, we may apply a further cut in the relaxed analysis by requiring a minimum number of crystals or segments to register an energy deposition (referred to from now on as "n-hit"). Fig. 8.8 shows an n-hit histogram for the events that passed the relaxed analysis cut described in the previous paragraph. This graph was created by generating an n-hit histogram for each of the 12 unique crystals, then weighting the results by the crystal multiplicity. By requiring an n-hit lower limit of 3 all the segmentation schemes, we will eliminate 10% of events from the unsegmented scheme, 2% from the 2×3 segmentation, and 0.3% from the 6×6 segmentation scheme. The usefulness of this cut can only be discussed with a Monte Carlo analysis of both the signal efficiency and the background levels. We will revisit this issue in the next Section.

With all of the strict and relaxed analysis cuts in place, we can calculate the efficiency of observing an excited-state two-neutrino double-beta decay using a single Majorana module. Table 8.1 shows the efficiencies in the 1×1 (i.e., unsegmented), 2×3, and 6×6 segmentation schemes in both the strict and relaxed analyses.

We might wonder why the strict analysis efficiency for 2×3 segmentation is not appreciably greater than that of an unsegmented crystal. There are two competing effects at work. On the one hand, the smaller the segments, the more likely the gamma rays are to escape the segment in which the decay occurred. On the other hand, the smaller the segments, the less likely it is that the gamma rays will deposit their full energy in a single segment. There will therefore be a segmentation scheme that will optimize the efficiency for the strict analysis, and given the fact that the 1×1 and 2×3 segmentation schemes provide efficiencies relatively close together compared to that of the 6×6 scheme, we can expect a relatively modest scheme would optimize the efficiency.

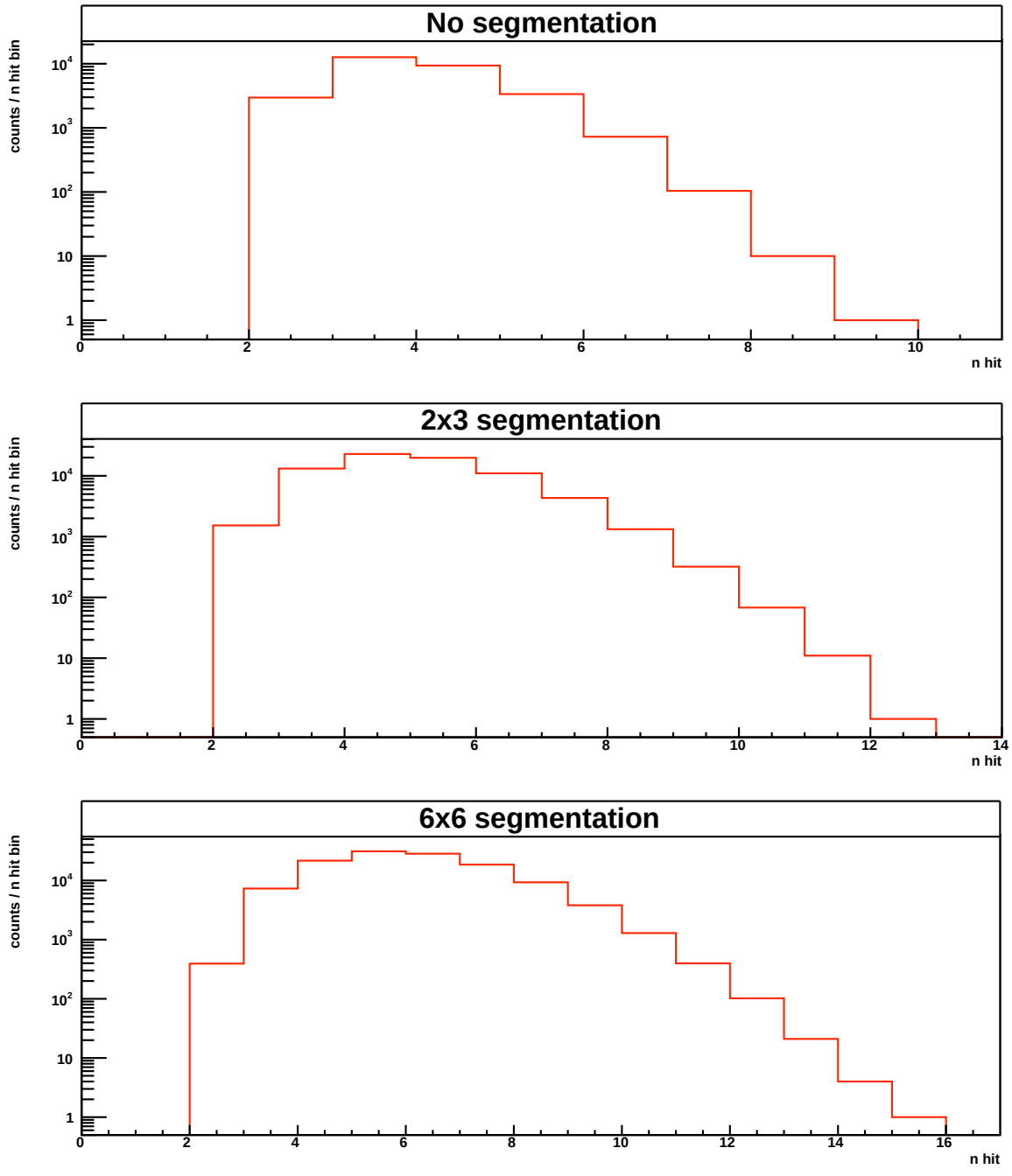

Figure 8.8: N-hit in the relaxed ES2$\nu\beta\beta$ analysis. If a lower limit on n-hit of 3 is required for each segmentation scheme, we will eliminate 10% from the no-segmentation, 2% from the 2×3-segmentation, and 0.3% from the 6×6-segmentation schemes.

Table 8.2: ES2$\nu\beta\beta$ false positives rate. The reported numbers are the rate of false positives as a proportion of the total events that pass the analysis cuts.

Segmentation	Strict analysis	Relaxed analysis
1×1	3.6(2)%	9.5(2)%
2×3	2.2(2)%	5.8(1)%
6×6	1.8(2)%	5.3(1)%

For the relaxed analysis, the higher the degree of segmentation the higher the observation efficiency, as the primary consideration is whether the gamma rays will escape the segment in which the decay occurred. The gamma rays are not required to deposit full energy in a single segment, though, for the relaxed analysis to interpret the event as an ES2$\nu\beta\beta$ decay.

We have a caveat regarding the analyses. It may be possible in both the strict and relaxed analyses to observe a false positive. In the case of the strict analysis, it is possible for the beta particles to deposit either 559 or 563 keV while one of the gamma rays deposits only some of its energy in an active crystal. In this case, the beta particles would be incorrectly interpreted as a gamma ray and the partially-escaped gamma ray would be incorrectly identified as the beta particles.

The assumption in the relaxed analysis is that the crystal or segment whose energy was removed contained the decay beta particles, and the gammas were fully absorbed in the remaining active germanium detectors. Unfortunately, it may be possible for the gamma rays to partially or even fully escape and yet have the event still look like an ES2$\nu\beta\beta$ decay. Consider the case where the first gamma ray deposits 500 keV in a single crystal and escapes the detector. Assume the second gamma ray deposits 400 keV and escapes. If the beta particles deposit 622 keV, then the first gamma ray and the beta particles total 1122 keV, and those particles are incorrectly interpreted as all being gamma rays. The second gamma ray is incorrectly interpreted as the beta particles depositing 400 keV of energy.

If there were a method to observe energy outside the germanium crystals but within the shielding, it might be possible to tag these events as false positives. No such instrumentation exists in the current proposal, nor is there any intention of installing such instrumentation. We therefore use the Monte Carlo data to count the number of false positives for the three segmentation schemes and two analysis methods. The results are shown in Table 8.2. It might be possible to reduce the rate of false positives by applying pulse shape discrimination to the crystal in which the decay was assumed to occur. Unfortunately, this pulse shape discrimination will not be able to distinguish between energy deposited by beta particles and energy deposited by a single Compton scatter from a gamma ray. Pulse shape analysis will reduce the rate of false positives somewhat, but cannot eliminate them.

We would at this point like to compare the efficiency of observation of a ^{76}Ge ES2$\nu\beta\beta$ decay in a Majorana module to the efficiency of observing the surrogate ^{77}Ge triple coincidence in the CLOVER detector. The experimental values for the surrogate observation efficiency were 0.0237% and 0.0260% (see Eqs. (6.3) and (6.4)). These observation efficiencies are almost two orders of magnitude below the observation efficiency of the double-beta decay. There are two reasons for this. One is that the ^{77}Ge decays had branching ratios of just 6.6% and 10.3%, respectively, while we assumed that as far as the double-beta decays go, we are looking at a pure data set with a branching ratio of 100%. Another issue that increases the double-beta decay observation efficiency is the increased active mass—the Majorana module has more crystals, each of which has about 47% more mass than the CLOVER crystals. The Majorana module is simply more likely to observe the full energy of the cascade gammas.

8.2.2 Calculating backgrounds to the ES2$\nu\beta\beta$ signal

The Majorana collaboration has set limits of acceptable background levels to reach its stated background contribution to the $0\nu\beta\beta$ region of interest. We use those target background levels to predict what the background to the ES2$\nu\beta\beta$ signal will be. The strongest anticipated radioactive contaminants in the germanium and copper are simulated in each unique part location. We then apply the unsegmented-crystal strict and relaxed cuts to the background data.

The strongest backgrounds internal to the germanium crystals come from ^{60}Co and the ^{238}U, ^{232}Th, and ^{68}Ge decay chains (though not necessarily in that order). The strongest backgrounds in the electroformed copper parts are the ^{238}U and ^{232}Th decay chains. We simulated one million events of each background source in each applicable germanium or copper part. An "event" in this case is a single beta decay in the case of ^{60}Co, or the entire decay chains of the other three radioisotopes. The only germanium parts are the crystals, and the copper parts in which backgrounds were simulated are the electroformed copper parts: the inner copper shield, stringer lids, stringer mount plate, and cryostat (except for the shield, all parts are visible in Figs. 8.2). The decay chains were assumed to be in equilibrium, so the entire decay chain was generated for every primary decay. For example, ^{68}Ge decays to ^{68}Ga, which decays to ^{68}Zn, which is stable. Thus in the case of ^{68}Ge, with 1 million primary decays there were actually 2 million total simulated decays.

We counted the number of background events that passed the analysis cuts. In the case of the crystals and StringerLids, the contribution from each unique location was weighted by that part's multiplicity, giving a non-integer number of counts. The results are shown in Table 8.3.

Unfortunately, the simulation data set was not great enough to give counts for some of the part / source pairs. We therefore estimate the contribution of those backgrounds based on the established ratios between the relaxed and strict background contributions. In the case of the ^{238}U backgrounds, we can use either the ratio for the stringer lids or the ratio for the cryostat. We go with the more

Table 8.3: ES2$\nu\beta\beta$ background rate per 1 million primary decays. For the radioisotopes that decay via a chain to a stable nucleus, the chain was assumed to be in equilibrium so that one decay for every radioisotope in the chain was created for a single primary.

Part	^{238}U		^{232}Th		^{68}Ge		^{60}Co	
	Strict	Relaxed	Strict	Relaxed	Strict	Relaxed	Strict	Relaxed
Crystals	10.67	221.7	7.649	2593	0.526	2089	5.877	2034
StringerLids	1.526	475.9	0.421	95.42				
StringerMountPlate	0	1	1	192				
Cryostat	1	716	0	104				
Inner shield	0	50	0	1				

conservative of these ratios (the stringer lids, with a ratio of 0.3%), and set a contribution of 0.003 for the stringer mount plate and 0.16 for the inner shield per million primary decays.

For ^{232}Th the more conservative ratio comes from the stringer mount plate, and is roughly 0.52%. We will therefore still estimate an upper limit on the ^{232}Th background contribution from the cryostat and inner shield at 0.54 and 0.0052 counts per 1 million decays, respectively.

8.2.3 The ES2$\nu\beta\beta$ sensitivity

ES2$\nu\beta\beta$ signal

Finally, to predict the sensitivity of a single Majorana module to the excited-state $\beta\beta$ signal, we calculate how many ES2$\nu\beta\beta$ decays there would be in 11 months of live time, assuming a half life of 10^{23} years (as a reminder, the ^{76}Ge 2$\nu\beta\beta$ decay half life to the ground state is 1.5×10^{21} years, see Table 2.1). An 11-month exposure is assumed because if Majorana is funded for two modules, the first module will be installed and running for 11 months before being shut down to commission the second module. We would therefore be interested in what results might be obtained during this single-module phase of the experiment.

A Majorana module will contain 53.9 kg of ^{76}Ge. With the above-stated half life, we would expect 2718 excited-state decays during the 11 months of live time. How many of those decays we observe would of course depend on whether we used the strict or relaxed analysis methods, and the segmentation scheme of the crystals. Table 8.4 shows the number of events we could expect to observe.

Table 8.4: Majorana module ES2$\nu\beta\beta$ sensitivity. Assuming an 11-month live time and an ES2$\nu\beta\beta$ half life of 10^{23} years, this table shows the number of counts we expect for three different segmentation schemes and using either the strict or relaxed analysis.

Segmentation	Strict analysis	Relaxed analysis
1×1	24.89(55)	65.0(1.4)
2×3	25.68(56)	198.1(3.9)
6×6	15.63(34)	331.0(6.4)

Table 8.5: Total number of primary background decays in 11 months. See text for details of calculations for obtaining these values.

Part	^{238}U	^{232}Th	^{68}Ge	^{60}Co
Crystals	0.05	0.05	3176	698
StringerLids	231	231		
StringerMountPlate	113	113		
Cryostat	978	978		
Inner shield	7666	7666		

Unsegmented background counts

To predict the number of background events, we need to know how many primary decays there are in 11 months of live time for each combination of source and part shown in Table 8.3. The target background level for both uranium and thorium is 1 μBq / kg of copper. Each of the 19 stringer lids is 0.421 kg, the stringer mount plate is 3.92 kg, the cryostat is 33.8 kg, and the inner shield is 265 kg. Within the germanium crystals, the level of ^{238}U and ^{232}Th is expected to be 30 pBq / kg, with each of the 57 Ge crystals being 1.1 kg.

While on the surface of the Earth, ^{68}Ge and ^{60}Co are cosmogenically produced in the germanium at a rate of 1 / kg·day, with a 100-day exposure. During this surface exposure time, 12 ^{68}Ge and 2 ^{60}Co nuclei per kg of germanium will decay, leaving behind 88 and 98 nuclei per kg respectively. (The half life of ^{68}Ge is 270.8 days, and for ^{60}Co the half life is 5.2714 years.)

Given these background levels, we can predict how many decays there will be during the 11 months of live time. Table 8.5 shows the number of primary decays for each combination of part and source. By multiplying these values by those in Table 8.3 and normalizing by the number of simulation decays (1 million), we calculate the total number of background counts to the ES2$\nu\beta\beta$ decay signal for both the strict and relaxed analyses. These results are shown in Table 8.6 and Figs. 8.9 and 8.10.

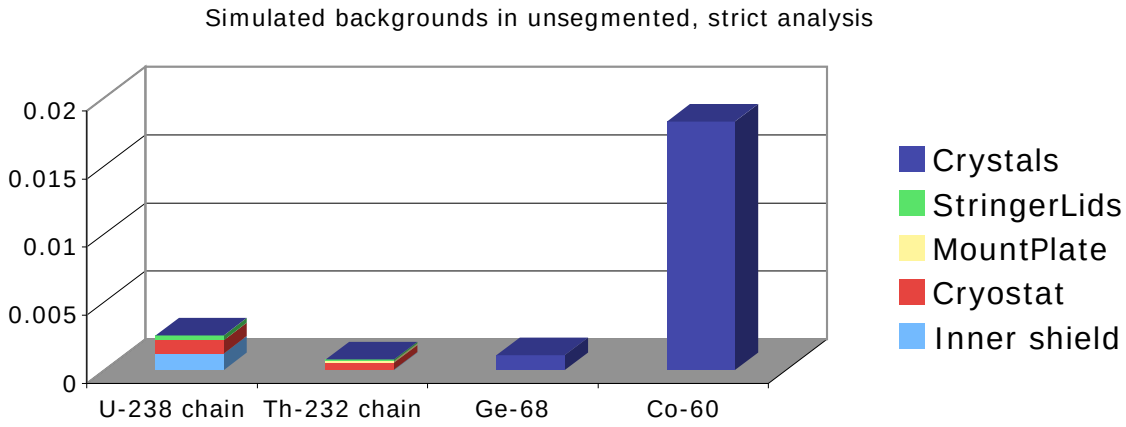

Figure 8.9: Total background counts with unsegmented, strict analysis. The largest single contributor to the background is ^{60}Co within the crystals, which contributes 80% to the total. The numbers shown are absolute simulated background counts over 11 months of live time for a single Majorana module.

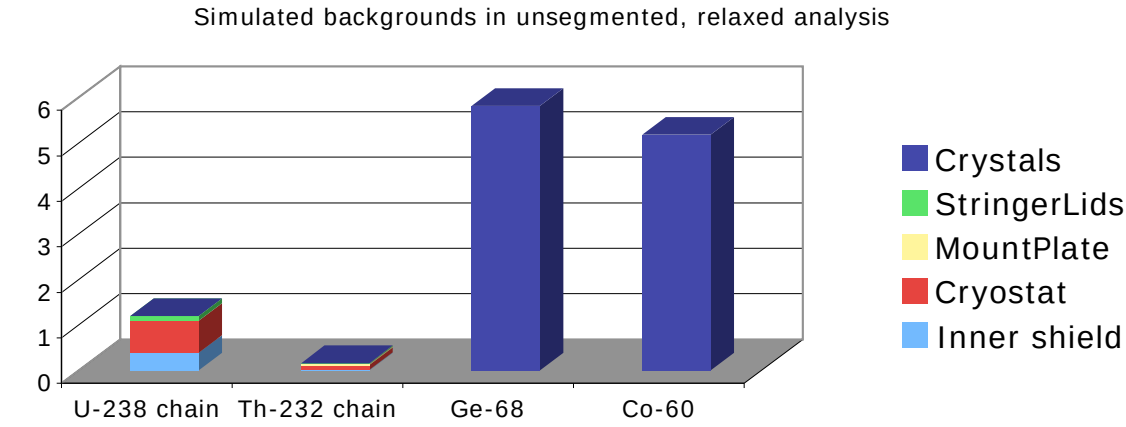

Figure 8.10: Total background counts with unsegmented, relaxed analysis. The largest contributors to the background are ^{68}Ge and ^{60}Co within the crystals, which contribute 89% to the total. The ^{68}Ge is the shortest-lived of these backgrounds, and the simulation assumed data taking from the day the germanium is brought underground. In reality, the ^{68}Ge will decay away somewhat before the start of production data taking, so the background will most likely be much less.

Table 8.6: Total ES2$\nu\beta\beta$ background counts in 11 months. The uncertainties on the background rates are approximately a factor of 2 for the strict analysis and 2% for the relaxed analysis. "SMP" stands for StringerMountPlate. Compare these numbers to the first line in Table 8.4. See text for details.

Part	^{238}U		^{232}Th		^{68}Ge		^{60}Co	
	Strict	Relaxed	Strict	Relaxed	Strict	Relaxed	Strict	Relaxed
Crystals	6e-7	1.2e-5	4e-7	1.4e-4	1.1e-3	5.8	1.8e-2	5.2
StringerLids	3.5e-4	0.11	9.7e-5	2.2e-2				
SMP	3e-7	1.1e-4	1.1e-4	2.2e-2				
Cryostat	9.8e-4	0.70	5.3e-4	0.10				
Inner shield	1.2e-3	0.38	4.0e-5	7.7e-3				
Subtotals	0.003	1.194	0.001	0.153	0.001	5.803	0.018	5.169

We simplify Table 8.6 by totaling the anticipated background counts during the 11-month live time:

$$\begin{aligned} \text{Total background counts in unsegmented, strict analysis} &= 0.023 \\ \text{Total background counts in unsegmented, relaxed analysis} &= 12.2 \end{aligned} \tag{8.2}$$

We make note of two issues concerning the backgrounds. First is that with a strict, whole-crystal analysis, even during 11 months of live time we expect the number of background counts to be much less than one—this analysis has essentially no background. Second, the ^{60}Co and ^{68}Ge backgrounds are the largest contributors to the backgrounds.

Segmented background counts

For the segmented analysis, we only analyze the largest contributors to the background: the ^{68}Ge and ^{60}Co in the crystals. Before presenting the results of the background analysis, however, we show the n-hit histograms for these isotopes in Fig. 8.11. These histograms should be compared to those shown in Fig. 8.8. It may be that there is a different n-hit cut that will strengthen the signal-to-background ratio, but a complete simulation of all backgrounds in all parts would have to be performed to verify the optimal n-hit cut. For now, though, we simply note that an n-hit cut may be an effective method to eliminate more background than signal.

With all the analysis cuts in use, we calculate the number of background counts from ^{68}Ge and ^{60}Co in the three segmentation schemes. Table 8.7 shows the results. The background in the unsegmented analysis was dominated by ^{68}Ge and ^{60}Co, and increasing the values in this Table by about 20% gives a good indication of the total background we can expect. We can see that the

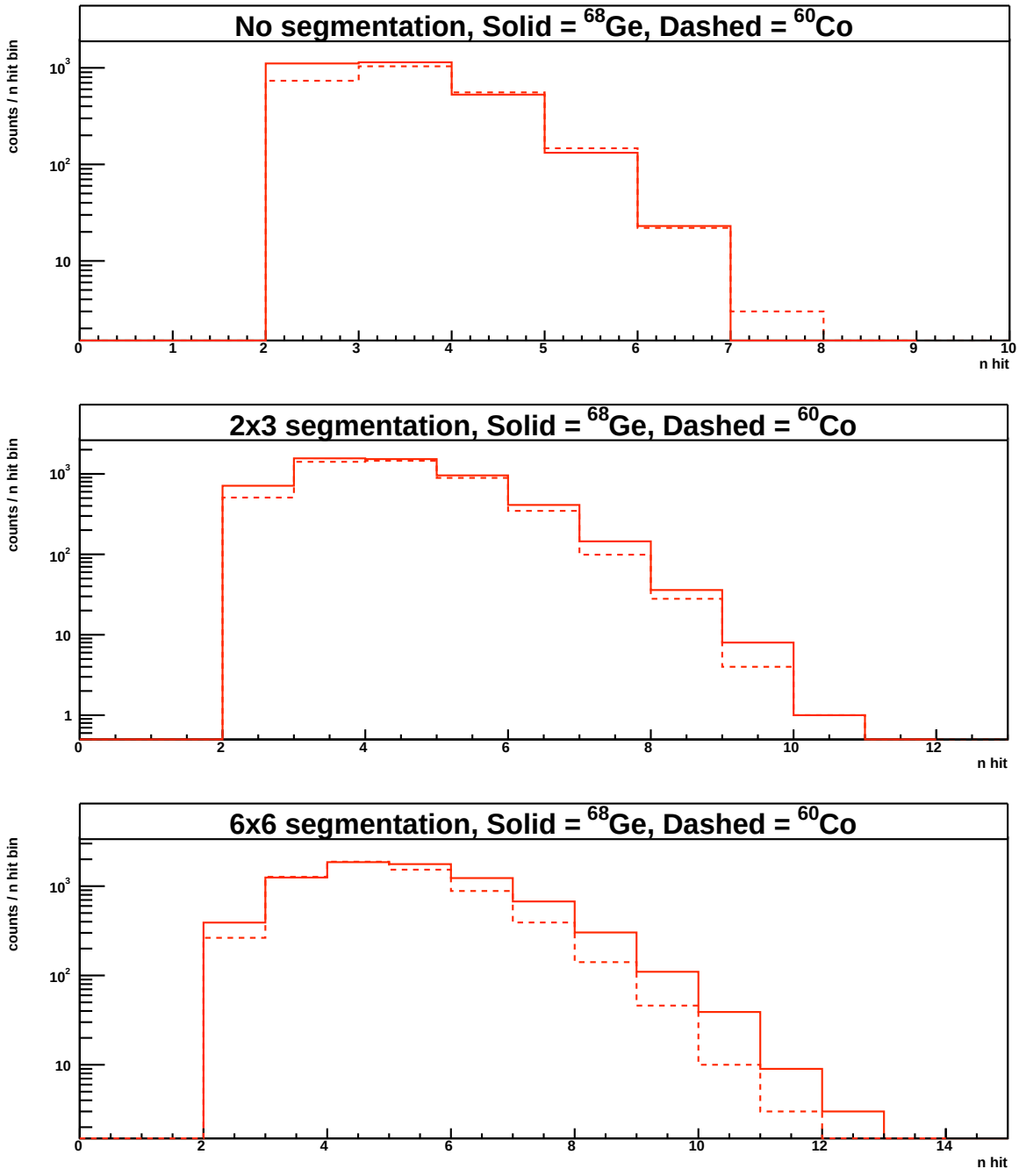

Figure 8.11: N-hit in the relaxed ^{68}Ge and ^{60}Co background analysis. A lower n-hit limit of 3 eliminates 38% (29%) of counts from the ^{68}Ge (^{60}Co) unsegmented analysis, 13% (10%) from the 2×3 segmentation, and 5%(4%) from the 6×6 segmentation analyses. The signal reduction is 10%, 2%, and 0.3% for the three segmentation schemes, respectively.

Table 8.7: Background counts from ^{68}Ge and ^{60}Co in various segmentation schemes. These values are the total number of expected background counts from ^{68}Ge and ^{60}Co internal to the crystals over 11 months of live time.

Segmentation	^{68}Ge		^{60}Co	
scheme	Strict	Relaxed	Strict	Relaxed
1×1	0.001	5.804	0.018	5.169
2×3	0.003	15.28	0.007	13.48
6×6	0.002	23.01	0.007	20.09

number of expected counts in the strict analysis remains well below 1, even with higher degrees of segmentation.

Thus we can use a strict analysis to virtually eliminate the background, or use a relaxed analysis to capture as many events as possible. Given that we do not yet know what the half life of the ES2$\nu\beta\beta$ decay is, we may use a strict cut to perform the half life measurement, but perform a relaxed analysis to plot the beta spectrum.

8.3 Reducing $0\nu\beta\beta$ Backgrounds in the Majorana experiment

As a further application of the utility of coincidence measurements, the backgrounds found in the search for neutrinoless double-beta decay can be reduced using coincidence techniques. As a reminder, the signal for $0\nu\beta\beta$ decay in ^{76}Ge is any event that survives all the cuts in a ±2 keV window around the double-beta endpoint energy of 2039 keV.

Our approach takes two paths forward: sources internal and external to the germanium crystals. This section is not meant to be an exhaustive search for and analysis of all backgrounds in the $0\nu\beta\beta$ signal, but rather to demonstrate a coincidence method that may identify these backgrounds as distinct from the neutrinoless decay of ^{76}Ge.

8.3.1 Reducing internal backgrounds

The internal sources of events in the region of interest are generally easier to reject than external sources, but they have a greater efficiency than external sources, and must therefore be studied on an individual basis to determine their levels in the neutrinoless ROI.

^{77}Ge

One example of an internal background is ^{77}Ge, which contains a gamma ray at 2037.78 keV. The branching ratio of this gamma is 0.0612%. If we assume a photopeak efficiency of 2% at this

energy for a 100-gram segment of germanium, and also assume that pulse shape analysis will reject approximately 80% of the resulting gammas, approximately one ^{77}Ge decay out of 400,000 will result in a count in the $0\nu\beta\beta$ region of interest. The background goal for the Majorana experiment of 1 count per tonne·year would be completely exhausted if there were 1 neutron capture in each crystal per day.

Fortunately, we have an few extra signals to reject this background. The most immediately useful signal is the beta particle emitted in the ^{77}Ge decay, with an endpoint energy of 188.75 keV. This beta particle is most likely to be observed by the crystal in which the decay occurred, so a simple single-crystal cut would eliminate the majority of these events. Unfortunately, if the energy threshold of an individual crystal is just 5 keV, then 1.5% of these beta particles would not be observed. Thus 1 neutron capture per crystal per day would consume 1.5% of the background budget.

There is a second signal of use, however, which comes from the gamma rays associated with the 2037.76 keV gamma ray mentioned above. The 2038 keV gamma is emitted from the 2513 keV energy level, resulting in the long-lived 475 keV energy level (the same level used to extract the beta spectrum shown in Fig. 6.9). The 475 keV level has a half life of 114 μs, thus if any energy deposition in the $0\nu\beta\beta$ region of interest is followed within a few milliseconds by any other energy deposition, it can be attributed to a decay of ^{77}Ge.

^{76}Ga

^{76}Ga can be created via ^{76}Ge(n, p) reactions. This isotope of gallium has a half life of 32.6 seconds, so its resulting decay will not be coincident with any cosmic rays that led to the (n, p) reaction. ^{76}Ga β^- decays back to ^{76}Ge, and has an associated 2040.70 keV gamma ray with a branching ratio of 0.33%. As in the case with ^{77}Ge decays, a single-crystal cut will eliminate most of the 2040.70 keV energy depositions. In the current case, the accompanying beta particle has an endpoint energy of 3058 keV, so the proportion of betas with energy less than 5 keV is only 0.007% of the total number of decays. Additionally, the 2040.70 keV gamma is accompanied by 1348 keV and 563 keV gamma rays, greatly raising the probability that more than a single crystal will observe an energy deposition.

One interesting twist on this decay is that while it is probably not a concern for the neutrinoless signal, the fact that it is a multiple-particle coincidence with one gamma energy at 563 keV makes it a potential background to the excited-state double-beta decay of ^{76}Ge. The rate of ^{76}Ga creation is related to the neutron flux through the detector, and as the detector will be deep underground and surrounded by a neutron moderator, this background rate is anticipated to be much lower than that from ^{68}Ge or ^{60}Co.

^{74}Ge

The last example of an internal background mitigated by coincidence techniques is that of neutron captures on ^{73}Ge. This capture results in an excited state of ^{74}Ge, and emits two gamma rays in the $0\nu\beta\beta$ ROI: 2037.03 and 2040.50 keV. Because the reaction is a neutron capture, we cannot rely on observing a beta particle with its high observation efficiency.

This background should be of little concern, for two reasons. One, these gamma rays are accompanied by other gamma rays that are likely to result in a multiple-crystal event. Two, the proportion of ^{73}Ge in the detector array is extremely small to begin with.

8.3.2 Reducing external backgrounds

Performing a single-crystal cut is very effective for eliminating internal sources of background, usually because they are accompanied by a beta particle with a very high energy-deposition efficiency. In the case of external backgrounds, however, it is far more rare for a beta particle, if one is created, to deposit energy in a germanium crystal.

^{206}Pb

Inelastic neutron collisions with ^{206}Pb nuclei can result in a 2041 keV gamma ray. These gamma rays will always be coincident with a 1704.5 keV gamma. The 1704.5 keV energy level of ^{206}Pb may be fed by processes other than this ^{206}Pb(n, n'γ) reaction, but Monte Carlo simulations coupled with a measurement of the height of the final spectrum at 1704.5 keV in the experimental data will provide an upper limit on this background.

^{65}Cu

Similar to the ^{206}Pb(n, n'γ) reaction, there is a $0\nu\beta\beta$ decay background in ^{65}Cu(n, n'γ) reactions. This copper gamma ray is at 2041 keV, and is accompanied 99.99% of the time by an 1116 keV gamma ray. Also similar to the ^{206}Pb-related background, Monte Carlo studies accompanied by a measurement of the area of an 1116 keV peak will place an upper limit on the rate of this background in the neutrinoless decay region of interest.

^{64}Cu

Neutron captures on ^{63}Cu result in prompt 2037.53 keV gamma. This gamma ray is accompanied by multiple related gamma rays. This is both a curse and a blessing–a curse because there is no single peak that can be used to limit the background around 2039 keV. It is a blessing because there are a

number of gamma peaks to search for that can all place an upper limit on the $0\nu\beta\beta$ ROI. Because of the complexity of this decay, the importance of careful Monte Carlo studies is increased.

^{66}Cu

Neutron captures on ^{65}Cu can result in a 2039.33 keV gamma. As in the case of ^{63}Cu(n,γ) reactions, there is more than one gamma ray accompanying the 2039.33 keV gamma. Careful Monte Carlo studies are again necessary to place a limit on the number of decays in the neutrinoless decay ROI.

Chapter 9

INTO THE FUTURE

The prospects of measuring the half life of ^{76}Ge $2\nu\beta\beta$ decay to an excited state of ^{76}Se are very high in the proposed Majorana detector. The backgrounds discussed in the previous chapter are negligible using a strict analysis, and represent only a conservative upper limit. The triple coincidence of this $2\nu\beta\beta$ decay allows for a backgroundless experiment, provided the target radiological contamination of the germanium and copper parts of the Majorana module is achieved. The techniques for finding excited state decays are applicable to background reduction in the search for neutrinoless double-beta decay.

The MaGe simulation framework was used to calculate the sensitivity and background level contributions to the ES$2\nu\beta\beta$ decay. To verify the performance of the simulation framework, a triple coincidence from ^{77}Ge that mimics the $2\nu\beta\beta$ excited-state decay was generated in a CLOVER detector. Using the most conservative results, the simulation and experimental efficiencies agree at approximately the 20% level.

In the year and a half since data taking started and this final chapter written, there have been a number of methods discovered that would improve the results. Some of these improvements would have very little effect on the final numbers, while others may substantially reduce the uncertainty of the experimental verification of the simulation. Here then, in no particular order with regards to the effect on the final comparison, are suggested improvements that may be applied to related experiments.

9.1 The CLOVER Detector

Trace length

The pulse signals were digitized and recorded from the CLOVER detector. These recordings were intended for application to pulse shape analysis, and only the primary rise of the pulse needed to be captured for offline analysis. The pulse record lengths only lasted 2 μs. Unfortunately, full charge collection may as long as 6 μs, making recreation of the energy filter output impossible, as the full pulse was not recorded. If the collaboration decided to write its own energy calculation software, we would have no way of appling this new code to the previously-recorded data, as that data would not be complete. The full charge collection time must be studied thoroughly for the Majorana crystals, and pulses recorded for a corresponding length of time to allow for complete reconstruction of the

pulse height.

Energy calibration

The energy calibration might be performed using a 4^{th}- or 5^{th}-order polynomial, rather than a quadratic fit. To avoid divergences outside the calibration region, however, the energy calibration needs to encompass as wide a range as possible. Calibration sources with high-energy gamma emission should be used to calibrate the detector, for example a ^{56}Co source with gamma energies up to 3548 keV may be used. Alternatively, neutron capture within the germanium (e.g., ^{73}Ge) may also leads to prompt gamma rays with energies in excess of 10 MeV. If a calibration were found to cover the full range of observed energies, then events in this work that fell outside the energy calibration range might have their resolution improved by as much as 50%.

In the low-energy range, X-rays might be used to perform a calibration down to 5-10 keV. This calibration may prove difficult, however, as there tend to be many X-rays very close in energy that create an artificially wide peak, making calibration difficult. If necessary, a low-energy gamma ray source such as ^{133}Ba may be used instead.

Even though high-energy gamma rays sources may be found, if there are processes which create energy depositions outside the calibration energy range, future calibrations may still decide to use a quadratic energy calibration, depending on the performance of the detector.

Gain adjustment

The gain on the CLOVER detector was set to have the greatest resolution out to the 2.6 MeV gamma from the decay of ^{208}Tl and ^{208}Pb(n,n'γ) reactions. Including a generous energy range above this value, we made the decision to be sensitive up to ~3 MeV. At this gain, our resolution was approximately 19 bins / keV.

We might have been better served to decrease our gain by a factor of four or so. One relevant tradeoff is how well the Gaussian curves might be defined. To this end, we would not recommend a DAQ resolution lower than 5 bins per keV (though this value is somewhat subjective...a more careful definition of the Gaussian curve would have, for instance, 10 bins per keV). Accuracy of peak width measurements must be balanced against energy scale. It may be that the highest-energy process of interest only deposits 5 MeV of energy, in which case the gain would be halved, giving a final 10 bins per keV.

And yet there is another wrinkle to consider. When binning the data into a histogram, care must be taken to not have more bins in the final histogram than was available in the raw digitized data. If rebinning is of concern, it may be possible to perform all analyses on the raw, uncalibrated data, and convert the raw value to a standard energy unit (e.g., keV) only at the end.

As far as this work goes, there would have been very little impact on the quality of the data if the gain were turned up a factor of 3 or 4. Indeed, the analysis would improve as a whole because of the ability to observe events at higher energies than previously obtainable.

^{77}Ge creation rate measurement

The statistical uncertainty in the measurement of the CLOVER triple coincidence could be reduced by straightforwardly taking more data. Unfortunately, the systematic uncertainties were almost as large as the statistical.

It may be possible to directly count the creation of ^{77}Ge nuclei by observing the decays of the ^{77m}Ge isomer. This isomer has a half-life of 53 seconds, and so will reach saturation in roughly 10 minutes. The isomer decays 19% of the time to the ground state of ^{77}Ge, emitting a 160 keV gamma ray in the process. With enough statistics during activation, the intensity of those 160 keV gamma rays may be accurately measured. From this intensity, we could extrapolate to the total number of decays from the ground state of ^{77}Ge by taking a ratio of the thermal neutron capture cross sections. This would eliminate the systematic uncertainties in the natural abundances of ^{74}Ge and ^{76}Ge

We would still need to take a ratio of thermal neutron capture cross sections of ^{76}Ge to both the ground and isomeric states of ^{77}Ge, which in this case would be

$$\begin{aligned} \frac{^{76}\text{Ge} \rightarrow {}^{77}\text{Ge n capture cross section}}{^{76}\text{Ge} \rightarrow {}^{77m}\text{Ge n capture cross section}} &= \frac{(0.06 \pm 0.01)\ \text{b}}{(0.10 \pm 0.01)\ \text{b}} \\ &= 0.60 \pm 0.12 \end{aligned} \tag{9.1}$$

This uncertainty is 19%, and thus is smaller than the 27% systematic uncertainty in Table 7.3. While with adequate statistics the method of focusing solely on the ^{77m}Ge decay rate may give results with a slightly smaller uncertainty, we reiterate that the best way to reduce the systematic uncertainty is to more accurately measure the thermal neutron capture cross sections, especially on ^{76}Ge.

Neutron anisotropy confirmation or refutation

Figs. 6.3 and 6.4 show a deviation from a constant fast neutron flux or thermal neutron flux. The results were unfortunately somewhat inconsistent with each other in that an increase in the fast neutron flux for a given activation was not necessarily accompanied by an increase in the thermal neutron flux. Yet in Figs. 5.8 and 5.9 we see that in keeping the neutron source in one place and taking consecutive runs provides a reasonably constant flux in both fast and thermal energies.

A more thorough study of the AmBe source would have to be performed to search for a potential anisotropy in the neutron emission. In the absence of a measured anisotropy, further study would be

required to identify the systematic effect that leads to the seemingly large range of fast and thermal neutron fluxes.

Indium placement

The ^{116m}In was a large background in the analysis of the 215 / 416 keV triple coincidence from ^{77}Ge. In the future, a CLOVER detector manufactured with substantially less indium may be used.

The CLOVER detector was always activated, however, with the AmBe source from one side. By activating the CLOVER from either the top or front of the cryostat, we might have been able to reduce the indium activation. As a side benefit, we might also have been able to determine the approximate cross-sectional area of the indium volume from three different axes, giving us further clues as to the geometry of the indium within the cryostat.

As far as the focus of this work is concerned, the indium had little impact on the quality of the results, because by looking for a 416 keV-coincident energy deposition at 215 keV, the indium decays added to the continuum around the 215 keV peak. Of the approximately 8 days of cooldown data, the time cuts to allow for indium to decay away removed only either 16 hours (for a 1-hour time cut) or 48 hours (for a 3-hour time cut) from the final data set. The statistical uncertainty would not have been greatly improved with the addition of this data. To bring the statistical uncertainty to the 5% level would have required 6 times as much data, not 33% more.

9.2 The MaGe Simulations

ES2$\nu\beta\beta$ decay sensitivity

The sensitivity of a single Majorana module to the excited-state $\beta\beta$ decay was calculated. The first Majorana module will be installed and acquiring data for 11 months before the second (if funded) is added. During this time, the calculation predicts that we will be able to observe roughly 25 counts with no background using a strict analysis. With a relaxed analysis the efficiency increases, but so does the amount of background. Table 9.1 shows the predicted number of signal and background counts in a Majorana module when applying the ES2$\nu\beta\beta$ analysis cuts.

If Majorana is funded for two modules, the sensitivity to the signal will increase by greater than a factor of two, as there would be more crystals to potentially observe the cascade gamma rays. Another MaGe simulation with both modules in place would be required to calculate the new sensitivity.

Additional backgrounds

As the Majorana experiment moves forward, more backgrounds may be identified. Each background needs to have a rate determined for every material in which it occurs, and contributions to the

Table 9.1: Comparison of ES2$\nu\beta\beta$ signal and background counts. Values assume 11 months of live time with a ES2$\nu\beta\beta$ half life of 10^{23} years. The strict-analysis background are augmented by 20% over the values shown in Table 8.7. For example, from Table 8.7 the ^{68}Ge and ^{60}Co backgrounds in the 1×1 strict analysis sum to 0.019 counts. Augmenting this value by 20% gives the 0.023 counts shown below. The relaxed-analysis background values have been augmented by 11%. See Section 8.2.2 for details of the background values.

Segmentation	Strict analysis		Relaxed analysis	
scheme	Signal	Background	Signal	Background
1×1	24.9	0.023	65.0	12.2
2×3	25.7	0.012	198	32.0
6×6	15.6	0.011	331	47.9

background calculated. It is assumed that additional backgrounds will be weaker than those already identified, though, and given the already very low number of anticipated background counts, we do not expect additional backgrounds to substantially alter the analysis.

Neutron simulations

The simulations performed in MaGe in this work have all been based in electromagnetic interactions. We can, however, also use the neutron data to determine the level of accuracy of the neutron simulations. This can be performed from a few standpoints:

1. Neutron capture on germanium
2. Neutron capture on hydrogen
3. Inelastic fast neutron collisions on germanium
4. Inelastic fast neutron collisions on lead
5. Neutron thermalization in polyethylene

As an example of the first study mentioned above, the efficiency of the ^{77}Ge triple coincidence can be recalculated. The simulation performed in this work assumed a homogeneous distribution of ^{77}Ge decays throughout a crystal. Yet the leading face of the crystals as seen by the AmBe source might have an observably higher activation rate. An exponential distribution of ^{77}Ge decays may change the observation efficiency, and may be required if the systematic and statistical uncertainties are much lower.

Other geometries

SEGA [27] and MEGA [28], two experiments closely related to Majorana, may be able to make a measurement of the excited state decay half life before one is available from the Majorana detector. As of this writing, these geometries are not yet a part of the MaGe simulation. These geometries need to be entered, and sensitivity and background analysis performed along the lines of those in Section 8.2.

Pulse shape discrimination

One method of background reduction barely mentioned in this work is pulse shape discrimination. The backgrounds levels are already shown to be negligible with a strict analysis, even in the absence of either segmentation rejection or pulse shape discrimination. Still, if a stray background count does manage to enter the excited state regions of interest, PSD may be applied to the three energy depositions, with the requirement that the 559 and 563 keV energy depositions be multi-site and the presumed beta particle be single-site.

9.3 Excited-state $0\nu\beta\beta$ surrogate signals

A focus of this work has been experimental verification of the ES2$\nu\beta\beta$ observation efficiency calculations via Monte Carlo simulations. We performed this study by mimicking the ES2$\nu\beta\beta$ signal using triple coincidences found in the decay of ^{77}Ge.

A natural extension of this work is experimental verification of the ES0$\nu\beta\beta$ signal efficiency using a surrogate signal. What properties would this surrogate signal have? A fundamental difference between the signature of excited-state zero-neutron and two-neutrino decays is that the former will have the beta particles sharing a sharply-defined energy, rather than a continuous spectrum between 0 and the endpoint energy. In parallel with the list shown on page 43, we add a requirement to the ES0$\nu\beta\beta$ list:

1. Triple coincidence: $\beta\beta$-γ-γ
2. β sum energy must be sharply defined
3. Homogeneously distributed throughout the germanium crystals
4. No β^+ emission
5. Simultaneous decay particles
6. Plentiful

It turns out that a perfect candidate for an ES0$\nu\beta\beta$ surrogate signal is pair production from a high-energy gamma ray. Take for instance the 2614.5 keV gamma ray coming from the decay of

^{208}Tl. Within a germanium detector, this gamma ray may pair produce, turning into a $\beta^+\beta^-$ pair, with a sharply defined kinetic energy sum of 1592.5 keV. The positron then annihilates, emitting two 511-keV gamma rays which can interact with the rest of the detector. This reaction has all the required traits shown in the list above.

The question remains of how to determine how many $\beta^+\beta^-$ pairs were produced. To this end, we can run a relatively simple Monte Carlo simulation of two 511-keV gamma rays emitted in opposite directions, with the starting locations homogeneously distributed throughout a crystal. We then count the proportion of times that both gamma rays fully escape the crystal in which they were created. Dividing the area of an experimentally-obtained double-escape peak by this proportion gives a measure of how many pair productions occurred during data taking.

What other gamma rays would be good surrogates for an excited-state, neutrinoless double-beta decay? The gamma ray should have a high branching ratio. Also, the higher the gamma ray energy the more likely the gamma ray is to produce a $\beta^+\beta^-$ pair. Unfortunately, the higher-energy gamma rays also tend to have lower branching ratios. What sources would work?

One possible source is ^{232}Th, as that contains the aforementioned ^{208}Tl. The 2614.5 keV gamma ray from the decay of ^{208}Tl has an absolute intensity of 99.16%, so the double-escape peak should be strong (indeed, this peak is visible in the background and cooldown spectra shown in Figs. 4.15–4.17 and 5.10–5.12, respectively).

We might also be able to use other sources as a check on systematic effects. ^{56}Co has a handful of higher-energy gamma rays. While they are all potential candidates, we can determine which gamma ray will give us the strongest signal by multiplying each gamma ray intensity by its cross-section for pair production. Table 9.2 shows the results for the highest-energy and most-common gamma rays from the decay of ^{56}Co.

We see from Table 9.2 that the best ^{56}Co candidates for the excited-state neutrinoless surrogate are the 2598.5 keV and 3253.4 keV gamma rays, as these will result in the greatest number of pair-productions. These gamma rays will create beta-energy depositions at 1576.5 keV and 2231.4 keV, respectively.

The task of experimentally measuring this triple-coincidence efficiency can the proceed as outlined in this work, with both strict and relaxed analyses (see Section 8.2.1).

9.4 Non-Standard Physics

At this point, we have discussed two-neutrino and zero-neutrino double-beta decays to both excited and grounds states of the final nucleus. With various mechanisms in place, we would like to reiterate a subject introduced in Section 3.5. In the $0\nu\beta\beta$ case, the ratio of decays to the ground state to decays to an excited state of the final nucleus may give an indication of the underlying decay mechanism (e.g., light- or heavy-neutrino exchange or a SUSY mechanism).

Table 9.2: ^{56}Co candidates for an ES0$\nu\beta\beta$ surrogate signal. The higher the energy of the gamma ray, the more likely it is to pair-produce, but higher energy rays are usually less intense. We multiply the pair-production cross-sections by the intensity to obtain a figure of merit. The higher the figure of merit, the more $\beta^+\beta^-$ pairs are created within the germanium. The cross-sections were obtained from XCOM [99].

γ Energy (keV)	Relative Intensity	Cross-section (barns / Ge atom)	Figure of merit
1771.4	15.69	0.125	1.961
2015.2	3.08	0.202	0.622
2034.8	7.88	0.209	1.647
2598.5	17.28	0.401	6.936
3009.6	1.049	0.542	0.569
3202.0	3.24	0.607	1.966
3253.4	7.93	0.623	4.941
3273.0	1.889	0.630	1.190
3451.2	0.953	0.688	0.656

Such a study would be far off in the future. Assuming the Klapdor-Kleingrothaus *et al.* claim [55] is substantiated, zero-neutrino decays to an excited state would take roughly 100 times as long to proceed, plus their efficiency of observation would only be on the order of 10%. Finally, the ratio of half lives would have to have sufficiently low statistical uncertainty to be able to differentiate between ratios of 50, 95, or 120. These factors combine to require a detector with 10^4 - 10^5 times the sensitivity of what is currently available.

9.5 The last word. For now.

The last fundamental aspects of the neutrino are coming closer and closer to our grasp. 60 years ago the neutrino question of the day was"Does it exist". Science has made great strides since then, and there are few yes/no questions left unanswered. "Is the neutrino its own antiparticle" is just such a question. Wrapped up in this question is "what is the mass of the neutrino".

If the neutrino *is* its own antiparticle, the mass can be determined from the half life calculation only via nuclear matrix elements, the quality of which is the point behind this thesis. May this work contribute in some way to this goal.

BIBLIOGRAPHY

[1] J. J. Thompson, "Cathods Rays", *Phil. Mag.*, **44** (1897) p.293.

[2] H. Geiger, E. Marsden, "On a Diffuse Reflection of the α-Particles", *Proc. Roy. Soc.*, **82**, 557 (1909) p.495-500.

[3] E. Ruthorford, "Collision of a Particle with Light Atoms", *Phil. Mag.*, **37** (1919) p.581.

[4] J. Chadwick, "Possible Existence of a Neutron", *Nature* **129** (1932) p.312.

[5] J. Chadwick, *Verhandlungen der Deutschen Physikalischen Gesellschaft* **16** (1914) p.383-391.

[6] "The Reines-Cowan Experiments: Detecting the Poltergeist", *Los Alamos Science*, **27** (1997).

[7] C. L. Cowan, Jr., F. Reines, F. B. Harrison, H. W. Kruse, A. D. McGuire, "Detection of the Free Neutrinos: a Confirmation", *Science* **124** : 3212 (1956) p.103-104.

[8] A. H. Becquerel, "On the rays emitted by phosphorescence", *Comptes Rendues*, **122** (1896) p.420-421.

[9] W. C. Röentgen, "Ueber eine neue Art von Strahlen", *Sitzungs-Berichte der Pysics.-med. Gesellschaft zu Würzburg* (1895).

[10] E. Rutherford, "The Connexion between the β and γ Ray Spectra", *Phil. Mag.* **28** 165 (1914) p.305-319.

[11] C. D. Ellis, W. A. Wooster, "The Average Energy of Disintegration of Radium E", *Proc. Roy. Soc. Lon. A* **117** (1927) p.109-123.

[12] *Physics Today*, September (1978), page XXX.

[13] Reines, F. and C. L. Cowan, Jr., "Detection of the Free Neutrino", *Physical Review Letters* **92** (1953) p.830-831.

[14] F. Mantovani, L. Carmignani, G. Fiorentini, M. Lissia, "Antineutrinos from Earth: A reference model and its uncertainties", *Phys. Rev. D.*, **69**, 013001 (2004).

[15] J. Boger *et al.*, "The Sudbury Neutrino Observatory", *Nucl. Inst. Meth. Phys. Res. A* **449** (2000) p.172-207.

[16] P. Vogel, "Future galactic supernova neutrino signal: What can we learn?", nucl-th/0111016

[17] J. Bonn *et al.*, "The Mainz Neutrino Mass Experiment", *Nucl. Phys. B (Proc. Suppl.)*, **91** (2001) p273-279.

[18] B. Aharmim *et al.*, "Electron energy spectra, fluxes, and day-night asymmetries of ^{8}B solar neutrinos from measurements with NaCl dissolved in the heavy-water detector at the Sudbury Neutrino Observatory", *Phys. Rev. C* **72**, 055502 (2005).

[19] Y. Ashie *et al.*, "Evidence for an Osciallatory Signature in Atmospheric Neutrino Oscillations", *Phys. Rev. Lett.* **93**, 101801 (2004).

[20] S. Eidelman *et al.*, *Phys. Lett. B* **592**, 1 (2004).

[21] M. Apollonio *et al.*, "Search for neutrino oscillations on a long base-line at the CHOOZ nuclear power station", *Eur. Phys. J. C* **27**, (2003) p.331-374.

[22] F. Šimkovic, A. Faessler, "Distinguishing the $0\nu\beta\beta$-Decay Mechanisms", *Prog. Part. Nucl. Phys.* **48** (2002) p201-209.

[23] L. Krauss, "What is the Role of Neutrinos in Shaping the Universe", astro-ph/0605378.

[24] A. Aguilar, *et al.*, "Evidence for neutrino oscillations from the observation of $\overline{\nu}_e$ appearance in a $\overline{\nu}_\mu$ beam", *Phys. Rev. D* **64**, 112007 (2001).

[25] http://www-boone.fnal.gov

[26] S. R. Elliott, V. M. Gehman, K. Kazkaz, D.-M. Mei, A. R. Young, "Pulse shape analysis in segmented detectors as a technique for background reduction in Ge double-beta decay experiments", *Nucl. Inst. Meth. Phys. Res. A* **558** (2006) p.504-510.

[27] A. Carpenter, E. Johnson, J. D. Kephart, D. McGhan, K. Saburov, W. Tornow, A. R. Young, "The SEGA Detector", *Triangle Universities Nuclear Laboratory Progress Report - XLII* (2002). Available from http://www.tunl.duke.edu/publications/tunlprogress/2003.

[28] K. Kazkaz, C. E. Aalseth, T. W. Hossbach, V. M. Gehman, J. D. Kephart, H. S. Miley, "MEGA: a low-background radiation detector", *IEEE Trans. Nucl. Sci.* **51**, 1029 (2004).

[29] K. Krane, *Introductory Nuclear Physics*, John Wiley & Sons, Inc., New York (1988).

[30] D. Griffiths, *Introduction to Elementary Particles*, John Wiley & Sons, Inc., New York (1987).

[31] J. R. Reitz, "The Effect of Screening on Beta-Ray Spectra and Internal Conversion", *Phys. Rev.* **77** (1950).

[32] V. M. Lobashev, "Study of the Tritium Beta-Spectrum in Experiment 'Troitsk ν-mass"', *Prog. Part. Nucl. Phys.* **48** (2002) p.123-131.

[33] L. Bornschein and the KATRIN Collaboration, "The KATRIN experiment – a direct measurement of the electron antineutrino mass in the sub-eV region", *Nucl. Phys. A* **752** (2005) p.14c-23c.

[34] H. Primakoff, S. P. Rosen, "Double Beta Decay", *Rep. Prog. Phys.* **22** (1959) p.121-166.

[35] R. B. Firestone, S. Y. F. Chu (Ed.), V. S. .Shirley (Ed.), *Table of Isotopes CD-ROM*, 8^{th} Edition, Version 1.0, Wiley Interscience (1996).

[36] A. P. Meshik, C. M. Hohenberg, O. V. Pravdivtseva, and Ya. S. Kapusta, "Weak decay of ^{130}Ba and ^{132}Ba: Geochemical measurements", *Phys. Rev. C* **64** (2001) 035205.

[37] M. Doi, T. Kotani, E. Takasugi, "Double Beta Decay and Majorana Neutrino", *Prog. Theor. Phys. Suppl.* **83** (1985).

[38] W. C. Haxton, G. J. Stephenson, Jr., "Double Beta Decay", *Prog. Part. Nucl. Phys.* **12** (1984) p.409-479.

[39] A. S. Barabash, "Average and Recommended Half-Life Values for Two Neutrino Double Beta Decay: Upgrade '05", nucl-ex/0602009.

[40] V. A. Rodin, A. Faessler, F. Šimkovic, P. Vogel, "Uncertainty in the $0\nu\beta\beta$ decay nuclear matrix elements", *Phys. Rev. C* **68** (2003) 044302.

[41] J. Suhonen, S. B. Khadkikar, A. Faessler, "Calculation of the Neutrinoless $\beta\beta$ decay of ^{76}Ge Using a Quark Model with Harmonic Confinement", *Nucl. Phys.* **A529** (1991) p.727-740.

[42] E. Caurier, F. Nowacki, A. Poves, J. Retamosa, "Shell Model Studies of the Double Beta Decays of ^{76}Ge, ^{82}Se, and ^{136}Xe", *Phys. Rev. Lett.* **77** 10 (1996) p.1954-1957.

[43] S. M. Bilenky, A. Faessler, F. Šimkovic, "The Majorana neutrino masses, neutrinoless double beta decay and nuclear matrix elements", hep-ph/0402250.

[44] H. Ejiri, "Double Beta Decays and Neutrino Masses", *J. Phys. Soc. Jpn.* **74** 8 (2005) p.2101-2127.

[45] S. Hannestad, "Cosmological limit on the neutrino mass", astro-ph/0205223.

[46] U.Seljak, A. Slosar, P. McDonald, "Cosmological parameters from combining the Lyman-α forest with CMB, galaxy clustering and SN constraints", astro-ph/0604335.

[47] S. R. Elliott, J. Engel, "Double-beta decay", *J. Phys. G: Nucl. Part. Phys.* **30** (2004) p.R183-R215.

[48] H. V. Klapdor-Kleingrothaus, A. Dietz, H. L. Harney, I. V. Krivosheina, "Evidence for neutrinoless double beta decay", *Mod. Phys. Lett. A* **16** 37 (2001) p.2409-2420.

[49] H. V. Klapdor-Kleingrothaus *et al.*, "Latest results from the HEIDELBERG-MOSCOW double beta decay experiment", *Eur. Phys. J. A* **12** (2001) p.147-154.

[50] C. E. Aalseth *et al.*, "Comment on 'Evidence for Neutrinoless Double Beta Decay"', *Mod. Phys. Lett. A* **17** 22 (2002) p.1475-1478.

[51] Yu. G. Zdesenko, F. A. Danevich, V. I. Tretyak, "Has neutrinoless double β decay of ^{76}Ge been really observed?", *Phys. Lett. B* **546** (2002) p.206-215.

[52] F. Feruglio, Al Strumia, F. Vissani, "Neutrino oscillations and signals in β and $0\nu2\beta$ experiments", *Nucl. Phys. B* **637** (2002) p.345-377.

[53] H. L. Harney, "Reply to the Comment on 'Evidence for Neutrinoless Double Beta Decay"', hep-ph/0205293.

[54] H. V. Klapdor-Kleingrothaus, "Reply to a comment of article 'Evidence for Neutrinoless Double Beta Decay"', hep-ph/0205228.

[55] H. V. Klapdor-Kleingrothaus, I. V. Krivosheina, A. Deitz, O. Chkvorets, "Search for neutrinoless double beta decay with enriched ^{76}Ge in Gran Sasso 1990-2003", *Phys. Lett. B* **586** (2004) p.198-212.

[56] A. Staudt, K. Muto, H. V. Klapdor-Kleingrothaus, *Eur. Lett.* **13** (1990) p.31.

[57] A. deShalit, H. Feshbach, *Theoretical Nuclear Physics Volume I: Nuclear Structure*, John Wiley & Sons, New York (1974).

[58] A. S. Barabash *et al.*, "Two neutrino double-beta decay of ^{100}Mo to the first excited 0^+ state in ^{100}Ru", *Phys. Lett. B* **345** (1995) p.408-413.

[59] J. Suhonen, O. Civitarese, "Weak-interaction and nuclear-structure aspects of nuclear double beta decay", *Phys. Rep.* **300** (1998) p.123-214.

[60] F. Šimkovic, P. Domin, S. V. Semenov, "The single state dominance hypothesis and the two-neutrino double beta decay of ^{100}Mo", *J. Phys. G: Nucl. Part. Phys.* **27** (2001) p.2233-2240.

[61] A. S. Barabash, F. Hubert, Ph. Hubert, V. I. Umatov, "Doule beta decay of ^{150}Nd to the first 0^+ excited state of ^{150}Sm", *Pis'ma v. ZhETF* **79** 1 (2004) p.12-15.

[62] W. C. Haxton, G. J. Stephenson, Jr., D. Strottman, "Double Beta Decay and the Majorana Mass of the Electron Neutrino", *Phys. Rev. Lett* **47** 3 (1981) p.153-156.

[63] Wick Haxton (private communication).

[64] www.scidac.org

[65] J. A. Halbleib, Sr., R. A. Sorensen, "Gamow-Teller Beta Decay in Heavy Spherical Nuclei and the Unlike Particle-Hole RPA", *Nucl. Phys. A* **98** (1967) p.542-568.

[66] T. Tomoda, "Double Beta Decay", *Rep. Prog. Phys.* **54** (1991) p.53-126.

[67] A. Faessler, F. Šimkovic, "Double Beta Decay", *J. Phys. G: Nucl. Part. Phys.* **24** (1998) p.2139-2178.

[68] S. R. Elliott, P. Vogel, "Double Beta Decay", *Annu. Rev. Nucl. Part. Sci.* **52** (2002) p.115-51.

[69] J. Suhonen, "Nuclear matrix elements of $\beta\beta$ decay from β-decay data", *Phys. Lett. B* **607** (2005) p.87-95.

[70] V. A. Rodin, A. Faessler, F. Šimkovic, P. Vogel, "Assessment of uncertainties in QRPA $0\nu\beta\beta$-decay nuclear matrix elements", *Nucl. Phys. A* **766** (2006) p.107-131.

[71] www.er.doe.gov/np/nsac/docs/NuSAG_report_final_version.pdf

[72] C. Arnaboldi *et al.*, For the CUORE Collaboration, "CUORE: a cryogenic underground observatory for rare events", *Nucl. Inst. and Meth. in Phys. Res. A* **518** (2004) p.775-798.

[73] K. Wamba, For the EXO Collaboration, "EXO: the Enriched Xenon Observatory for Double Beta Decay", hep-ph/0210186.

[74] C. E. Aalseth *et al.*, "The proposed Majorana ^{76}Ge double-beta decay experiment", *Nucl. Phys. B (Proc. Suppl.)* **138** (2005) p.217-220.

[75] C. J. Martoff, P. D. Lewin, "COSMO - a program to estimate spallation radioactivity produced in a pure substance by exposure to cosmic radiation on the earth", *Comp. Phys. Comm.* **72** (1992) p.96-103.

[76] E. Schopper, G. Mauck, E. Lorhmann, "Nukleonen in der Atmosphäre", *handbuch der Physik* **46** 2 (1967).

[77] Canberra, 800 Research Parkway, Meriden, CT 06540, USA, www.canberra.com

[78] X-Ray Instrumentation Associates, 8450 Central Avenue, Newark, CA 94560, USA, www.xia.com

[79] W-IE-NE-R, Plein & Baus, Ltd., 300 East Auburn Avenue, Springfield, OH 45505, USA, www.wiener-us.com

[80] WaveMetrics, Inc., P. O. Box 2088, Lake Oswego, OR 97035, USA, www.wavemetrics.com

[81] R. Brun, F. Rademakers, "ROOT – An Object Oriented Data Analysis Framework, Proceedings AIHENP '96 Workshop, Lausanne, Sep. 1996", *Nucl. Inst. and Meth. in Phys. Res. A* **389** (1997) p.81-86. See also http://root.cern.ch/

[82] XIA, Inc., *User's Manual Digital Gamma Finder (DGF)*, v3.04, January (2004), p. 13, 18-21.

[83] G. F. Knoll, *Radiation Detection and Measurement, 3rd Ed.*, John Wiley & Sons, Inc. (2000).

[84] G. Fehrenbacher et al., "Fast neutron detection with germanium detectors: computation of response functions for the 692 keV inelastic scattering peak", *Nucl. Instr. and Meth. in Phys. Res. A* **372** (1996) p.239-245.

[85] H. W. Kraner, "Fast neutron damage in germanium detectors", *IEEE Trans. Nucl. Sci.* **NS-27** 1 (1980) p.218-234.

[86] J. W. Marsh, D. J. Thomas, M. Burke, "High resolution measurements of neutron energy spectra from Am-Be and Am-B neutron sources", *Nucl. Instr. and Meth. in Phys. Res. A* **366** (1995) p.340-348.

[87] S. F. Mughabghab, M. Divadeenam, N. E. Holden, *Neutron Resonance Parameters and Thermal Cross Sections,* 4th *Ed.*, Academic Press, New York (1981).

[88] T. W. Raudorf et al., "Performance of reverse electtrode HPGe coaxial detectors after light damage by fast neutrons", *IEEE Trans. Nucl. Sci.* **NS-31** 1 (1984) p.253-257.

[89] R. B. Firestone, L. P. Ekström, *LBNL Isotopes Project – LUNDS Universitet WWW Table of Radioactive Isotopes*, Version 2.1(2004). http://ie.lbl.gov/toi/index.asp

[90] G. P. Škoro et al., "Environmental neutrons as seen by a germanium gamma-ray spectrometer", *Nucl. Inst. and Meth. in Phys. Res. A* **316** (1992) p.333-336.

[91] F. Rösel, H. M. Fries, K. Alder, H. C. Pauli, "Internal conversion coefficients for all atomic shells", *At. Nucl. Data Tab.* **21** (1978) p.91-289.

[92] J. K. Tuli, *Nuclear Wallet Cards April 2005*, National Nuclear Data Center, Office of Nuclear Physics, Office of Science, US Department of Energy (2005).

[93] GEANT4 Collaboration, S. Agostinelli *et al.*, "GEANT4: A Simulation Toolkit", *Nucl. Instr. and Meth. A* **506** (2003) p.250. See also http://geant4.cern.ch/

[94] http://www.postgresql.org

[95] http://www.mpi-hd.mpg.de/ge76/home.html

[96] http://www.nndc.bnl.gov/ensdf

[97] O. A. Ponkratenko, V. I. Tretyak, Yu. G. Zdesenko, "Event Generator DECAY4 for Simulating Double-Beta Processes and Decays of Radioactive Nuclei", *Phys. At. Nucl.* **63** (2000) p.1282-1287.

[98] The Majorana Neutrinoless Double-Beta Decay Experiment, Experiment Proposal, 10 March 2006.

[99] M. J. Berger *et al.*, "XCOM: Photon Cross Sections Database", *NIST Standard Reference Database 8 (XGAM)* (1998). http://physics.nist.gov/PhysRefData/Xcom/Text/XCOM.html

[100] M. Matsumoto, T. Nishimura, "Mersenne Twistor: A 623-diminsionally equidistributed uniform pseudorandom number generator", *ACM Transactions on Modeling and Computer Simulation*, **8** No. 1 (1998) p.3-30.

Appendix A

^{77}GE DECAY SCHEME

Table A.1: Dominant gamma rays from the decay of ^{77}Ge. Data shown in order of decreasing intensity. Data taken from [89], which has a full list.

Energy (keV)	Relative intensity
264.44(3)	54
211.03(3)	30.8(9)
215.51(3)	28.6(9)
416.33(3)	21.8(5)
558.02(3)	16.1(4)
367.40(3)	14.0(3)
714.35(3)	7.17(16)
631.82(3)	6.95(16)
1085.19(3)	6.05(13)
1368.4(5)	3.3(3)
1193.26(3)	2.57(5)
810.35(3)	2.27(5)
634.39(3)	2.08(4)
194.76(3)	1.77(7)
784.77(3)	1.32(3)
461.38(3)	1.27(3)
419.75(3)	1.23(3)
928.85(3)	1.046(22)
781.26(3)	1.013(22)

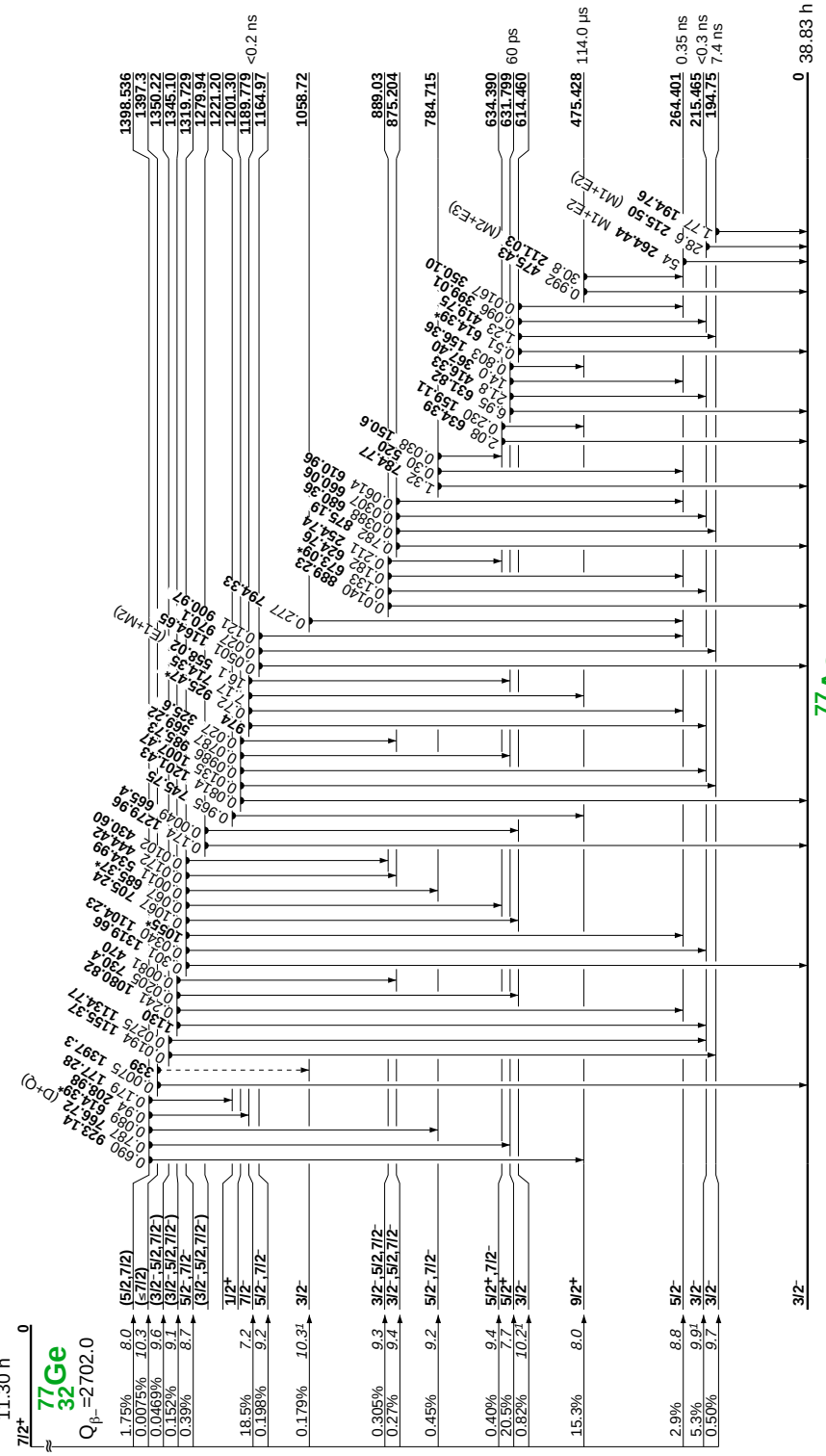

Figure A.1: ^{77}Ge decay scheme, 1 of 3. Figure taken from [35].

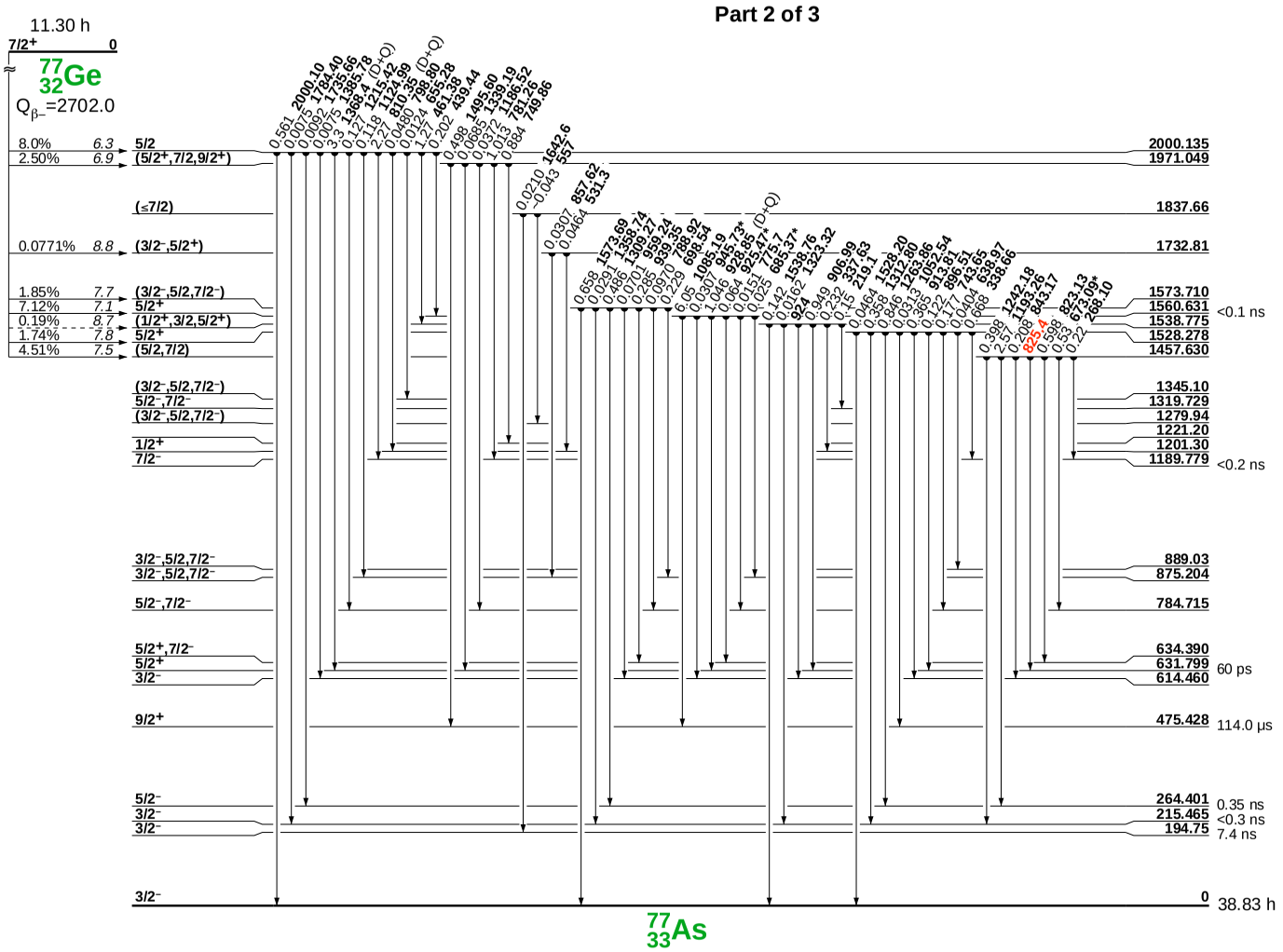

Figure A.2: ^{77}Ge decay scheme, 2 of 3. Figure taken from [35].

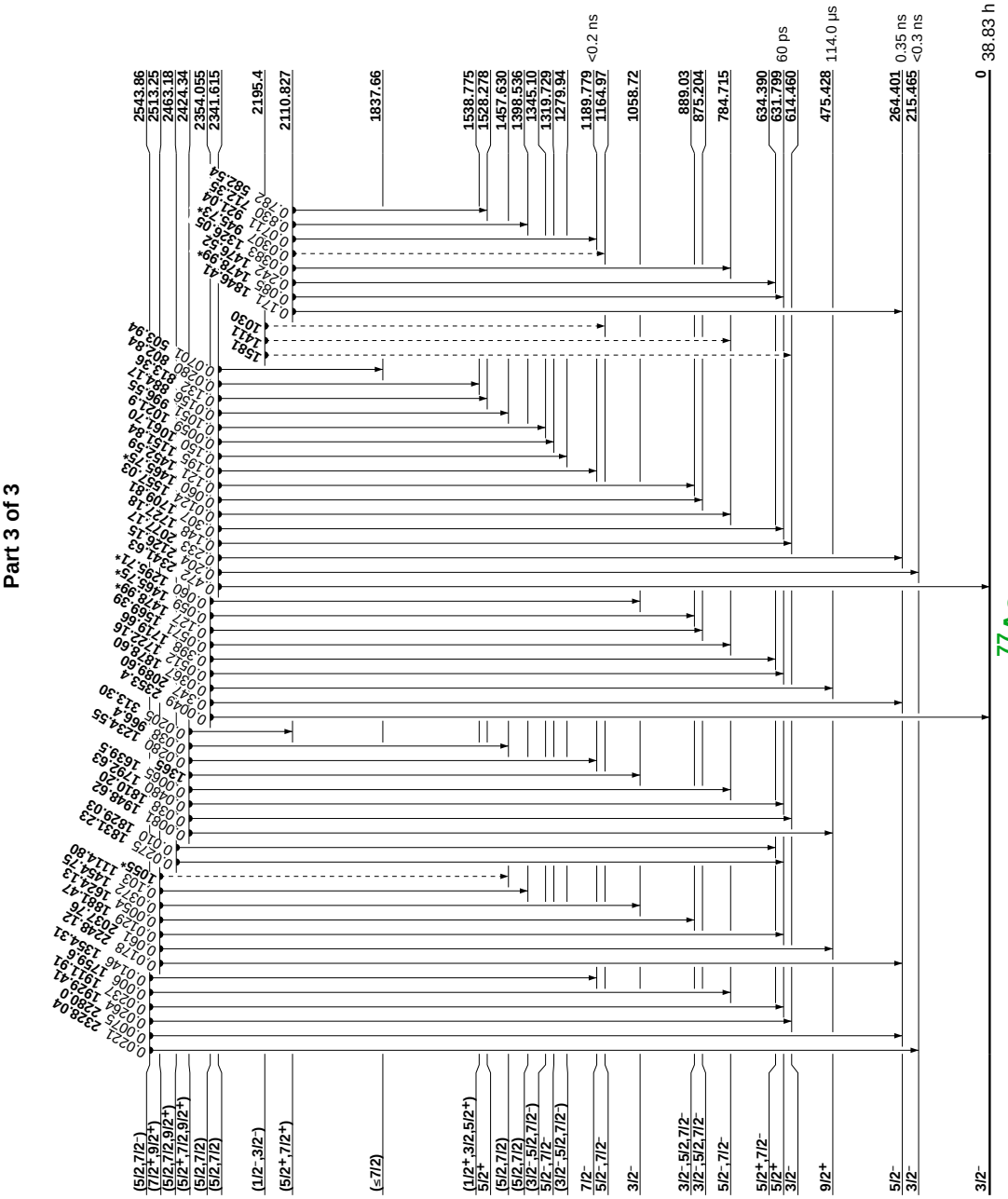

Figure A.3: ^{77}Ge decay scheme, 3 of 3. Figure taken from [35].

Appendix B

NEUTRON CAPTURE EFFICIENCY OF THE CLOVER CRYSTALS

The basic equation for calculating the efficiency of capturing a thermal neutron is

$$\text{Capture efficiency} = 1 - e^{-d\sigma\rho} \tag{B.1}$$

where σ is the thermal neutron capture cross section, ρ is the number density of the target nuclei, and d is the thickness of the target. For natural germanium, σ is (2.30 ± 0.07) barns and ρ is 4.41×10^{22} cm^{-3}

Since the crystals are hollow cylinders the value of d changes with the impact parameter; thus, integration is required. This integral divides the crystals into two sections, one that extends the length of the solid crystal, and the other that extends the length of the hollow core.

The derivation starts with two simplifications. One is that the paths of the thermal neutrons through the crystals are all parallel, and are perpendicular to the axis of the crystal. The second simplification is that the crystal is a simple, regular, hollow, right cylinder of nothing but germanium (i.e., no curvature to the outside corner of the crystals, no dead layers, no inner electrical contacts), though this second simplification will be refined by the end of the calculation. Fig. B.1 shows the geometries used in the integrals.

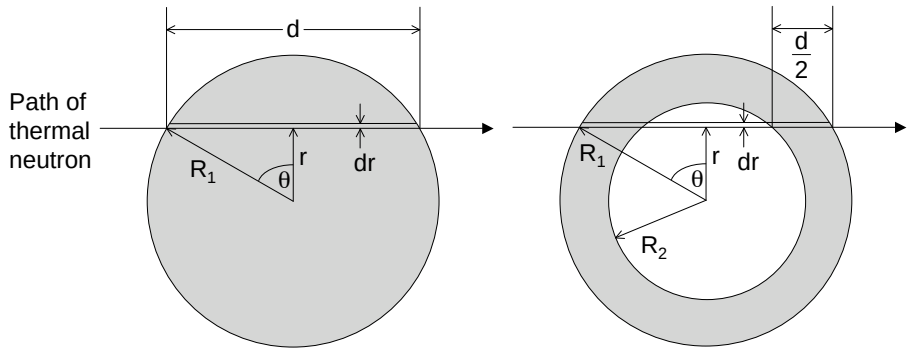

(a) A simplified cartoon for the solid extent of the CLOVER crystals

(b) A simplified cartoon for the hollow extent of the crystals

Figure B.1: Geometry of solid crystal and thermal neutron path. The length of germanium traversed by the neutron, d, is a function of the impact parameter r.

The first integral involves the solid part of the crystal (i.e., the geometry in Fig. B.1(a)). For this integral, the relevant path length is

$$\begin{aligned} d &= 2\,R_1 \sin\theta \\ &= 2\,R_1 \sqrt{1-\left(\frac{r}{R_1}\right)^2} \end{aligned}$$

The integral will be performed from $r = 0$ to $r = R_1$. The ratio of neutrons hitting the crystal with impact parameter r is therefore dr/R_1. Performing the integral of Eq. (B.1) gives

$$\text{Capture efficiency} = \frac{1}{R_1}\int_0^{R_1} dr\left(1 - e^{-2\sigma\rho R_1\sqrt{1-(r/R_1)^2}}\right) \tag{B.2}$$

Turning our attention to the geometry in Fig. B.1(b), we see that for $r > R_2$ the integral is the same. What about when $r < R_2$? We subtract the hollow path length from the total path length to obtain $d/2$. Also, the proportion of thermal neutrons with impact parameter r is still dr/R_1:

$$\begin{aligned} \frac{d}{2} &= R_1\sqrt{1-\left(\frac{r}{R_1}\right)^2} - R_2\sqrt{1-\left(\frac{r}{R_2}\right)^2} \\ \Rightarrow\ \text{Capture efficiency} &= \frac{1}{R_1}\int_0^{R_2} dr\left(1 - e^{-2\sigma\rho\left(R_1\sqrt{1-(r/R_1)^2} - R_2\sqrt{1-(r/R_2)^2}\right)}\right) \end{aligned} \tag{B.3}$$

With the integrals in place, we must take into account the proportion of the crystals that are solid and the proportion that is hollow. Let the solid length be L_1 and the hollow length be L_2. Then the final expression for the thermal neutron capture efficiency of a CLOVER crystal is

$$\begin{aligned} \text{Capture efficiency} = &\frac{L_1}{L_1+L_2}\frac{1}{R_1}\int_0^{R_1} dr\left(1 - e^{-2\sigma\rho R_1\sqrt{1-(r/R_1)^2}}\right) \\ &+ \frac{L_2}{L_1+L_2}\frac{1}{R_1}\int_{R_2}^{R_1} dr\left(1 - e^{-2\sigma\rho R_1\sqrt{1-(r/R_1)^2}}\right) \\ &+ \frac{L_2}{L_1+L_2}\frac{1}{R_1}\int_0^{R_2} dr\left(1 - e^{-2\sigma\rho\left(R_1\sqrt{1-(r/R_1)^2} - R_2\sqrt{1-(r/R_2)^2}\right)}\right) \end{aligned} \tag{B.4}$$

At this point we include one refinement of the geometry. Instead of integrating r out to the original radius of the crystal, 2.5 cm, we instead integrate out to 2.25 cm to take into account two of the flat sides of the crystals. Thus in addition to the values of σ and ρ, we have the following values:

$$L_1 = 1.5 \text{ cm}$$
$$L_2 = 6.5 \text{ cm}$$
$$R_1 = 2.25 \text{ cm}$$
$$R_2 = 0.5 \text{ cm}$$

Plugging these values into Eq. (B.4) and numerically integrating the expression gives the result

$$\text{Capture efficiency} = 0.288 \pm 0.009 \tag{B.5}$$

where the uncertainty, based on very generous machining tolerances, is 3% the final value.

If the crystals were simply modeled as a solid right rectangle 5 cm thick, the capture efficiency would be 0.398, which would result in a 20% change in the measured thermal neutron flux. If the average thickness of the solid crystal, 1.57 cm, were used in a solid right rectangle model of the crystals, the neutron capture efficiency would be 0.147, a 50% deviation from the more careful result of Eq. (B.5). These percentage differences are on the order of or larger than the largest uncertainties involved in the calculation itself, so a simpler approach could have potentially had a noticeable impact on the final results of this thesis.

The crystals themselves are not actually cylindrical, but have four sides machined flat and a rounded outside corner. What effect might this have on the neutron capture efficiency? A right cylinder with a hollow bore of the dimensions of the crystals would have a volume of

$$\begin{aligned} V &= (8 \text{ cm})\, \pi\, (2.5 \text{ cm})^2 - (6.5 \text{ cm})\, \pi\, (0.5 \text{ cm})^2 \\ &= 152 \text{ cm}^3 \end{aligned}$$

This volume would have a mass of 809 g, but we know from Table 4.1 that the masses are roughly 750 g. Thus there is a volume difference between the modeled crystals and the actual crystals of 11 cm^3. Yet we have already accounted for two of the four flat sides, so the volume difference is closer to 5.5 cm^3.

The volume of the hollow core is 5.1 cm^3. Given the similar differences in volume, we may estimate the effect of not taking into account the remaining flat sides of the crystals by measuring the effect of not taking into account the hollow core. The efficiency of a solid right cylinder with two flattened sides parallel to the neutron trajectory is 0.298, or a difference of 0.955%. This value will therefore be subtracted from the value calculated in Eq. (B.5), giving

$$\text{Capture efficiency} = 0.278 \pm 0.008 \tag{B.6}$$

Given that these corrections are second-order, the total uncertainty will be held at 3%. Note again that this correction does not take into account either the bulletization or the internal electrical contact.

Appendix C

ACTIVATION / COOLDOWN DATASET CATALOG

Table C.1: Activation and cooldown timestamps. The units are in minutes, with minute zero being the start of the first activation through the 4" moderator. The actions incorporating run numbers ("Cooldown0001", "Cooldown0002", and so on) refer to the details of the actual data taking. In cases where a cooldown data run ended and the AmBe source put in place in the same minute, the source was not placed until the data run ended.

CLOVER Activation	Data run	Time (m)
Activation start		0
Activation end	Begin Cooldown0001	4256
	End Cooldown0001	5777
	Begin Cooldown0002	5779
	End Cooldown0002	7046
	Begin Cooldown0003	7047
	End Cooldown0003	8143
Activation start		8211
Activation end	Begin Cooldown0010	9690
	End Cooldown0010	10402
	Begin Cooldown0011	10403
Activation start	End Cooldown0011	11222
Activation end	Begin Cooldown0020	12689
	End Cooldown0020	12891
Activation start		14105
Activation end	Begin Cooldown0030	15443
	End Cooldown0030	15451
	Begin Cooldown0031	15465
	End Cooldown0031	15467
	Begin Cooldown0032	15468
	End Cooldown0032	15736
	Begin Cooldown0033	15831

Continued on next page

Table C.1 – continued from previous page

CLOVER Activation	Data run	Time (m)
	End Cooldown0033	15915
Activation start		16029
Activation end	Begin Cooldown0040	16893
	End Cooldown0040	17133
	Begin Cooldown0041	17261
Activation start	End Cooldown0041	17420
Activation end	Begin Cooldown0050	18212
	End Cooldown0050	18862
Activation start		18895
Activation end	Begin Cooldown0060	19711
	End Cooldown0060	20507
Activation start		20533
Activation end	Begin Cooldown0070	21882
	End Cooldown0070	23388
Activation start		23423
Activation end	Begin Cooldown0080	24110
	End Cooldown0080	24598
Activation start		24639
Activation end	Begin Cooldown0090	25469
	End Cooldown0090	26099
Activation start		26181
Activation end	Begin Cooldown0100	26921
	End Cooldown0100	27543
Activation start		27560
Activation end	Begin Cooldown0110	28335
	End Cooldown0110	28971
Activation start		28973
Activation end	Begin Cooldown0120	29699
	End Cooldown0120	30474
Activation start		30569
Activation end	Begin Cooldown0130	31393
	End Cooldown0130	32026
Activation start		32033

Continued on next page

Table C.1 – continued from previous page

CLOVER Activation	Data run	Time (m)
Activation end	Begin Cooldown0140	32732
	End Cooldown0140	33359
Activation start		33435
Activation end	Begin Cooldown0150	34234
	End Cooldown0150	35765

Appendix D

MAGE CODE EXAMPLES

The power of using object-oriented code the MaGe framework can at times be seen most easily in the code itself. This appendix displays examples of code used in MaGE to show how the various parts of MaGe interact.

D.1 The Database subsystem

In this database code example, we see the MJGeometryCloverDetector object created with a pointer to the database object:

```
MJGeometryCloverDetector::MJGeometryCloverDetector(G4String serNum):
MGGeometryDetector(serNum), theDBdetector(0) {
     theDBdetector = MJDatabase::GetCloverDetector(serialNumber);
}
```

Each geometry detector object contains a ConstructDetector method, in which the relevant database values are read in and stored for later use:

```
...
string *crystalSerialNumbers = theDBdetector->GetCrystalSerialNumbers();
...
```

Then later in the ConstructDetector method, the individual crystals are instantiated:

```
...
for( G4int index = 0; index<4; index++ )
     theCrystals[index] =
          new MJGeometryCloverCrystal(crystalSerialNumbers[index]);
G4PVPlacement *thePhysicalCrystals[4];
...
```

The MJCloverCrystal object has a similar setup, with a pointer to the CLOVER crystal database object specified by the crystal's serial number.

D.2 The Geometry subsystem

Below is a demonstration of how a detector part is built within MaGe. These code fragments assume a basic understanding of GEANT4 volume construction, so the specific calls and parameters will not be explained in detail. In this example, the detector part is a CLOVER crystal, and the database object has already been instantiated.

```
G4double crystalRadius = theDBcrystal->GetCrystalRadius();
G4double height = theDBcrystal->GetCrystalHeight();
G4double cornerRadius = theDBcrystal->GetCornerRadius();
G4double coreRadius = theDBcrystal->GetCoreRadius();
G4double coreDepth = theDBcrystal->GetCoreDepth();
G4double coreBubbleRadius = theDBcrystal->GetCoreBubbleRadius();
G4double topDeficit = theDBcrystal->GetTopDeficit();
G4double bottomDeficit = theDBcrystal->GetBottomDeficit();
G4double rightDeficit = theDBcrystal->GetRightDeficit();
G4double leftDeficit = theDBcrystal->GetLeftDeficit();
G4Material *crystalMaterial =
     G4Material::GetMaterial( theDBcrystal->GetMaterialName() );
```

With the crystal dimensions and material set, the crystal itself is constructed:

```
In this section of code, two solids are combined to make a third.
G4Tubs *bulkCrystal1Solid = new G4Tubs( "bulkCrystal1Solid", 0*cm,
     (crystalRadius-cornerRadius)*cm, (height/2)*cm, 0*deg, 360*deg );
G4Tubs *bulkCrystal2Solid = new G4Tubs( "bulkCrystal2Solid", 0*cm,
     crystalRadius*cm, ((height-cornerRadius)/2)*cm, 0*deg, 360*deg );
G4double x = 0;
G4double y = 0;
G4double z = cornerRadius/2;
G4VSolid *bulkCrystal3Solid = new G4UnionSolid( "bulkCrystal3Solid",
     bulkCrystal1Solid, bulkCrystal2Solid, 0,
     G4ThreeVector(x*cm,y*cm,-z*cm) );

The fourth solid is created and combined with the third solid to create a fifth solid.
G4Torus *bulkCrystal4Solid = new G4Torus( "bulkCrystal4Solid", 0*cm,
     cornerRadius*cm, (crystalRadius-cornerRadius)*cm, 0*deg,
```

```
     360*deg );
x = 0;
y = 0;
z = height/2 - cornerRadius;

G4VSolid *bulkCrystal5Solid = new G4UnionSolid( "bulkCrystal5Solid",
     bulkCrystal3Solid, bulkCrystal4Solid, 0,
     G4ThreeVector(x*cm,y*cm,z*cm) );
```

Continuing the theme, the fifth and sixth solids are combined to make a seventh.

```
G4Box *bulkCrystal6Solid = new G4Box( "bulkCrystal6Solid",
     (crystalRadius - (rightDeficit+leftDeficit)/2)*cm,
     (crystalRadius - (topDeficit+bottomDeficit)/2)*cm,
     (height/2 + .01)*cm );
x = (leftDeficit - rightDeficit)/2;
y = (bottomDeficit - topDeficit)/2;
z = 0;
G4VSolid *bulkCrystal7Solid = new G4IntersectionSolid(
     "bulkCrystal7Solid", bulkCrystal5Solid, bulkCrystal6Solid, 0,
     G4ThreeVector(x*cm, y*cm, z*cm) );
```

With this last solid, bulkCrystal7Solid, a logical volume is created utilizing the material obtained from the database.

```
theCrystalLogical = new G4LogicalVolume(
     bulkCrystal7Solid, crystalMaterial, "theCrystalLogical" );
```

Note that in this geometry code, references to the values obtained from the database were used throughout rather than hardcoded values.

D.3 The I/O subsystem

This first line sets the logging level. There are five levels, ranging from "debug", which prints out the most information, to "fatal", which only prints out information related to the simulation crashing.

```
/MG/manager/mglog routine
```

MaGe has the ability to read in a number from the /dev/random file, and use that as a seed for the random number generator. MaGe includes the ability to explicitly set the

seed so that the same simulation can be run multiple times for testing purposes. The randomization algorithm used is the Mersenne Twistor [100] pseudorandom number generator.

```
/MG/manager/heprandomseed 13015
```

To choose a different geometry, the name of that geometry would simply be substituted in for the word "clover" in the following line.

```
/MG/geometry/detector clover
```

These next two lines set the output scheme to that of the Los Alamos CLOVER without pulse shapes, and set the name of the output file.

```
/MG/eventaction/rootschema LANLCloverNoPS
/MG/eventaction/rootfilename ./Clover/Ge-77.root
```

In some instances, we are more concerned with higher-energy depositions, and do not need to track down particles to the keV level. In the case of double-beta decay, however, we do want to track energies to that level of detail. This next line tells the simulation to track particle energies closely. In exchange for greater accuracy, the simulation might take much longer to run.

```
/MG/processes/realm BBdecay
```

This next line sets up the progress reporting. In this case, a line will be written to the log every 100000 events, with a time stamp for benchmarking purposes.

```
/MG/eventaction/reportingfrequency 100000
```

This next line instantiates the simulation subsystems, except for the generator.

```
/run/initialize
```

The generator is set in these next five lines. In this case, the Radioactive Decay Manager creates decays from the ground state of Ge-77, with essentially no kinetic energy (the isotope is at rest). The decays are homogeneously distributed throughout the active parts of the germanium crystals. The active parts were defined in the geometry code.

```
/MG/generator/confine volume
/MG/generator/volume activeCrystal
/MG/generator/select RDMiso
/gun/energy 1e-20
/grdm/ion 77 32 0
```

Now that the detector, output file, generators, and supporting information is specified, the simulation can be run. In this case, 10 million decays of Ge-77 will be created.

```
/run/beamOn 10000000
```

VITA

Kareem Kazkaz has lived in La Trônche, Chicaco, Boumerdes, Minneapolis, Seattle, Los Alamos, and New York. He received his Bachelor of Arts in Physics from Carleton College in 1995, a Master of Science in Physics from the University of Washington in 2001, and a Doctor of Philosophy in Experimental Nuclear Physics from the University of Washington in 2006. Kareem considers himself a samurai physicist in the mold of Buckaroo Banzai, and lives in New York with his wife and two cats.